FRANZIUS-INSTITUT
für Wasserbau und
Küsteningenieurwesen

Leibniz
Universität
Hannover

Franzius-Institut für Wasserbau und Küsteningenieurwesen

Mitteilungen Heft 97

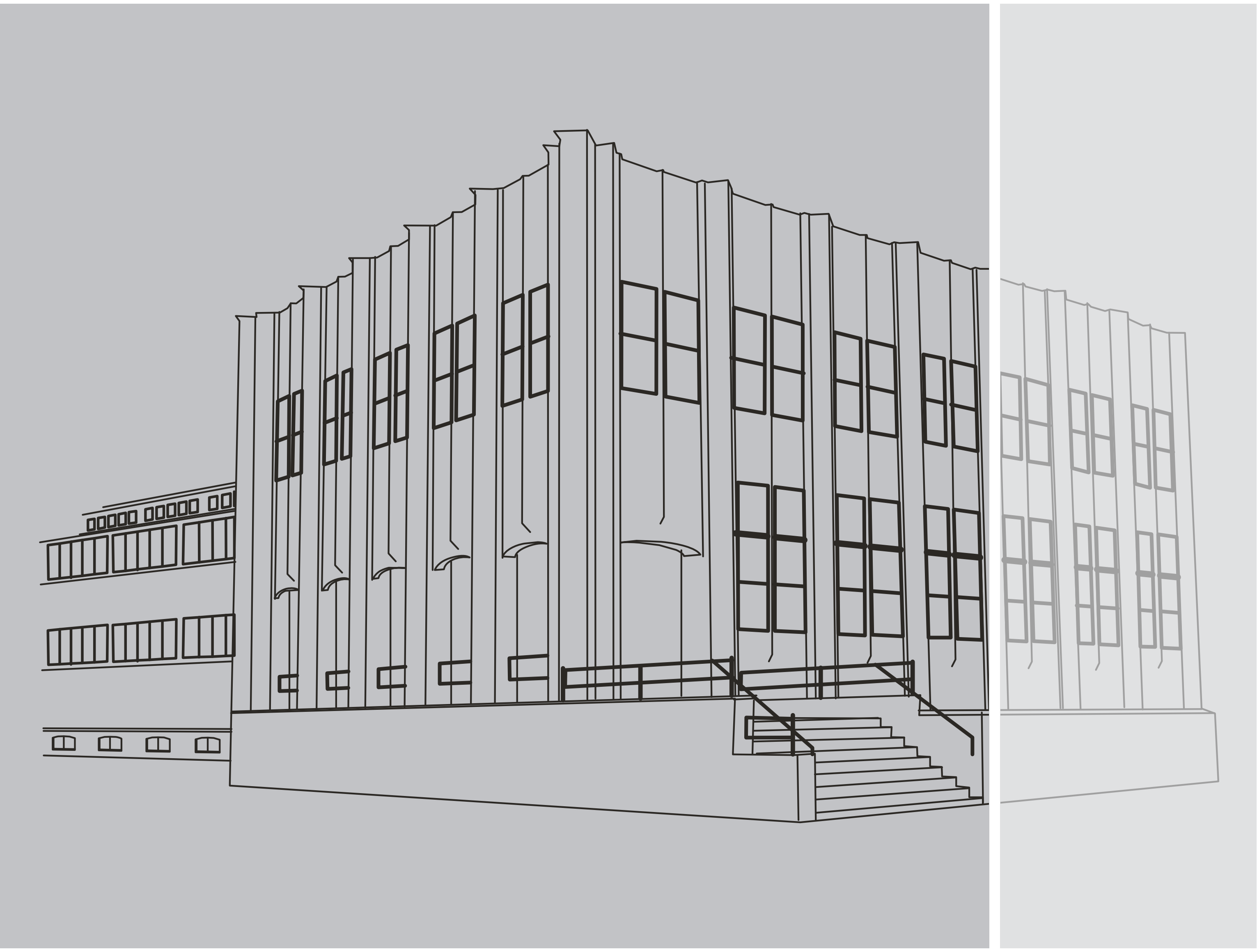

The Run-up of Long Waves - Laboratory-scaled Geophysical Reproduction and Onshore Interaction with Macro-Roughness Elements

Nils Goseberg

Mitteilung des Franzius-Instituts für Wasserbau und Küsteningenieurwesen, Heft 97

The Run-up of Long Waves –
Laboratory-scaled Geophysical Reproduction and Onshore Interaction with Macro-roughness Elements

Dr.-Ing. Nils Goseberg

Dissertation, genehmigt von der
Fakultät für Bauingenieurwesen und Geodäsie
der Gottfried Wilhelm Leibniz Universität Hannover, 2011

Impressum
Leibniz Universität Hannover
Franzius-Institut für Wasserbau und Küsteningenieurwesen
Nienburger Str. 4, D–30167 Hannover
Tel.: +49 511 762-2573
Fax.: +49 511 762-4002
Mail: sekretariat@fi.uni-hannover.de
URL: http://www.fi.uni-hannover.de
ISSN: 0340-0077

Eigenverlag des Franzius-Instituts, 2011

Content

Editorial Preface

Society is becoming ever more vulnerable to natural extreme hazards, especially on the coasts, largely as a consequence of population growth and globalization. Without any doubt tsunami are one of the most devastating geophysical hazards setting countless coastal stretches worldwide at risk. This argument has not just been proven by the disastrous consequences of the great Sumatra-Andaman earthquake and succeeding tsunami of December 2004 which caused massive loss of life and property damage. Yet, our most recent experiences from Japan are still vividly present in our minds and pinpoint even stronger to advance knowledge on tsunami and cascading effects by research and by taking action on preparation and counter measures.

In this regard the present PhD thesis by Dr. Nils Goseberg denotes a considerable contribution to help filling this scientific gap by establishing a new generation technique to allow laboratory-scaled geophysical reproduction of long waves, i.e. tsunami, in laboratory facilities. Moreover, it is revealed by experimental means how long waves evolve on sloping beaches in spatial domain and to what effect they interact with idealized coastal structures, i.e. macro roughness elements on the shoreline.

Thus, the author pleasingly disproves the commonly applied methodology to mimic tsunami by means of solitary waves in laboratory wave flumes and in consequence opens a new chapter to properly generate and fully examine long waves in physical models by means of a newly developed volume-driven wavemaker. Dr. Goseberg analyzes the run-up of long waves and achieves sound agreement with a newly derived theoretical approach. He further determines parameterized run-up charts of long waves on sloping beaches with and without structures to assess inundation extents of long waves for practical design purposes. By following this novel approach consequently, Dr. Goseberg also addresses new aspects on long waves, i.e. reflection processes, impacts on structures and energy losses during run-up which might be further elucidated in ongoing research.

Hoping that you enjoy studying this thesis and obtain a number of fruitful new insights on laboratory generated long waves in order to advance scientific knowledge, to stimulate new research approaches and to progress the exchange in between research institutions.

Hanover, April 2011

Prof. Dr. Torsten Schlurmann
(Franzius-Institute, Managing Director & Chair)

Danksagung

Die im Rahmen der Schriftenreihe der Franzius-Mitteilungen erscheinende Dissertation ist während meiner Zeit als wissenschaftlicher Mitarbeiter am Franzius-Institut für Wasserbau und Küsteningenieurwesen der Leibniz Universität Hannover entstanden.

In diesem Zusammenhang gilt mein besonderer Dank Herrn Prof. Dr.-Ing. habil T. Schlurmann, der mir durch seine Begleitung und Förderung in dieser Zeit die Anfertigung der Doktorarbeit möglich gemacht hat. Sein Vertrauen, das er in mich gesetzt hat, sowie seine vielfältigen Ideen und Vorschläge sind für mich eine wertvolle Quelle der Motivation und Information gewesen. Weiterhin danke ich Herrn Prof. Dr.-Ing. H. Schüttrumpf, der das Zweitgutachten angefertigt hat. Seine sorgfältige Durchsicht des Manuskriptes und seine konstruktiven Vorschläge sind sehr hilfreich gewesen. Auch den weiteren Mitgliedern der Prüfungskommission - Herrn Prof. Dr.-Ing. K.-H. Rosenwinkel, der den Vorsitz übernommen hat, Prof. Dr. Behrens und Prof. Dr. rer. nat. I. Neuweiler - möchte ich für Ihren Einsatz und Ihre Zeit danken.

Daneben möchte ich auch meinen Kollegen und Freunden am Franzius-Institut danken. Ohne eure Kollegialität und euer Interesse wäre mancher Tag während der letzten dreieinhalb Jahre nicht so schön gewesen. Dankbar bin ich auch Dr.-Ing. Andreas Wurpts für die fachlichen Diskussionen und Gespräche im Zusammenhang mit der Entwicklung der Wellengenerierung und den damit verbundenen Möglichkeiten. Sein Ansporn, das angewandte Verfahren immer noch weiter zu optimieren, war sehr motivierend und hilfreich. Dr.-Ing. Daniel Bung hat mir stets mit seinen profunden Kenntnissen beim Schreiben und Auswerten geholfen. Auch allen weiteren wissenschaftlichen Mitarbeitern, die an dieser Stelle ohne namentliche Erwähnung bleiben müssen, gilt mein ausdrücklicher Dank.

Dank gilt auch den Bearbeitern von studentischen Arbeiten. Die Kollegen Dipl.-Ing. A. Stahlmann, Dipl.-Ing. F. Verworn und Dipl.-Ing. M. Frieden haben mit der Anfertigung ihrer Diplomarbeit in erheblichen Maße zum Gelingen dieser Arbeit beigetragen. Meike Schubert, Michael Stresser und Patrick Gütz haben mit ihrem Fleiß dazu beigetragen, dass die Vielzahl der Versuche durchgeführt werden konnte. Ein großes Dankeschön sei auch allen Mitarbeitern aus Technik und Verwaltung für ihren Beitrag und ihr Engagement ausgesprochen. Für die kritische Durchsicht des Manuskripts oder Teilen davon bedanke ich mich bei Dipl.-Ing. M. Schollmeyer, Dipl.-Ing. K. Krämer und Dr.-Ing. D. Bung.

Mein größter Dank gilt abschließend meiner gesamten Familie. Meinen Eltern danke ich dafür, dass sie in all den Jahren und in jeglicher Hinsicht eine große Unterstützung gewesen sind. Meiner Schwiegermutter Ruth Job danke ich besonders für ihr großes Engagement im Zusammenhang mit der sprachlichen Korrektur der Texte. Meiner Frau Eva-Maria danke ich für ihre Liebe und ihre Unterstützung, die sie mir in der gesamten Zeit der Bearbeitung und darüber hinaus hat zuteil werden lassen.

Hanover, April 2011 Nils Goseberg

The Run-up of Long Waves –
Laboratory-scaled Geophysical Reproduction and Onshore Interaction with Macro-roughness Elements

Von der Fakultät für Bauingenieurwesen und Geodäsie
der
Gottfried Wilhelm Leibniz Universität Hannover

zur Erlangung des Grades eines
DOKTOR-INGENIEURS
Dr.-Ing.

genehmigte Dissertation

von

Dipl.-Ing. Nils René Goseberg
geboren am 12.10.1978
in Iserlohn

Hannover, Januar 2011

Supervisor:	Prof. Dr.-Ing. habil. Torsten Schlurmann
2nd committee member:	Univ.-Prof. Dr.-Ing. Holger Schüttrumpf
Day of doctorate:	11.03.2011

Abstract

The evolution of long waves similar to tsunami on a $1/40$ sloping beach and their interaction with idealized urban developments onshore is investigated by experimental means. The undisturbed wave run-up is firstly analyzed. Then the idealized urban development, which is represented by solid, cubic concrete blocks, is assessed. Four different configurations of those so-called macro-roughness elements are defined and the differences with regard to the effectiveness of reducing the long wave run-up are studied. Variations of the four macro-roughness element configurations are obtained through different distances between the individual obstacles and a variation of the number of obstacle rows in the onshore direction. As a result, empirical nomograms are proposed which relate the effective relative run-up and the associated run-up reduction to the surf similarity parameter and the non-linearity of the incident wave.

In contrast to commonly applied solitary waves, sinusoidal waves of one wave period with a leading depression wave are applied. Solitary waves are substituted by sinusoids of geophysically sound quantities. The correct reproduction of temporal and spatial wave properties is of major importance for the investigation of the near- and onshore interaction with macro-roughness elements and it is doubted that solitary waves comply best with these prerequisites specified by realistic events. The generation of the sinusoids is accomplished by a redeveloped, volume-driven wavemaker which is capable of reproducing waves of arbitrary wave length at laboratory scale as well as an intrinsic treatment of the reflected wave components.

The undisturbed long wave run-up is analyzed and good agreement with an existing theoretical approach to the two-dimensional run-up problem is found. An empirical fit of the experimental data on the basis of the existing theory can be expressed by a supplement of exponents. The reflection of long waves is analyzed on the basis of standard laboratory procedures. The resulting reflection coefficients, which are found to be fairly small, suggests that the reflection of long waves at mild sloping beaches should be re-examined.

The characteristic velocity flow pattern which arises during the inundation of the obstructed onshore area is illustrated qualitatively and quantitatively. Higher velocities occur during the run-up and run-down in cases of aligned macro-roughness configurations whereas velocities are smaller in staggered alignments. The rotation angle of the individual obstacles also contributes to the velocities to first order.

The acquired data sets of the experimental study, focusing on the wave run-up and the interaction with macro-roughness elements onshore, is well-suited for the validation and calibration of existing numerical models.

Keywords

long wave, wave run-up, wave run-down, macro-roughness element, wave generation, tsunami, geophysical reproduction, physical model

Zusammenfassung

Die Entwicklung von langen Wellen wie beispielsweise bei einem Tsunami auf einem $1/40$ geneigten Strand and die Interaktion mit idealisierter städtischer Bebauung auf dem Strand wird experimentell untersucht. Ausgehend von einer Untersuchung des Wellenauflaufs auf den Strand ohne störende Einflüsse gelingt ein Rückschluss auf die Auswirkungen durch die idealisierte Bebauung, die durch massive, würfelförmige Betonblöcke modelliert wird. Hierfür werden vier verschiedene Anordnungen der sogenannten Makro-Rauheitselemente definiert, die ihrerseits hinsichtlich der seitlichen Abstände und der Rotation zur Wellenangriffsrichtung variiert werden. Weiterhin wird die Auswirkung einer unterschiedlichen Anzahl von Störkörperreihen untersucht. Im Ergebnis werden empirische Nomogramme vorgestellt, die den Wellenauflauf sowie die effektive Reduktion im Vergleich zum ungestörten Fall mit dem Brecherparameter und der Nichtlinearität der Welle korrelieren.

Im Gegensatz zu herkömmlich verwendeten Wellen nach der Theorie der Einzelwelle werden in dieser Studie Sinuswellen mit einem Periodendurchgang verwendet. Das Wellental führt die Welle jeweils an. Die Sinuswellen werden deshalb verwendet, weil es für die Interaktion mit Störkörpern auf dem Strand essentiell wichtig ist, dass die verwendeten Wellen dem Naturphänomen Tsunami in geophysikalischer Hinsicht gut entsprechen. Eine ausreichende Übereinstimmung der zeitlichen und räumlichen Ausdehnung der Laborwellen für den küstennahen Flachwasserbereich kann anders als bei den verwendeten Sinuswellen für Einzelwellen nicht bestimmt werden. Die Erzeugung der Sinuswellen mit der notwendigen Wellenlänge erfolgt mit einer neuartigen Wellenmaschine, die auf dem Prinzip des Volumenstroms basiert. Das Wellenerzeugungsprinzip ermöglicht die Generierung von beliebig langen Wellen im Labor unter Berücksichtigung der reflektierten Wellenkomponenten.

Der maximale Wellenauflauf an den Strand wird analysiert und es zeigt sich eine gute Übereinstimmung mit einem existierenden theoretischen Ansatz. Durch eine weitere Anpassung der Gleichungen läßt sich mit Hilfe eines Zusatzes in einigen Exponenten eine weitere Verbesserung erzielen. Die Beurteilung der Reflektion langer Wellen an diesem flach geneigten Strand ergibt geringere Reflektionsgrade als erwartet. Die laborbasierte Reflektionsanalyse sollte hinsichtlich der Eignung für Fragestellungen mit langen Wellen verifiziert werden.

Die charakteristischen Strömungsmuster, die sich bei der Durchströmung der Makro-Rauheitselements zeigen, werden qualitativ und quantitativ analysiert. Im Vergleich mit dem ungestörten Fall entstehen hohe Geschwindigkeiten für gefluchtet angeordnete Störkörper. Die Geschwindigkeiten in versetzter Anordnung sind dagegen geringer. Neben der Ausrichtung untereinander spielt die Rotation der Störkörper zur Wellenangriffsrichtung ebenfalls eine große Rolle.

Die dargestellten Datensätze für den Wellenauflauf und die Interaktion mit Makro-Rauheitselementen auf dem Strand sind prinzipiell gut geeignet, um bestehende numerische Modelle zu validieren und auf ihre Eignung hinsichtlich der anschließenden Simulation größerer Stadtgebiete mit ausgeprägter Bebauung hin zu überprüfen.

Schlüsselwörter

Lange Welle, Wellenauflauf, Wellenablauf, Makrorauheitselement, Wellenerzeugung, Tsunami, geophysikalische Abbildung

Table of Contents

List of Figures

List of Tables

Symbols

Symbols are consistently utilized throughout the document according to the table below unless otherwise stated. In this case the different notation is given in the context of the equations in order to preserve the original notation of the references. In addition the listed subscripts are used in the thesis.

Symbol	Notation	Unit
a	coefficient Eq. (2.1.17)	[-]
a_0	Amplitude at the pump-station positive inlet	$[m]$
b_{mr}	width of macro-roughness element	$[m]$
b_{st}	width of space between macro-roughness elements (streets)	$[m]$
β	beach slope angle	[°]
c	wave celerity	$[m/s]$
C	coefficient Eq. (2.1.20)	[-]
χ_{elev}, χ_{velo}	parameter for shore line elevation and velocity Eq. (2.1.27)	[-]
δ	threshold value	[-]
ϵ	non-linearity H_0/h_0 or a_0/h_0	[-]
η	water surface elevation	$[m]$
ΔE_i	energy loss term	$[m]$
$\hat{\eta}$	non-dimensional water surface elevation η/h_0	[-]
φ	macro-roughness element angle	[°]
g	acceleration due to gravity	$\left[m/s^2\right]$
γ	beach slope angle Eq. (2.1.27)	[°]
Γ	macro-roughness element combination	[-]
h_0	water depth of the even bottom	$[m]$
H	general wave height	$[m]$
H_0	wave height at the pump-station inlet	$[m]$
$\mathcal{H}$	Nondimensional wave height Eq. (2.1.15)	[-]

Continued on next page

Continued from previous page

Symbol	Notation	Unit
k_d	beach permeability	$[m/s]$
k_{sf}	surface roughness (bottom/walls)	$[m]$
k_{mr}	surface roughness (macro-roughness elements)	$[m]$
K	coefficient	[-]
K_{is}	parameter for isoceles N-waves Eq.(2.1.26)	[-]
K_R	reflection coefficient	[-]
K_S	equivalent sand roughness / roughness height	$[m]$
L	general wave length	$[m]$
L_0	wave length at the pump-station inlet	$[m]$
λ	wave length	$[m]$
L_{mr}	length of macro-roughness area	$[m]$
L_s	length of solitary wave, Eq. (5.3.6)	$[m]$
M_f	momentum flux Eq. (2.1.20)	$[N/m]$
μ	relative wavelength h_0/L	[-]
n	number of macro-roughness rows in on-shore direction	[-]
ν	kinematic viscosity	$\left[m^2/s\right]$
ω, Ω	frequency	$(1/s)$
Π	non-dimensional variable, chapter 3.1.3	[-]
ψ_{2d}	two-dimensional obstruction ratio $\psi_{cs}\psi_{ls}$	[-]
ψ_{cs}	rate of obstruction (cross-shore)	$[m/m]$
ψ_{ls}	rate of obstruction (long-shore)	$[m/m]$
ψ_{mr}	non-dimensional obstructed height	$[m/m]$
Q_{req}	required discharge	$\left[m^3/s\right]$
R	wave run-up, cp. Fig. 3.1	$[m]$
$\boldsymbol{R}$	Nondimensional wave run-up Eq. (2.1.15)	[-]
S	stroke of a piston-type wavemaker	$[m]$
ϱ	density	$\left[kg/m^3\right]$
s	wave steepness	[-]
σ_{am}	standard deviation	[-]
ς	surface tension	$\left[kg/\left(s^2m\right)\right]$
θ	incident wave angle	[°]
t	time	$[s]$

Continued on next page

Continued from previous page

Symbol	Notation	Unit
$\hat{t}$	non-dimensional time $t\sqrt{g/h_0}$	[-]
T	wave period	$[s]$
τ	friction factor Eq. (2.1.17)	$\left[N/m^2\right]$
u_h	horizontal fluid velocity	$[m/s]$
u_s	fluid velocity Eq. (2.1.17)	$[m/s]$
U	Ursell parameter	[-]
v_x	velocity in run-up direction	$[m/s]$
$\hat{v}_x$	non-dimensional velocity $v_x/\sqrt{gh_0}$	[-]
v_y	velocity lateral to run-up direction	$[m/s]$
$\hat{v}_y$	non-dimensional velocity $v_y/\sqrt{gh_0}$	[-]
x	spatial coordinate in wave run-up direction	$[m]$
$\hat{x}$	non-dimensional spatial coordinate x/h_0	[-]
ξ_s	solitary wave surf similarity parameter	[-]
ξ_∞	surf similarity parameter in deep water	[-]
y	spatial coordinate lateral to wave run-up direction	$[m]$
$\hat{y}$	non-dimensional spatial coordinate y/h_0	[-]

Subscript	Notation
$()_{cr}$	wave crest
$()_{cs}$	cross shore
$()_e$	elasticity
$()_g$	gravitation
$()_i$	inertia
$()_{ls}$	long shore
$()_M$	model dimension

Subscript	Notation
$()_\nu$	viscosity
$()_P$	prototype dimension
$()_p$	pressure
$()_\sigma$	surface tension
$()_s$	solitary wave
$()_{sd}$	stroke of the wavemaker
$()_{tr}$	wave trough

Preface

This doctoral thesis is primarily motivated by a research project which investigated the inundation and the flow dynamics at the city of Padang, Indonesia on the basis of credible tsunami scenarios. The project was funded by the German Federal Ministry of Education and Research. Related to the numerical treatment of the problem setup, a practical aspect of the solution of the given objective was to map the seafloor of the coastal waters near Padang. Correct and highly-resolved bathymetry data sets are substantial in an adequate modeling of the near-shore hydrodynamics. On this basis an actual, accurate inundation map of the city was aimed at.

Moreover, the mission gave our team the chance to eyewitness not only the rich, diverse culture of the region but taught my colleagues and me how awe-inspiring a major earthquake could be. On the September 12th, 2007, only few hours after our arrival at Padang, the main shock with moment magnitude 8.5 struck the region. Later this day a second tremor, which was felt even stronger in Padang, reached a strength of 7.9 moment magnitude. In the light of this extraordinary experience, the panic which took possession of our survey team at that time is still in vibrant remembrance.

Only recently, the city again faced much, but probably unexpected interest from the international media when a recurrent earthquake hit the region on September 30th, 2009 at 10:16:10 UTC-time with a moment magnitude of 7.6. Although equal to the event in 2007, the tsunami risk at Padang was low. The impact of the shaking of the ground resulted in an official death-toll of 1,115, many severely damaged buildings and strongly affected livelihoods of many.

What deeply touched us during our measurement campaign in 2007 was the urban pattern of Padang, consisting of densely constructed quarters, often situated in the direct neighborhood of the shoreline. More than once our discussions touched the imagination of a potential tsunami attacking the city and the coastline of the beautiful island of Sumatra.

To close the circle, the aforementioned project which I had the honor to contribute to, also dealt with evacuation modeling and recommendations to the local government based on a realistic, numerical modeling of the hydrodynamics involved in the potential inundation due to tsunami. Yet the question how to adequately model the influence of houses and buildings (which I would like to call macro-roughness elements in the following) could not be fully answered. Unsatisfactorily, no data sets were available to rely on for the calibration of the numerical model. Hence the idea was born to start investigating the influence of those macro-roughness elements exposed to a strong unsteady flow experimentally, as for instance brought about by an approaching tsunami. While the experimental, technical capabilities had not been in place beforehand, the engagement in the experimental details brought to face more and more unknown aspects which made it impossible to cover them all. Thus my thesis only represents a small segment out of the field of interest.

Conclusively, the word *tsunami* whose meaning will be explained in the introduction is either used as singular or plural in the English language in parallel. The invariable plural is used in this text only etymologically following the Japanese origin of the word. Equally often in everyday language it appears that the word *tsunami* is expanded to *tsunami wave* which is likewise avoided herein. The word *tsunami wave* shapes a pleonasm which redundantly addresses the same phenomenon.

1 Introduction and Objective

1.1 Tsunami

The phenomenon tsunami represents a wave or a series of waves propagating in oceans, bays, lakes or reservoirs caused by a sudden, vertical displacement of a column of water. The linguistic root of the word "tsunami" originates from the Japanese language. Japanese fishermen created the term as a combination of the words *'tsu'* (port, harbour) and *'nami'* (wave) when they repeatedly observed coastal devastation or flooded villages around their home ports. The devastation presumably was meant to stem from exceptionally high waves onshore while no indication for such wave heights could be observed by the Japanese fishermen in open water. A second characteristic of a tsunami is the sudden, life-threatening convention in which the waves make landfall after evolving from long waves and give way to a series of broken disintegrated shorter waves riding on top of a momentum-loaded surge. The waves are often hardly detectable on time to take precautionary measures. The devastating impact of those waves on coastal communities gives rise to an increase of scientific diligence and pursuit to intensify the insight into the wave propagation and the run-up process, which might finally lead to decreasing fatalities in future incidents.

Reports of tsunami can already be found in early historic documents although many more occurrences must have happened even earlier but were forgotten since threatened communities did not always have a pronounced writing culture at their disposal. Among the most destructive tsunami occurring in the past the Boxing Day tsunami in 2004 around the Indian ocean, killing more than 230,000 people or the Meiji-Sanriku tsunami in 1896 on the Japanese coastline causing an exceptionally high run-up up to $38.6\ \mathrm{m}$ (Wiegel, 1964; Bryant, 2008), could be mentioned.

The causes of long wave generation are numerous and statistical reoccurrences of these triggering events do not follow simplified rules but depend on many complex processes such as material properties, tension level, solid state mechanics and other more random factors. Nowadays, a few distinct processes are relevant in triggering long waves in several environments. Müller (1995) summarized a comprehensive list of generative mechanisms which are liable to cause impulsive and long waves – rock/landslide, avalanches and ice slides, ice calving, slump of ice crusts of alpine seas, (submarine) earthquakes and gas eruptions. In addition, volcano eruptions such as the Krakatau eruption in 1883 (Lange et al., 2001) are well known to cause severe tsunami events. Also impacts of asteroids in marine environments are a - though more infrequent - source of potential tsunami waves. Yet at least two thirds of the earth's surface is covered with water and thus could be target of solid projectiles (Weiss et al., 2006).

The main characteristic of a tsunami is probably its fast propagation in deep water, equivalent to the square root of the water depth times the gravitational acceleration associated with only little surface displacement as long the water depth remains deep. Secondly those waves are generally much longer compared to wind waves. Fig. 1.1 depicts a basic classification of some waves with respect to their frequency. Long-period waves where tsunami together with waves generated by storm systems belong to are classified as waves with periods in the range of $5 \text{ min} - 24 \text{ h}$ (Kinsman, 1965) while earthquake generated tsunami should be further limited in their range of periods to $5 \text{ min} - 60 \text{ min}$. The initial surface elevation of tsunami which is generated by one of the above listed sources is primarily restored under the influence of gravity but especially over longer propagation distances the Coriolis force also influences its wave motion.

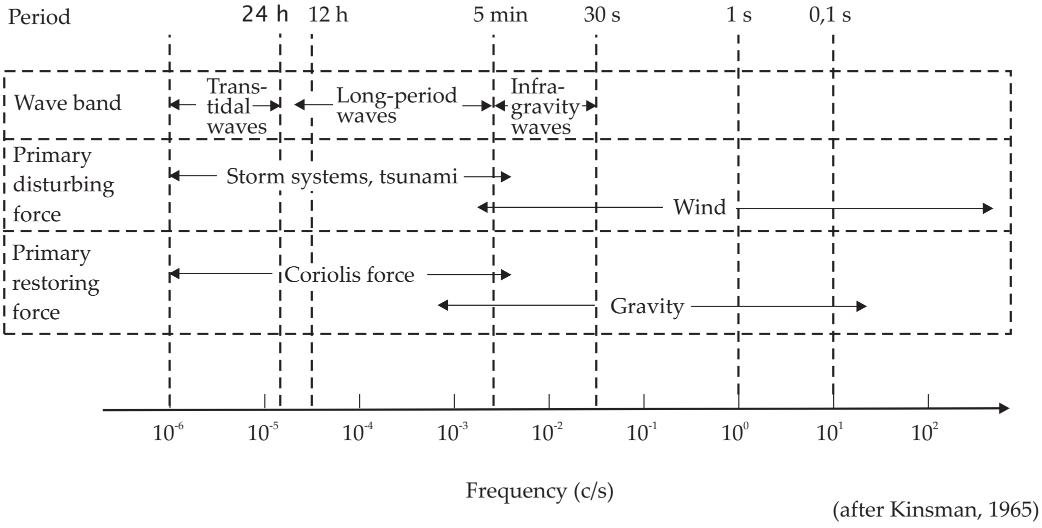

Figure 1.1 Classification of long-period waves and their primary disturbing and restoring forces (after Kinsman, 1965)

Over the course of time the wave or the wave train transforms as it enters shallower water depth or approaches continental shelves. While generally the wavelength decreases and the propagation speed slows down, in contrast wave heights increase significantly. Those substantial water surface gradients in combination with high flow velocities towards the coast during run-up and backwards during run-down essentially constitute the perilousness of the phenomenon. A segment thereof – the interaction of macro-roughness elements with the run-up of long waves – will be addressed in this thesis. The following section summarizes the main objectives.

1.2 Objective and Scope

The main objective of this study is the analysis of the interaction between the long wave run-up on a plane beach and coastal urban structures. Long waves which approach from deep into shallow coastal waters steepen manifold in amplitude, any of these may eventually inundate flat, low-lying coastal plains. While in particular wave propagation along with the effect of frequency and amplitude dispersion is well understood today, most processes in the run-up and surge flow stage when the tsunami actually impacts coasts are less clearly understood. This is because these complicated processes often involve a two-phase flow with water and suspended sediment, strong turbulences, energy dissipation caused by bottom roughness effects, and wave structure interaction. Generally, due to varying land use pattern, the actual run-up process is highly complex and non-linear.

The methodical approach which has been chosen is purely experimental due to the fact that the investigation by means of analytical or numerical techniques is not expected to adequately reproduce the detailed, sophisticated interdependencies between the approaching wave and the idealized coastal development. The idealization of coastal developments in the laboratory is achieved by abstracting vertical structures on the shore and near the shoreline with pattern of regularly arranged solid blocks.

Thus first of all, the wave run-up has to be reinvestigated experimentally, without the presence of bottom friction. Comparisons to existing analytical approaches need to validate the experimental reliability. In order to match those physical models with geophysical spatial and temporal scales, a novel wave generation methodology has been established that allows for the generation of arbitrary long waves in the laboratory. As it is not intended to focus on intrinsic surface or micro-roughness effects (friction arising from the bottom and the wall in the presented case) boundary layers should be excluded to the greatest extent by experimental means. On the other hand macro-roughness due to idealized coastal settlement represents the focal point.

Nowadays coastal areas and cities face an increase in population worldwide. Recently improved census data and supporting digital elevation models allow an analysis of population density along world's coastlines. Small and Nicholls (2003) point out that the population inhabiting the near-coastal zone, which in their study is defined from $100\ \mathrm{km}$ away and $100\ \mathrm{m}$ above the coastline, is about $1.2 \cdot 10^9$ people or in other words is about $23\ \%$ of the global population of the year 1990. According to the report it is equally apparent that the average population density in the near-coastal zone (112 people/km^2) is roughly three times higher than the average global population density (44 people/km^2).

This tendency in turn results in higher building densities along threatened coasts. Existent and newly constructed buildings serve for residential, commercial or recreational purposes. Thus, size, height and width as well as stability varies considerably and in consequence of enhanced technology and income, buildings become more stable and rigid in coastal areas. Building density, which represents an important influencing factor in the context of tsunami run-up, varies according to different characteristics of urban quarters. Despite the diverse urban pattern observed in coastal cities around the globe, this study aims at investigating the effects of wave interaction in regard to coastal urban structures in a generalized, abstract manner. Structures and buildings are therefore handled as solid, quadratic blocks throughout the experiments and no distinctions are made to model macro-roughness divergently. The width, length and height of the idealized macro-roughness elements is kept constant. In contrast, streets between houses that serve as flow paths for the surging water are modeled with uniform (throughout one macro-roughness combination) but varying street width over the complete set of experimental runs.

The interaction of obstacles in or exposed to a steady-state fluid movement have been studied by mechanical, civil and coastal engineers during the past decades. Though not closely related to a tsunami at first glance, a prominent example of these investigations is the constriction of a river course due to bridge piers or building excavations in rivers that as a result lead to an upstream impoundment (bridge pier backwater) and accelerated flow in the proximity and in-between the bridge pillars (Bollrich, 2000, § 6.6.3). Due to the steady-state flow conditions Rehbock (1921) found analytical solutions to the backwater height by means of classification and parametrization of a bridge pier cross-sectional shape. Another example in the field of river hydraulics is the use of protruding boulders in rock chutes, which are now more frequently deployed in order to facilitate river restoration (cp. Pagliara and Chiavaccini, 2006, and references therein). As opposed to these two examples, where generally uniform flow conditions could be assumed, the objective of the present study is to investigate the effects of macro-roughness conditions caused by human settlements. The macro-roughness elements defined herein were exposed to unsteady non-uniform flow (due to tsunami surge flow) and appeared an order of magnitude bigger than their counterpart boulders in rock chutes. While analytical formulation of the impact of the flow could be quantified straightforward for uniform flow, it will be seen that only empirical means allow for a formulation of the effects in the non-stationary flow in the tsunami case.

Besides the characteristic flow conditions in tsunami inundation, which will be used in the study, the focus will lie explicitly on non-breaking long waves. As perceptible in recent literature (Madsen et al., 2008; Madsen and Fuhrman, 2008; Madsen et al., 2009) it is likewise assumed that the phenomenon tsunami in coastal waters mainly consists of long-period wave motion ($8 - 30\ \mathrm{min}$) which very seldom breaks (cp. also Section 2.1). Associated waves of much shorter wave periods ($10 - 15\ \mathrm{s}$) which potentially evolve while propagating in deep water are in these cases anticipated to ride on top of the long-period wave motion. These waves are assumed to eventually break when the physical breaking limit is reached. In regard to wave run-up and wave-structure interaction, these shorter waves of lower energy supposedly only minimally contribute to the maximum wave run-up. Therefore the objective is consecutively studied without these diverting effects additionally induced by wave breaking.

1.3 Outline

A review of previous studies which deal with general aspects of the long wave run-up, with long wave generation techniques and with wave-structure interaction is presented in Chapter 2. Consequences relevant to the outlined objectives derived from the survey of the existing literature are also outlined. In Chapter 3 the applied wave flume, general considerations of the experimental procedures and the developed wave generation mechanism are described in detail. The results of the entire run-up experiments as well as the scope of the different experiment layouts are reported in Chapter 5. Discussion and conclusions of the physical modeling of macro-roughness effects are comprised in Chapter 6.

2 Survey of Previous Literature

2.1 The Run-up of Long Waves

A quantification, or at least a sound estimation of the maximum run-up of long waves onto natural beaches, is one of the quintessential questions that arise in the context of the geophysical phenomena tsunami because evacuation procedures and hazard mitigation measures depend on the temporal and spatial distribution of the on-land flooding due to incoming waves or wave trains. In literature, analytical, physical and numerical methods have been adopted to determine the wave run-up depending on the incoming wave height and wave steepness, the beach slope and the wave length. A valuable source of information on the historical evolution of the research topic is included in the review paper written by Synolakis and Bernard (2006). Also, a comprehensive chronological compilation of publications on the subject of periodic wave run-up is given in Müller (1995). The run-up itself is commonly defined as the height an incident wave will rise on a structure or a natural beach (for a schematic drawing please cp. Fig. 3.1). Both breaking and non-breaking waves have been addressed in literature. Also linear, cnoidal and solitary wave theory have been applied for the investigation of long wave run-up (Kaplan, 1955; Hall and Watts, 1953; Synolakis, 1987, e.g.).

The basic governing equations for analyzing approaching waves propagating in the water are already known for more than 150 years. These are the Navier-Stokes (NS) equations incorporating the conservation of mass and momentum. Until now the practical utilization of this set of equations is limited because it is markedly difficult to solve them either analytically or numerically for an actual geophysical free-surface flow problem. Under the assumption that tsunami are long waves, the most common simplification consists of the elimination of viscous stress and vertical gradients in the equations, so that the classic wave equation $\nabla^2\eta = c^{-2}\partial^2\eta/\partial t^2$ with η surface elevation, $c = \sqrt{gh}$ (wave celerity) for the even bottom case (g = acceleration of gravity, h water depth) and the linear shallow water (LSW) equation evolves for the case with varying sea floor. When nonlinear terms remain after simplification, the emerging equation is known as the nonlinear shallow water wave (NSW) equation. Further incorporating dispersive terms lead to Boussinesq equations whereas an elimination of the viscous terms in the NS equations yield the Euler or potential flow equations (Synolakis and Bernard, 2006).

For the first time Hall and Watts (1953) investigated the run-up of a single long wave approaching a sloping beach. The waves which they utilized resembled the classic shape of solitary waves as first described by Russell (1845). The authors determined maximum wave run-up according to their empirically generated solitary waves for a beach setup attached to an even bottom section and found a run-up law by means of dimensional analysis. As reproduced in Synolakis and Bernard (2006) the run-up normalized by the offshore water depth d is expressed in the form $R/d = \alpha(\beta)(H/d)^{f(\beta)}$, where $\alpha(\beta)$ and $f(\beta)$ were empirical coefficients, which are dependent on the beach slope. However no distinction was made between breaking and non-breaking waves. Also, similar experiments conducted by Camfield and Street (1969) have been reported that show early attempts to study the evolution of solitary wave behavior on a mild slope.

Kaplan (1955), who generated periodic waves climbing up a sloping beach after traveling over a flat bottom region, derived two empirical expressions for the wave run-up. Eq. (2.1.1) and (2.1.2) directly depend on the wave steepness while the beach slope is depicted by limiting the validity of the equations. According to Synolakis (1987) the report about experimental results shows the disadvantage that neither breaking/non-breaking wave conditions nor short/long waves were differentiated nor data tabulated. The empirical formula was nevertheless utilized to validate theoretical and experimental studies for a long time. It reads

$$\frac{R}{H} = 0.381\left(\frac{H}{L}\right)^{-0.316} \quad \text{for} \quad \tan\beta = 1/30 \tag{2.1.1}$$

$$\frac{R}{H} = 0.206\left(\frac{H}{L}\right)^{-0.315} \quad \text{for} \quad \tan\beta = 1/60 \tag{2.1.2}$$

where R/H denotes an amplification factor of the incident offshore wave height H, L is the wave length and β is the beach slope.

With focus on seawall and breakwater design Hunt (1959) reprocessed former published experimental studies, conducted additional experiments and analyzed these with respect to the interaction of incident waves and coastal defense structures. Besides reflection and heat disposal due to turbulence, as well as surface roughness, the author depicted potential energy in form of a wave run-up as first order energy dissipation/transformation in the near beach coastal processes. With the objective to gain insight into the driving physical processes, a careful examination by means of dimensional analysis yielded a run-up formula for breaking and surging waves. Wave breaking on the structure or beach occurs when $\tan\alpha \geq \sqrt{H/T^2}$ with $\tan\alpha$ the beach slope, H the (offshore) wave height and T the period of the incident wave. For the breaking case, normalized wave run-up due to regular waves can be given in the form of equation (2.1.3)

$$\frac{R}{H} = \frac{K\tan\alpha}{\sqrt{\frac{H}{T^2}}} \quad \text{for} \quad \begin{cases} \sqrt{\frac{H}{T^2}} > \tan\alpha \\ H \approx H_0 \end{cases} \tag{2.1.3}$$

In the original paper the coefficient $K = 2.3$ is measured in units of ft$^{1/2}/s$. Eq. (2.1.3) can easily be recast to the dimensionally homogeneous Eq. (2.1.5) by means of a gravity constant in imperial units and the definition of the well known deep water wave length (Hughes, 2004). The right hand side of the equation depicts the so-called surf similarity parameter which relates the non-dimensional run-up of waves to the beach slope divided by the square root of the wave steepness. The non-breaking upper limit of wave run-up on a uniform slope is then given according to (CEM U.S. Army Corps, 2002) reading

$$\frac{R}{H_0} = \sqrt{2\pi}\left(\frac{\pi}{2\beta}\right)^{\frac{1}{4}} \tag{2.1.4}$$

Until now, these findings hold true for the conventional wave run-up and are widely used in engineering practices, though validity is limited to slopes steeper than $\geq 1/10$ since equations (2.1.3) and (2.1.4) were found and fitted empirically from laboratory test results. Nevertheless these achievements mark an important milestone and it will be later seen that the surf similarity parameter is of equal importance in long wave run-up.

Then Battjes (1974) comprehensively described the idea of surf similarity in a physically sound manner and outlined the consequences for breaker type classification and also for wave run-up relationships given as (2.1.5)

$$\xi = \frac{s}{\sqrt{H/L_0}} = \frac{sT}{\sqrt{2\pi}}\sqrt{\frac{g}{H}} \tag{2.1.5}$$

where $H =$ wave height at an deep water depth h, $T =$ wave period, and $L_0 =$ deep water wave length. The author also derived his results from a dimensional analysis of relevant physical variables which were able to interfere with and affect the surf zone dynamics. It turns out that a simple dependency of beach slope and the square root of the wave steepness H/L_0 exists.

With regard to the applicability of wave theories to various wave phenomena and also to the question how the so-called long-wave paradox[1] could be explained, Ursell (1953) elucidated the problem setting and derived a non-dimensional factor which is nowadays often used by coastal engineers. It reads

$$\frac{\eta_0 \lambda^2}{h_0^3} \sim U = \frac{\epsilon}{\mu^2} = \frac{H_0 \lambda^2}{h_0^3} \tag{2.1.6}$$

where $\epsilon = \eta_0/h_0$ denotes the relative wave height, $\mu = h_0/\lambda$ denotes the dimensionless wave length, λ is a characteristic horizontal scale and h_0 is the depp water depth. In his important work long waves are generally classified as waves whose wave length is much larger than the water depth. In the course of the work three different equations were derived classifying the wave types given by (cp. also Svendsen, 2006)

$$U \equiv \frac{\epsilon}{\mu^2} \begin{cases} \ll \mathcal{O}(1) & \text{linear shallow water waves} \\ = \mathcal{O}(1) & \text{cnoidal and solitary waves} \\ \gg \mathcal{O}(1) & \text{non-linear shallow water waves} \end{cases} \tag{2.1.7}$$

It was shown by Ursell (1953) that for the Ursell parameter ranging in the order of unity, $\epsilon = \mathcal{O}\left(\mu^2\right) \ll 1$ or $\epsilon/\mu^2 = \mathcal{O}(1)$ holds true and all the non-linear terms can be retained. It results in a wave theory of moderate amplitudes, which is applicable to cnoidal and solitary waves. Linear wave theory is valid if the following applies: $\epsilon/\mu^2 \ll \mathcal{O}(1)$. Consequently all non-linear terms vanish. Finally when $\epsilon/\mu^2 \gg \mathcal{O}(1)$ holds long waves of large amplitude are addressed which can accurately be described by the non-linear shallow water wave equations.

Hammack (1972) presented theoretical and experimental studies which deal with arbitrary bed movements of a fluid domain capable of generating water waves. The chosen basic approach aimed at representing the generation of a tsunami by means of seismic disturbances in prototype and the following deep water propagation in constant water depth. In the experiments, the wave generation had been accomplished by a vertically moving bottom section at one end of the wave flume in a either positive or negative direction. For the positive upthrust it interestingly appears that the dis-

---

[1] Seemingly in contradiction to the observation of Rayleigh, who postulated solitary waves to be of permanent form, Airy found that if the pressure at any point in a fluid is equal to the hydrostatic pressure caused by the above water column, any wave form can only propagate in shallow water with changes in the wave form.

placement of the water surface after a period of time evolved into a series of solitary-like waves, led by the highest wave crest and trailed by smaller oscillatory waves of smaller amplitude than the first one. It was reported that the series of waves which evolved after wave generation remained symmetric in amplitude and period while the waves itself continued to separate from each other in terms of distance or nodal period due to higher wave celerity $c = \sqrt{g\left(h+\eta\right)}$. The separation process is also sometimes called solitary wave fission. Even though solitary waves had been studied beforehand by some researchers without directly linking them to the tsunami (e.g. Russell, 1845) the findings of Hammack (1972) drew attention to this wave form in the context of modeling tsunami especially in continental shelf and shallow water conditions.

From that time on until present various authors did research on solitary waves in the aforementioned context of tsunami and much progress on that topic has been achieved. Among those one of the most prominent, substantial works was published by Synolakis (1987), who determined correlations between the normalized wave run-up and beach slope, wave height and water depth of breaking and non-breaking solitary waves. His results were obtained by experimental studies in a flume which is described in detail in Chapter 2.2 for an even bottom section attached to a plane impermeable beach. It should also be noted that this work summarized the state-of-the-art knowledge at that time and categorized the available run-up laws of linear and nonlinear periodic and solitary waves. The presented experimental results were also fortified by analytical means. For this, the author derived exact solutions of the linear and nonlinear shallow water wave equations for the climb of long waves on plane beaches. These solutions were compared to his laboratory results and good agreement was found. Unfortunately only minimal discussion was focused on the assumption that solitary waves adequately model tsunami behavior on a continental shelf. Although important to link the experiments to prototype conditions, an analogy between model dimensions and horizontal and vertical length scales is absent. Thus, geophysical scales of solitary waves in context of tsunami were questioned recently. Later, this argument will be picked up again. As a limiting case of the cnoidal wave theory an incoming solitary wave can be expressed as (Wiegel, 1964)

$$\eta\left(x,t\right) = H\mathrm{sech}^2\left[\sqrt{\frac{3}{4}\frac{H}{h^3}}\left(x-ct\right)\right], \quad c = \sqrt{gh\left(1+\frac{H}{h}\right)} \qquad (2.1.8)$$

The run-up law for breaking and nonbreaking solitary waves which Synolakis (1987) derived is written as follows

$$\frac{R}{d} = 2.831\sqrt{\cot(\beta)}\left(\frac{H}{d}\right)^{5/4} \qquad \textit{nonbreaking} \tag{2.1.9}$$

$$\frac{R}{d} = 0.918\left(\frac{H}{d}\right)^{0.606} \qquad \textit{breaking} \tag{2.1.10}$$

with $d =$ offshore water depth. According to Fuhrman and Madsen (2008) it can be elegantly shown that Eq. (2.1.9) can again be recast into Eq. (2.1.11), expressing the normalized wave run-up in terms of the surf similarity parameter under the assumption of small non-linearity in the deeper region offshore, hereby neglecting some non-significant constants. This leads to a novel solitary wave surf similarity parameter $\xi_s = s/(H/d)$.

$$\frac{R}{H} = 2.831\left(\frac{H}{d}\right)^{-1/4}\xi_s^{-1/2} \tag{2.1.11}$$

According to Synolakis (1987), single non-periodic breaking or non-breaking long waves have rarely been investigated experimentally and solitary waves have been applied instead. Solitary waves are basically characterized by a positive amplitude while they miss out wave depression which is often observed during tsunami events in nature. This is likely due to problems arising in existing long wave generation techniques. A broader discussion on assets and drawbacks of long waves generation techniques apparent in literature is presented in Chapter 2.2. However (2.1.9) addressing solitary wave run-up was extensively applied to validate numerical models in later studies.

The problem how to relate maximum solitary wave excursion to wave run-up expressions which are similar to the surf similarity concept was addressed by Kobayashi and Karjadi (1994). Outlining the fact that problems arise in the definition of specific periods of solitary waves it was proposed to introduce a threshold value δ for the free surface equation of the wave. This effectively yielded a representative period T_S or wave length containing its characteristic wave energy. The authors chose a threshold value of $\delta = 0.05$ but also admitted that not much variation for the resulting run-up formula occurred. The results from a numerical model were applied and subsequently compared to experimental data of Synolakis (1987) and fitted well. A parametrized run-up law involving the surf similarity parameter was then proposed for the threshold $\delta = 0.05$ of the solitary wave given as (2.1.12).

$$\frac{R}{H} = 2.955\xi_S^{0.395} \qquad \text{valid for} \qquad 0.125 \leq \xi_S \leq 1.757 \tag{2.1.12}$$

Here R/H is the non-dimensional run-up and ξ_S is the surf similarity parameter of a solitary wave. The coefficients to fit the experimental data to the formula yield a correlation of 0.996 for thresholds $\delta = 0.01$, 0.05 and 0.1. The wave length of the solitary wave was defined as $L_0 = gT^2/2\pi$ where T was the representative wave period used in (2.1.5). By introducing the surf similarity parameter for solitary waves, an attempt was made of an advanced interpretation of characteristics of the evolution of solitary waves onshore. A demand for additional data sets was also identified in order to broaden the understanding of the run-up of such waves especially for gentler slopes.

A research program dedicated to important physical parameters of tsunami run-up, starting in 1992, was funded by the National Science Foundation (NSF) of the United States. It augmented the limited experimental data until then, also including three-dimensional tsunami run-up experiments. Briggs et al. (1995b) reported on portions of the experimental results that were achieved in relation to the aforementioned research program. Call for large scale physical experiments at geophysically relevant scales motivated the research agenda. Solitary waves on a $1/30$ slope had been investigated in both a wave basin and a wave flume. The authors stated that physically relevant idealized tsunami conditions should be addressed. Especially the chosen beach slope seems to be more realistic than those of other studies and compared to prototype conditions. Whereas, initial wave lengths of the applied solitary waves appear to contradict their positive approach to generate prototype-alike large scale data sets. Wave heights that were reported suggest a length scale $\approx 1 : 100$ and the wave length therefore would at prototype have to range in the order of tens of kilometers. However the reported wavelengths were at least well below a power of ten. The experimental results are yet of importance because run-up values are consistently below the empirical run-up curve for solitary waves what might be due to an apparent influence of milder beach slopes as pointed out by Fuhrman and Madsen (2008).

Motivated by two devastating tsunamigenic earthquakes in 1992 (Sept. 2nd, Nicaragua and Dec. 12th, Flores Island) Tadepalli and Synolakis (1994) made an advance in modeling near-shore tsunami run-up by means of a class of N-shaped waves. As an example isoceles N-waves are given by Eq. (2.1.13)

$$\begin{aligned} \eta\left(x,0\right) = \frac{3\sqrt{3}}{2} H \mathrm{sech}^2\left(K_{is}\left(x-x_1\right)\right)\tanh\left(K_{is}\left(x-x_1\right)\right) \\ K_{is} = \frac{3}{2h}\sqrt{\frac{H}{h}\sqrt{\frac{3}{4}}} \end{aligned} \tag{2.1.13}$$

While at the time of formulation state-of-the-art numerical models underpredicted the absolute magnitude of the maximum observed run-up, leading depression waves were proposed as an alternative to the canonical tsunami run-up problem. The canonical tsunami run-up problem is what is referred to as a long wave propagating over a region of constant depth, and then climbing up a beach of constant slope. The formalism of shallow water wave equations was used to derive a solution to the qualitative run-up of different types of N-waves which are physically correct to first order. Fig. 2.1 depicts a leading depression N-wave in comparison with a solitary wave. The maximum run-up for isosceles N-waves given by Eq. (2.1.13) as an example of the class of N-waves is given by (2.1.14)

$$\boldsymbol{R} = 3.86\left(\cot\beta_0\right)^{\frac{1}{2}}\mathcal{H}^{\frac{5}{4}} \tag{2.1.14}$$

where $\boldsymbol{R}$ denotes maximum wave run-up, β_0 beach slope angle and $\mathcal{H} = H/h_0$ nondimensionalized wave height. A comparison between (2.1.9) and (2.1.14) reveals that assuming similar wave amplitudes of leading-elevation N-wave and the solitary wave N-waves cause 36.4% higher run-up values. This finding highlights an important step in modeling near-shore tsunami events.

$$\frac{\boldsymbol{R}|_{N-wave}}{\boldsymbol{R}|_{solitary\ wave}} = 1.364 \tag{2.1.15}$$

Run-up of solitary, impulsive waves, which were generated by means of sliding masses along an inclined plane, have been investigated experimentally by Müller (1995). A dimensional analysis of the dominant physical quantities and multi-regression analysis revealed a run-up law which is valid at relatively steep slopes (vertical wall, 1:1, 1:3). The objective of the study was to gain insight into wave run-up and overtopping due

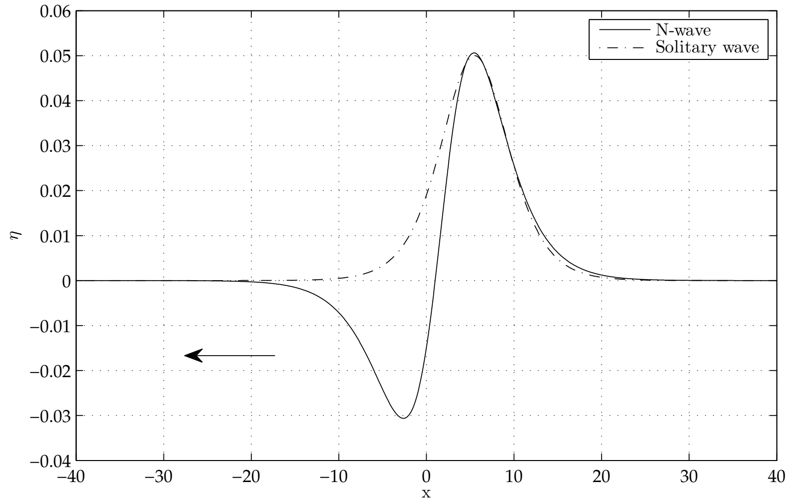

Figure 2.1 Surface elevation of a N-wave in comparison with a solitary wave. The wave profile of the N-wave is described by $\eta(x,0) = (\epsilon\mathcal{H})(x - X_2)\,\mathrm{sech}^2[\gamma_s(x - X_1)]$, with η being the surface elevation at a position x at time $t = 0$, ϵ a scaling parameter for the amplitude, and a distance $L = X_2 - X_1$. The surface of the N-wave is given by $\epsilon = 0.345$, $L = 1$, $\mathcal{H} = 0.05$.

to mass failure in alpine environments as in Switzerland at concrete and gravity dams. The normalized run-up R/h is given as

$$\frac{R}{h} = 1.25\left(\frac{\pi}{2\beta}\right)^{\frac{1}{5}}\left(\frac{H}{h}\right)^{\frac{5}{4}}\left(\frac{H}{L}\right)^{-0.15} \tag{2.1.16}$$

where h is the water depth, β the slope angle, H/h the normalized wave height and H/L the wave steepness. Thus, the run-up is almost proportional to the wave height of the incoming wave, whereas major wave length induces higher run-up for the investigated setup.

A set of studies focuses on the effects of permeability and surface roughness on sloping beaches. Energy dissipation at the run-up tongue and during the up-rush or surge flow phase along the beach slope, resulting from momentum exchange and turbulence effects, increases according to augmented permeability and roughness at the surface. Yet most experiments in literature are designed to preclude roughness effects in order to circumvent decrease in wave run-up and deviations in horizontal velocities. Explicit focus was first laid on that matter by Kishi and Saeki (1966). The authors investigated the shoaling, breaking and run-up of solitary waves on impermeable rough slopes. With reference to Freeman and Le Méhauté (1964) the normalized wave run-up is given by Eq. (2.1.17)

$$\frac{R}{h_0} = \left(\frac{u_s^2}{2gh_0}\right)\frac{(1+a)(1+2a)}{1+(f/a^2S)} \tag{2.1.17}$$

where R is run-up, h_0 water depth at the beach toe, u_s fluid velocity in the leading wave element at the shoreline, f friction factor defined by $\tau = \rho f u^2$ and $a =$ an empirical coefficient. The effect of friction on the beach surface leads to deformations of the run-up tongue during the up-rush on the beach slope that converts from a leading edge into a leading wave element with a parabolic wave front. From their experiments a favorable agreement was found with Eq. (2.1.17). Similarly, Heitner and Housner (1970) investigated tsunami run-up numerically and subsequently compared their results with previous experimental studies. Wave run-up was also found to be proportional to the wave steepness as well as to the beach slope. Increasing run-up was discovered with a decrease in wave steepness and decrease in beach slopes. Also bottom friction caused significant reduction of the wave run-up whereas the reduction is appreciably more on milder slopes. In addition, Teng et al. (2000) further analyzed bottom roughness influence to wave run-up on beach slopes because at that time no consensus was obtained on the question which roughness coefficient formula was to be applied to numerical models in general. Solitary waves were applied in that context and wave run-up was measured experimentally at varying beach slopes. As a result it was found that a decrease in normalized run-up was caused when rough conditions were tested. In that regard shallower beach slopes had greater contribution to the run-up reduction. Consequentially it was concluded that especially on very shallow natural coasts the calculation of tsunami run-up by means of an inviscid wave theory could cause major errors and could probably not be adequate for predicting the run-up accurately. The effect of permeability, due to a beach surface covered with an armor layer, was addressed by Gedik et al. (2005) who examined wave run-up at a 1:5 sloping smooth, sandy and armored beach of non-breaking solitary waves. A decrease in wave run-up of nearly 50% was determined and an empirical run-up law was proposed.

Based on field observations there is evidence that maximum wave run-up under natural conditions is mostly forced by long-period wave motion. That is attributed to the fact that offshore wave energy in longer portions of the incoming wave spectrum is usually not dissipated by wave breaking in the surf zone. Liu et al. (1991) summarized several studies and made contributions in that matter supporting the fact that also the long wave run-up related to a tsunami is affected by wave breaking only to second order.

A non-compliant though interesting empirical approach has been reported by Plafker (1997) who suggested that the run-up is never more than twice the height of the deformed sea floor offshore, except in areas where extreme coastal steepness contributes to tsunami evolution (see also Synolakis and Bernard, 2006). Later Okal (2004) confirmed Plafker's rule of thumb by means of a sequence of numerical studies at least for near-field tsunami and proved its usefulness as a rough estimate of expectable inundation spread.

At this time analytical run-up expressions were derived by linearisation of the governing equations. Synolakis (1987) presented a derivation of his approximate nonlinear theory on the solitary wave run-up based on a simplified set of the transformation first published by Carrier and Greenspan (1958). Then, Li and Raichlen (2001) found that differences arise when the complete transformation was applied in deriving the exact nonlinear theory of solitary wave run-up onto a sloping beach. The author identified the importance to include higher-order correction terms in the run-up law stated by Synolakis (1987) (R_s/h_0, Eq. (2.1.9)). The maximum run-up when the shoreline velocity equals zero is given by (2.1.18a)

$$\frac{R}{h_0} = \frac{R_s}{h_0} + \frac{R_{cr}}{h_0} = \frac{R_s}{h_0}\left(1 + \frac{R_{cr}}{R_s}\right) \tag{2.1.18a}$$

with

$$\frac{R_s}{h_0} = 2.831\sqrt{\cot\beta}\left(\frac{H}{h_0}\right)^{5/4} \tag{2.1.18b}$$

$$\frac{R_{cr}}{h_0} = 0.293\,(\cot\beta)^{3/2}\left(\frac{H}{h_0}\right)^{9/4} \tag{2.1.18c}$$

$$\frac{R_{cr}}{R_s} = 0.104\cot\beta\frac{H}{h_0} \tag{2.1.18d}$$

where $R_{cr}/h_0 =$ the normalized correction of the approximate theory based on the non-linear approach by Li and Raichlen (2001). From Eq. (2.1.18d) it is apparent that in addition, the run-up due to non-linear theory is further enlarged and the non-linear fraction is proportional to the slope angle as well as to the initial relative incident wave height (cp. also. Li, 2000). These findings emphasized the importance of both beach slope and incident wave height on the highly non-linear run-up process of solitary waves even though the overall influence is negligible in practical engineering applications.

Aiming at an estimation technique for the run-up of breaking and non-breaking waves Hughes (2004) first re-examined the existing wave run-up formula and subsequently presented a novel wave parameter representing the maximum depth-integrated wave momentum flux occurring in a wave of permanent form. This parameter was then correlated to available data of normally incident, breaking and non-breaking wave run-up on smooth impermeable plane beaches. Assuming that the weight of the water volume at maximum wave run-up above the still water line is proportional to the maximum depth-integrated wave momentum flux and after a few mathematical transformations the author derived an approximate run-up law

$$\frac{R}{h_0} = CF\left(\alpha\right)\left[\frac{M_f}{\rho g h^2}\right]^{1/2} \tag{2.1.19}$$

where C is an unknown constant and $F\left(\alpha\right)$ is a function of slope to be determined empirically. In Eq. (2.1.19) the normalized run-up is directly proportional to the square root of the maximum depth-integrated wave momentum flux that could be derived by Eq. (2.1.20) under the assumption that the sea surface slope at maximum wave run-up is a straight line.

$$M_f\left(x,t\right) = \int_{-h}^{\eta(x)} \left(p_d + pu^2\right) dz \tag{2.1.20}$$

where p_d = instantaneous dynamic pressure, u = instantaneous horizontal particle velocity, ρ = density, h = water depth, $\eta\left(x\right)$ = sea surface elevation and z is the vertical positive upward direction. When experimentally obtained run-up data in the case of non-breaking solitary waves are fitted mathematically, it results in an approximate run-up law that predicts the wave run-up remarkably well. I reads

$$\frac{R}{h_0} = 1.82\left(\cot\alpha\right)^{1/5}\left(\frac{M_f}{\rho g h^2}\right) \tag{2.1.21}$$

Hughes (2004) also speculated that the utilization of the deep water based surf similarity parameter in the non-breaking wave run-up would not attain adequately verified results.

In contrast to his assessment, a series of papers was recently published (e.g. Madsen and Fuhrman, 2008) on the applicability of the surf similarity parameter, especially in the context of tsunami and long wave run-up. Initially Fuhrman and Madsen (2008) derived an equivalent surf similarity parameter for the commonly applied solitary wave example of a tsunami under the assumption of small offshore non-linearity, the omission of further constants and a representative wave period that reads

$$\xi_s = \frac{s}{H/h_0} \tag{2.1.22}$$

where s denotes the beach slope, H/h_0 the wave height-to-depth ratio. The Eq. (2.1.11) that was already presented above could then be derived by introducing Eq. (2.1.22) into Eq. (2.1.9) where the fundamental dependencies in terms of surf similarity are thus apparent analogously to the surf similarity of sinusoidal waves.

Subsequently Madsen and Fuhrman (2008) reviewed and re-examined the classical analytical solutions for the periodic long wave run-up at infinitely long slopes as well as at finite slopes attached to a constant bottom region. The authors presented solutions for the maximum run-up of periodic long waves based on linear and non-linear theory. A link was established between periodic long waves and non-periodic waves such as tsunami under the supposition that tsunami behave quasi-periodic in some ways. This is facilitated by few observations, e.g. the depth sounding of yacht Mercator (referenced in Ward and Day, 2008). Also, numerical modeling based on realistic or hypothetical ocean bottom displacements yielded tsunami wave forms that intriguingly resemble the intermittency of regular ocean waves (cp. Borrero et al., 2006, Fig. 3 therein). The surf similarity which already proved its usefulness in the classification of breaking and run-up of wind waves was then consequentially adopted to the long wave run-up. In the case of a flat bottom attached to an oblique sloping beach, the normalized run-up law can be expressed as

$$\frac{R}{A_0} = 2\pi^{3/4}\left(\frac{A_0}{h_0}\right)^{-1/4}\xi^{-1/2} \tag{2.1.23}$$

where $A_0 = H/2$ denotes the offshore wave amplitude and ξ the surf similarity parameter expressed in Eq. (2.1.5). The run-up velocity v is then given as

$$\frac{v}{\sqrt{gA_0}} = \frac{\sqrt{\pi}}{\xi}\left(\frac{R}{A_0}\right) \tag{2.1.24}$$

The theoretical breaking criterion of long waves was deduced under the assumption that a wave breaks as soon as the surface elevation during draw-down becomes vertical. In terms of surf similarity it was expressed as

$$\frac{R_{\text{break}}}{A_0} = \frac{1}{\pi}\xi^2 \tag{2.1.25}$$

Madsen and Fuhrman (2008) further elaborated that in the case of a tsunami the combination of extreme flow depths and high flow velocities at the shore and on land constitute the specific danger. Surf similarity parameters within the range $3 \lesssim \xi \lesssim 6$ result in largest run-up where the transition from nonbreaking to breaking waves occurs (cp. Fig. 3 and 4 in Madsen and Fuhrman, 2008). According to Eqs. (2.1.23) and (2.1.24) they further pointed out that especially combinations of long wave periods or wavelengths along with mild slopes result in extreme run-up and near shore velocities. By means of adopting a high-order Boussinesq type numerical model, the validity of the analytical results were further confirmed as the results of the run-up and the associated velocities of the numerical model excellently agree except for minor discrepancies between run-up and draw-down not covered by their theory.

Finally, the publication by Madsen and Schäffer (2010) could be seen as a watershed in the investigation of tsunami propagation and the associated run-up process. Whereas until then it had been common practice to consider solitary waves or N-waves as an adequate model for tsunami, the authors proposed analytical solutions on the run-up and run-down based on the non-linear shallow water theory for single waves, where the duration and the wave height could be specified separately in order to overcome the length scale deficiency of available long wave models. Also transient wavetrains governed by the linear Korteweg–de Vries (KdV) equations were addressed and convolution integrals provided a basis for the determination of the wave run-up. This analytical approach resulted in establishing run-up/run-down and velocity formula for various waveforms such as isoceles N-waves, single waves and sinusoidal waves but with the important exception that these waveforms did no longer exhibit a tie to wave height-to-depth ratio. On the basis of assuming linear waves at the beach toe Madsen and Schäffer (2010) proposed the following expressions for the amplification ratio of incoming waves and the associated velocities

$$\frac{R_{\mathrm{up/down}}}{A_0} = \chi_{\mathrm{elev}} \left(\frac{\Omega^2 h_0}{g\gamma^2} \right)^{1/4}, \quad \frac{\gamma V_{\mathrm{up/down}}}{\Omega A_0} = \chi_{\mathrm{velo}} \left(\frac{\Omega^2 h_0}{g\gamma^2} \right)^{1/4}, \tag{2.1.26}$$

where R = run-up/run-down, A_0 = offshore wave amplitude, χ_{elev} and χ_{velo} = shoreline elevation and velocity, $\Omega = 2\pi/T$ = a duration in analogy to the common wave period, h_0 = offshore water depth, g = acceleration due to gravity and γ = beach slope. They further outlined that in correspondence with the observation in Madsen and Fuhrman (2008) the normalized run-up in Eq. (2.1.26) could also be recast in terms of the surf similarity parameter Eq. (2.1.27) that reads

$$\xi = \sqrt{\pi} \left(\frac{A_0}{h_0} \right)^{-1/2} \left(\frac{\Omega^2 h_0}{g \gamma^2} \right)^{-1/2} \tag{2.1.27}$$

The normalized run-up/run-down according to their theory is summarized in the Eq. (2.1.28) as a function of the surf similarity parameter

$$\frac{R_{\text{up/down}}}{A_0} = \chi_{\text{elev}} \pi^{1/4} \left(\frac{A_0}{h_0} \right)^{-1/4} \xi^{-1/2} \tag{2.1.28}$$

Interpreting their novel run-up law, that is no longer bound to waves of limited length, period or duration, it was concluded that the highest run-up results from isoceles N-waves while single waves yielded the lowest run-up. "For a given wave shape and a given value of A_0/h_0, the relative run-up R_{up}/A_0 increases for decreasing values of ξ as long as breaking does not occur. The smaller the A_0/h_0, the larger the amplification R_0/A_0 (Madsen and Schäffer, 2010)". Furthermore, they numerically computed the maximum run-up for physically sound long waves. These results were then compared to either solitary waves that resembled the prototype vertical length or time scales. As a result either attempt ended in significant deviations from their analytical theory. It was therefore concluded that it is not recommended to utilize the commonly applied solitary wave in neither numerical nor experimental studies in the future.

2.2 Physical Tsunami Run-up Modeling

The physical long wave modeling, the origin of the waves, their propagation and evolution have been investigated frequently in literature. During the past decades this field of interest was subject to technical and scientific improvements which led to significant innovations, especially in experimental facilities. Long waves which might be categorized in terms of their generative source (i.e. landslide, sub-oceanic earthquake and impacts such as meteors, pyroclastic, volcano eruption) were thus generated differently to laboratory scale according to their source mechanism. A common concern had always been the translation of prototype scales into model scales (cp. Section 3.3) and in contrast to other experimental targets tsunami investigations compounded for modeling space towards horizontal and vertical length scales.

Hence this section is intended to review existing laboratory techniques, their application to long wave phenomena in particular and key publications within the field of interest. In that respect a comprehensive yet worthwhile illustration of advances in physical long wave modeling was found in the publications by Liu et al. (1991); Yeh et al. (1995); Liu (2008). Also, more detailed information on general physical modeling techniques is provided in Yalin (1971); Hughes (1993b). Different approaches in terms of wave generation could be determined from literature. What follows is mostly sorted according to the wave generation mechanism. Advantages and disadvantages are discussed at the end of each subsection. Readers should also be pointed to Tab. 2.1 at the end of the section which summarizes details of a number of milestone experiments. Besides the modeling techniques, which were intended to model tsunami due to sub-oceanic earthquakes presented in the following, also documentation about landslide induced tsunami generation was vastly found in literature. Those waves are usually generated by sliding objects in various ways (see e.g. Wiegel, 1955; Iwasaki, 1987; Heinrich, 1992; Watts, 2000; Synolakis and Kanoglu, 2009). Although landslide generated long waves are beyond the scope of the objective those few citations should have been mentioned for the sake of completeness.

Piston-Type Wave Generation

Predominantly, in order to generate long waves to laboratory scale, scientists often laid out their experiments on the basis of piston-type wavemakers which release wave energy to the water column by horizontally moving a wave paddle (e.g. Dean and Dalrymple, 1991; Dalrymple, 1989).

In terms of waveforms, early experiments were conducted which addressed the run-up of solitary waves as a representation of long waves (Synolakis, 1987). The applied facility comprised a $31.73\ \mathrm{m}$ long, $40\ \mathrm{cm}$ deep and $61\ \mathrm{cm}$ wide wave tank consisting of 12 identical sections. The applied beach slope amounted to $1/19.85$ and the stroke of the piston wavemaker is $2.44\ \mathrm{m}$. The dimensionless wave heights used in these experiments ranged between $H/d = 0.005 - 0.607$ whereas dimensionless wave periods were reported to be $T\sqrt{g/d} = 9.8 - 113.2$ (Synolakis, 1987, T3.1).

Thereafter Synolakis (1990) reports on the generation of long waves in experimental investigations. His review of the progression of the wavemaker theory summarized important landmark publications on the generation of waves by a vertical moving partition, the wave plate. A prerequisite for the applicability of the early theory was that the plate motion had to be small while the boundary conditions had to be specified only at the initial plate position rather than at the instantaneous position. He further referred to theoretical and experimental work done by Goring (1979) who established a theory for the generation of long waves of permanent form, i.e., solitary or cnoidal waves. The developed algorithm has been multiply applied in modern laboratory investigations whereas Synolakis (1990) expanded the theory to allow for waves that are not of permanent form but evolve during propagation in the laboratory. He concluded that these findings facilitate the generation of arbitrary finite-amplitude waves at any distance away from the wavemaker.

Similarly, Briggs et al. (1993) reported experiments studying the solitary wave run-up on a plane, impermeable 1 vertical to 30 horizontal beach (cp. also Briggs et al., 1995b). The wave conditions in these experiments were varied a lot but as a summary, solitary waves with $H/d = 0.01 - 0.50$ were deployed while the water depth was kept at $h = 0.32$ m. Besides a wave basin which was equipped with a wavemaker exhibiting a stroke of $s = \pm 0.15$ m additional experiments were conducted in a 42.4 m long, glass-walled flume. Though especially wave periods of at least 15.8 s were attained, generated waves of that period were, due to their solitary waveform, also smallest in the experiments. In Liu et al. (1995), Briggs et al. (1995a) and Yeh et al. (1994) tsunami run-up experiments on a conical island accomplished at U.S. Army Engineer Waterways Experiment Station, Vicksburg were reported. A directional spectral wave generator (DSWG) which was already used by Briggs et al. (1995b) was likewise used to generate solitary waves of $0.05 - 0.20$ m in a 27.4 m long wave basin. The parameters of the generated wave comprised $L = 3.60 - 9.46$ m and $T = 3.41 - 8.03$ s.

A significant improvement in terms of the absolute stroke, which could be attained during the experiments, was reported by Moronkeji (2007). He conducted experimental studies on the run-up and draw-down of solitary and cnoidal waves over a movable bed at two different beach slopes (Tab. 2.1). Wave generation at the O.H. Hinsdale Wave Research Laboratory, University of Oregon is brought about by 29 wave boards driven by electric motors. The range of wave period is given as $T = 0.5 - 10.0$ s and the maximum stroke of the wave boards reaches 2.10 m. Wave length for the cnoidal wave is stated to be in the range of $L = 8.0 - 12.0$ m.

A variation of the commonly used piston type wavemaker principle had been reported by Teng et al. (2000). Generation of solitary waves was obtained through a submerged vertical plate fastened to a carriage which was driven with a motor of adjustable speed. By varying the speed and distance of the movement to the carriage and the plate, solitary waves of different amplitude were generated. As a unique advantage the method improved the problem related to limited stroke length of commercial and custom-made piston type wavemakers because the path of the carriage could be specified independently. Although this appears to mark a step forward in generation of arbitrary long waves, this test arrangement would only be restrictedly capable of generating wave troughs and typical wave lengths could not be obtained due to the limited volume of the wave flume. Yet, a comparison of the generated solitary wave agreed reasonably to the theoretically predefined waveform.

An equally substantial investigation was conducted by Schmidt-Koppenhagen et al. (2007) who reported a set of hydraulic experiments in an extremely large wave flume in Germany (cp. also Tab. 2.1), that reaches a maximum stroke of 4.00 m tested in a wave flume length of 330.00 m. As incident waves, the solitary wave-type had been applied to the experiment setup modeling the total propagation distance from the generation in deep water into the shallow waters. The deduced wave period from time series depicted in the paper is estimated at $\approx 20.0 \text{ s}$. Though this value reflects the longest wave period which was traceable from literature by means of a wave generator with an enormous stroke, limitations remain in terms of flexibility of generated wave forms, periods and lengths even for this kind of large scale facility.

Dam-break Analogy

Another approach to generate long waves and surge flow in the laboratory incorporates the analogy between dam-break induced bores and surge flow resulting from tsunami (Ippen, 1966; Hughes, 1993b). Commonly and in line with piston-type driven long wave generation, those experiments are likewise designed by Froude similitude. Its model performance is only at a lower level, affected by scale effects and distortion due to viscosity or surface tension. Yeh et al. (1989) were among the first who presented an experimental procedure where a single bore was generated by means of lifting a thick aluminium plate gate. The gate which initially separated the quiescent water on the beach from the higher water level behind the gate was actuated with the aid of a pneumatic cylinder and this in a very short time. The instantaneous opening of the gate was able to generate bores in a remarkably repeatable manner.

Moreover Chanson et al. (2003) and Chanson (2006) presented a technique where water was released by an overhead water tank at the beginning of the wave flume by an orifice gate. Though, by means of this technique a significant level of turbulence is introduced into the physical model even before any wave propagation or breaking had taken place in the prototype of the model. Likewise, Gomez-Gesteira and Dalrymple (2004) cited a small-scale experiment performed by Yeh and Petroff at the University of Washington referred to as a “bore in a box”, where a dam-break wave impacted a free-standing rectangular structure. A complementary wave generation technique, where a hinged gate releases a body of water to flow into the physical model domain, was then reported in Nistor et al. (2009) additionally benefiting from the fact that the tail of the dam-break induced bore was supportingly maintained by two pumps discharging into the back of the collapsing water volume.

Vertical Wave Board Motion

Another approach in long wave generation in a laboratory had been described by Monaghan and Kos (2000). They made use of original ideas of Scott Russell, who first considered a sinking box in 1844 to illustrate the formation of a solitary wave in a long rectangular tank. Since then, numerical models had been validated (cp. also Abadie et al., 2008) with the assistance of the results obtained from Russell's early laboratory findings. In the light of confined technical resources and limited insight into the subject, the presented generation methodology was strikingly capable of generating a solitary wave. Nonetheless it has to be mentioned that in the region of wave triggering, vortexes and turbulent, undirected fluxes are possibly generated in the body of water. These at least are suspect to influence the wave propagation in the laboratory. Apart from generating a wave motion through downwards directed wavemaker motion Raichlen (1970) first mentioned wave generation by up/downwards moving wave flume bottom which aimed at generating long waves in accordance to the trigger motion from tectonic movements of the seafloor at plate boundaries.

A follow-up investigation again reported experiments taking advantage of a vertically moving piston for wave generation at one end of a wave flume. A detailed description of this study was presented in-depth by Hammack (1973); Segur (2007). Both authors however explicitly distinguished between a generation section and a downstream section of the wave evolution in their experiments. It is therefore concluded, that the utilization of the 'moving bottom' generation technique resembling the earthquake stimulation is not well suited in the case of physical run-up modeling of prototype shallow water conditions. Modeling of the entire process chain would in turn result in large, yet still unavailable facilities due to extremely long distances in nature.

Table 2.1 Review of important experimental configurations, dimensions, technical and geometrical data, wave parameters as per availability

Citation	Generation technique	Beach slope	Water depth	Wavelength/-(period)	Stroke
Synolakis (1987)	Piston-type	$1/19.85$	$6.3 - 38.3$ cm	$H/d = 0.005 - 0.607$, $T\sqrt{g/d} = 9.8 - 113.2$[a]	2.44 m
Briggs et al. (1995b)	Piston-type	$1/30$	0.32 m	$H/d = 0.01 - 0.50$, $L = 2.28 - 16.10$ m, $T = 2.07 - 15.81$ s	± 0.15 m
Moronkeji (2007)[b]	Piston-type	$1/10$, $1/15$	$1.0 - 1.1$ m	$T = 0.5 - 10.0$ s, $L = 8.0 - 12.0$ m	2.1 m
Schmidt-Koppenhagen et. al. (2007)[c]	Piston-type	$1/25$	2.5 m	≈ 20.0 s	4.0 m

[a] tabulated dimensionless wave parameters ranges do not necessarily relate to each other, therefore conversion into dimensional values demands original tables

[b] wavemaker velocity: 2.0 m/s, a movable bed consisting of natural beach sand had been applied to study wave-induced beach evolution

[c] segmented longitudinal section consisting of a sandy beach wedge with movable bed, details apply to the shore section

Volume-driven Wave Generation

Finally, a novel modeling approach in tsunami wave generation has been presented in literature. The origin of the essential idea of the approach reaches back to the early 1950s when Wilkie and Young (1992) introduced the pneumatic tide generator which had been designed to assure a simple, flexible and economic generation of tidal motion in hydraulic models though traces of the idea's origin could also be found in the fundamental work of Reynolds (1887). The pneumatic wave generator succeeded in earlier developmental stages and at that time was depicted as versatile equipment for a wide range of purposes and model scales. In principle, tidal wave generation functioned by means of an inverted box at the seaward end of the physical model fixed to the flume floor. The flume-wards facing box side ended at a distance above the bottom forming an outflow gap and allowed for water to leave or enter the box chamber. The outflow had been smoothed in order to suppress detaching wakes and turbulence in the flow. Operation of the wave generator was enabled by means of a controllable fan which exhausted the box and in combination with a motor-operated valve the air pressure in the box controlled the amount of water drawn from or released into the model. Water levels in the model were thus adjusted according to a defined time series. Again focusing on physical models of tidal environments, a follow-up was published by Allen et al. (1992) who reviewed available modeling techniques and described convenient digital control mechanisms for the originally analogue controller. By means of the optimized system, sinusoidal and asymmetric tidal curves were generated with satisfactory accuracy.

On that basis a further modified version of the old principle of storing water in a tank and releasing it under the control of a value-pump system had been constructed (Allsop et al., 2008; Rossetto et al., 2009). Controller scheme and hardware of the tidal wave generator had been optimized in order to adapt to tsunami. Compared to formerly generated tidal waves, tsunami exhibit significantly shorter in wavelength and period . This in turn resulted in increasing performance of valve speed, pump capacity and controllability. These demands were met with the aid of a quieter, high-capacity vacuum pump, faster controller algorithms, optimized valves and servo motors. Additionally, an analysis on the basis of computational fluid dynamics led to altering the box design which was amended with internal baffles to prevent sloshing of water inside the box during rapid water level changes.

2.3 Run-up-Structure Interaction

Besides the objective to investigate wave run-up to plane, impermeable beaches and to contribute to long wave generation, the current study had also been dedicated to broaden insight into interaction of landwards surging water with macro-roughness elements located at the beach and in the coastal hinterland. Sad episodes have repeatedly occurred in so many tsunami events when macro-roughness elements such as buildings collapsed and buried victims that expected to be sheltered by these structures. It is therefore consequential and underlined in literature, that the evidence of long wave run-up, surge flow and structure interaction should generally be focused on research concerning wave forces on buildings, especially from an engineering point of view. Numerous researchers were involved in this important objective (e.g. Ramsden and Raichlen, 1990; Ramsden, 1996; Arnason, 2005; Yeh, 2006). Against the background of the diverse literature this section is intended to summarize few sources that deal with the topic either experimentally, numerically or analytically without following a strict chronological order. Mainly, all of the mentioned investigations adopted solitary waves or dam-break induced flood waves to relate the impact at the beach showing either the maximum run-up or the forces/pressures at solid structures located in proximity to the shoreline.

Assessment of Forces and Pressure Distribution

Fenton and Rienecker (1982) proposed an analytical Fourier method in order to study solitary wave run-up and forces on a vertical wall. Their derivation assumed oppositely traveling solitary waves in uniform water depth of equal wave height and zero velocities at the meeting point of their wave crests similar to those velocities apparent when a solitary wave would impinge on a vertical wall. By integrating the assumed pressure distribution, forces on the wall were obtained as a function of the wave height and the water depth at the wall.

An investigation by Ramsden (1993) experimentally and numerically reflected the prevailing knowledge regarding wave forces due to incident long waves and related phenomena such as undular and turbulent bores as well as surges over a dry bed at vertical walls. While it was found that prototype celerities of an approaching tsunami, as deduced from eye-witness reports, agreed reasonably well with accomplished experiments, differences in impact forces were conveyed compared to hydrostatic theory. Also, at the transition from undular to turbulent bores approaching the investigated $1/50$ beach slope, discontinuities in the maximum surface slope arise, which was associated with a rapid increase in the measured run-up, force and momentum on the wall. Bores and surges also differed in regard to their temporal impact history and run-up. In tendency it was found that bores characterized by steeper water surface slopes in the wave front exhibited higher maximum run-up, and initial peaks in the pressure history were apparent while impinging on the vertical wall. Surges over dry bed in contrast were characterized by slower growth of forces exposed to the vertical wall (Ramsden, 1996). It was also indicated that non-negligible vertical accelerations exist during the run-up phase. Those accelerations which were observed in the experiments may deviate from the prototype processes (cp. also the discussion in Section 2.4). The experiments mark an important step in order to estimate forces on vertical walls due to long waves approaching at the coast.

Tomita et al. (2007) mentioned two laboratory experiments assessing the effect of submerged breakwaters as well as transformation of the wave during the run-up on a beach with $1/200$ uniform slope. Validating a three-dimensional numerical model, the authors were able to deduce temporal information about the wave-induced pressure on a vertical wall. Pressure history could facilitate in concluding maximum loads on buildings in order to estimate their stability. Later the same numerical model was utilized to recalculate inundation caused by the Boxing Day tsunami 2006 in Galle, Sri Lanka on a much broader scale; under consideration of solid objects resembling local settlements exposed to onland flow (Tomita and Honda, 2007). A validation of the simulation generally showed good agreement with survey data after the bottom roughness coefficient had been numerically adjusted and wave forces could have been deduced in order to state potential damage in the city.

Pedro et al. (2007) investigated the impact of a wave on a square column numerically in three dimensions. Hydrodynamic loads occasioned by impacting waves of a tsunami or a hurricane need to be assessed primarily in order to design constructions appropriately. It was stated that the applied numerical models function sufficiently to obtain design values for constructions, but further insight into hydrodynamical quantities would need more accurate modeling of the situation. Important experimental findings were reported by Riggs et al. (2008) who applied either solitary or cnoidal waves resulting in tsunami bores and subsequently measured forces on structural components of a multistory building. Square and rectangular columns in different configurations, horizontal slabs as well as a solid wall were considered while either direct impact or shielded situations were modeled. This experimental data could further facilitate the validation of numerical models. Additional experiments utilizing the identical facility, wavemaker and beach setup underpinning the same purpose were reported by Robertson et al. (2008).

After that Xiao and Huang (2008) modeled solitary wave run-up deploying Reynolds-averaged Navier-Stokes equations in a vertical plane. The model, which was validated against two sets of experimental data, was found to reproduce them reasonably well. Subsequently forces and overturning moments, due to wave run-up, were analyzed for varying cross-sectional positions of an idealized beach front house. The outcome was that wave forces and overturning moments increase with decreased distances between the obstacle and the shoreline.

Analysis of Group Effects

While macro-roughness at the beach is of significant influence, submerged obstacles, i.e. reefs, were also recognized to interact with incoming long waves. Fujima (2001) examined such influences by means of experiments and subsequently compared his results to numerical simulations. The author advised on how to properly tune bottom roughness coefficients in relation to the governing equations that were actually solved. Equally, Lynett (2007) found in a more detailed, though exclusively numerical study, that submerged obstacles in a shelf region almost always result in a reduction of maximum run-up at the beach. The applied obstacles which were introduced as trapezoids with a side slope of $1/5$ had varying configurations under water. On the other hand, a small obstacle length reduced the observed effect especially in combination with large incident waves.

An analogy could also be drawn between the stated objective of the current work and the effects of riverine flooding or flash flood events that already often severely implicate bordering residential districts by hazardous water level rise and resulting inundation. Those incidents are less prone to cause loss of life and fatalities for the very reason that water levels change slower. But it still results in enormous economic loss rates especially when highly developed industrial estates are affected. The addressed analogy concerns temporal and spatial evolution of residential area flooding, again involving flow-obstacle interaction even though at a lower level of impact. The problem had been numerically tackled by Hashimoto and Park (2008) who expanded the two-dimensional shallow water wave equations besides the well-known bottom roughness terms accounting for bottom shear stress with an additional term accounting for drag forces induced by the presence of buildings. The model which was validated against a flood disaster in Fukuoka, Japan explicitly differentiates four obstacle types attributed with drag coefficients and also accounts for building density. As a result recommendations were given how to choose those coefficients appropriately.

When using the weak analogy between long wave run-up and dam-break induced flood wave, two pioneering papers have been published on transient flow interacting with structures. Soares-Frazão and Zech (2008) investigated the effect of structures resembling an idealized city, though not to scale, to a given sudden surge induced by a dam-break type generation while focusing on urban flooding i.e. due to flash floods. Flow velocities as well as flow depth were recorded and subsequently compared to a numerical model in order to assess how well numerical tools are able to capture such flows. The experiments, whose data were also provided in detail by Testa et al. (2007), provided a full set of data for validation purposes of numerical models and moreover investigated the effects which were related to the orientation of the idealized settlements to the angle of approaching flume wave. Qualitatively the authors determined that the presence of obstacles in the flow was coupled with higher water levels in front of the settlement while changes from sub- to supercritical flow and vice-versa happened along the streets, formed by the single obstacles. In addition, rotations led to increased levels of complexity in the flow pattern during inundation. Intricate interactions consisting of reflections and asymmetric hydraulic jumps were observed especially at the crossroads. While in the above investigation shallow-water wave equations with a shock-capturing scheme and impervious boundaries resembling the obstacles were deployed to govern the flow, Guinot and Soares-Frazão (2006) and Soares-Frazão et al. (2008) paved the way for treating urban settlement in a more accurate numerical manner, adopting porosity terms in the governing equations. It had been common practice so far to abstract from urban pattern or dense vegetation to simple equivalent bottom roughness coefficients by empirical means notwithstanding the fact that results could be significantly biased through volumetric differences in the flooded areas. The concept of porosity which had been attributed to a whole city quarter instead of single obstacles accounted for the loss of energy that is related to dissipative processes during an inundation phase. It appeared that results of classical approaches and the novel approach presented by Guinot and Soares-Frazão (2006) and Soares-Frazão et al. (2008) were promising in terms of accuracy and computational costs. Although a closer look at the agreement between experimental data and numerical results revealed a significant error in the order of $20 - 30\%$ especially measured at water level gauges inside the modelled settlement quarter, that should not be neglected.

Already in the early eighties, experiments which are possibly closest to the objective of the current study were published by Goto and Shuto (1983). The authors aimed at investigating the effect of sufficiently solid buildings and low sea walls capable of reducing the overall inundation height numerically and experimentally. Though not directly related to a horizontal length scale, they set up experiments where wooden pillars were exposed to varying discharges. The obstructed area in the applied flume, reported in their work, amounted to $23.5 - 48.6$ %. The number of element rows were also varied from $2 - 5$. The effects of bridge piers were equally associated with the problem under investigation and because more than one row of obstructing elements was used the authors divided the obstructed area into three distinct zones. A zone of primary contraction of the flow was located at the first element row, the second zone was composed of the remainder element rows, whereas the third zone comprised the last element row in the propagation direction where the flow expands again. An energy loss term ΔE_i was defined for each of the detected zones, deduced from the continuity and the energy equation. It was expressed as a factor of the energy head of the flow which was related to the obstruction ratio and the local Froude number. After comparing the experimental results with subsequently conducted numerical studies, it was then concluded that it is hence possible to circumvent a detailed description of the energy loss and instead the utilization of an equivalent friction factor would yield satisfactory results.

Lately Cox et al. (2009) scrutinized a portion of the town Seaside, Oregon with a hydraulic model of $1 : 50$ length scale. Though partially idealized, many of the existing features such as the seawall and a major hotel were kept realistic in order to investigate the propagation of an approaching bore front developed out of an error function-induced or solitary wave. The flow properties were recorded by means of conventional sensors as well as by an adapted video system to provide high-resolution space-time information of the wave propagations through urban macro-roughness. Finally, experimental results were compared to calculations accomplished by two individual numerical tools and good agreement was obtained. Also, these findings first-ever indicated the demand to relate prototype conditions to model.

2.4 Consequences

In consideration of the vast amount of literature available in context of either tsunami run-up to plane beaches, to physical model tests in shallow waters or to the treatment of obstacles in steady-state/transient flow conditions, consequences manifest to what extent the current objectives have to be addressed. In the following it is outlined how the present methods were chosen in order to shed light on discovered research demands and potential gaps in the current knowledge.

Firstly, from what was reviewed in Section 2.1, it becomes clear that the solitary wave paradigm no longer uniquely applies to approaching tsunami waves. The groundbreaking work by Madsen et al. (2008, 2009) impressively demonstrated that despite their universal utilization, solitary waves are lacking in terms of comparability to geophysical scales, when scaled down to laboratory size. Errors in the order of a magnitude in temporal and spatial duration would occur when this wave theory is applied to physical models especially dealing with near-shore effects and wave impact investigations. Especially in the shallow water region solitary waves eventually become shorter and shorter as their wavelength L over depth h ratio shows an asymptotic behavior with increasing nonlinearity H/h (Madsen et al., 2008, cp. their fig. 8). It is therefore paramount not only to introduce the appropriate waveform resembling prototype similitude but also by this means verify existing theoretical work (Madsen and Schäffer, 2010) relevant to long wave run-up and substantiate their applicability to such issues.

Secondly, Tadepalli and Synolakis (1994) augmented the widely known canonical problem of tsunami run-up by means of a class of N-waves yet argued that in order to model tsunami run-up a shift should take place from parametric studies of assumed waveforms to the explicit determination of coastal effects by parametric studies of source motion. Conversely, the analysis of numerical or physical tsunami run-up models has to be based on waveforms that intrinsically mimic geophysical scales and the adjunctive source motions that led to specific near-shore waveforms. Either numerical studies that investigate wave generation and propagation in prototype on the basis of shallow water wave equations or realistically derived sea surface time histories (such as the sounding profile of Mercator yacht), should be employed in studies on the canonical run-up problem instead of solitary waves which were never found to resemble tsunami traveling in shallow water depth.

Thirdly, already Heitner and Housner (1970) mentioned the demand to model tsunami by means of comparable wave steepness as well as mild beach slopes that adequately mimic natural conditions. Aside from that, most imperiled coastal areas were colonized for the reason of flat fertile agricultural areas, which in turn exhibit mildly sloping coastal hinterland prone to severe flooding in the event of a tsunami. This condition is often coupled with mild slope bathymetry which also constitutes optimal hunting grounds for fishing. Such environments usually promoted intense population growth. Though historically deduced, it demonstrates the tie between high vulnerability of larger coastal cities and mild topographic conditions which have to be represented accordingly when expedient predictions should be provided by means of scientific methodology in the context of disaster preparation and emergency planning. To date only few studies apply to mild beach slopes in experimental studies in combination with adequate waveforms mostly for the reason that those requirements demand much laboratory space when i.e. length scales are in the order of $1 : 100$. Beach or foreshore slopes utilized in experimental studies ranged between $1/10$ and $1/30$ when approaching tsunami-like waves were considered. In contrast to these commonly utilized beach slopes Cuypers (2004) presented a study of breakwater stability under the attack of a potential tsunami at the Nicaraguan coastline. In this study the continental slopes and the foreshore slopes were varied in order to investigate the wave reflections of approaching waves numerically. It was found that steeper continental slopes result in shorter arrival times of the waves whereas the wave heights and wave forms did not change significantly. The influence of the foreshore slope to the wave propagations and the reflection had not been discussed in detail. Nevertheless it became apparent that the reflection coefficient of a coastline tends to unity with increasing foreshore slopes. Thus it shows that physical modeling only leads to realistic results when a given prototype geometry is modeled as exactly as possible. For many foreshore slopes worldwide, especially in urbanized regions, the commonly used beach slopes in the laboratory are far too steep.

Fourthly, most of the existing laboratory techniques evident in literature lack the opportunity to generate waves, which combines the demand of optimal control over the water surface elevation in general and the capability to process positive and negative surface elevation signals. Although theoretically possible, piston-type generation of course allows for periodic waves but stroke dependent correlations prohibit wave generation of arbitrarily long waves. Assuming a periodic, sinusoidal wave as simplest level of modeling a tsunami time series with a period of $T_M = 90\,\mathrm{s}$ and an amplitude of $H_M = 0.1\ \mathrm{m}$ leads to a shallow water wave length of $\lambda_M = 154.4\ \mathrm{m}$ in a water depth of $h_M = 0.3\ \mathrm{m}$. The subscript $_M$ denotes scaled laboratory wave properties. Further assuming Froude similitude and a length scale of $M_L = 1 : 100$ results in prototype wave properties of $T_P = 15\ \mathrm{min}$, $H_P = 10.0\ \mathrm{m}$ and $\lambda_P = 15.44\ \mathrm{km}$ in a water depth of $h_P = 30.0\ \mathrm{m}$ with $_P$ denoting prototype or nature properties. The time scale amounts to $M_T = 1 : 10$. Admittedly, these assumptions could easily be verified by means of either eye-witness reports or analysis of available echo soundings or by other means. This attempt to apply a piston-type wavemaker would first of all require to estimate the stroke length in a laboratory. Galvin (1964) proposed a method to determine the stroke length by means of a comparison between the total volume of water displaced by the entire stroke S in the water depth h_M to the volume contained by a wave crest of a sinusoidal wave which is intended to be generated by the wavemaker. Eq. (2.4.1c) integrates the positive sinusoidal wave crest of a sinusoid according to Airy wave theory and equals the volume of water contained in the wave crest to the stroke length times water depth required for the wave generation. In laboratory scales it reads under the assumption $t = 0$

$$V_{\text{sd}} \equiv V_{\text{cr}} \tag{2.4.1a}$$

$$V_{\text{sd}} = S \cdot h_M, \quad V_{\text{cr}} = \int_{-\lambda_M/4}^{\lambda_M/4} \eta\,(x,t)\ \text{dx}, \quad \eta\,(x,t) = a_M \cos\,(kx - \omega t) \tag{2.4.1b}$$

$$S = \frac{1}{h_M} \int_{-\lambda_M/4}^{\lambda_M/4} a_M \cos\,(kx)\,\text{dx} = 8.19\ \text{m} \tag{2.4.1c}$$

$$\left(\frac{2a_M}{S}\right) = kh_M = 2\pi \left(\frac{h_M}{L_M}\right) \tag{2.4.1d}$$

where V_{sd} = displaced paddle volume, V_{cr} = volume contained in the wave crest of sinusoid, $\eta\,(x,t)$ water surface elevation as a function of x, t, $k = 2\pi/\lambda_M$ = angular wavenumber, $\omega = 2\pi/T_M$ = angular frequency and $a_M = H_M/2$ = wave amplitude. The stroke of $S = 8.19$ m needed to generate a sinusoidal wave corresponding to the above denoted example demonstrates the demand for more sophisticated laboratory facilities. It is also easily seen in Eq. (2.4.1d) that the model scale wavelength is linearly dependent on the stroke length for a given wave height in an associated water depth. The resulting stroke length which would be needed to generate a geophysically realistic sinusoid, in order to investigate long waves in an adjusted manner, becomes enormous (Dean and Dalrymple, 1991, p. 171). An alternative to avoid such large stroke length would be laboratory models at greater depth though associated with longer wave flumes due to longer waves in deeper water. Hence, neither wavemakers with enormous strokes nor large scale physical models are preferable from a financial and practical point of view. On the other hand, the application of dam-break like wave generation aiming at generating a sinusoidal waveform, parametrized above, would intrinsically malfunction because only positive waves could be generated by this means. What is more, when dam-break like methods are applied only limited control of the generated wave is achieved, because wave propagation is only controlled by gravity force. Therefore, the resulting wave shape is strongly dependent on the volume of water and the height of the initial water body. Yet, it is questionable if dam-break like generating techniques could accurately reproduce wave shapes similar to real-world tsunami signals in the laboratory. Though their utilization in the context of investigating impact-driven forces to constructional elements is undoubted. Hence it is concluded that a novel approach in long wave generation should break the mold. As outlined in Section 4 it is not only feasible but also provable in regard to the objectives of the current study. It is acknowledged that Allsop et al. (2008) also assessed the demand for innovations in that matter and adapted the long-known tidal wave generator to suit long wave generation. The basis of their adapted wavemaker, the tidal wave generator, highlights one extreme in the frequency range of water waves which could be modeled while short waves denote the other extreme. Though the final testing stage has not been completed to date it is anticipated that the described facility is going to start, hereby bridging the gap between long waves in laboratory and their adequate generation.

Fifthly, wave-structure interaction is crucial for the identification of maximum wave run-up in urban settlements where the vulnerability of inhabitants and economy is manifoldly higher than in rural areas. Macro-roughness in literature is treated by either experimental or numerical means. To date numerical tools exist which are capable of modeling long wave impact to and estimating forces resulting from pressure distributions at flow-exposed buildings and obstacles. In any case, the numerical tools need to be validated against experimental data to verify the results. Although numerics could cope with restricted domains with a reasonable resolution, a holistic approach to include larger urban settlements does not seem feasible with the prevailing technology, due to extensive computational cost. Hence, classical laboratory experiments remain a valuable instrument – and are therefore chosen in the current study – in the attempt to study how groups of macro-roughness elements interact with the long wave run-up in general. Moreover, experiments could also assist to investigate long wave impact on single buildings in detail.

Sixthly, the numerical treatment of macro-roughness elements and its verification against experimental results was only minimally covered in literature. One reason for that seems the lack of available benchmark data sets. The current study is therefore also intended to allocate benchmark data. On the other hand it was not addressed at all on how to process the storage of water volume inside of macro-roughness elements as well as partial throughflow numerically. Both effects are believed to affect the wave run-up in urban areas as water volume stored inside of obstacles cannot further participate in the run-up process; or in case of throughflow, it seems obvious that kinetic energy is extracted from the surrounding flow field by means of momentum exchange inside of macro-roughness elements. The proposed experimental setup is in principle also suitable to investigate momentum exchange inside a single obstacle taking into account that scale effects might influence the results.

3 Physical Model Test

3.1 Theoretical Background

3.1.1 General Remarks

Generally, coastal engineers rely on three different approaches when investigating the behavior of complex fluid flow, wave action to beaches or coastal structures and morphodynamic problems. Besides **observations in nature** which are often also called the prototype, researchers apply either miniaturized **physical** or **mathematical models**. On the one hand observations in nature have the advantage that all physical effects are well represented but on the other hand no control is given to influence the boundary conditions of the nature experiment. Physical models are scaled down to laboratory proportions with the aim to simplify observations on the basis of smaller, less expensive models yet preserving the important physical correlations. Numerical models are usually formulated by means of governing equations, then discretized and solved by computers. Accuracy and efficiency are directly associated with the available computational capacity. The degree of detail as governed by the mathematical formulation has to be chosen to the effect that the problem can be solved in a reasonable time. In numerical models the determination of the correct boundary condition is often crucial and could give rise to errors in the results. Although numerical models are generally well applicable to many engineering problems in many other cases, mathematical analysis only grants limited insight to the problem solution, especially when wave breaking, strong turbulence and bottom friction is involved. Against the background of the fast development of computational power, the utilization of physical models is still indicated when solving engineering problems. Particular benefit may arise from the mutual utilization of numerical and physical models sometimes named **hybrid modeling** that interlinks either numerical or physical model results at a boundary of the adversed model category (Hughes, 1993b). In light of the objectives of the current work dealing with the interaction of long wave run-up and macro-roughness it was obvious that a physical model would be most qualified to resemble the prototype behavior because of the difficult flow interactions present in the run-up/run-down phase of the approaching long wave in the proximity of the macro-roughness element groups. Reflections, hydraulic jumps and momentum exchange between the main flow and still water areas in the back of macro-roughness elements were found right from the beginning of the experiments. Moreover attempts with three-dimensional numerical models, solving the run-up of a solitary wave and subsequently interacting with a single, solid, cubic object on the shore, revealed the limitations of current numerical models.

Historically hydraulic models were favored by many famous scientists such as *da Vinci* (description and drawings of flow phenomenon), *Newton* (first theoretical treatment of similitude criteria), *Smeaton* (first scale-model experiments), *Froude* (experiments with ships in a towing tank) or *Reynolds* (movable bed experiments) who elaborated on many of the fundamental principles of hydraulic modeling. Instead of repeating the historical milestones of physical modeling it is referred to Hughes (1993b, and references therein) for a comprehensive overview. The following is meant to discuss the theoretical background and the physically relevant quantities in Subsection 3.1.2 and 3.1.3. The wave generation technique used for the experiments as well as the assets and drawbacks are outlined in Section 4. The wave flume, where the experiments took place, is described in detail in Section 3.2. An illustration of the experimental procedure is finally given in Section 3.3 for completeness.

3.1.2 Froude Similitude

According to Le Méhauté (1976) three approaches to similitude exist: dimensional analysis, inspectional analysis and the most general method to deduce the rules of similitude is from the Navier-Stokes equation and the equation of elasticity. The first approach is defined by Hughes (1993b) as: "Dimensional analysis is a rational procedure for combining physical variables into dimensionless products, thereby reducing the number of variables that need to be considered". Given a certain process which has been observed, the first task is to decide on the important independent variables and in a second task the dependent variables have to be identified as well. Thirdly the variables have to be recast in terms of dimensionless products and the number of system variables need to be reduced to a reasonable number as a final step. It is either possible to form the dimensionless products by means of inspection, by means of formal dimensional analysis or by a combination of both.

Similitude of hydraulic models and their relation to the prototype counterparts is often expressed in literature as a result of dimensional analysis. Different model representations can be given such as Froude, Reynolds, Weber, Chauchy, etc. similitude.

Le Méhauté (1976) remarked that first and foremost the Froude similitude is deployed in physical scale models and that other similitude laws are hardly feasible in laboratory practice. Instead, the engineer will mostly deduce the laws of similitude by an inspectional analysis - which differs from dimensional analysis - involving knowledge and understanding of the phenomenon under consideration along with insight in the influence of second order and scale effects. Yet, besides Froude models, in practice also Reynolds models are deployed in hydraulics when the flow in pressure pipes are investiged.

The Froude similitude is mostly applied in hydraulic physical model tests in the case of free surface flow. The downscaling firstly demands that the prototype and the model remain geometrically similar. The principle of similitude in physics claims that geometric similar processes, either scaled down or up, result in physically similar behavior. The differential equations governing the physical process need to describe the processes at all scales. This requires in turn, that the disputable processes are mechanically similar Martin and Pohl (2009). Besides the geometrical similitude, which is satisfied when all sizes in prototype and model scale are in a constant ratio, full mechanical similitude also aims at kinematic similitude, resulting in similar motions in the prototype and in the model scale. If kinematic similitude is given, particle paths in a model are also geometrically similar in the prototype and time-dependent processes also remain similar after the downscaling. However also forces acting on boundaries and objects have to continue similarly. It is therefore necessary that the prototype-to-model ratios of masses and forces are also constant. Newton's law of motion which e.g. describes the forces in a fluid mechanics problem can be written as (Hughes, 1993b)

$$P_i = P_p + P_g + P_\nu + P_\sigma + P_e \tag{3.1.1}$$

with P_i =inertial force, P_p = pressure force, P_g = gravitational force, P_ν = friction/viscous force, P_σ = forces due to surface tension and P_e = elastic compression force. The overall dynamic similitude is only realized if Eq. (3.1.2) is complied

$$\frac{(P_i)_p}{(P_i)_m} = \frac{(P_p + P_g + P_\nu + P_\sigma + P_e)_p}{(P_p + P_g + P_\nu + P_\sigma + P_e)_m} \tag{3.1.2}$$

Further perfect similitude is only given if all force ratios between prototype and model are equal as expressed in Eq. (3.1.3).

$$\frac{(P_i)_p}{(P_i)_m} = \frac{(P_p)_p}{(P_p)_m} = \frac{(P_g)_p}{(P_g)_m} = \frac{(P_\nu)_p}{(P_\nu)_m} = \frac{(P_\sigma)_p}{(P_\sigma)_m} = \frac{(P_e)_p}{(P_e)_m} \tag{3.1.3}$$

The equality of the force ratios expressed in Eq. (3.1.3) assures that the relative influence of the single forces interacting in the physical system is well balanced. Without this condition, errors would arise if results from physical scale models are transferred back into prototype scales. Martin and Pohl (2009) outline that a model which obeys the above criterion is not feasible either economically or technically. A medium, which attempts to fulfill the perfect dynamical similitude, has not been found yet.

Instead, in engineering applications it is usually assumed which force ratios are dominant in the physical process and at the same time it is also justified which force ratios can be neglected without significantly altering the dependencies in the scaled model. The Froude similitude, commonly deployed in coastal and hydraulic engineering, is therefore derived by assuming that the square root of the ratio of inertial forces to gravity forces equals in prototype and physical models (cp. Eqs. (3.1.4), (3.1.5)). It reads

$$\frac{\text{inertial force}}{\text{gravity force}} = \frac{P_i}{P_g} = \frac{\rho L^2 V^2}{\rho L^3 g} = \frac{V^2}{gL} \tag{3.1.4}$$

with $P_i = \text{mass} \cdot \text{acceleration} = \left(\rho L^3\right)\left(V^2/L\right) = \rho L^2 V^2$ describing the inertial force and $P_g = \text{mass} \cdot \text{gravitational acceleration} = \rho L^3 g$ describing the gravity force, which in turn leads to the requirement stated in Eq. (3.1.5)

$$\frac{(P_i)_p}{(P_g)_p} = \frac{(P_i)_m}{(P_g)_m} \qquad \Longrightarrow \qquad \left(\frac{V}{\sqrt{gL}}\right)_p = \left(\frac{V}{\sqrt{gL}}\right)_m \tag{3.1.5}$$

From the equality of the squared Froude numbers different scales can be deduced, which are tabulated in Tab. 3.1. Physical modeling by means of Froude similitude should always be considered when viscous and surface tension forces tend to be negligible compared to inertia and gravitational forces in the physical process. This is valid assumption for a variety of civil engineering problems such as the flow over a spillway, water waves (Le Méhauté, 1976), in the case of fully developed turbulence, i.e. free surface flow, open channel flow, flow over weirs, negative surges or hydraulic bores (Martin and Pohl, 2009).

The Froude similitude is therefore attributed to model the physical question which has been outlined in Chapter 1 and 2 with sufficient accuracy. From the viewpoint of the experimenter, the wave motion under investigation is found to resemble either a short tidal wave or a combination of long negative surge and a hydraulic bore in the laboratory. The commonly addressed problem of water-air-mixtures, which is present for example in physical modeling of stepped spillways, (Bung, 2009) does not play a dominant role in the modeling of long wave interaction with macro-roughness

Table 3.1 Similitude ratios for Froude model similarity

Quantity	Dimension	Similitude ratio
Length	$[L]$	$L_p/L_m = N_L$
Area	$[L^2]$	$L_p^2/L_m^2 = N_L^2$
Volume	$[L^3]$	$L_p^3/L_m^3 = N_L^3$
Time	$[T]$	$T_p/T_m = \sqrt{N_L}$
Velocity	$[L/T]$	$V_p/V_m = \sqrt{N_L}$
Discharge	$[L^3/T]$	$Q_p/Q_m = \sqrt{N_L^5}$

elements. Yet in prototype, the run-up and run-down of long waves is usually accompanied with significant sediment transport and debris flow. A dimensional analysis presented in Subsection 3.1.3 serves as a basis for determining the predominant factors of long wave interaction and to delineate the capabilities of the presented physical model tests.

3.1.3 Dimensional Analysis

Identification of Process Background

The dimensional analysis is an engineering tool that allows to express and describe physical processes by means of dimensionless terms after the dependent variables for the process have been deduced and delineated. The description of the fundamental context of a physical process has to be independent of the chosen system of measurements (Kobus, 1974). A mechanical quantity is a combination of the numerical value and the entity which emphasizes the action or effect. Neglecting electrical and thermal quantities, a mechanical quantity can be made of the fundamental units which are length, time and mass. On the other hand a unit $[a]$ of a quantity a can always be phrased by a power product of the form (Yalin, 1971)

$$[a] = L^{\alpha} T^{\beta} M^{\gamma} \tag{3.1.6}$$

where the nature of the quantity a is reflected by the numerical values of the exponents. The characteristics of the dimensional quantity is given by the following constraints

$$\begin{array}{llllll} \alpha \neq 0 & \beta = 0 & \gamma = 0 & \Longrightarrow & \text{a geometric quantity} \\ \alpha \neq 0 & \beta \neq 0 & \gamma = 0 & \Longrightarrow & \text{a kinematic quantity} \\ \alpha \neq 0 & \beta \neq 0 & \gamma \neq 0 & \Longrightarrow & \text{a dynamic quantity} \end{array}$$

In the special case of $\alpha = \beta = \gamma = 0$ the quantity is called a dimensionless quantity. By means of the theorem of Buckingham it is hence possible to reduce an equation of the form

$$f(x_1, x_2, \ldots, x_n) = 0 \tag{3.1.7}$$

containing n physical variables x with a dimension matrix of order r into an equation of the following form by recasting into dimensionless Π terms

$$F(\Pi_1, \Pi_2, \ldots, \Pi_{n-r}) = 0 \tag{3.1.8}$$

The dimensionless variables Π are composed of power products of the former dimensional variables x. The resulting equation exhibits usually two (kinematic characteristics) or three (dynamic characteristics) fewer unknown dimensionless quantities $(n - r)$ (cp. also Yalin, 1971; Kobus, 1974; Le Méhauté, 1976; Hughes, 1993b; Heller, 2007; Martin and Pohl, 2009).

The problem setup of long waves which are climbing up a plane, sloping beach is depicted in Fig. 3.1. During their run-up, the approaching waves interact with macro-roughness elements positioned at different distances to each other and in different combinations on the beach area above the still water line. It is assumed that the first macro-roughness element row is always at the same distance to the coastline and only one possible element combination is sketched in the Fig. 3.1 to demonstrate the principle. In order to estimate the scale effects that are associated with the physical model applied in the current study, a dimensional analysis is conducted. The dependent and independent variables which influence the physical process of wave run-up and macro-roughness interaction are firstly listed and grouped . Kobus (1974) states that on the one hand if the selection of variables is not amply comprehensive, important effects might be overseen and on the other hand if too many variables have been detected it is possible that irrelevant parameters arise in consequence. In accordance with the sketch shown in Fig. 3.1 the Tab. 3.2 lists the variables related to the

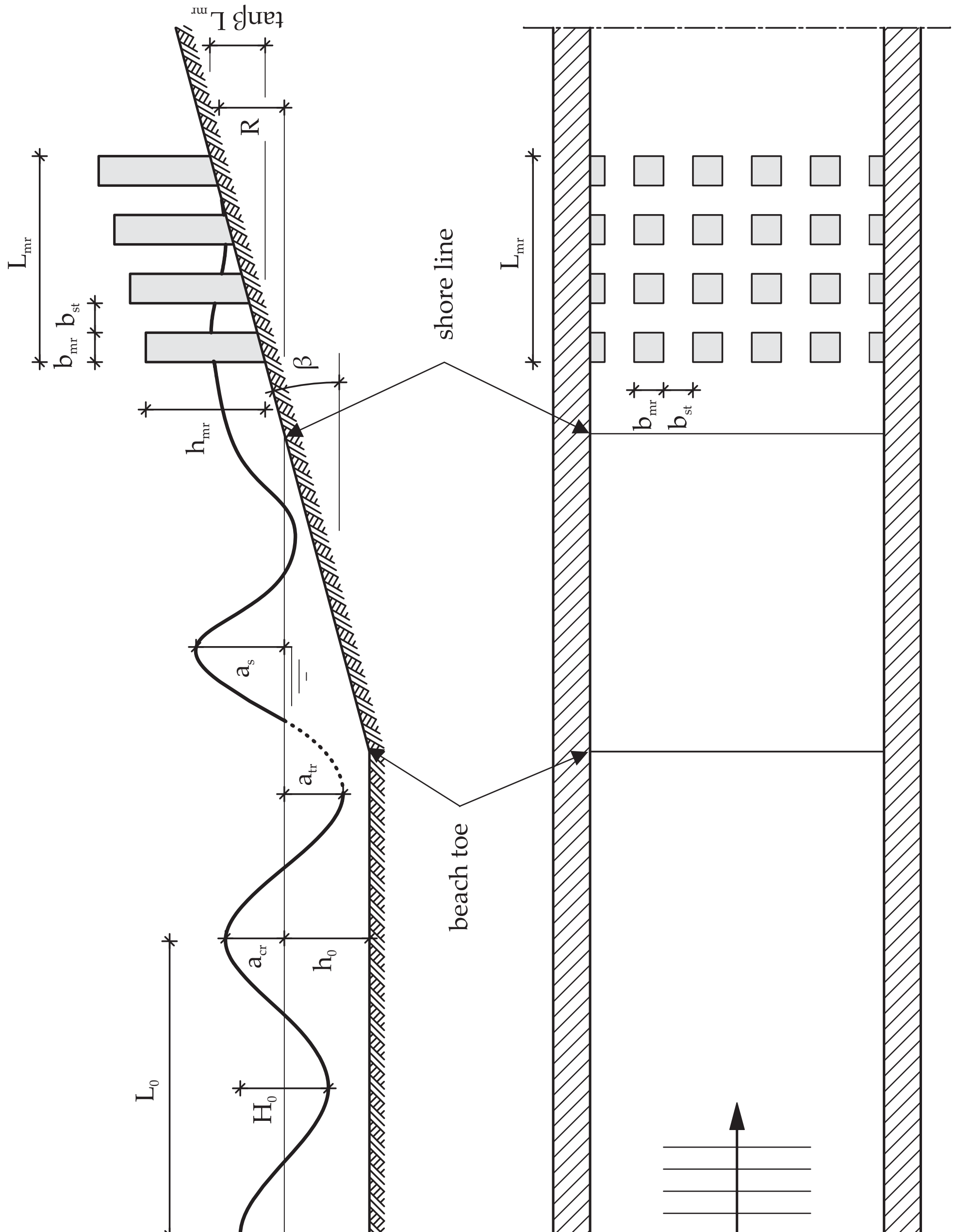

Figure 3.1 Sketch of the problem setup and the definition of the used variables, $h_0 =$ water depth, H_0 wave height and L_0 = wave length at the even bottom section, a_{cr} = and a_{tr} = amplitude of the wave crest and trough, β = slope angle, R = wave run-up, b_{mr} and h_{mr} = width and height of the macro-roughness elements, b_{st} distance between the macro-roughness elements

wave motion, Tab. 3.3 renders the physical variables of the fluid and Tab. 3.4 presents the geometric variables of the macro-roughness elements and their configuration. A good example of a dimensional analysis presented in Müller (1995) rendered good assistance in that context.

Table 3.2 Variables of wave motion used in the dimensional analysis

Notation	Value	Unit
Wave height	H_0	$[m]$
Amplitude	a_{cr}, a_{tr}	$[m]$
Period	T	$[s]$
Wave length	L_0	$[m]$
Wave steepness	s	$[-]$
Wave celerity	c	$[m/s]$
Incident wave angle	θ	$[°]$

Some of the variables specified in Tab. 3.2 can be recast in terms of more fundamental variables. One has

$$H_0 = a_{cr} + a_{tr} \quad \text{or} \quad (H_0 = 2 \cdot a) \rightarrow \text{sinusoidal wave} \tag{3.1.9a}$$

$$L_0 = cT \tag{3.1.9b}$$

$$s = H_0/L_0 \tag{3.1.9c}$$

$$a = F\left(H_0, L_0, h_0\right) \tag{3.1.9d}$$

In the case at issue the incident wave angle is not important but listed for completeness. In the prototype, oblique wave attack is of course present for tsunami. Yet common wave refraction is usually not fully capable of allowing for the wave to strike the beach head-on. In principle, the incident wave angle has to be accounted for but since this study aims at generalized wave interaction with macro-roughness in a wave flume, oblique wave run-up has been excluded from the objective.

The experiments have been conducted with water of constant density ϱ and viscosity ν while the ambient temperature was roughly $15 - 20°$. Due to constant temperature, fluid and boundary surfaces, it is assumed that the surface tension also behaves constant. The influence of surface tension in general will be discussed in the following. Beforehand the geometric parameters associated to the physical problem are tabulated in Tab. 3.4

Table 3.3 Fluid-related variables, physical properties of water relevant for the run-up process and the interaction with the macro-roughness elements

Notation	Value	Unit
Density	ϱ	$\left[kg/m^3\right]$
Kinematic viscosity	ν	$\left[m^2/s\right]$
Surface tension	ς	$\left[kg/\left(s^2 m\right)\right]$
Gravitational acceleration	g	$\left[m/s^2\right]$

Table 3.4 Geometrically relevant variables for the run-up process and the interaction with the macro-roughness elements

Notation	Value	Unit
Topography		
Beach profile		
Surface roughness (bottom/walls)	k_{sf}	$[m]$
Surface roughness (macro-roughness elements)	k_{mr}	$[m]$
Water depth	h_0	$[m]$
Beach slope	β	$[°]$
Beach permeability	k_d	$[m/s]$
Width of macro-roughness element	b_{mr}	$[m]$
Width of space between macro-roughness elements (streets)	b_{st}	$[m]$
Number of macro-roughness rows in on-shore direction	n	$[-]$
Macro-roughness element angle	φ	$[°]$
Macro-roughness element form		
Macro-roughness element combination	Γ	$[-]$
Length of macro-roughness area	L_{mr}	$[m]$
Non-dimensional obstructed height	ψ_{mr}	$[m/m]$
Rate of obstruction (cross-shore)	ψ_{cs}	$[m/m]$
Rate of obstruction (long-shore)	ψ_{ls}	$[m/m]$

The roughness of the bottom surface can be given as an equivalent sand roughness for the used PVC board (Section 3.2) which amounts to $k_{sf} = 0.0015$ mm (Bollrich, 2000). The roughness of the flume walls as well as of the macro-roughness of element surfaces is up by three orders of magnitude. The surfaces are made of concrete plaster while the macro-roughness elements were fabricated by means of steel casings compacted with a vibrating table (cp. Section 3.2). Those surfaces are attributed with an equivalent sand roughness of $k_{sf} = 0.1 - 1.0$ mm and $k_{mr} = 0.1$ mm respectively (Bollrich, 2000). On the one hand it is obvious that the bottom surface roughness plays a tangential role in the energy dissipation during the run-up process. From an engineering perspective the experimental results therefore lead to an evaluation of the process which is on the safe side. That is, the maximum run-up is overestimated compared to the prototype counterpart because tsunami run-up in the prototype also involves, besides macro-roughness dominated energy dissipation in urban areas, energy dissipation due to bottom roughness. Effects related to bottom roughness in transient flow conditions have not been addressed in the current study but depict an important field of interest for the future.

On the other hand, the wall roughness of the flume walls results in a turbulent boundary layer while a viscous sublayer is not present due to hydraulically rough conditions. The unintended energy dissipation attributed to the turbulent boundary layer violates the postulation of two-dimensionality and symmetry at the two flume walls. Yet it will be later seen that the resulting moving shoreline which would ideally form a straight shore parallel line, mostly diverges as far as a distance of $3 - 5$ cm from the flume walls. As far as the run-up measurements are concerned, those areas in the maximum run-up are excluded in order to avoid those laboratory effects which impinge on the validity of the experiments. Furthermore the surface roughness of the macro-roughness elements can be warranted with the fact that the prototype process has already been extensively idealized so that surface roughness effects do not dominate influences due to water storage effects, momentum exchange processes at the macro-roughness walls and partial or full destruction. Hence for the further analysis roughness effects shall be disregarded.

In addition, beach permeability which is listed for completeness is not present in the experiments. It is - again on the safe side - not meant to influence the run-up and run-down process significantly.

The flume width in the laboratory or the beach width in the prototype respectively is not involved in altering the run-up results as long as the physical problem can be defined as truly two-dimensional. It has been assured in the scaled model that the prerequisite of two-dimensionality holds true. Nevertheless final evidence of two-dimensionality in the model can only be delivered when a much wider wave flume will have been constructed. For the remaining time it is thus assumed that the influence of the flume width can be neglected. The topography, the beach profile and the macro-roughness form had not been varied during the experiments, whereas it is beyond debate that these parameters influence the physical process. Yet, the first two of them belong to the more general question of long wave run-up which is not in direct focus of the current study. As far as the macro-roughness element form is concerned, other than the quadratic form chosen is possible (such as a circular form), yet less common as building layout in the prototype. Rectangular layout forms are also possible but were excluded in order to keep the experimental workload feasible.

The length of the obstructed beach area can be given by Eq. (3.1.10a) as a sum of street and macro-roughness element width. More important than the actual length of the area is the non-dimensional obstructed height ψ_{mr} based on the beach slope and the number of macro-roughness elements. It is convenient to relate it to the incident positive wave amplitude a_{cr}. The obstructed height ψ_{mr} can be deduced from the length of the macro-roughness area in the on-shore direction L_{mr} and the beach slope angle β as given by Eq. (3.1.10b). For a fixed wave amplitude which attacks the shore the ratio ψ_{mr} increases when the number of macro-roughness element rows and associated therewith the vertical projection of the length of the obstructed beach increases. The height of the macro-roughness elements would also influence the run-up process if the condition $\eta_s \geq h_{mr}$ is admitted, where η_s denotes the wave height at the shoreline or on the first macro-roughness row. Though this condition is also excluded in order to focus on the flow around (and not over) the idealized buildings during the run-up process.

$$L_{mr} = n\left(b_{mr} + b_{st}\right) - b_{st} \tag{3.1.10a}$$

$$\psi_{mr} = \frac{\tan\beta L_{mr}}{a_{cr}} \tag{3.1.10b}$$

The cross- and long-shore rates of obstruction ψ_{cs} and ψ_{ls} listed in Tab. 3.4 can be defined with the geometric properties sketched in Fig. 3.1 as follows

$$\psi_{cs} = \frac{\hat{b}_{mr}}{\hat{b}_{mr} + b_{st}} = \frac{b_{mr}/\cos\varphi}{b_{mr}/\cos\varphi + b_{st}} \tag{3.1.11a}$$

$$\psi_{ls} = \frac{L_{mr}}{n\hat{b}_{mr}} = \frac{n\left(\hat{b}_{mr} + b_{st}\right) - b_{st}}{n\hat{b}_{mr}} = \frac{n\left(b_{mr}/\cos\varphi + b_{st}\right) - b_{st}}{nb_{mr}/\cos\varphi} \tag{3.1.11b}$$

where $\hat{b}_{mr} = b_{mr}/\cos\varphi$ denotes the width of the macro-roughness elements according to their angle of rotation and with respect to the incident wave direction. The cross-shore rate of obstruction increases according to Eq. (3.1.11a) when the ratio of the macro-roughness width to the sum of the street width plus the macro-roughness element width tends to unity. A cross-shore rate of obstruction of unity is equivalent to a complete obstruction of the beach and results in full reflection of the wave and the run-up tongue. The long-shore rate of obstruction depends on the ratio of the number of element rows times the width to the length of the macro-roughness area in on-shore direction. This geometrical ratio accounts for the obstruction exposed to the in-land propagating flow. The ratio ψ_{ls} decreases if the street width tends to zero, $b_{st} \to 0$. The ratio also grows if the number of macro-roughness rows is increased. Yet the influence of the number of rows is not meant to be linear because the energy dissipation varies non-linearly with the distance from the still water line. The variables contributing to the unknown quantity R, depicting the long wave run-up of sinusoidal long waves (cp. 5.1.1) which is investigated herein can be given by Eq. (3.1.12)

$$f\left(\underbrace{g, \varrho, \nu, \varsigma}_{\text{fluid properties}}, a, T, \beta, b_{mr}, b_{st}, n, \varphi, \Gamma, c\right) = 0 \tag{3.1.12}$$

In non-dimensional notation Eq. (3.1.12) can be recast into Eq. (3.1.13). Besides geometrical variables and rearranged new variables the Froude, Reynolds and Weber numbers are found to determine the physical process. It should also be mentioned that the dimensionless wave period and the wave length are interlinked and strictly speaking are not truly independent so that the reduction of variables claimed by the Buckingham theorem holds true. Yet for the sake of completeness the terms are kept included. The scaled model was intended to follow Froude similitude and as a result it turned out that also Reynolds and Weber numbers contribute to the physical process. The model and scale effects will therefore be elaborated in the following and the influence of those effects are going to be discussed.

$$F\left(\frac{a_0}{h_0}, T\sqrt{g/h_0}, \beta, \frac{h_0}{L_0}, \psi_{mr}, \psi_{cs}, \psi_{ls}, \Gamma, \underbrace{\frac{c}{\sqrt{gh_0}}}_{\text{Fr}}, \underbrace{\frac{ch_0}{\nu}}_{\text{Re}}, \underbrace{\frac{c^2 h_0 \varrho}{\varsigma}}_{\text{We}}\right) = 0 \tag{3.1.13}$$

Before doing so, the relationship between the dimensionless variables and the wave properties known from the relevant literature have to be established. A dimensionless number itself can be multiplied, divided or raised to a higher power (Yalin, 1971). Eqs. (3.1.14), (3.1.15) and (3.1.16) present the non-dimensional wave length, wave steepness and the surf similarity parameter which have already been shown in Chapter 2 in various formulations.

$$\frac{L_0}{h_0} = \left(\frac{c}{\sqrt{gh_0}}\right)\left(T\sqrt{g/h_0}\right) \tag{3.1.14}$$

$$\frac{2a_0}{L_0} = \frac{2a_0/h_0}{\left(\frac{c}{\sqrt{gh_0}}\right)\left(T\sqrt{g/h_0}\right)} \tag{3.1.15}$$

$$\xi = \frac{\tan\beta}{\sqrt{\frac{2a_0}{L_0}}} \tag{3.1.16}$$

Including the above equations the non-dimensional wave run-up R/a_0 is a function of the non-dimensional variables given by Eq. (3.1.17) which reads

$$\frac{R}{a_0} = F\left(\frac{2a_0}{h_0}, s = \frac{2a_0}{L_0}, T\sqrt{g/h_0}, \beta\right) \tag{3.1.17}$$

Furthermore the influence of a number of macro-roughness elements in the surging wave, due to a sudden uplift or subsidence of the seafloor, is prognosticated to reduce the maximum run-up by means of reflections and energy dissipation processes in the course of the water through the element configuration. The non-dimensional wave run-up reduction $R^\star/a_0$ diminishes the original wave run-up of a long wave without the presence of macro-roughness elements R/a_0 as described in Eq. (3.1.18) resulting in a final non-dimensional wave run-up R_{new}/a_0

$$\frac{R_{new}}{a_0} = \frac{R}{a_0} - \frac{R^\star}{a_0} \tag{3.1.18}$$

The run-up reduction $R^\star/a_0$ relates to the remaining non-dimensional variables listed by Eq. (3.1.13).

$$\frac{R}{a_0} = F\left(\underbrace{\frac{2a_0}{h_0}, s = \frac{2a_0}{L_0}, T\sqrt{g/h_0}, \beta}_{\text{long wave}}, \underbrace{\psi_{mr}, \psi_{cs}, \psi_{ls}, \Gamma}_{\text{macro-roughness}}\right) \tag{3.1.19}$$

Scale and Model Effects

The effects of viscosity and surface tension in the scaled model have to be discussed in order to prevent major error when the results are re-scaled to the prototype. First the wave propagation along the wave flume might be influenced by the viscosity. Dispersion effects acting on the wave height and the celerity are related to the viscosity. Boundary layers in free surface flow are found to be turbulent in the prototype while in many scale models laminar effects take place. Resistance therefore behaves differently in the prototype and in the scale model (Müller, 1995).

What is more, Sobey (2009) evaluated the existing techniques how to deal with wetting and drying of beaches and the coastal hinterland. He appraised the influence of boundary shear to be negligible in all but very shallow water depth. The inertia of the flow is basically the sum of gravity and boundary shear forces which becomes significantly influenced by the latter with decreasing water levels whereas the friction factor is meant to increase in turn. Especially in the neighborhood of the moving wave front the relative roughness height $k_S/\left(h+\eta\right)$ may rapidly increase and because it is not expected that the depth-averaged flow velocity changes strongly, also the boundary shear is going to take part in the momentum balance (Sobey, 2009). This fact is yet taken into account experimentally by means of the utilization of quite smoothly manufactured PVC boards which exhibit a rather small friction height.

Based on the wave celerity in the formulation of the Airy theory of linear water waves Biesel (1949) derives an equation for the wave celerity involving the kinematic viscosity ν which reads

$$c=\sqrt{\frac{gL_0}{2\pi}\tanh\left(2\pi\frac{h_0}{L_0}\right)}\cdot \left[1-\left(\sqrt[4]{\frac{gL_0^3}{2\pi^3\nu^2}\tanh\left(2\pi\frac{h_0}{L_0}\right)}\sinh\left(4\pi\frac{h_0}{L_0}\right)\right)\right]^{-1} \tag{3.1.20}$$

which reduces to Eq. 3.1.21 under the assumption of shallow water conditions $\sinh\left(kh_0\right)\approx\tanh\left(kh_0\right)\approx kh_0$ and the following substitutions $c=\sqrt{gh_0}$, $kh_0=2\pi h_0/L_0$ with k = the wave number, $\mathrm{Fr}^2=c^2/\left(gh_0\right)$ and $\mathrm{Re}=ch_0/\nu$ (cp. also Schüttrumpf, 2001).

$$\mathrm{Fr}^2=\left[1-\left(2\sqrt{\mathrm{Re}\cdot kh_0}\right)^{-1}\right]^2 \tag{3.1.21}$$

Fig. 3.2 depicts the relation between the Froude number and the Reynolds number given by Eq. (3.1.21) on the basis of the linear waves theory which should be deployed in the present case as a first order estimation to the given propagation and run-up problem.

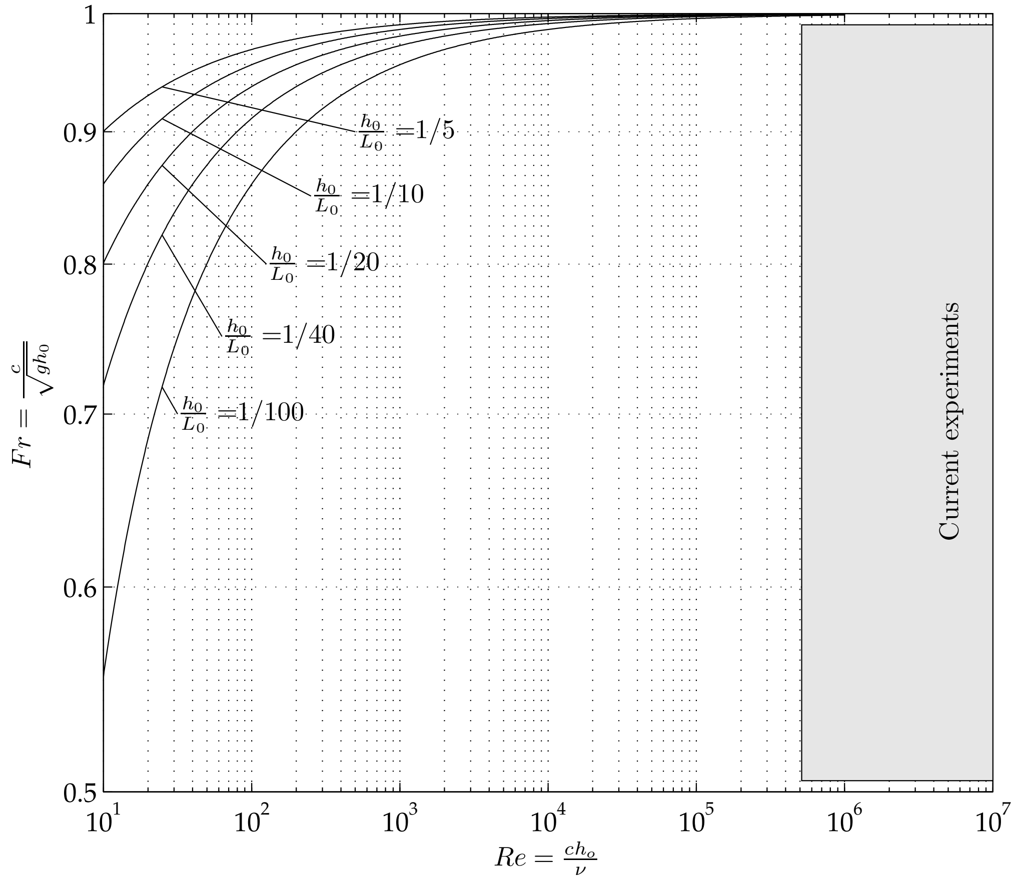

Figure 3.2 Relation of the Froude Fr to the Reynolds number Re of a wave given for different dimensionless water depth, the shaded area represents the flow regime of the current study

It is apparent that the Reynolds number during the wave propagation (Re $= ch_0/\nu = 1.71 \cdot 0.3/10^{-6} \approx 5.1 \cdot 10^5$) is high enough to exclude significant influences of scale effects. During the wave run-up and run-down no longer the wave celerity marks to dominant velocity but the actual run-up velocity should find expression in the calculation of the Reynolds number. It is then obvious that the decreasing flow velocity and also flow depth with increasing distance of the still water position of the shoreline in the course of the run-up of the wave subsequently results in a decreasing Reynolds number. At the maximum run-up the wave motion is at rest and the Reynolds number vanishes. In the time before the phase of the run-up motion the influence of viscosity is meant to slightly affect the results of the experiments. Schüttrumpf (2001) defined a threshold of $Re_{\text{crit}} = 10^3$ for overtopping experiments. Accordingly it is assumed for the current experiments that the experimental scale adds to scale effect imperfections which need to be considered in case that the findings should be employed to estimate prototype circumstances.

Besides the phase of wave propagation over an even horizontal bottom where the effects of viscosity are only weak in the physical model, it has to be demonstrated that viscous effects remain insignificant while the wave interacts with the macro-roughness elements on the beach. The average Reynolds number during that phase of the run-up motion can be defined similarly to the propagation phase except for a change in the characteristic length scale of the turbulence generation. Hence the characteristic length scale is in the order of the horizontal macro-roughness element width and length, which is $b_{mr} = 0.1$ m. During the wave run-up and the interaction with the macro-roughness elements it holds true

$$\text{Re} = \frac{v_{local} b_{mr}}{\nu} = \frac{0.2 \cdot 0.1}{10^{-6}} = 2 \cdot 10^5 \tag{3.1.22}$$

where v_{local} is the local horizontal velocity in the direction of the wave run-up, b_{mr} is the characteristic length scale and ν is the kinematic viscosity. Eq. (3.1.22) yields Reynolds numbers which are in the order of $\mathcal{O}\left(10^5\right)$ for some velocities that were measured within the underlying set of experiments (cp. Chap. 5.5). This indicates that viscous forces are equally not significant during the run-up phase of the long wave since inertial forces outweigh the viscous forces in the scales model. It is also obvious that the Reynolds number is decreasing with decreasing horizontal velocity. This fact also suggests that the viscosity develops into a significant parameter only when smaller flow velocities occur. The error stemming from these scale effects is present though negligible since it only appears at a spatially limited area of the entire wave run-up motion.

Besides the effects of viscous forces to the wave propagation, which overall appear to be marginal, it has to be discussed how viscosity affects the run-up process especially for the mild sloping beach which is applied in the current study. Le Méhauté (1976) demands a minimal flow depth in physical models which should not be smaller than $h = 2.0$ cm and $T = 0.35$ s. During the run-up of the long wave the influence of the viscosity increases with decreasing flow velocity in the run-up tongue. It is therefore concluded that scale effects due to the small length scales are present though the effects are basically limited to the foremost moving wave front where the water depth falls short of the limiting value given by Le Méhauté (1976). It can be assumed that the influence depends on the beach slope. An investigation dealing with the run-up of dam-break induced waves mimicking tsunami (Nakamura et al., 1969) indicates that viscous effects are marginal at steep beaches while run-up due to wind waves on mild sloping beaches is affected by scale effects up to $21~\%$ (SPM, 1977), whereby the wave run-up in downscaled models is generally underestimated.

Schulz (1992) demonstrated with deep water waves that the influence of viscosity increases mainly with decreasing beach slopes and subsequently correcting terms have to be adjusted. In the case of non-breaking deep water waves an overall damping of the wave run-up of up to $25~\%$ was stated. Of primary influence proved to be basically the beach slope and the roughness of the beach surface in the scaled models. In the case of wave run-up and overtopping of sea dikes due to short waves (Schüttrumpf, 2001; Schüttrumpf and Oumeraci, 2005) and mass failure induced surging waves at reservoir and river dams (Müller, 1995) the scale effects of viscosity could be virtually eliminated because the water depth at the beach and the dike crest was almost always high enough and in the latter case because the run-up distance was small and of a short duration. In the case of approaching long waves climbing up a mild sloping beach viscosity effects in the order of $10 - 20~\%$ cannot be precluded, though as will be later seen, comparisons to analytical results yield much lower differences. As a matter of fact, the scale effects to such long waves on gently sloped beaches have not been sufficiently addressed in literature and experiments with varying model families at different length scales (which could give valuable insight into the scale effects) have not been performed until now.

A relation of the Weber number which incorporates the dependency of the surface tension to the fluid motion in the context of the long wave propagation and run-up was already defined by Eq. (3.1.13). While in the prototype scale waves are rarely transformed under the forces carried to the water surface by surface tension, the effect might gain significant influence in small scale models. Especially short waves, which regularly have to be investigated in laboratory studies, can reach the region of capillary waves when the model length scale of a hydraulic scale model is designed too small. Dingemans (1997) expressed the effectiveness of the surface tension in an increase of gravitational acceleration but outlined that the influence of surface tension to wave action is dominant when capillary waves for example are investigated. Even though the waves under consideration are extraordinary long, it shall be demonstrated that the surface tension influence is small enough to be negligible in the current context, as deduced from the dispersion relation in the framework of linear wave theory. In order to quantify the influence of the surface tension Le Méhauté (1976) again uses the linear wave theory as a first order approximation to the wave propagation. The extended dispersion relation reads ((cp. Schüttrumpf, 2001))

$$c^2 = \left(\frac{gL_0}{2\pi} + \frac{2\pi\varsigma}{L_0\varrho}\right)\tanh\left(2\pi\frac{h_0}{L_0}\right) \tag{3.1.23}$$

Eq. (3.1.23) reduces to the relation given in Eq. (3.1.24) where the Froude number (Fr) and the Weber number (We) are linked to the wave number k. It reads

$$1 = \frac{1}{\text{Fr}^2} + \frac{(kh_0)^2}{\text{We}} \tag{3.1.24}$$

assuming that the relations $\tanh(kh_0) \approx kh_0$, $c = \sqrt{gh_0}$, $kh_0 = 2\pi h_0/L_0$ with $k =$ the wave number, $\text{Fr}^2 = c^2/(gh_0)$ and $\text{We} = c^2 h_0\varrho/\varsigma$ hold. Fig. 3.3 shows the relation between the Froude number to the Weber number for linear waves, which at first order may represent the long waves used during the experiments. It falls into place that the longer the waves in a given water depth, the smaller the Weber numbers grows and in turn that a significant influence of surface tension has to be expected only when short waves are investigated in laboratory studies. The relevant region of the current experiments is also endorsed in Fig. 3.3. The actual Weber number for the experiments equals

$$\text{We} = \frac{c^2 h_0 \varrho}{\varsigma} = \frac{\left(\sqrt{9.81\ \text{m/s}\cdot 0.3\ \text{m}}\right)^2 \cdot 0.3\ \text{m}}{72.86\ \text{N/m}} = 12.12$$

Hence a Weber number of that order is in the range of critical Weber numbers found in literature. A comprehensive review of small scale models and the influence of the Weber number has been presented in Peakall and Warburton (1996). Due to the nature of surface tension, its effect on fluid motion amplifies where the fluid surface exhibits small radii of the liquid surface or when the distance to solid boundaries is small, i.e. for drops, bubbles or larger river models. During long wave propagation in the wave flume, the inertia forces are still dominating the surface tension effects. Peakall and Warburton (1996, cp. e.g. their Fig. 1) summarized various recommendations on the critical flow depth in small models with Weber numbers in the range of $\text{We} = 2.5 - 160.0$.

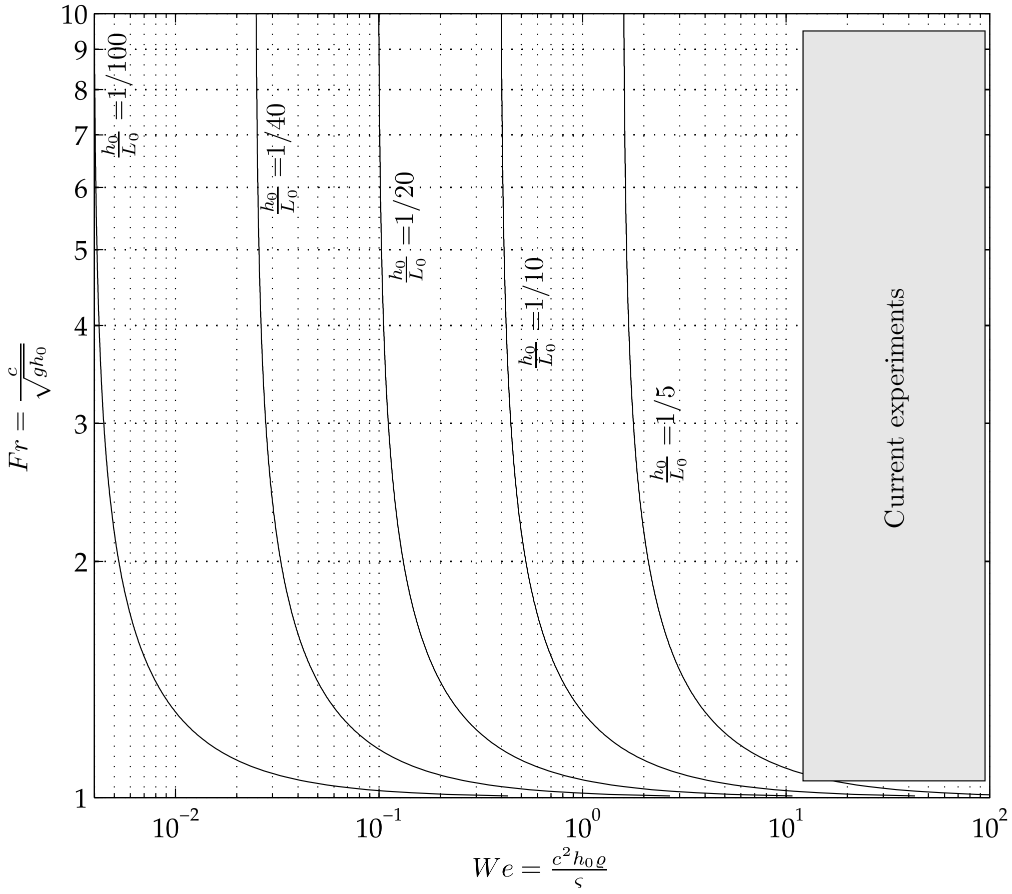

Figure 3.3 Relation of the Froude Fr to the Weber number We of a long wave given for different dimensionless water depth, the shaded area represents the flow regime of the current study

In addition Novak and Cabelka (1981) state that in order to reduce surface tension effects, a scaled model should at least comprise a minimum wave length of ≥ 1.7 cm, a velocity at the water surface of ≥ 0.23 m/s and a minimum water depth of ≥ 1.5 cm, bearing in mind that these conditions apply to steady state flow conditions. Finally, besides the viscosity which was found to contribute slightly to the scale effects in the conducted laboratory test, also the surface tension turns out to affect the experimental results to a certain degree because the Weber number is in the range of a critical Weber number where the ratio of capillary forces to inertia forces tends to unity.

Conclusions

In summary, the wave propagation in the flume can be conceived to be almost unaffected by scale effects. Neither the Reynolds nor the Weber number fall below a critical threshold where influences significantly dominate or bias the current findings and results. Yet the current investigation involving the run-up of long waves and the interaction with macro-roughness elements is marginally affected by scale effects. Though not ultimately quantifiable due to limited laboratory space for further model families, the scale effects are meant to overestimate the wave run-up with and without macro-roughness elements exposed to the transient flow due to the special geometry of the run-up tongue (and associated, their shallow flow depth). Nevertheless it will be seen that the findings agree well with analytical run-up results which a priori exclude scale issues. It is therefore argued that the validity of the experiments is satisfactory and the scale effects are mostly attributed to either very shallow water conditions which are still spatially limited or to the slowly moving run-up tongue which is spatially and temporally also limited to the foremost run-up area.

3.2 The Wave Flume

The experiments in the closed-circuit wave flume were carried out at the Franzius-Institute for Hydraulic, Waterways and Coastal Engineering. The flume, erected in solid construction, consists of lime brick walls which are 0.175 m thick.
A schematic drawing of the flume is shown in Fig. 3.4. Its total length comprises 27.23 m and its total width is 8.24 m. The clear width of the flume amounts to 1.00 m. The radius of the curve measured from the center to the flume axis is 3.435 m. The maximum water depth at the lowest flume wall comprises 0.90 m. The surface of the side walls is made of cement plastering 0.5 cm, while a 3.13 m long section consists of plate glass panels retained by I-shaped steel beams. The bottom of the flume consists of smoothed floor pavement. The inner flume walls are supported by buttresses made of sand-lime brick housed inside the water storage basins. A more detailed technical drawing of the flume dimensions could be found in the annex A.2.

Five different parts of the flume are distinguished through their function as denoted in Fig. 3.4. First, the pump station indicated as position (a) drives the water in the flume in either forward or backward direction. Water pumped into forward direction propagates along the propagation section marked as position (b). Conversely, water that is pumped out of the propagation section is stored in the reservoir section (c) until the experimental procedure requires additional volume of water. The sloping beach section denoted as position (d) models the bathymetry of a natural beach and its adjacent coastal hinterland. The water storage basins are located at the inner ends of the closed-circuit flume store the water volume for case of installing and overhauling.

A ramp was installed in the straight section of the flume as a fixed bed setup. The still water depth is kept constant from the pump station to the toe of the ramp. It amounts to $h_0 = 0.31$ m. The slope of the beach that is attached to the constant depth region exhibits 1 vertical to 40 horizontal (i.e. $\beta = 1.43°$). The toe of the beach is situated 0.76 m away from the end of the curve. The surface of the ramp is constructed of unplasticized polyvinyl chloride (PVC) boards with 2.00 m length and 0.99 m width. The PVC boards are 0.5 cm thick. The residual slot between the PVC board and the flume walls due to imperfections in the straightness of the walls was sealed with silicone thus preventing the surging water from draining away into the ramp construction.

The substructure of the ramp consists of six wooden cases, which are 2.50 m long and 0.788 m wide. The open-top cases are made of 2.1 cm thick film-faced plywood fastened with yellow chromate chipboard screws. To augment the stability of the

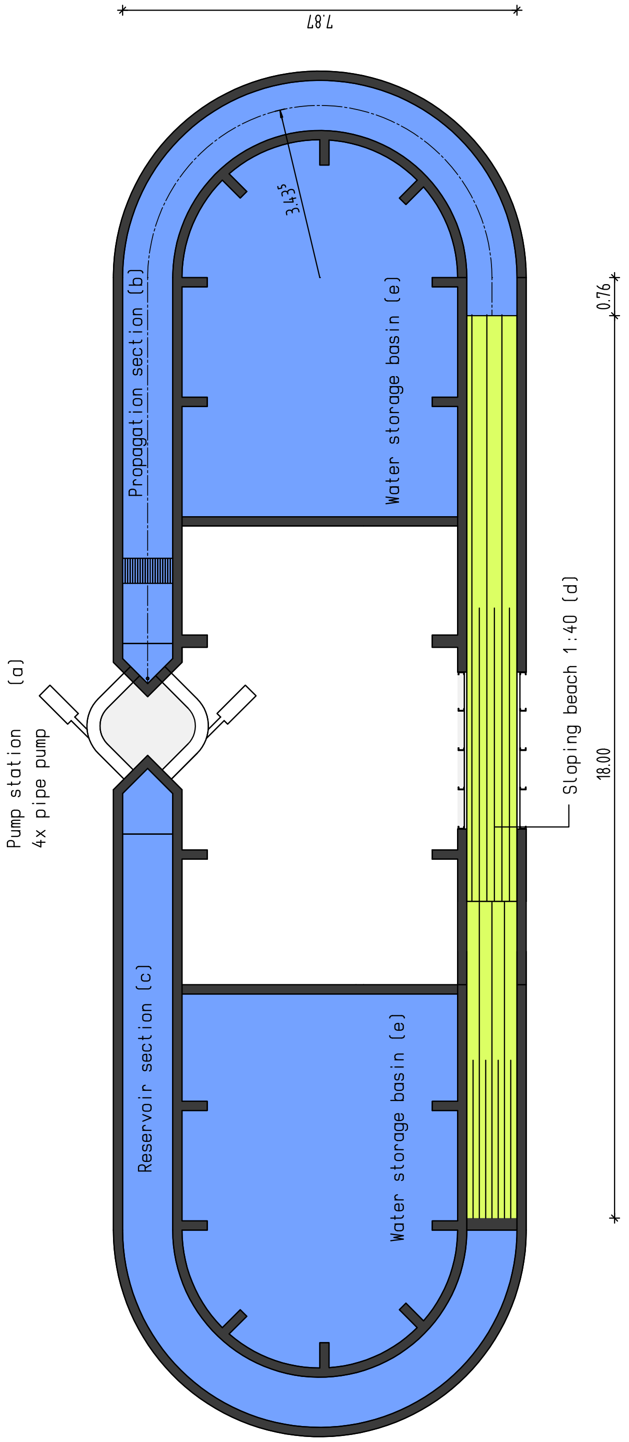

Figure 3.4 Schematic drawing of the closed-circuit flume and its equipments, (a) pump station, (b) propagation section, (c) reservoir section, (d) sloping beach, (e) water storage basin

cases, a perforated bottom is fixed $2.0\ \mathrm{cm}$ above the bottom edge. Additionally $0.12\ \mathrm{cm}$ high stiffener boards were fixed in the transverse edgewise direction at a distance of $0.20\ \mathrm{m}$. The head and base plate of the cases were bolted together with zinc plated steel carriage bolts after assemblage of the cases in the flume. The vertical positions of the cases were corrected against a tight string and firmly shimmed with PVC spacers. The transverse direction of the ramp was controlled by a digital water level with $\pm 0.50°$ accuracy. Two photographs of the ramp assemblage are shown in Figs. 3.5(a) and 3.5(b)

(a) Downstream view of the plywood cases (b) Stiff-jointed connection between two cases

Figure 3.5 Photographs of the assemblage of the ramp construction with ballast concrete paving slabs

Afterwards, the cases were weighed down with concrete paving slabs and a topping of fine-grained sand. Outside the cases of the flume walls, the space was also backfilled with fine-grained sand. The sand fill was leveled out $4.0\ \mathrm{cm}$ beneath the projected surface elevation of the ramp. The remaining height above the sand fill was filled in with floating screed to support the PVC boards (Fig. 3.6(a)). As a final surface finishing, the PVC boards were attached to the plywood boards of the ramp cases by stainless steel chipboard screws every $15.0\ \mathrm{cm}$ (Fig. 3.6(b)), to assure a tight fit under any pressure condition. The joints of the short board edges were sealed with silicone. The grooves were flattened at the level of the PVC boards. The planarity of the manufactured surface was evaluated with a $2.0\ \mathrm{m}$ straightedge to ensure flatness and levelness. The total deviation of the surface to the straightedge yields $\pm 0.5\ \mathrm{mm}$.

(a) Downstream view of the beach wedge and the installation of the floating screed (b) PVC board, the finished floating screen and the cable duct for the pressure sensor connections

Figure 3.6 Photographs of the assemblage of the ramp construction with floating screed and pressure sensor installation

The walls of the wave flume generally consist of a lime brick wall but one section had been engineered with windows made off glass panels and supported by a rigid steel frame. It is hence possible to observe the fluid motion from outside without disturbing the flow. The position of the window section can be taken from Fig. 3.4 or the more detailed Fig. A.2 in the annex.

Pressure sensors were installed inside the ramp at different positions which are further outlined in Subsection 3.3.3. The pressure sensors were mounted with their transducers facing to the water body. The installation length of the pressure sensors is $120\ \mathrm{mm}$ and therefore it was important to keep a hollow space in the ramp free to install the sensors properly. The hollow space was kept free by means of vertically oriented PVC pipes. The electric leads were wired in a main cable duct at one side of the flume whereof branch lines were connected to the mounting positions of the PVC pipes (cp. Fig. 3.6). Each pressure sensor which possesses a quarter inch thread at its transducer head is fitted to a borehole in the PVC board by means of an adaptor socket unit fastening the sensor with stainless screws. This arrangement assured a non-intrusive measurement of the water level above the pressure sensor (cp. Subsection 3.3.5).

Fig. 3.7 additionally shows the used macro-roughness elements which were applied to model urban pattern and buildings exposed to a flow induced by a surging long wave. The macro-roughness elements were implemented as solid, cube-shaped cement blocks with an edge length of $0.1\ \mathrm{m}$ manufactured of standard concrete mixture. As form work a standard cube mold was utilized to pour in the concrete. A total number of 100 whole cubes and 20 half cubes were manufactured and they were cured for at least 28 days in a bucket filled with water. Fig. 3.7(a) depicts an example configuration of the macro-roughness elements in the flume. It is obvious that some minor imperfections came up during the production of the macro-roughness elements (blowholes, dents) but in summary the quality of the concrete cubes was satisfactory for the experiments. The wall treatment can be found in Fig. 3.7(b) and additional explanation on the symmetry requirements of the conducted experiments is outlined in Subsection 3.3.2. The configurations of the macro-roughness elements, the number of macro-roughness element rows as well as the orientation of the elements to the approaching wave were varied in the experiments reported herein. For the sake of completeness all the tested configurations were drawn to scale and inserted in the annex.

At the upper end of the ramp a solid $0.175\ \mathrm{m}$ wide and $0.475\ \mathrm{m}$ high sand-lime brick wall separates the reservoir section and the sloping beach in order to avoid that water flows out of the reservoir. The separating wall is constructed transverse to the flume axis. It is connected impermeably to the flume walls with cement mortar. An opening of $20.0\ \mathrm{mm}$ was left between the separation wall and the PVC surface of the ramp facilitate sufficient ventilation of the ramp body.

A 1 vertical to 1 horizontal inclined tetrapod embankment was set up at the reservoir facing side of the separation wall. It acts as a cushioning element during and after an experiment took place and restricts the experiment time span since full reflection at the separating wall is prohibited.

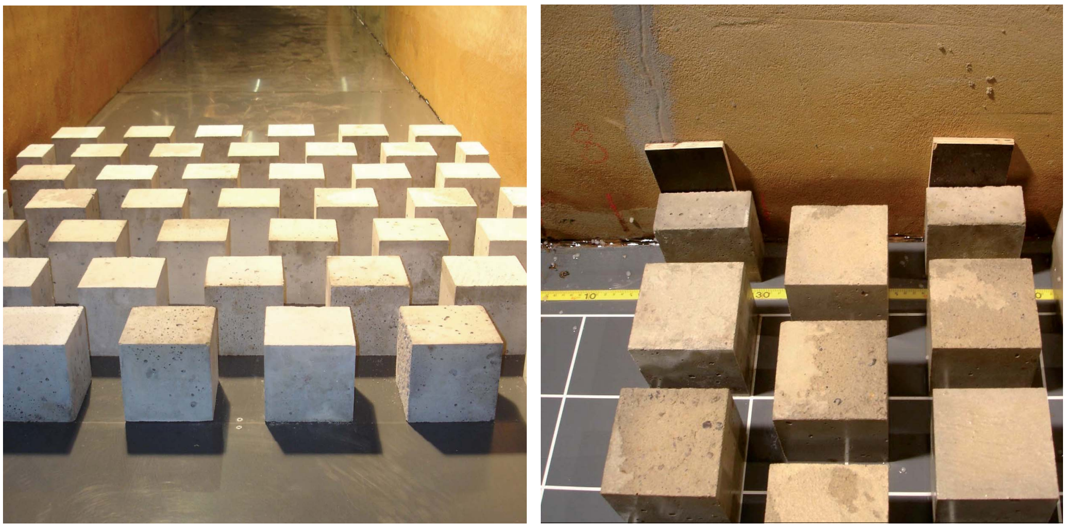

(a) Staggered macro-roughness element configuration

(b) Half cubes used at the flume walls

Figure 3.7 Photographs of the macro-roughness element implementation

3.3 Experimental Procedures

3.3.1 General Considerations

A typical experimental procedure encompasses the wave generation described in Section 4, the run-up measurements, the wave height and water depth measurements at various positions as well as the velocity measurements. After a long wave has been generated it propagates along the flume and climbs up the sloping beach until its maximum run-up elevation is reached. Thereafter the particle velocity turns negative and the run-down phase follows. All measured quantities are recorded until the water level along the sloping beach has reached its minimum. Then the wave generation procedure halts when the pipe pump control is switched off. After each experimental cycle the water level inside the flume calms down for ≈ 1080 s until the instantaneous pressure sensor indicates water level deviations below a threshold of $3 \cdot 10^{-3}$ V.

Generally, the surface of the beach wedge was initially wetted before each experimental run. Only few accounts in literature were found that deal with differences in wave propagation over dry and wet bottoms. Yet, Zelt and Raichlen (1991) investigated the run-up of solitary waves which were analogously generated as given by Synolakis (1987). Defining its unique setup, the beach exhibited a zero slope angle to the horizontal beginning in the vicinity of the initial shore line. The surface of the installed beach slope was made of lucite whereas the horizontal region was fabricated of glass board. Dry and wet cases were adjusted by small differences in the water level of the applied flume. As a result, the investigator found that the wave front appeared to move significantly faster over the dry bed compared to the corresponding wet-bed case while peak inundation front speeds were reduced $10-15\%$ for propagation over the wet bed as compared to the dry one. Bottom friction was of importance especially in the initially dry region. Also for the aim of this analysis, to model prototype conditions adequately, a dry bed would be prefereble over a wet bed as tsunami waves in nature usually also propagate over dry beds. Yet, for the current study, it is assumed that the differences between dry and wet cases are beneath the effects found by Zelt and Raichlen (1991), due to the fact that the applied wave forms are not propagating over a horizontal bottom but a constant slope. Therefore the deviations in the propagation wave front are conjectured to be dominated by the restoring forces, due to gravity, in the run-up phase over frictional forces. Secondly, and for reasons of practicality, the beach slope was wetted before each experimental run and especially in the morning in order to assure invariable experimental conditions as it was literally impossible to dry the surface between two runs.

3.3.2 Symmetry Requirements

A prerequisite for the experiments was the strict observance of two-dimensionality and thus symmetry. Besides the influence of the wall boundary layer discussed in Subsection 3.1.1 the requirement of two-dimensionality is additionally offended when the macro-roughness element configurations are arranged without regarding symmetry. In preliminary studies the macro-roughness elements were positioned according to even street widths b_{st} (e.g. $2, 4, 6, 8$ cm) with the aim to achieve commensurability between subsequent experimental runs of rotated and non-rotated macro-roughness combinations. However this approach yielded residual distances of the last macro-roughness element to the respective flume wall. Unless these spaces were closed it appeared that the approaching wave front formed a jet-like current along the flume wall leading to significantly higher wave run-up in the wall regions.

The configuration of the macro-roughness elements and the definition of the axis of symmetry is drawn in Fig. 3.8 for a staggered, rotated and staggered, non-rotated configuration in order to demonstrate the procedure. A half macro-roughness element was always positioned at the flume wall with the aim to prevent biased run-up results. The remaining space was partitioned subsequently to position the remaining macro-roughness elements. A street width b_{st} was defined as the smallest distance be-

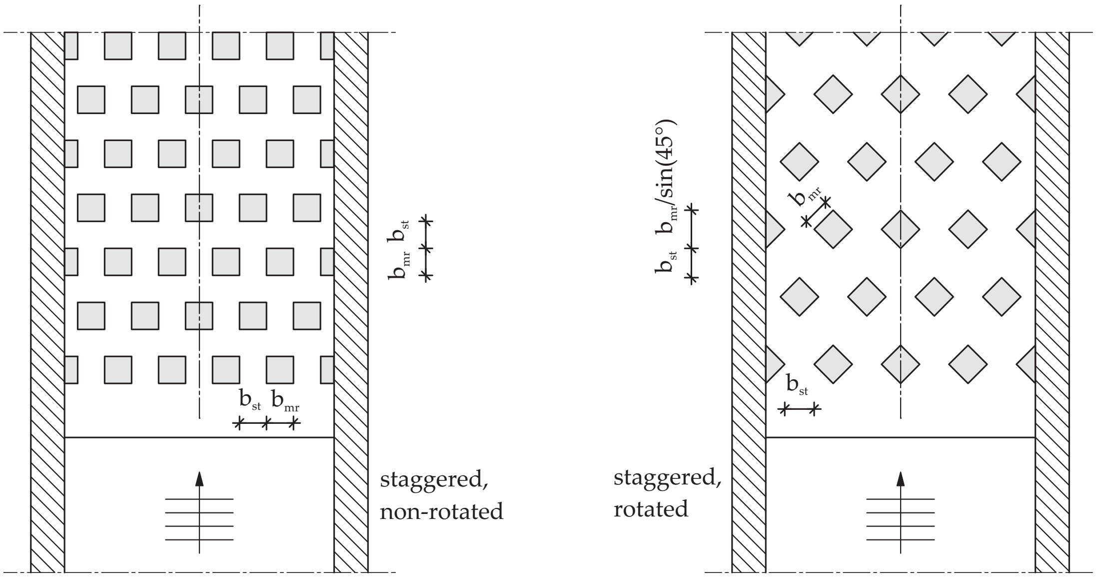

Figure 3.8 Symmetry requirements for the configuration of the macro-roughness elements for a staggered, non-rotated configuration (left) and a staggered rotated configuration (right), drawing not to scale, demonstration of the axis of symmetry at the flume wall, which always cuts a macro-roughness element in the middle

tween two macro-roughness elements in either the rotated or the non-rotated configuration. The long-shore distances were defined in accordance. The symbol definitions are also registered in Fig. 3.8.

3.3.3 Instrumentation and Data Recording

A detailed description of the mounting positions of the sensors is depicted in Fig. 3.9 and 3.10. All sensors that were used during the experiments are referenced in the technical drawing and abbreviations denote the devices for further assignment. When multiple devices were used, consecutive numbers were assigned. A device that was positioned at different points is identified by an underscore and alphabetical order.

The sensors and instruments which are positioned along the sloping beach are connected to their corresponding measurement amplifiers according to the technical specifications and the output voltage level. After measured signals are conditioned hereby, analog (A) input is converted into digital (D) signals by a A/D hardware converter *National Instruments USB-6259 BNC*. In total 16 differential analog inputs can be connected via bayonet connectors (BNC) while 4 analog output channels are available. Detailed information about the A/D converter is given in Tab. 3.5. The sampling

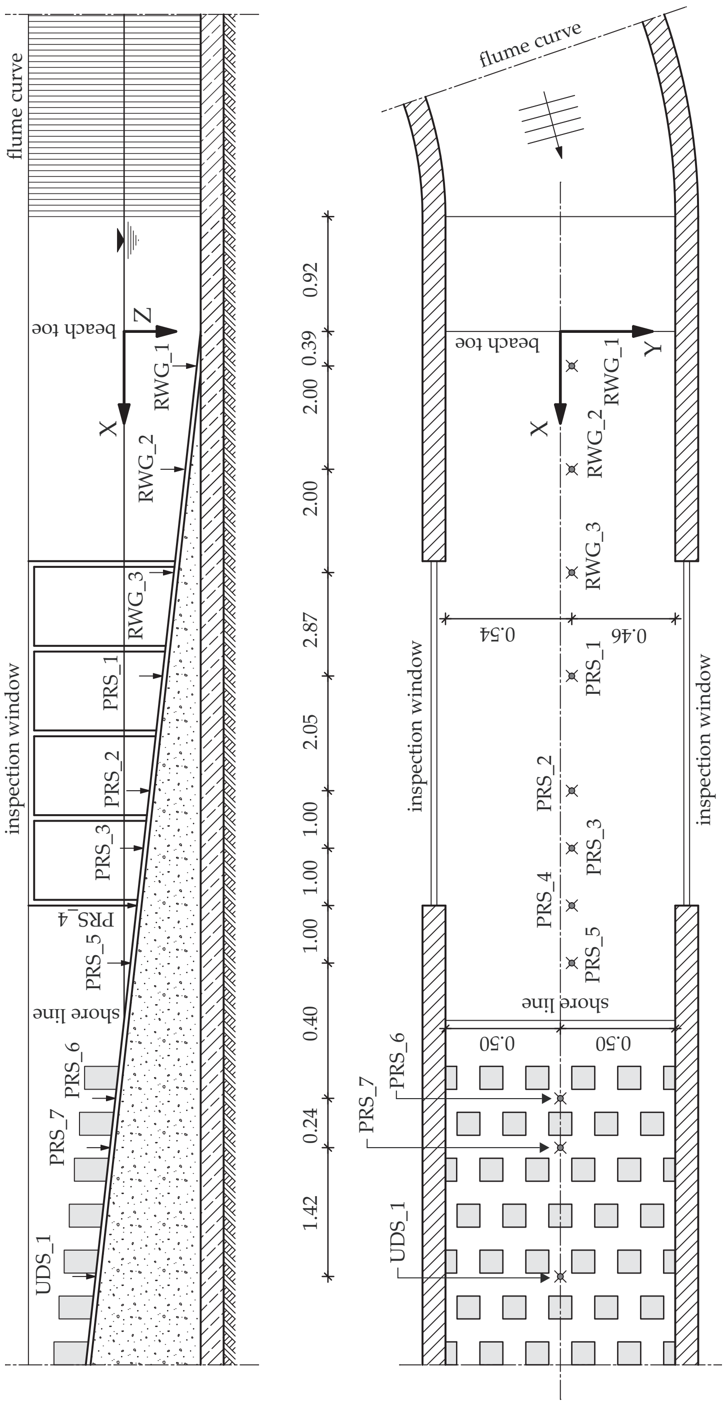

Figure 3.9 Layout drawing of the used pressure sensors and wave gauges for the experimental setup, abbreviations denote the following devices: PRS – pressure sensor, RWG – resistance wave gauge, UDS – ultrasonic distance sensor; for more than one device consecutive numbers are given, not to scale

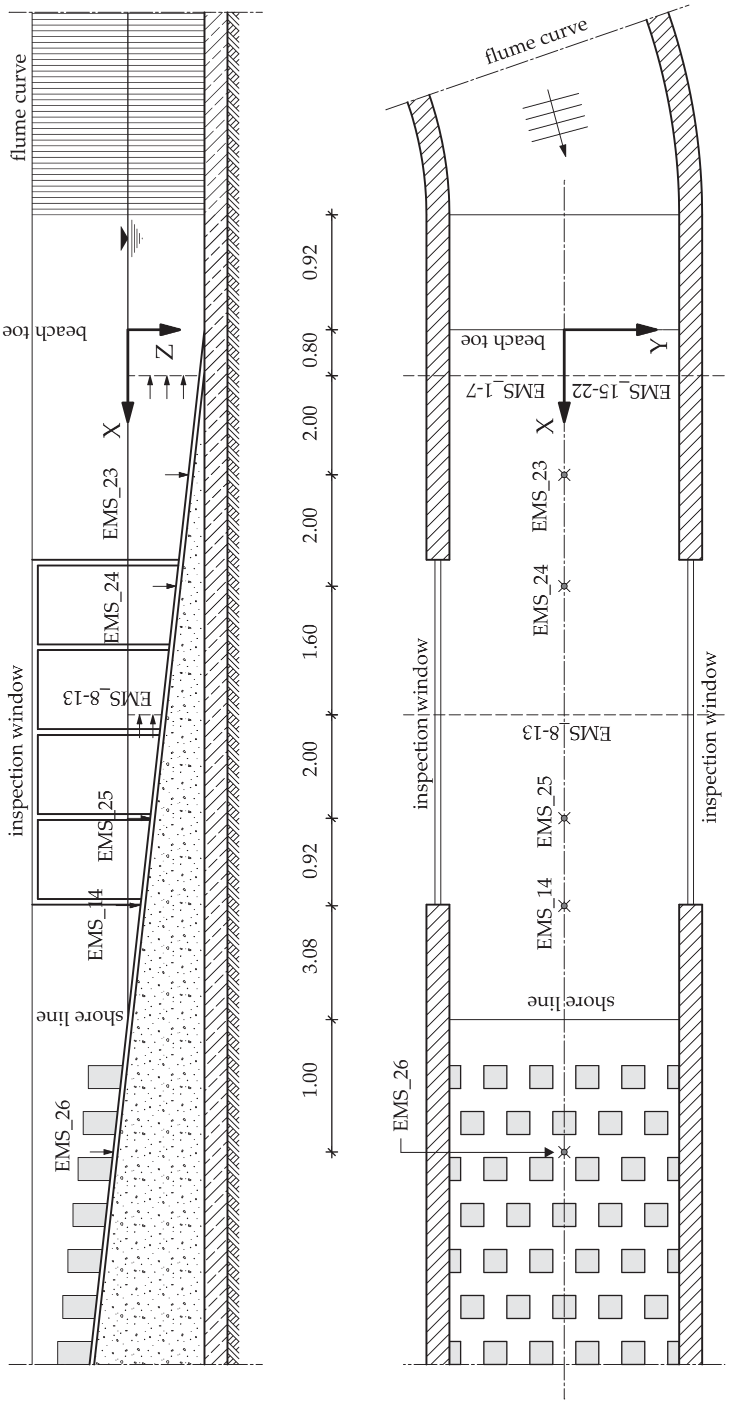

Figure 3.10 Layout drawing of the used electro-magnetic probe for the experimental setup, abbreviations denote the following devices: EMS – electromagnetic velocimeter; for more than one device consecutive numbers are given, not to scale

rate of the A/D converter was set to 1.0 kHz even though the sampling rates of individual sensors was below. This was due to the fact, that the output signal for the CCD camera control had to be resolved in this high frequency manner. For later use, the recorded sensor time series were filtered and averaged in post-processing.

Table 3.5 Technical specification of the analog/digital converter used to record the individual channels at each experiment

Item	Value
No. of analog channel (input)	16
No. of analog channel (output)	4
No. of counter/clock	2
ADC resolution	16 bit
Input voltage range	$\pm10, \pm5, \pm2, \pm1, \pm0.5, \pm0.2, \pm0.1$ V
Sampling rate	1.0 MS/s (multi-channel)

The D/A converter was connected to a standard personal computer via universal serial bus (USB). A *NI-DAQmx* driver software was used to make the hardware available together with the *National Instruments DIAdem* (V 10.2) data acquisition software, that was applied to record and file the data of the measured sensors on the computers hard drive. A data logging application was generated with the standard graphical programming interface of *DIAdem*.

Internally *DIAdem* uses a circuit layout which bases on software control in order to interlink the hardware components and the data recording on a storage medium. The circuit layout deployed here is shown in Fig. A.3. The yellow channels are utilized for the clock frequency transmission while the green channels depict the data stream. The displayed circuit blocks ensure the input and output, the data storage, the clock generation and the visualization on the software side.

3.3.4 Run-up Measurements

A measurement of key importance has been the correct detection of the maximum wave run-up. Besides visual detection, a couple of techniques exist in literature. For example, Oumeraci et al. (2001) used a capacitive type wave gauge which was mounted parallel to the beach slope, consisting of two parallel stainless steel wires. Although a similar in-house developed device is still available, it was not deployed for two main reasons. First, the parallel steel wires used for this type of run-up gauge need to be fixed to the beach surface at a distance of at least 2.0 mm. Even though this mounting distance is generally not problematic it turns out to be a source of inaccuracy in conjunction with the relatively gentle beach slope. Second, mounting of the steel wires requires high strain that could only be achieved with massive clamps at their ends. It emerges however, that the mounting clamps obstruct the run-up area too much and so distort the effective run-up.

Alternatively to the approach found in literature, the highest wave run-up at each individual experiment is detected by means of two measures. A CCD camera, that is specified in Section 3.5 together with the description of the integration into the whole measurement procedure, is operated at a frame rate of 25 frames/s pointing at the run-up area. A $80.0\ \mathrm{cm}$ wide and $3.0\ \mathrm{m}$ long white plastic film is attached to the beach surface that constitutes a modular grid of $10\mathrm{x}10\ \mathrm{cm}$ where the grid lines are $0.3\ \mathrm{cm}$ thick. The basic idea resembles the popularly known drift line at natural beaches where deposited debris is one potential demarcation of the highest run-up of the incoming sea condition. In the experiments, run-up values are in analogy, determined in manual post-processing of the drift line after each experiment from the recorded, sequential images as well as from the actual drift line after the experiment. Along with an imaging technique, a tracer indicator method was additionally deployed to capture the maximum run-up on the shore. As tracer material two different granulates were used. A low-density polyethylene granulate of $\approx 0.91 - 0.94\ \mathrm{g/c^3m}$ density and an average diameter of $2 - 3\ \mathrm{mm}$. Also beige-colored, peeled sesame seeds were utilized as run-up tracers, that counteract the surface tension based trend of granular to agglomerate due to its oleaginous substances. Sesame seeds exhibit granular diameters of $\approx 1 - 2\ \mathrm{mm}$. Similar run-up results were found with the three applied granulates. Compare Subsection 3.1.3 for additional information regarding the scale effects due to the chosen experimental scale .

Even though the experiments were designed fully two-dimensional by exploiting the symmetry in cross-shore direction, measured run-up results vary along the flume width. The maximum run-up indicated by the applied tracers is not distributed along a straight line but parabolic with the apex in the flume axis. This phenomena arises from the fact that wall roughness of the plastering contributes to the energy dissipation in the boundary layer of the flume walls. On the other hand stochastic perturbations and laboratory effects account for deviations from an ideal parabolic arc. The true wave run-up, that is referred to in the following, is therefore defined as the mean of the lowest and the highest maximum run-up measured in each experimental run. The measurement took place by using a straightedge positioned at the lowest and the highest deposit of the tracer granulate rectangular to the flume axis. But, in order to circumvent influences from wall effects, areas in $5.0\ \mathrm{cm}$ distance to the walls were excluded from the run-up determination. The procedure of deriving the run-up data is further depicted in Fig. 3.11.

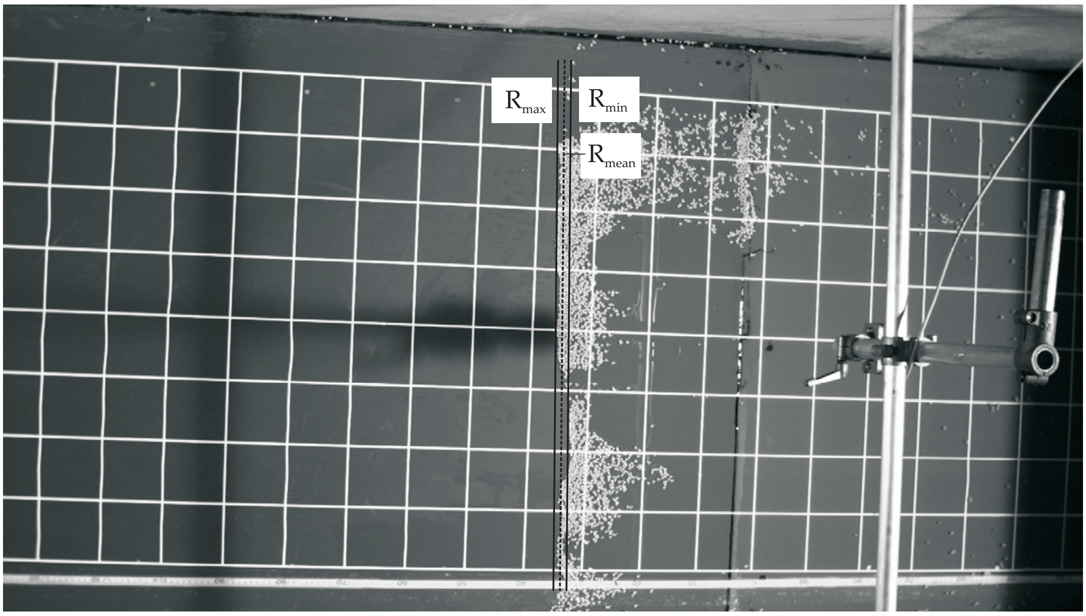

Figure 3.11 Maximum wave run-up detection in the laboratory with the aid of a straightedge, defined as the mean of the lowest and the highest maximum run-up

3.3.5 Wave Height and Water Depth Measurements

Resistance wave gauge

Resistance wave gauges were used to measure wave heights in the deeper region of the beach wedge ($d \gtrsim 0.20\ \mathrm{m}$), where pressure sensors could not be mounted due to their installation length. The mounting positions are indicated in figure 3.9. Since the wave gauges show a slight tendency to drift electronically after a few experimental runs, the instruments were zeroed manually at the beginning of every new experimental run. The tendency to drift does not influence the measurement quality significantly when a single experiment is evaluated. The so-called wave-height meters, manufactured by the instrumentation department of *Delft Hydraulics Laboratory*, consist of a gauge with integral pre-amplifier and a separate main amplifier. The device operates according to an electrical resistance meter that is composed of two parallel stainless steel rods (electrodes) connected to the pre-amplifier above the water level. Potentially influencing effects due to conductivity fluctuations are diminished through the use of a reference electrode mounted at the lower bridge connecting the steel rods. The wave gauges were mounted on a bracket of an aluminium tube in the flume axis. The lower ends of the gauges were positioned on the PVC surface of the beach wedge in order to obtain greater stability of the wave gauge. Further details are depicted in Tab. 3.6. Before being sturdily mounted inside the flume, the wave gauges were calibrated in a calibration container with the aid of a calliper.

Table 3.6 Technical specification resistance wave gauge (RWG) applied at the lower end of the sloping beach to record water level variations

Item	Value
Level-electrodes	stainless steel rods, 4 mm
Reference electrode	platinum, $5 * 2$ mm
Non-linearity	0.5% of selected range
Analogue voltage output	± 10 mDC
Range	± 50 cm

Pressure sensor

Synolakis (1987) reports on the difficulty to measure wave heights close to the shoreline and in shallow water. In order to circumvent a technically elaborate alternative documented by Battjes and Roos (1971) the author developed a new flexible array of capacitive wave gauges on the basis of a steel rod in a glass capillary mounted on an aluminium bracket, that features a uniform distance of the transducers to the surface of the beach. Additionally, the device was easy to calibrate. However, such an alternative array of wave gauges had not been available for the present study. Instead, upward facing pressure sensors (PRS) were implemented inside the beach slope to capture water level variations during the experiments. Two different sorts of sensors were in operation - TM/N sensors by *STS AG* and PDCR 1830 by *GE Druck*. Mounting position and notation of each individual sensor is depicted in Fig. 3.9. Both sensor types measure pressure relative to the ambient pressure by means of piezo-resistive measuring elements. The force collector uses the piezo-resistive effect of the strain gauge to detect strain due to applied pressure. Ambient pressure is compensated by means of a drill hole inside the sensor body, connected to the atmosphere via an inner tube inside the connection cable. Before mounting all sensors were calibrated against a calibration unit. For more detailed information on the pressure sensors refer to Tab. 3.7. At all times before the first experiment started in the morning, the beach and especially the sensors positioned in the initially dry region were wetted, to ensure that the sensor membrane was moistened. Then, all pressure sensors were zeroed manually to measure the surface deviations due to the propagating waves. In contrast to the previously reported measurement techniques mentioned above, pressure sensors have the basic advantage that they do not interfere with the incoming flow by the long wave surging up and down the sloping beach.

Table 3.7 Technical specification of the applied pressure sensors inside the beach wedge, TM/N manufactured by *STS AG* and PCDR 1830 by *GE Druck*

Item	Description TM/N	 PDCR 1830
Manufacturer	STS AG	GE Druck
Measuring range	$0.00 \ldots 1.50$ mH_2O 70 mm	$0.00 \ldots 0.70$ mH_2O
Supply voltage	5.0 VDC	
Analogue voltage output	$0 \ldots 20$ mV	$0 \ldots 20$ mV
Protection rating	IP 68	IP 68
Response time	≤ 1 ms$/10 - 90\%$FS	[-]
Non-linearity, Hysteresis	$\pm 0.25\%$ FS	$\pm 0.1\%$ FS BSL
Thread diameter sensor body	G 1/2″	M14 x 1.5

The question arises how pressure head variations measured at the bottom of the water column can be transferred into concurrent water level changes at the surface of the flume. Correspondence between the two quantities has to be investigated more closely, especially in the context of short ocean waves (Grace, 1978). Generally, vertical accelerations in the water column above the pressure transducer alter pressure measurements. Thus first of all, further processing allowed for accurate prediction of wave heights from the pressure history. The measured time series were adjusted by means of vertical velocity corrections based on linear or higher wave theory. In contrast, the length of the waves referred to in the current analysis exhibits almost no vertical acceleration, even when shoaling occurs along the beach slope, so that pressure and wave height history can easily be equated.

The pressure sensors and the wave gauges were calibrated before the experiments started by means of a calibration container and a calliper. The sensors were mounted at the calliper and were immersed into the water contained in the calibration container in distinct steps of $2.0\,\mathrm{cm}$. The measured values were recorded and a linear regression yielded a regression line for each of the sensors. Tab. 3.8 lists equation of the regression line for the sensors whose positions are drawn in Fig. 3.9 correlating the measured voltage x with the adjusted water depth $f(x)$. The y-intercept is generally in the order of $10^{-3} - 10^{-4}$ which is in the measurement accuracy of the overall system accuracy.The slopes of the particular regression lines agree well with the intended factor of 0.02 to convert between the measured voltage and SI-units. For the post processing of the recorded measurements the regression equations were utilized instead of the intended conversion factor according to the particular sensors.

Table 3.8 Equations of the calibrated pressure sensors and the resistance wave gauges as drawn in Fig. 3.9, measuring characteristics modelled by means of linear regression

No.	Sensor label	Equation
1	RWG_1	$f(x) = 1.98e10^{-2}x - 5.56e10^{-4}$
2	RWG_2	$f(x) = 2.02e10^{-2}x - 8.92e10^{-4}$
3	RWG_3	$f(x) = 1.92e10^{-2}x - 4.79e10^{-4}$
4	PRS_1	$f(x) = 1.95e10^{-2}x - 2.97e10^{-3}$
5	PRS_2	$f(x) = 2.02e10^{-2}x - 2.00e10^{-3}$
6	PRS_3	$f(x) = 2.03e10^{-2}x - 3.42e10^{-3}$
7	PRS_4	$f(x) = 1.97e10^{-2}x - 4.11e10^{-3}$
8	PRS_5	$f(x) = 2.00e10^{-2}x - 4.45e10^{-4}$
9	PRS_6	$f(x) = 2.02e10^{-2}x - 2.75e10^{-3}$
10	PRS_7	$f(x) = 1.98e10^{-2}x - 2.58e10^{-3}$

Ultrasonic distance sensor

An ultrasonic distance sensor (UDS) detects water level variations in the landward facing beach area behind the macro-roughness elements. The device UDS is manufactured by *Dr. D. Wehrhahn*. It bases on the non-intrusive impulse echo principle, which evaluates attributes of a target by interpreting the echoes from the emitted ultrasonic sound waves respectively. The ultrasonic transducer converts electrical energy into ultrasonic sound waves by means of a piezoelectric transducer. Hence the runtime of sound waves and the temperature compensated sound velocity yield the effective distance. The specification of the instrument is listed in Tab. 3.9.

Table 3.9 Technical specifications of the ultrasonic distance sensor UAS employed during the experiments in the wave flume

Item	Value
Max. sensing distance	$2000\ \mathrm{mm}$
Min. sensing distance	$70\ \mathrm{mm}$
Supply voltage	$18\ldots32$ VDC
Analogue voltage output	$0\ldots10$ V or $0\ldots20\ \mathrm{mA}$
Thread diameter transducer	M32 x 1.5

The exact position of the instrument is denoted in Fig. 3.9. The sound transducer is mounted $0.40\ \mathrm{m}$ above the PVC board surface pointing rectangular to the beach inclination. Since a wave run-up ensues rising water level at the instrumental position actual water depth is indirectly defined by the difference of the reference measurement at the beginning of each experiment to the instantaneous value.

3.3.6 Velocity Measurements

Two independent velocity measurements have been conducted for the study. Punctual measurements of run-up and run-down velocities were recorded by means of a programmable electromagnetic liquid velocity meter (EMS). Further, spatial measurements were conducted by means of particle image velocimetry (PIV, cp. Section 3.5) utilizing a charge-coupled device (CCD) camera. In the following the different techniques and the technical equipment is outlined below.

Electro-magnetic Probe

The programmable electromagnetic liquid velocity meter (or electro-magnetic probe) is an instrument for laboratory research, engineering studies and open channel stream gauging is distributed by *Delft hydraulics*, the Netherlands. The device outputs velocities at its sensor head in two distinct directions, which correlate in a planar XY frame. The spherical sensor contains a coil that induces a magnetic field. Two pairs of platinum electrodes sense the Faraday-induced voltages produced by the flow past the sensor head. For further studies the reader is directed to the manufacturer's user manual. During the experiments the probe position was altered and an overview of the used positions is given in Fig. 3.10. The $30.0\ \mathrm{mm}$ ellipse-type sensor head was always mounted as stiffly and sturdily as possible and precaution was taken to keep the magnetic field away from perturbations of metal, magnetic material or electric currents. By default, the probe is synchronized at 50 Hz to prevent interferences from the power supply. Further details are listed in Tab. 3.10. The factory-provided calibration was used and a qualitative comparison with a hydrometric vane agreed fairly well.

Table 3.10 Technical specifications of the programmable electromagnetic liquid velocity meter (EMS) employed during the experiment in the flume

Item	Value
Sensor head	"E"-type (30.0 mm)
Analogue voltage output	$0 \dots 10$ V
Range	$0 \dots \pm 1.0$ m/s or ± 2.5 m/s
In-accuracy	± 0.01 m/s $\pm$ 1% of value measured

Further velocity measurements beyond punctuate assembly were conducted by means of camera-based image processing technique. Particle image velocimetry (PIV) was especially deployed in close vicinity of the macro-roughness elements exposed to the flow. The covered area is denoted in Fig. 3.12. Detailed description of the subjacent methodology is given in Chapter 3.5. During conventional experimental runs the field of vision was disturbed, due to instrument mounting brackets. So, for these measurements additional experimental runs had been carried out because unobscured visibility by the camera is prerequisite for the PIV measurement.

CCD camera

An industrial (CCD) camera manufactured by *Basler AG* was utilized for the digital recording of the images for an extract of the onshore macro-roughness area. The recorded images were applied to a standard particle image velocimetry (PIV) technique (for details cp. Section 3.5) in order to deduce the temporal and spatial variation of the velocity field within the area of interest. The camera of type *piA1900-32gc* exhibits the specifications listed in Tab. 3.11.

A camera with a high resolution 25 mm optical lens was used, produced by *Pentax*. It was connected to the camera body by a standard C-mount. The light reception is specified F1.4 and the special lens coating maintains a level of image sharpness and luminosity which is demanded in the given case of high contrast. The adjustment of sharpness during the camera operation was permanently maintained by means of the available locking screws. Additionally reflections of the water surface, due to the illumination of the scene in combination with the varying motion of the flow dynamics, were diminished with a circular polarization filter with special coating by *Hoya, Cir-Pl,* 72 mm.

Table 3.11 Technical specifications of the CCD camera employed during the extra experiments in the flume to record image sequences of the flow interaction with the macro-roughness area

Specification	piA1900-32gc
Sensor Size (H x V pixels)	1920 x 1084
Sensor Type	Kodak KAI-2093 Progressive Scan CCD
Max. Frame Rate (at full resolution)	32 fps
Video Output Type (Interface)	Gigabit Ethernet
Synchronization	External or software trigger, free run
Housing Size (L x W x H in mm)	86.7 x 44 x 29
Software Driver	*Pylon* driver package
Typical Power Consumption at 12V	< 5.5 W

The camera was controlled by a in-house developed C++ grabbing script on the basis of the *Pylon* driver package by *Basler AG,* running on a separate personal computer. The individual frames of the data stream were grabbed software-based, queued, buffered and subsequently saved on disk as raw gray-scale pixel images. An external hardware trigger signal as a periodic block function was generated by the data recording personal computer and sent to the camera as a ±5.0 V signal. The rising edges of this signal triggered the camera to record an image. The sampling rate specified by the periodic block function targeted at a frequency of 20 Hz. An exact time stamp was stored in the file name together with each individual photo to account for the delay possibly due to hardware-based internal time shifts.

3.4 Data Processing

The recorded data of the conducted experiments, which were stored on hard drive, in the first place reflect voltage signals per time unit. The calibration procedure yielded the ability to convert the data into respective physical units. Moreover the signals were superimposed with noise by means of specific sensors applied in the laboratory. The sampling rate of the recorded signals was originally 1.0 kHz. Hence for the further analysis it was impractical to proceed with the enormous amount of data and with the biased signals.

The data processing aimed at converting, filtering, smoothing and decimating the recorded signals. The decimation of the data was accomplished by means of extracting every fiftieth data point from the signal after it was filtered and smoothed. For the entire set of experiments a digital experiment notebook was structured where the processed data were stored for further visualization and analysis. In addition to the originally recorded data also the following listed data were calculated and stored: a character for the experiment repetition, the position of the *EMS* sensor, the percentage of the wave amplitude, the configuration tag, the minimum and maximum values of the horizontal run-up extent and the vertical run-up $R_{v,min}$, $R_{v,max}$, the cross- and long-shore obstruction ratio ψ_{cs}, ψ_{ls}, the obstructed height ψ_{mr}, the wave period T, crest a_{cr} and trough a_{tr} amplitudes and wavelength L_0 at the wavemaker, the wave number k, the reflection coefficient K_r, the Ursell number U, the frequency Ω and the deep water surf similarity parameter ξ_∞.

In addition, instead of commonly applied filtering techniques such as moving average techniques or bandpass filters, which generally result in a significant time shift of the original signal, the empirical mode decomposition (EMD) technique was utilized for the signal filter, with good performance.

This non-linear technique for an adaptive representation of non-stationary signals considers oscillations in signals at a very specific level. The oscillations are iteratively decomposed into so-called intrinsic mode functions (IMFs) (Huang et al., 1998). The iterative process is commonly referred to as 'sifting'. The sum of the obtained set of individual modes yields the original signal and under the assumption of noise in the signal it is therefore possible to filter the original signal by means of omitting the IMFs which represent the noise portions in the signal (Flandrin et al., 2004). The effective algorithm includes the identification of all extrema, the interpolation between the minima, the calculation of the mean of the maxima and minima, the extraction of the detail and an iteration of the residual of the previous four steps (Flandrin et al., 2004). The methodology is further enhanced to the ensemble empirical mode decomposition (EEMD) which accounts for the possibility that in the original EMD mode-mixing with the draw-back of coherent signal fragments can occur (Wu and Huang, 2009). The theoretical background is only lightly touched here and the reader is instead referred to more comprehensive works (Huang et al., 1998; Flandrin et al., 2004; Schlurmann, 2005).

In this thesis, the filtering process with the aforementioned EMD method achieved good results for the omission of the first four IMFs of the pressure sensors (*PRS*) and the resistance wave gauges (*RWG*). In contrast stable filter results were possible for the electro-magnetic probe (*EMS*) and the ultrasonic distance sensor (*UDS*) under the omission of the first seven modes.

3.5 Particle Image Velocimetry

The measurement of two-dimensional velocity fields was performed by means of standard particle image velocimetry with the purpose to elucidate the qualitative flow pattern around the applied macro-roughness elements. In the following a short description of the theoretical background will be given and practical details of the experiments are described subsequently. For the result of the analysis of the image sequences the reader is referred to Section 5.5.

3.5.1 Theoretical Considerations

Particle image velocimetry (PIV) is a powerful laboratory technique which attains velocity fields out of a sequence of images. The recorded scene could either be a section of a fluid or a fluid surface under motion. Seeds of various materials are utilized to trace the bi-directional velocity components in the flow. The scene is either illuminated by laser sheets or by spotlights. The resulting flow fields allow for a complete analysis not only of the velocities but also of the more complex features of the flow such as flow separation, Reynolds stresses and turbulent characteristics (Sveen and Cowen, 2004).

Generally, qualitative imaging techniques can be categorized by means of the spatial density of the tracers added to the flow of interest. Herein PIV is referred to as an imaging technique where a moderate tracer density in the flow is maintained in the phase of the run-up and run-down of the long waves. Moderate density in accordance with the definition given in Sveen and Cowen (2004) means that the distance between individual tracers is in the order of a few particle diameters. The resulting velocity field, which is obtained with the aid of the PIV, is strictly speaking the velocity field of the tracers conveyed by the flow. The velocity of the tracers and the flow can approximately be equaled under two assumptions. First, the temporal difference between a pair of images is sufficiently small so that the instantaneous velocity can be replaced by the difference quotient (Westerweel, 1993). Secondly, the tracers need to act passively in the sense that they do not significantly alter the flow compared to an undisturbed observation.

The analysis of the flow field is achieved by means of basic pattern matching principles. A pair of two consecutive images with a distinct temporal distance Δt are generally considered and the matching of the pattern of tracers in the two images is obtained with a cross-correlation analysis. A transformation of the two-dimensional signal, made of the color-spectrum stored in the rows and columns of the digital image, into the frequency domain accelerates the computation time of the PIV analysis. The cross-correlation is performed for a scalar number of sub-windows dividing the original image. The PIV technique is nowadays often performed and it is not necessary to repeat the complete theory here in detail but it is instead referred to the ample and comprehensive paper work by Westerweel (1993); Goldstein (1996); Sveen and Cowen (2004). In the following Subsection the practical realization of the measurements is described.

3.5.2 Practical Realization

Five experimental runs were chosen out of the available set of experiments. Besides an undisturbed case where no macro-roughness elements are present onshore the remaining four configurations $\Gamma = 1 - 4$ were selected. The obstructed cross-sectional ratio for the non-rotated cases amounts to $\psi_{cs} = 0.50$ and for the rotated cases it is $\psi_{cs} = 0.39$. A non-linearity of $\epsilon = 0.058$ (60 % of the highest crest amplitude at the wavemaker) was used for all of the PIV experiments. The main focus of the experiments was to deepen the insight into the flow pattern of the different macro-roughness configurations.

On the more practical side, the papers by Fujita et al. (1998) and Weitbrecht et al. (2002) proved to be a useful source of information and many helpful hints on the choice of seeding density and particle diameters were found in these sources.

The applied camera hardware and its control mechanism is described in Subsection 3.3.6. Peeled sesame seeds were deployed as tracer material equivalently to the run-up tracers mentioned in Subsection 3.3.4 because the smallest tendency to conglomerate was found for this material. The spread of the seeds was always accomplished manually in order to assure a constant seeding density on the water surface during the non-stationary run-up and run-down phase. Fig. 3.12 highlights the positioning of the camera's field of vision as well as the analyzed section of this scene.

The illumination of the scene was implemented through two pairs of spotlights. The front and the back of the scene with respect to the approaching wave direction was illuminated with mercury vapor lamps and the sides were brightened with two halogen spotlights. However this illumination arrangement resulted in disadvantageous light reflections at the edges of the field of view. Hence it was indispensable to reduce the full image to the remaining section of 1160×920 pixel depicted in Fig. 3.12. A raster foil of 10×10 cm with a line thickness of 3.0 mm was symmetrically affixed to the PVC board starting from the still water line.

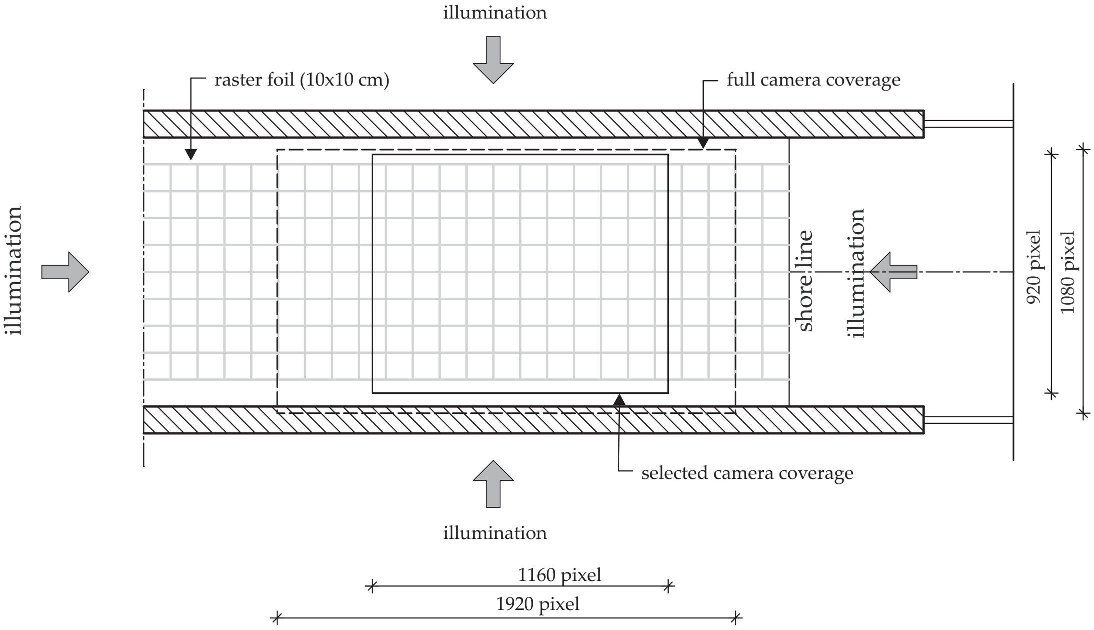

Figure 3.12 Coverage of the CCD camera (dashed line) and the selected analysed coverage (solid line), indication of the illumination direction with the mercury vapour lamps and halogen spotlight

Once the sequence of images was taken and stored, the PIV analysis was performed. The *Matlab*-based software *matPIV* (Sveen, 2004) was adopted for this task. Before further processing the image sequence, the barrel distortion of the applied optical lens was satisfactorily corrected by means of a iterative variation of the cubic correction term amplitude ($a = 1.5 \cdot 10^{-8}$) after transforming the image into spherical coordinates (Born and Wolf, 2002). The settings of the PIV algorithm are listed in Tab. 3.12.

A total number of four sub-window iterations were applied with good performance. The temporal distance between a pair of images was deduced from the time stamp stored in the file name. The images of the experimental runs where macro-roughness was present were masked manually in order to reduce the processing time. The reference of the world coordinate system to the pixel coordinate system was accomplished with the raster foil affixed to the beach surface.

Table 3.12 Settings of the PIV analysis with the *matPIV* toolbox (Sveen, 2004)

Parameter	Value
Correlation method	'multin'
Sub-window size	$[64 \quad 64; 64 \quad 64; 32 \quad 32; 32 \quad 32]$
Overlap	0.75
SNR threshold	1.3
Global threshold	3.0
Local threshold	2.7
Kernelsize	3.0

The resulting velocity fields which were obtained with the aid of the cross-correlation method had to be filtered afterwards in order to remove unwanted outliers caused by erroneous correlation results. The four implemented standard filters were applied with the filter values given in Tab. 3.12 with satisfactory enhancement of the vector fields.

4 Long Wave Generation

4.1 Functional Outline

The generation of long waves has been reviewed in Section 2.2 and it has been concluded that deficiencies exist in the state-of-the-art long wave generation. On the one hand controllability of the intended water surface profile is limited in some generation techniques and on the other hand wave length or periods respectively are constrained by means of economically feasible stroke length of classical piston-type wavemakers. Thus alternative approaches seem indispensable when it comes to adequate models of near-shore inundation and its related impact to coastal settlements. In the following an alternative long wave generation technique by means of pipe pumps is outlined. The so-called volume-driven wavemaker, which is capable of accelerating and decelerating water in either positive or negative direction, is controlled in a feedback control system. A proportional–integral–derivative controller (PID controller), which is widely used in industrial control systems, is adopted. The controller is available as a standard solution. The volume-driven wavemaker impelling the wave generation process is described in Section 4.2, the controller solution is outlined in detail in Section 4.3 and performance analysis is depicted thereafter.

4.2 Volume-driven Wavemaker

The closed-circuit wave flume introduced in Section 3.2 exhibits a pump station at one of its straight segments (cp. fig. 4.1). While the ramp is constructed at the lower straight, the pump station is located at the opposite side of the flume in the middle of the upper straight. The disruption of $1.17\ \mathrm{m}$ distance in the flume forms a gap and both ends of the flume are closed by reinforced concrete walls which are orientated at an angle of $45°$ away from the flume axis to the outer flume walls. In the proximity of the pump station the bottom level is deeper than in the remaining flume sections. A 5 vertical to 12 horizontal slope ($22.62°$) smooths the two different bottom levels which overall differ by 0.5 m. The deeper portions at both intakes of the pump station serve as sump pits and also prevent air intrusion into the pumps during operation.

The four pipe pumps connecting the disruption are each mounted inside a pipe elbow. This elbow is connected to the flume walls by means of several pipe lengths (inner pipe diameter 250 mm) connected to the concrete walls with sealing gaskets. Two pumps are always arranged on one side of the flume disruption, each superimposed on the other. The pump propellers are driven by $4 \cdot 3.7$ kW (nominal capacity) engine power of four electromotors of type *Lenze G 132-1* manufactured in March 1979 (Lenze Elektronische Antriebstechnik KG) which are assembled on a steel frame. Each of the motors, exhibiting a critical engine speed of 2000 rpm, is controllable at variable speed (cp. Subsection 4.3). The electrical input of a single electromotor amounts to 160 V/28 A. The controlled direct current drive designed in a 4-quadrant-operation ascertains that engine speed and equally torsional moment may occur with either positive or negative sense of direction. Hence, this type of circuit results in forward and backward sense of rotation and associated flow directions in the flume. The breaking work during the deceleration of the electromotors is appropriated for energy recuperation. Synchronous operation is obtained on the basis of internal relay of the electromotor controllers. The first controller serves as the master controller and all others are thereby triggered as slave controllers.

Each of the pumps (Fig. 4.2) holds a maximum flow capacity of $500\ \mathrm{m}^3/\mathrm{h}$ and a maximum rotational speed of 1430 rev/min. The pumps were manufactured in the early seventies by Weise&Monski *Type PL X II*. The discharge head of the pumps is specified in the range of $0.35 - 0.62$ m (mean: 0.5 m) and its specified maximum power is equal to 1.85 HP. Standard pipes of a nominal inner diameter (DN) of 250 mm with a nominal pressure (PN) of 6.0 bar could be connected to the pipe pumps at the flanges. The shaft connecting the electromotors and the propeller pump is sealed by means of a gland seal. Brazen cast propellers enclosed in the cast steel housings are balanced to assure low-vibration operation of the pumps. The pumps are needed to convey water and sediment in suspension while slide bearings protect the seals from corrosion by means of scavenging water inflow. This external source of water volume results in higher water levels after a few experimental runs. Determined by the water depth in the flume either the two lower pumps can be deployed in separate operation or if the water level exceeds a depths of 0.4 m also the upper pumps can be put into function to accelerate or decelerate the water. As the water depth for the current study had been too shallow, the upper pump intakes were closed with tubing plugs and the pumps were disconnected from the main controller circuit.

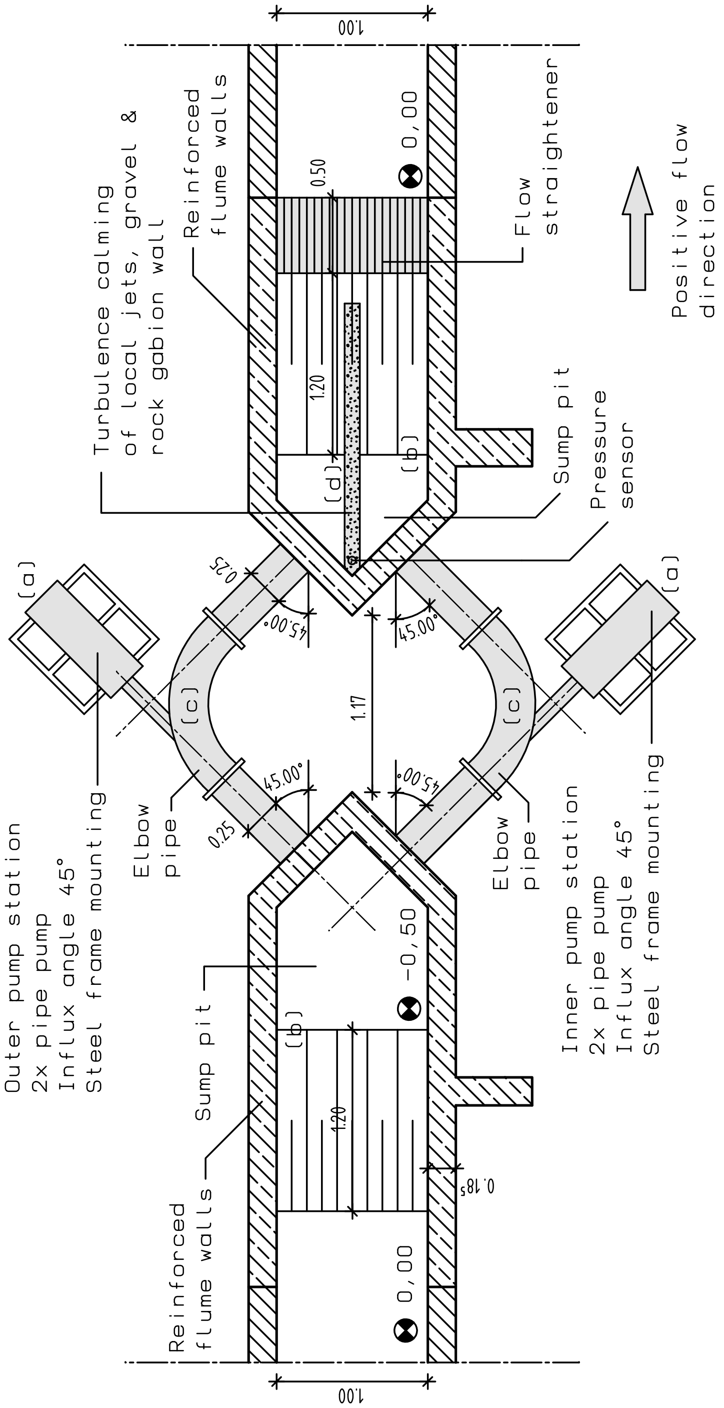

Figure 4.1 Technical drawing of the pump station and its details, (a) inner and outer pumps mounted to steel frame, (b) sump pit and sloping bottom, (c) pipe connections and elbow pipe, (d) turbulence calming by means of gravel and rock gabion wall, (e) pressure sensor

During the experiments reported herein only the lower pumps generated the flow measured at a maximum amount of ≈ 0.60 m/s in constant operation mode, given that the beach wedge is not incorporated in the closed-circuit flume.

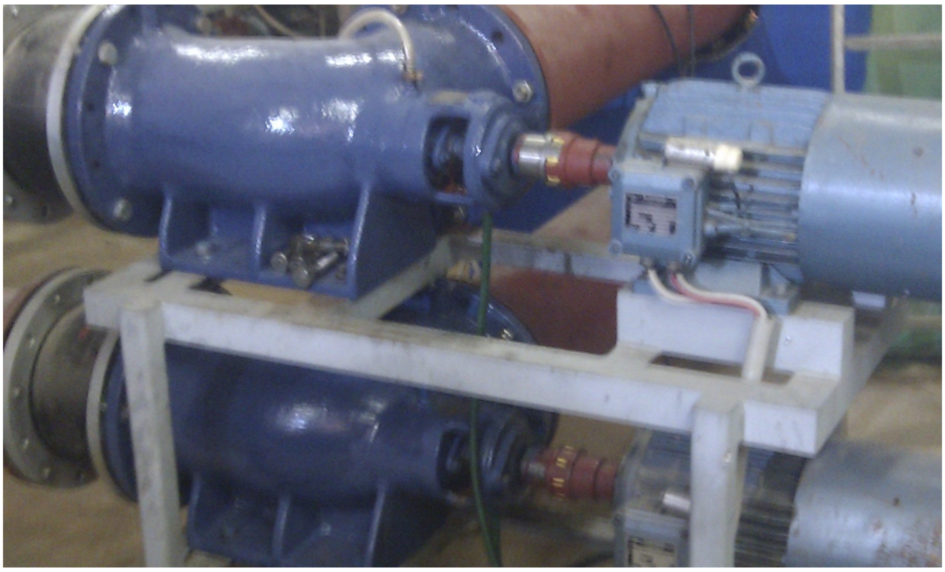

Figure 4.2 Photograph of the inner pump station assembled on a steel frame, elbow pipe with pipe pump (darker blue), seal and electromotor (gray-blue)

As the facility had formerly been designed to investigate tidal waves and scour evolution at the same section where in the current experiments the beach wedge is located, less steep water surface gradients were applied during those experiments. In result, during tidal wave generation the presence of eddies and colliding tube flow jets at the side of the positive pump direction (cp. Fig. 4.1) were less marked. In contrast, the generation of long waves mimicking a tsunami in shallow-water, scaled to the laboratory size, involves much steeper surface gradients and results in distinct eddies and turbulent states where the flow enters the quiescent water of the sump pit. As outlined in Subsection 4.3 a special controller scheme was chosen to drive the wavemaker on the basis of a feedback control system. For this purpose a pressure sensor was installed for instantaneous water level input. This was done on basis of theoretical considerations and ideally located as near as possible to the control variable (the pressure in the current system). With this in mind it has been a major concern to eliminate surface disturbances from the colliding tube flow jets for the most part and to position the pressure sensor at an optimized spot nearest possible to the control variable. Best controller performance was obtained with the pressure sensor positioned as shown in Fig. 4.1 indicated as position (e) in functional interaction with a gravel and rock gabion wall (d) which was constructed along the flume axis over the entire water depth. While most of the turbulent energy induced by the colliding jets is dissipated inside the gravel packet, the water surface is efficiently flattened in order that the measured pressure time series becomes intrinsically averaged. In turn, the feedback control system operates at its best level. Additionally, a $50~\mathrm{cm}$ high flow straightener made of $5.0~\mathrm{cm}$ diameter polyethylene tubes, parallelly stacked up in the flume, was installed and weighed down by sand-lime brick. This measure further reduces vertical velocity components induced by the slope attached to the sump pit. Fig. 4.3 thoroughly illustrates the outlined setup of the sump pit at the positive flow direction. It needs to be mentioned that the problematic stage in the wave generation had always been the wave crest of the control signal while the wave trough generation appeared steady. The negative inflow into the pipes can be described as a directional, steady intake flow with low turbulence.

Figure 4.3 Photograph of the flume intake and the calming of the flow by means of a gravel and rock gabion wall and polyethylene tubes

4.3 Controller Scheme

Besides the pipe pumps and assemblage of the pump station, the adopted proportional–integral-derivative controller (PID controller) constitutes the centerpiece of the long wave generation methodology. The collocation of the component parts of the utilized controller setup is outlined in Fig. 4.5. The digital-analog converter with connection to a personal computer for data logging and signal output is further depicted in Subsection 3.3.3. In addition to the input channels two output channels were occupied. The first one transmits a trigger signal to an adopted CCD camera whereas the second one communicates the set point signal time history to the PID controller. Secondly the control variable, which is the static water pressure at the inlet, is fed into the controller. Simultaneously the feedback control system whose principles are depicted in Fig. 4.4 processes deviations between those two input signals and adjusts the output level, which in turn is communicated to the pipe pump controller unit described in Subsection 4.2.

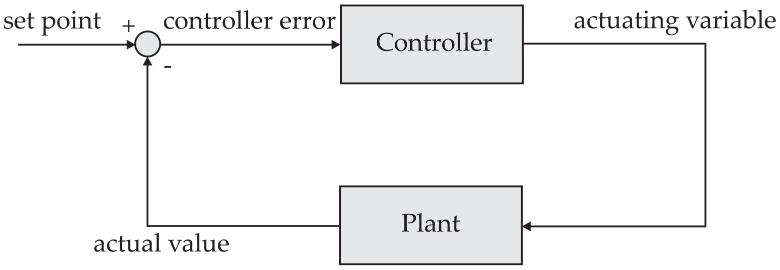

Figure 4.4 Basics of a feedback control system applied in the long wave generation

The operation of hydraulic models depicts an application of a suitable system which is well controllable by means of feedback control systems. Allen et al. (1992) demonstrated the utilization of a controlling algorithm, similar to the one applied in the current work, which adopted the principles of a proportional-integral controller (PI-controller). The authors deployed the controller to operate a tidal wave generator and found that the control principle generally worked out well.

In general, elementary feedback control systems include three components (cp. Fig. 4.4), a plant (i.e. an actuator, pump valve), a sensor which is meant to measure the output of the plant under control and the controller itself which assures the input of the plant (Ang et al., 2005). The process performance of the controller depends basically on the quality of the sensor output, which is usually biased due to noise (Doyle et al., 1990). The controller performance is optimally tuned when the controller reduces the error between the predefined input signal (set point) to the plant and the measured sensor input (process or control variable). The utilized controller in this study (manufactured by *atr Industrieelektronik*) is implemented as an analog plug-in circuit board. The adjustable parameters of the controller are then set by means of potentiometers.

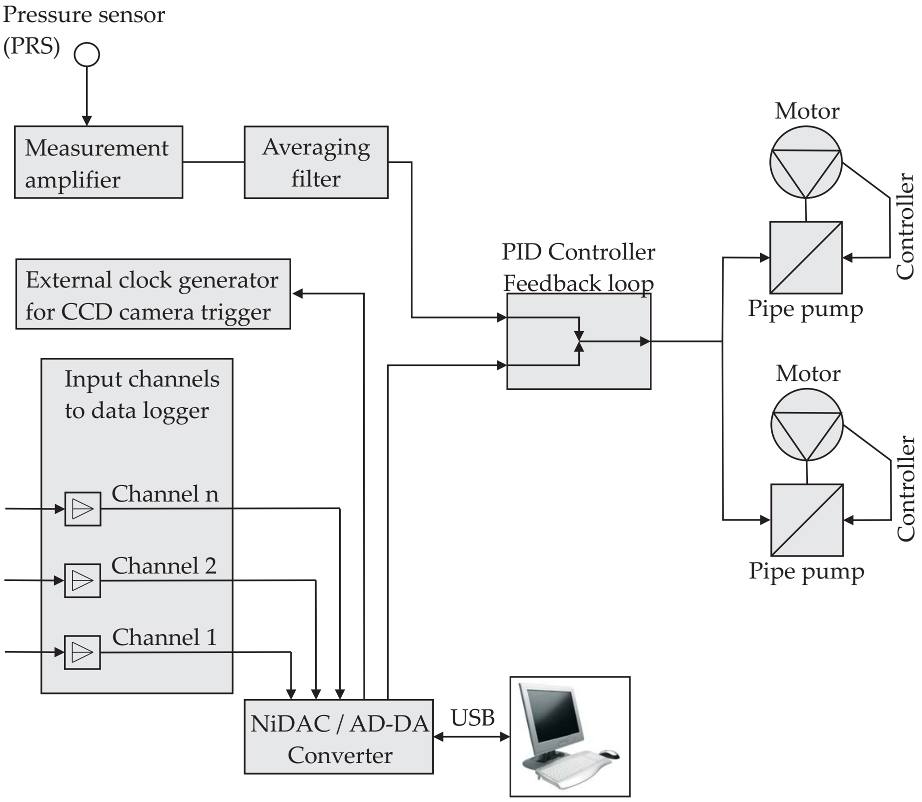

Figure 4.5 Schematic overview of the long wave generation controller scheme and established links between its component parts

The utilized principle is called negative feedback because the manipulated signals are changed adversely to the process variable. Besides the simplest control strategy - the on-off control - many other strategies (proportionality, integrals or derivatives of error or combinations thereof) are possible to minimize the error of the control system (Åström and Hägglund, 1995). One of the mostly adopted controllers is the PID controller and it is mathematically described by Eq. (4.3.1)

$$u(t) = K\left(\underbrace{e(t)}_{\text{P-term}} + \underbrace{\frac{1}{T_i}\int_0^t e(\tau)\,\partial\tau}_{\text{I-term}} + \underbrace{T_d\frac{\partial}{\partial t}e(t)}_{\text{D-term}}\right) \tag{4.3.1}$$

where u denotes the actuating variable (output variable) and e is the control error ($e = y_{sp} - y$, with $y_{sp} =$ set point value and $y =$instantaneous value of the control variable). According to Åström and Hägglund (1995) the control variable is thus a sum of three addends: the P-term which is proportional to the error, the I-term which is proportional to the integral of the error and the D-term which is proportional to the derivative of the error. The controller parameters are then proportional gain K, integral time T_i and the derivative time T_d. Application of controllers which only include the proportional term are basically suitable for processes which can be described in static models. On the other hand the integral term functions in that the process output always targets to equal the set point in steady state condition of the target signal. This minimizes the error by means of decreasing or increasing the actuating signal, no matter how small the error is. Finally derivative action aims to improve the overall system stability. Deviations in the actuating variable would become apparent with a distinct delay due to the dynamics of the non-stationary process. The influence of the derivative term might be seen as a 'prediction' by means of an extrapolation of the tangent of the error curve.

When designing the controller scheme of the long wave generation it was specifically difficult to decide where to place the pressure sensor delivering the process variable because the specific geometry of the positive intake chosen first evoked significant distortions of the sensor signals. Tests with the pressure sensor further away from the pipe pump station yielded a system dynamic with large, dominant dead times. The response to control action on the pump resulted in oscillatory unstable control modes and the long wave generation was unsatisfactory. Much improvement was achieved by optimizing the positive intake as described in Subsection 4.2. Secondly, residual oscillations in the pressure sensor signal - due to water surface disturbances at the intake - were diminished with the aid of a moving average filter. This filter had a window length of 0.5 s and was carried out by the measurement amplifier of the pressure sensor.

The appropriate adjustment and tuning of the above outlined parameters of the PID controller is of most crucial concern with regards to generating optimal long waves in the facility. A standard approach consisting of two methods to determine the adequate parameters - called Ziegler-Nichols Method - are represented in literature Åström and Hägglund (1995). The first one, the step response method had been applied to pre-adjust the parameters at first. Subsequently, manual fine-tuning of the controller combined with an optimization of the intake geometry yielded a minimum error between the desired process variable (static water pressure) and sensor values of the actuating variable at the intake for the experimental runs.

Although the delineated procedure for the controller tuning revealed tidy controller performance, more sophisticated control approaches are conceivable which would also include automated parameter specification. Such attempts were yet not persevered during the wave generation test. Instead, the results and the general performance of the proposed alternative methodology when generating long waves became possible with the outlined equipment which is described in the ongoing Subsection 4.4.

4.4 Wavemaker Performance

The wavemaker performance is demonstrated with reference to two different water surface elevation curves. Time histories of these example curves, serving as the set point, are input into the controller. The number of revolutions of the pipe pump system (actuating variable) is instantaneously adjusted by means of the controller scheme outlined in Subsection 4.3. The two surface elevation examples have firstly been chosen in view of their applicability to existing analytical run-up formula (sinusoidal example, cp. Fig. 4.6) and secondly with view on demonstrating that the outlined laboratory facility is capable of tracking a downscaled tsunami marigram effectively (cp. Fig. 4.7).

The first example represents a near sinusoidal long wave with a leading depression wave. The wave parameters are $\omega = 2\pi/T = 0.104$ 1/s, $k = 2\pi/L = 0.061$ 1/m, $h_0 = 0.3$ m and $a_0 = 0.06$ m. The Fig. 4.6 depicts the time series of the set point and the control variable in the upper sub-figure, whereas the progress of the control error normalized by the maximum positive amplitude a_0 is indicated in the lower sub-figure. The sinusoidal long wave has been recorded from an early controller setup where the PID parameter yielded only reasonable performance of the wave generation methodology. After the initial mismatch in water level ($\hat{\eta} = 0 - 25$) the control error strives slowly towards zero, which indicates that the I and P-terms are not properly adjusted. The control properties are mostly dominated by the linear proportional influence of the P-term. The normalized control error ranges between zero and 0.1 while the wave trough is being generated ($\hat{\eta} = 25 - 225$). During the generation of the monotonically nondecreasing wave crest ($\hat{\eta} = 225 - 310$) it is obvious that the control error drifts towards positive values. The monotonically nonincreasing half of the wave crest ($\hat{\eta} = 310 - 400$) then is characterized by greater control errors, which at their maximum reach 0.2. Characteristically for this PID parametrization and in addition to the pronounced oscillations around the set point curve, the control variable on an average tends to be located below the targeted set point. Though, the general performance of the wavemaker already seems suitable to render the properties of the waveform.

The performance of the wavemaker was determined by means of the root mean square error (RMSE). As a measure of accurateness the square root of the variance σ^2 has been calculated for the surface elevation vectors resulting from the wavemaker performance test according to Eq. (4.4.1) (Bronštein and Semendjaev, 2001)

$$\sigma_{am} = \sqrt{\sum_k (x_k - \mu_X)^2 p_k} \tag{4.4.1}$$

with σ_{am} = standard deviation or root mean square error, μ_k = arithmetical mean and p_k^{-1} = length of vector. The root mean square error for the first long wave generation example yields $\sigma_{am} = 0.2201$. Admittedly, the performance of the controller scheme is only reasonably adjusted. By means of the second example it should be shown that a thorough though time-consuming adjustment of the PID parameters renders a much better wavemaker performance, finding expression in smaller RMS errors.

Fig. 4.7 represents a PID controller setup finally chosen to perform sufficiently well on the basis of the controller equipment on hand. The waveform which was selected originates from former numerical modeling of the near-shore long wave dynamics at the city of Padang conducted by the author.

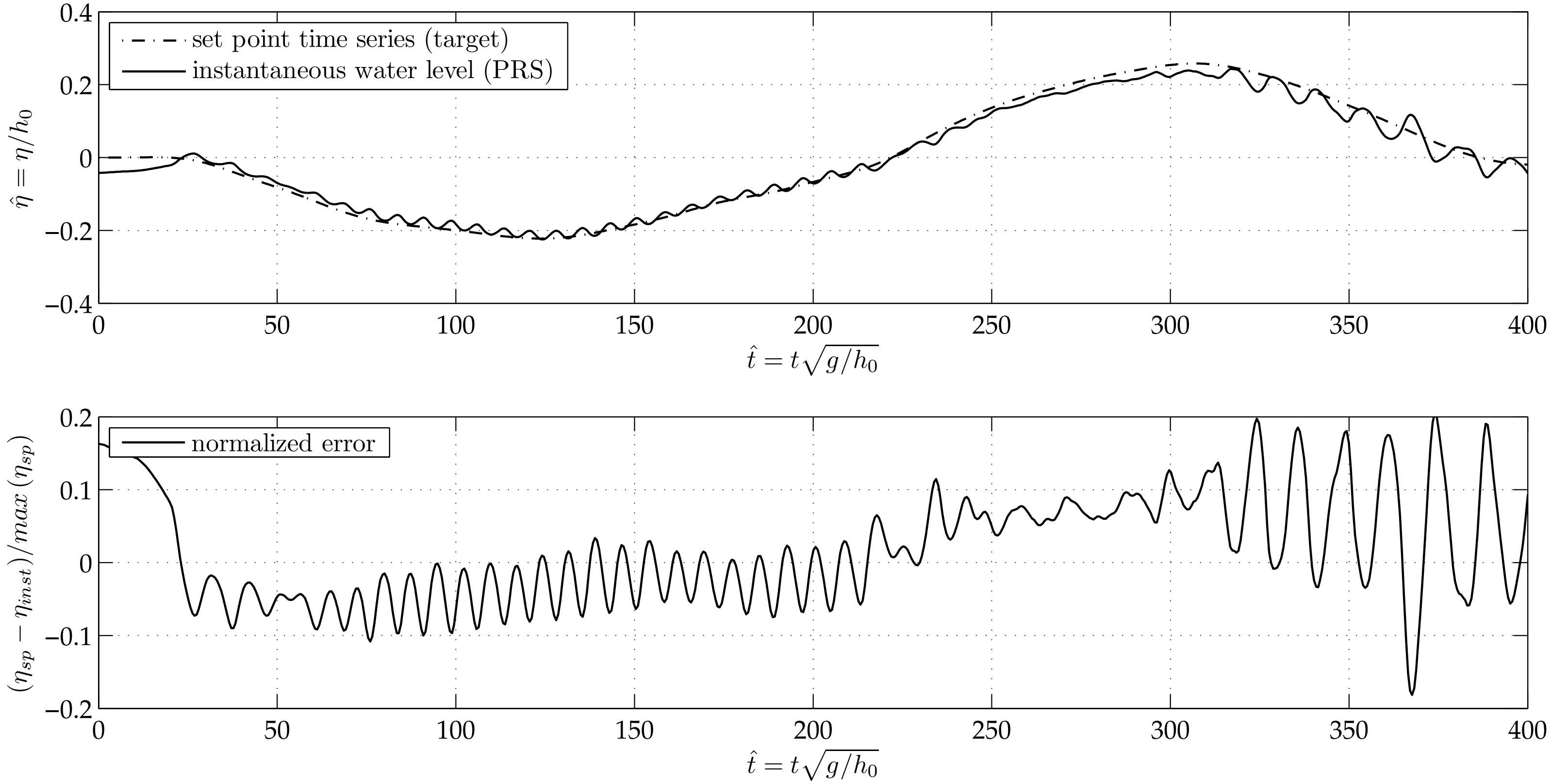

Figure 4.6 Illustration of the wavemaker performance for a sinusoidal waveform with $T = 60.0$ s, $h_0 = 0.3$ m and $a_0 = 0.06$ m, upper sub-figure of the figure depicts the non-dimensional water surface elevation η/h_0 of the set point signal and the control variable in regard to the dimensionless time $\hat{t} = t\sqrt{g/h_0}$, lower sub-figure shows the control error normalized by the amplitude of the set point signal over non-dimensional time

The utilized numerical model and the general methodology is described in Goseberg and Schlurmann (2008, 2009); Schlurmann et al. (2010). A resulting representative marigram was abstracted from the numerical results at a water depth of $30.0\ \mathrm{m}$. The time history was scaled down according to the Froude similitude relation outlined in Section 3.1.3 and the chosen temporal and spatial scales. Additional to the downscaling and in order to derive a meaningful set point curve for the wavemaker control, it was decided to adopt the wave period to fit together with the lower bound of the prototype tsunami periods periodically reported (Bernard et al., 2006). As shown in Fig. 4.7 the set point curve depicts a quasi-periodic long wave with the following wave parameters: $\omega = 2\pi/T = \pi/25\ 1/\mathrm{s}$, $k = 2\pi/L = 0.073\ 1/\mathrm{m}$, $h_0 = 0.3\ \mathrm{m}$, $a_{tr} = 0.03\ \mathrm{m}$ and $a_{cr} = 0.06\ \mathrm{m}$.

The resulting waveform, which is in much better agreement with the set point curve, represents a quasi-periodic wave generated with a leading depression wave. In the starting phase of the wave generation minor water surface fluctuations still occur due to remaining fundamental oscillations from former experimental runs. These result in adequate controller action and thus lead to minor control errors. Hence it can be seen, that those errors remain small and a step-up of oscillations is successfully prevented with the controller setup utilized. Significant deviations arise at the beginning of the monotonically nonincreasing wave trough ($\hat{\eta} = 80 - 100$). The control error, which amounts to -0.1 as a peak, rather stems from the control variable lagging behind the set point curve. The oscillations, especially in the downward movement of the water surface, remain small and the controller action results in a time lag. The following plateau phase is characterized by minor oscillations located barely below the zero error value of $-0.02 - 0.03$. Again it appears that the controller scheme tracks the water surface barely below the set point. A positive control error arises as soon as the wave crest has to be generated by the wavemaker. Referable to the positive intake (cp. Subsection 4.2) it had always been more problematic to generate wave crests than wave troughs. The control error reaches a peak while the monotonically nondecreasing portion of the wave crest is generated ($\eta_{sp} - \eta_{inst}/\max\left(\eta_{sp}\right) = 0.14$). Better performance is yielded in the monotonically nonincreasing branch of the wave crest. The overall appearance of the generated wave seems improved compared to the first sinusoidal example. The root mean square error amounts only to $\sigma_{am} = 0.0576$.

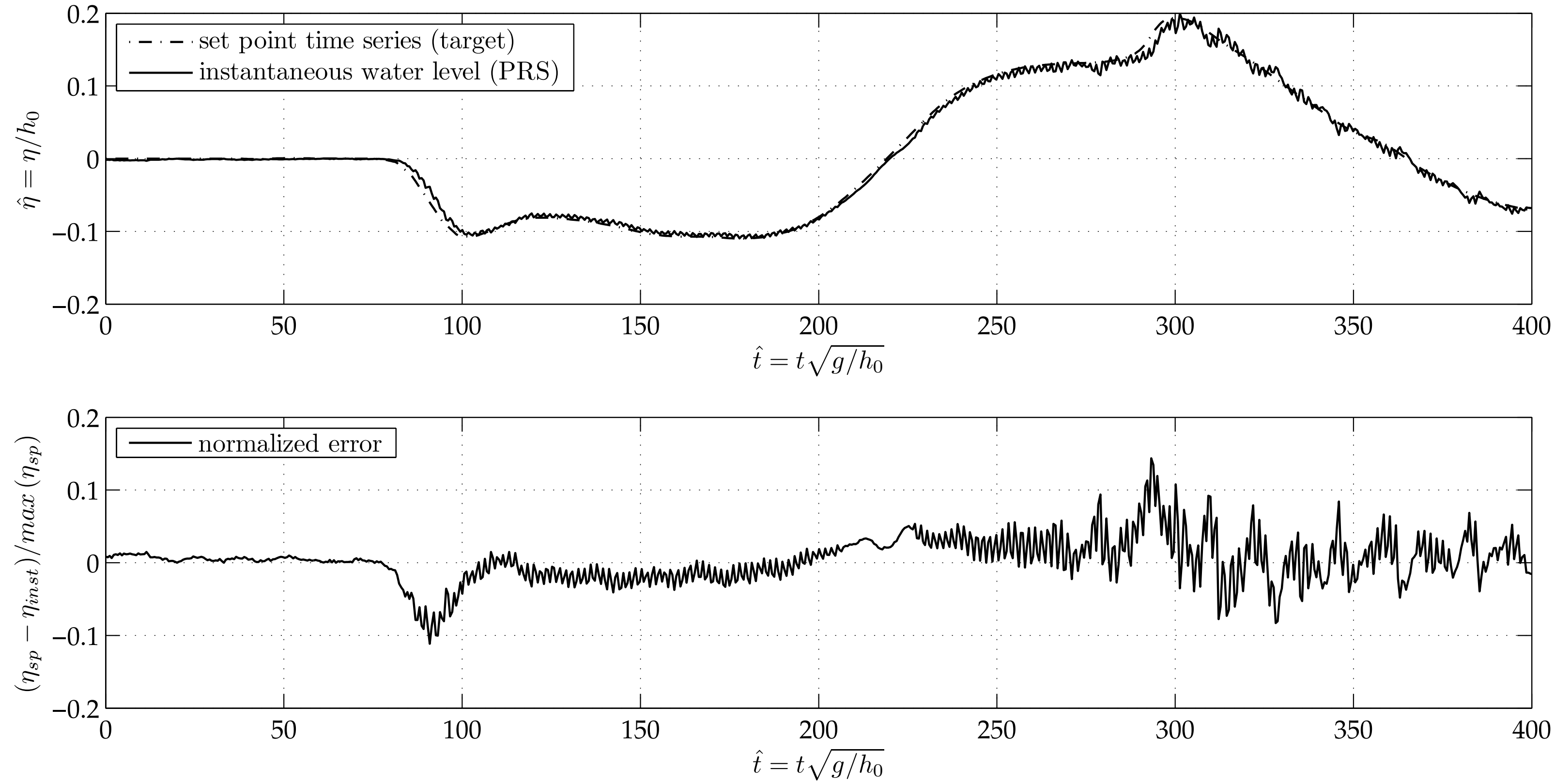

Figure 4.7 Illustration of the wavemaker performance for a prototype waveform deduced from numerical modelling for the city of Padang (Goseberg and Schlurmann, 2009) with $T = 50.0$ s, $h_0 = 0.3$ m, $a_{tr} = 0.03$ m and $a_{cr} = 0.06$ m, upper sub-figure of the figure depicts the non-dimensional water surface elevation η/h_0 of the set point signal and the control variable in regard to the dimensionless time $\hat{t} = t\sqrt{g/h_0}$, lower sub-figure shows the control error normalized by the amplitude a_{cr} of the set point signal over non-dimensional time

4.5 Wavemaker Limits

Besides the outlined capabilities of the wavemaker facility, conditions were detected which limit the applicability to special wave climate, wave length and non-linearities. Basic calculations on the basis of first-order linear wave theory are presented in the following in order to estimate how the wavemaker behaves for a range of theoretically possible waves.

At first, the geometry of the wave flume depicts an upper bound. Fig. 4.8 shows the volumetric ratio of the wave crest to the water volume, contained in the reservoir section of the wave flume (cp. Fig. A.2).

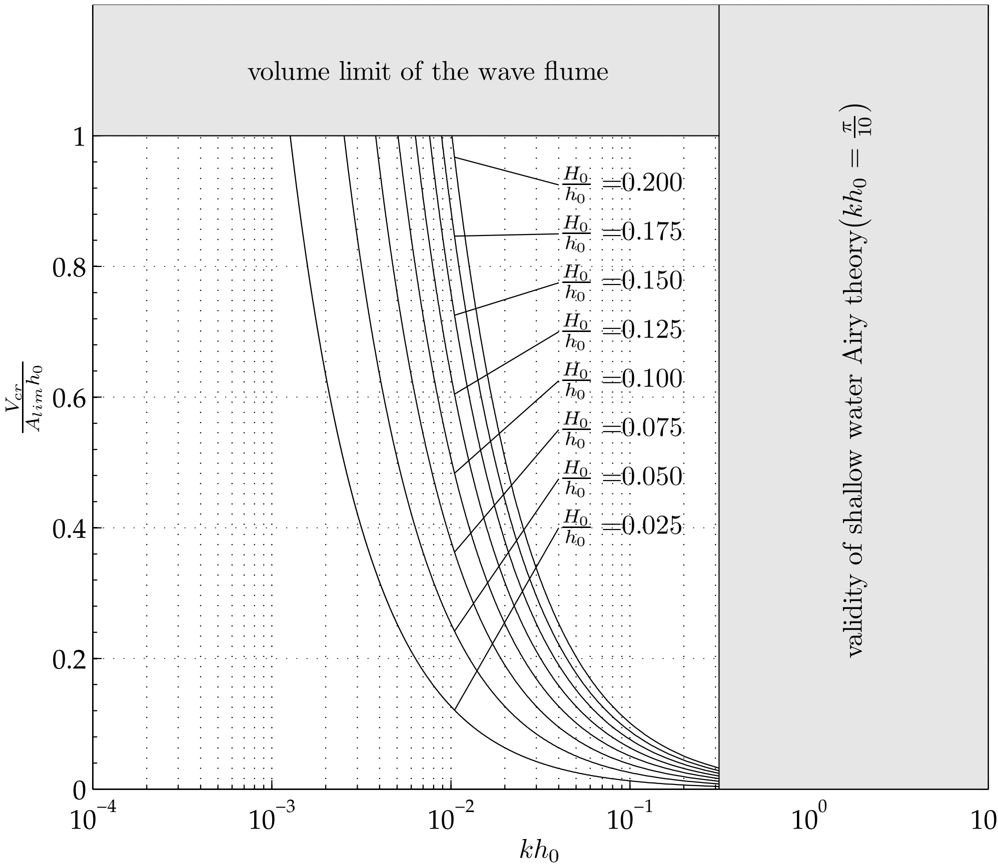

Figure 4.8 Volumetric limits of the applied wavemaker facility based on an estimating description of the used waves by means of the linear Airy theory of small amplitude waves in shallow water conditions, $V_{cr}/\left(A_{lim}h_0\right)$ = ratio of the wave crest volume to the volume capacity of the wave flume over kh_0 = ratio of water depth to wave number, various non-linearities $\epsilon = H_0/h_0$ are shown

The total area of the reservoir amounts to $19.745\ \mathrm{m}^2$ while the water depth in the flume is $0.31\ \mathrm{m}$. The crest volume of the applied waves is calculated according to Eq. (2.4.1d). The chosen approach incorporates that the total amount of water, originally stored in the reservoir, is used to form the wave crest in the flume. This assumption is somewhat weak because at a certain water depth it takes too long to fill the sump pit with enough water to be conveyed into the wave flume in positive direction. On the other hand it is absolutely clear that the physical wave length range, which can be generated with the proposed approach, is far longer than the length of the propagation section of the flume and therefore not the entire wave crest volume is needed to form the wave in the flume. In this case and with the restriction that the reflection coefficient of the beach yields almost unity, it can be concluded that a far smaller volume of water is necessary to generate the entire wave because portions of the re-reflected wave contribute to the wave generation process.

It becomes apparent that the wave length, which can be generated at the volumetric limit, reduces with increasing non-linearity of the waves because waves of greater non-linearity also contain a greater volume of water in their crest. In the current study the generation of shorter waves, which does not fall into the region of geophysically relevant tsunami-like waves, had not been investigated. It is therefore not clear how the wave generation mechanism is going to perform when shorter waves are applied. Yet it is anticipated that even shorter waves can be generated as long as the controller can be satisfactorily adjusted.

The returning, reflected and in the course re-reflected, waves in the flume which apparently turn out to facilitate the wave generation process in volumetric respect have the additional advantage that they are automatically absorbed by the PID-controller mechanism in an active manner. This kind of absorption control functions on the basis of the feedback loop which is outlined in Subsection 4.3. The waves are controllable by indirect means, that is to say pumping water in or out when the reflected wave approaches the flume wall at the pipe pump station, resulting in changing water surface gradients predefined as set point curve. The reason for the indirect characteristic of the volume-driven wavemaker is also the applied wave flume head wall at the pump-station which is only partially perfused. As opposed to this, the generation of short waves by a piston-type wavemaker can be seen as direct wave generation because the horizontal paddle movement directly results in a wave motion.

Secondly, also the pipe pump station may contribute to the overall wave generation performance and its limits. In the following it is intended to demonstrate how the discharge capacity of the utilized pipe pumps influences the wave generation. Fig. 4.9

displays the ratio of the required discharge Q_{req} on the basis of the horizontal particle velocity of a shallow water wave (Eq. (4.5.1a)) to the discharge capacity Q_{max} of the pipe pumps installed in the wavemaker.

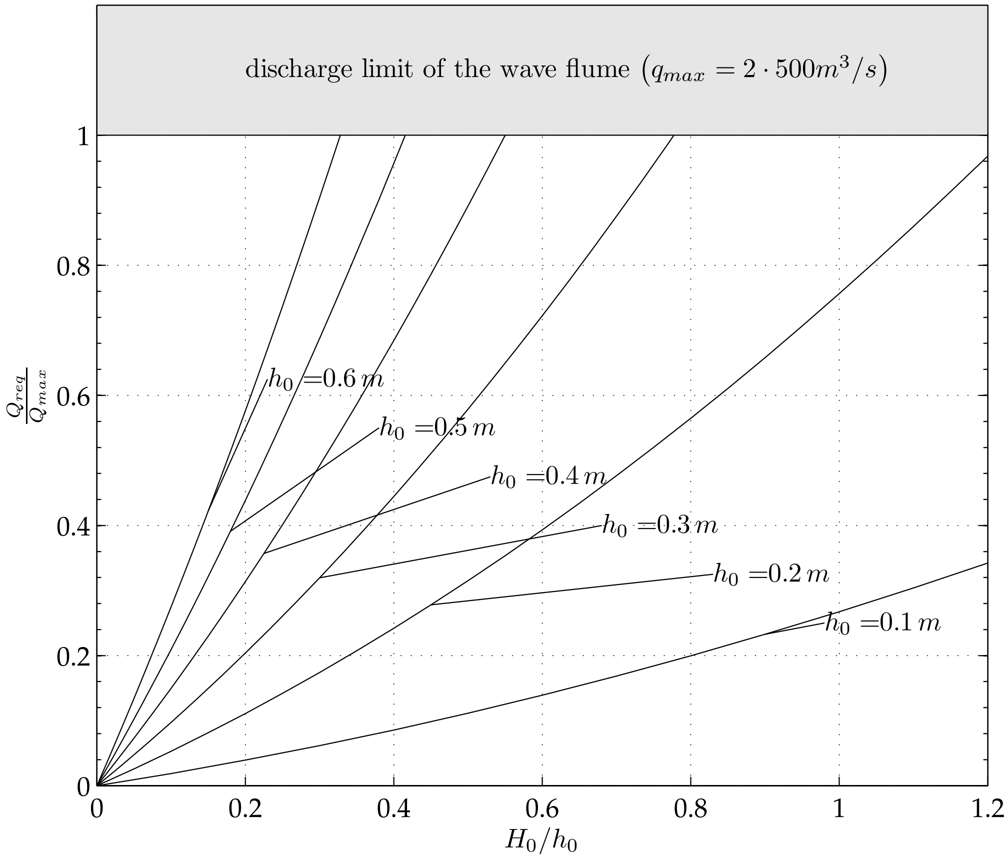

Figure 4.9 Discharge limits of the applied wavemaker facility based on an estimating description of the used waves by means of the linear Airy theory of small amplitude waves in shallow water conditions, Q_{req}/Q_{max} = ratio of the required discharge on the basis of horizontal particle velocity of the shallow water wave in the wave flume to the discharge capacity of the pipe pumps over H_0/h_0 = ratio of the wave height to the water depth, various water depths are shown

On the one hand it can be seen that the discharge demand for a given water depth increases quadratically with increasing dimensionless wave height. Eq. (4.5.1b) was used for the calculations relating the discharge ratio to the dimensionless water depth. It reads

$$u_h\left(x,t\right) = \frac{H_0}{2}\sqrt{\frac{g}{h_0}}\cos\left(kx - \omega t\right) \tag{4.5.1a}$$

$$Q_{req} = u_{max,h} A_{cs} = \frac{H_0}{2} \sqrt{\frac{g}{h_0}} \left(h_0 + \frac{H_0}{2} \right) \tag{4.5.1b}$$

with u_h = horizontal particle velocity of a linear wave, A_{cr} = cross sectional area of the wave flume (discharge area), Q_{req} = required discharge to fulfill the horizontal velocity property of a linear (long) wave.

On the other hand it is apparent that an increase in water depth automatically results in higher discharge in the cross sectional area at the peak of the wave while the wave heights achievable with the wavemaker facility are reduced. The influence of the water depth applied in the wave flume is found to influence the wavemaker performance stronger than the non-linear property of the waves. Therefore care has to be taken when experiments are designed and the obtainable boundary conditions for the experiments have to be chosen at a water depth which can easily be generated in the laboratory.

4.6 Summary and Conclusions

A methodology for the generation of arbitrary long waves was developed. It mainly functions on the basis of accelerated and decelerated water volumes which drive the wavemaker. The methodology overcomes former limitations of other wave generation techniques such as piston-type wave generation, dam-break analogy or vertical wave board motion. The generation of arbitrary long waves can be obtained by means of a set of high capacity pipe pumps under the control of a feedback loop system implemented as a proportional–integral–derivative controller.

The main advantage of the new methodology is the adequate generation of long waves which geophysically exhibit commensurable wave length or periods when applied in down-scaled physical models. While wave periods which are reproducible by means of techniques found in literature are questionably short, it can be shown that the wave periods generated with the aid of the new methodology are in the proper order of magnitude. Either quasi-periodic waves or numerically deduced tsunami time series of the surface elevation can be generated by this means. Moreover the control error during the generation which may serve as a measure of quality is satisfactorily small. The error is not likely to disturb the wave propagation and eventually its wave run-up. An estimation of the wavemaker limits reveals that in addition both shorter and longer waves of varying non-linearities are theoretically possible when the geometrical and technical prerequisites are given. The methodology depicts a suitable tool in the field of coastal engineering to study near-shore, long wave motion and run-up dynamics in a scaled, yet geophysically adjusted manner.

5 Results of Physical Modeling

5.1 General Consideration

General features of the applied waves, their form, surface elevations and velocities at different positions are described at first in the following. The results of the physical modeling comprise findings associated with the reflectivity of the investigated beach wedge (Section 5.2), with the run-up of long waves with (Section 5.3) as well as without macro-roughness elements (Section 5.4) which obstruct the effective flow cross-section. The findings are outlined in the following subsections and if available the results are always compared with existing theoretical or experimental studies.

5.1.1 Wave Control Signals

The surface elevation history of the utilized waves at the positive pump outlet is presented in Fig. 5.1 in non-dimensional form. The surface elevation history $\hat{\eta}$ is given as a function of the non-dimensional time $\hat{t}$. The utilized wave form is a sinusoid with varying amplitude. The waves were generated in a constant water depth of $h_0 = 0.31$ m. The set point curve for the six different waves was generated according to Eq. (2.4.1b). The surface elevation values were subsequently converted into voltage signals to obtain a first wave form. The variation of the amplitude was achieved by hardware means. During the experiments it was assured by means of a precise potentiometer, interconnected between the controller and the pump, that the six chosen waves were always of the same form and duration only differing in amplitude. Starting with the highest wave and defining it to be 100%, the remaining five wave heights were defined in decending 10% steps. Tab. 5.1 associates these wave height percentages to the actual non-linearities ϵ of the waves.

Hence the waves are usually consistently labeled according to their percentage of the highest wave. Fig. 5.1 additionally states the averaged standard deviation $\bar{\sigma}_{std}$ for each group of waves, expressing the repeatability of the surface elevations. It generally ranges in the order of 10^{-4} which represents a remarkable performance

Table 5.1 Relation of the applied waves to the maximum positive amplitude at the wavemaker, their labels and the associated non-linearities for a water depth of $h_0 = 0.31$ m

Label/Notation	$0.5\,A_{cr}$	$0.6\,A_{cr}$	$0.7\,A_{cr}$	$0.8\,A_{cr}$	$0.9\,A_{cr}$	$1.0\,A_{cr}$
Percentage of maxA_{cr}	50 %	60 %	70 %	80 %	90 %	100 %
Non-linearity ϵ	0.050	0.058	0.066	0.075	0.086	0.095

of the wavemaker. The experimental procedure guaranteed that the results are not biased by the quality of the approaching waves.

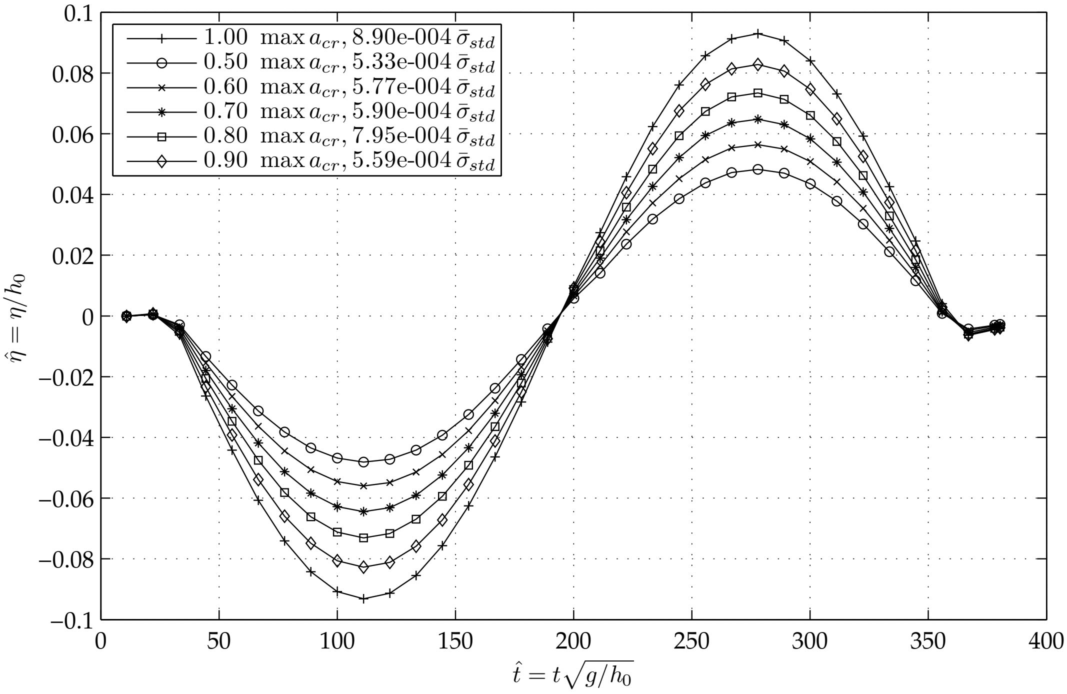

Figure 5.1 Averaged non-dimensional surface elevation history for the six utilized waves, the markers denote the different waves heights, $\bar{\sigma}_{std}$ is the averaged standard deviation calculated from the entire number of experiments in each group

Tab. 5.2 further outlines the number of experiments and the applied wave conditions during the experiments. The wave conditions are classified according to their percentage of the highest wave which was applied. It is apparent that the number of experiments related to the macro-roughness combinations is smaller for the staggered combinations. This is due to the fact that less combinations are generally possible. For a detailed presentation of the investigated combinations the reader is referred to Annex B.

Table 5.2 Summary of the conducted experiments classified according to the utilized wave forms depicted in Fig. 5.1 and to the macro-roughness combinations

	$0.5\,A_{cr}$	$0.6\,A_{cr}$	$0.7\,A_{cr}$	$0.8\,A_{cr}$	$0.9\,A_{cr}$	$1.0\,A_{cr}$	$\sum$
no elements	2	39	2	2	2	31	78
aligned, $\varphi = 0°$	12	12	12	12	12	13	212
aligned, $\varphi = 45°$	9	9	9	9	9	10	
staggered, $\varphi = 0°$	8	8	8	8	8	8	
staggered, $\varphi = 45°$	6	6	6	6	6	6	
$\sum$	37	74	37	37	37	68	290

The varied variables which make up the macro-roughness element configurations are the distance between the elements b_{st}, the number of macro-roughness element rows n, the angle of the elements with respect to the incident wave direction φ and the choice of an offset between the element rows. In case of the aligned configuration, four street widths were realizable in the flume which are $10.0\ \mathrm{cm}$, $6.6\ \mathrm{cm}$, $4.2\ \mathrm{cm}$ and $2.5\ \mathrm{cm}$ whereas for the staggered configuration only three street widths were used ($10.9\ \mathrm{cm}$, $5.9\ \mathrm{cm}$, $2.5\ \mathrm{cm}$) due to the fact that the flume width is limited. Two element angles $\varphi \in (0°, 45°)$ are further conceivable. Additionally three different numbers of macro-roughness element rows were tested in order to investigate the influence of the obstructed long-shore length, $n \in (1, 5, 10)$.

5.1.2 Surface Elevation Time Series

The transformation of waves with two different non-linearities climbing up a $1/40$ sloping beach is illustrated in Figs. 5.2 and 5.3. The first surface elevation time series is associated to the pressure sensor directly at the positive inlet of the pipe pump station (*PRS_inst*) whereas the remaining wave gauges (second to last panel) are entirely distributed along the beach wedge. The fixed positions of the sensors are drawn in Fig. 3.9.

At first it is noticeable that the transformation process of the waves is very similar. No clear reflection wave can be determined from the available wave gauges. Yet it is obvious that reflection takes places because the surface elevation at the beach toe (*RWG_1*) differs widely in the wave period and the wave height. This observa-

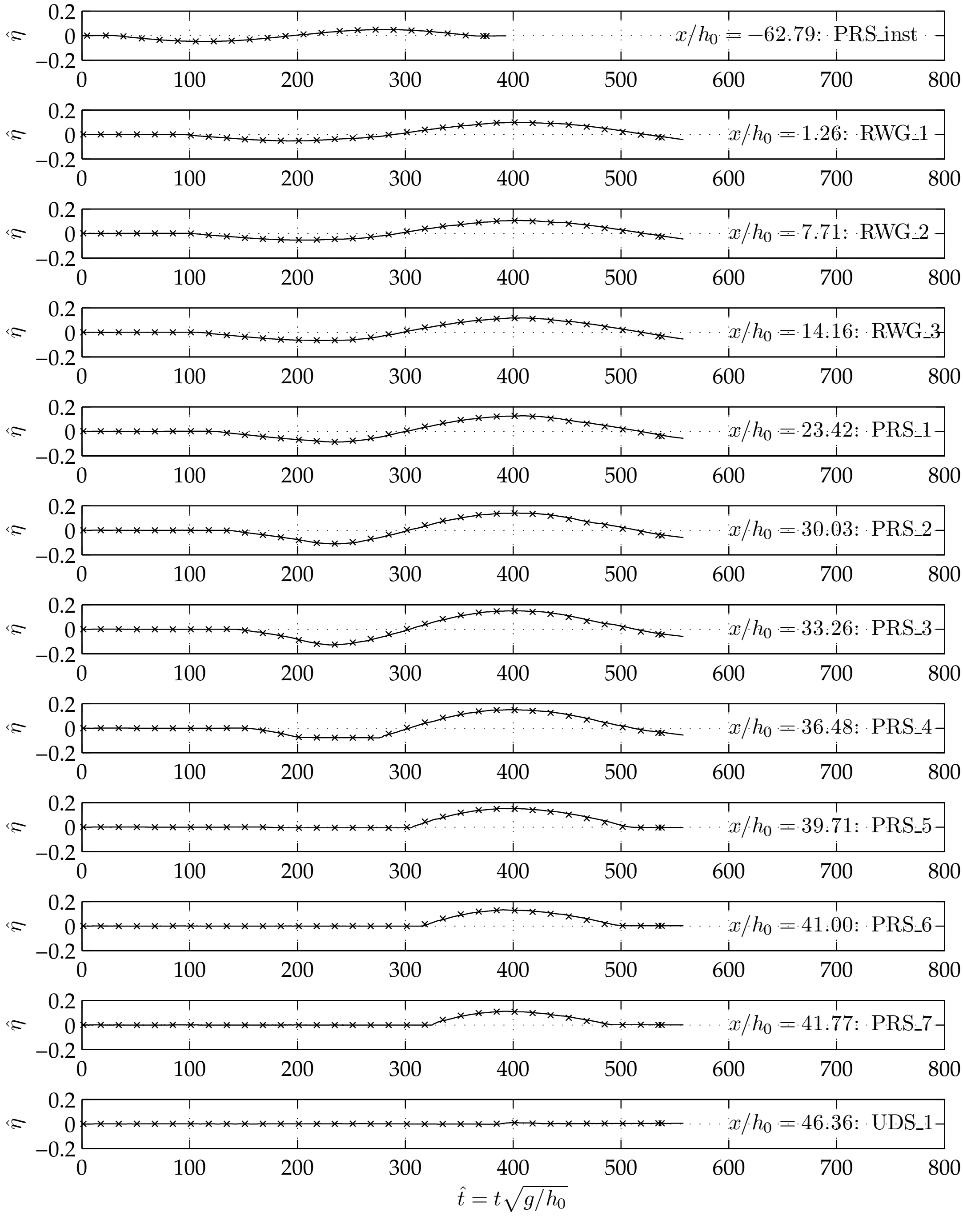

Figure 5.2 Time series of the surface elevation $\hat{\eta}$ for a wave with a non-linearity of $\epsilon = 0.05$ at different positions x/h_0 as a function of the non-dimensional time $\hat{t} = t\sqrt{g/h_0}$.

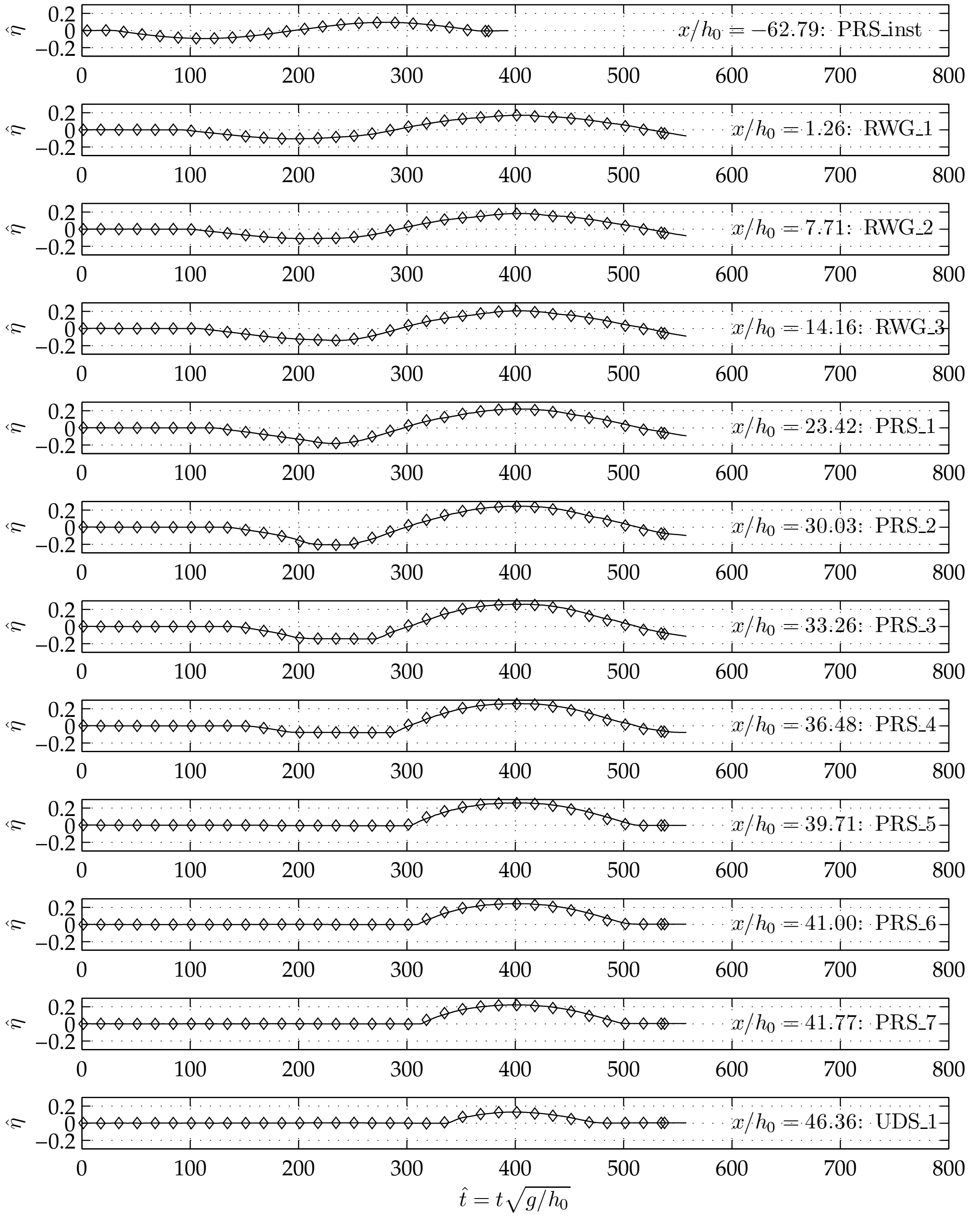

Figure 5.3 Time series of the surface elevation $\hat{\eta}$ for a wave with a non-linearity of $\epsilon = 0.093$ at different positions x/h_0 as a function of the non-dimensional time $\hat{t} = t\sqrt{g/h_0}$.

tion, which is clearly due to the wave reflection, is discussed in detail in Section 5.2. Secondly it becomes apparent that the draw-down of the long wave is much more pronounced for waves with greater leading depression waves. The draw-down is detectable as low as the sensor *PRS_2* for the non-linearity of $\epsilon = 0.093$ whereas it is only apparent to the sensor *PRS_4* ($\epsilon = 0.05$, cp. Fig. 5.2 for the positions).

The transformation of the approaching waves climbing up the $1/40$ beach can be studied based on Fig. 5.4. The transformation on the beach is defined in analogy to common wave shoaling as the ratio of the wave amplitude at the distinct position of interest to the incident wave amplitude a_{cr} at the wavemaker and as a function of the wave length at the wavemaker L_0 normalized by the still water depth at the sensor position.

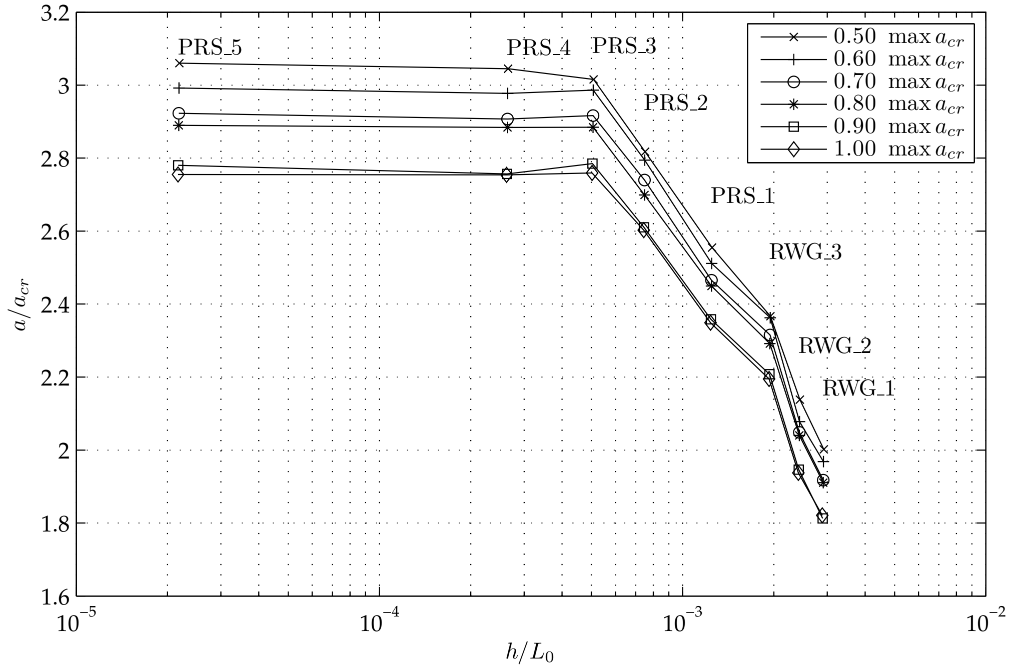

Figure 5.4 Wave transformation during the climb of quasi-periodic long waves of different non-linearity at various sensor positions (cp. Fig. 3.9 for the distances)

It should be noted that the time series for the calculations were averaged for the experiments belonging together. The calculations for the Fig. 5.4 depict the wave transformation under the assumption that the wave reflection is uniformly distributed along the beach wedge. With reference to the reflection analysis in Chapter 5.2 it is however not fully clear if this assumption holds true. For that reason it is hence not admissible to speak of a shoaling coefficient in the classical sense but refer to wave transformation instead.

An increase of relative wave amplitude is noticeable when the still water depth decreases. In general the influence of the non-linearity is less significant to the wave transformation. The decreasing water depth predominantly contributes to the wave transformation. From the pressure sensor *PRS_3*, which is located at $x/h_0 = 32.0$, the wave amplification coefficient remains constant for all non-linearities. The sensors which are located further onshore with relation to sensor *PRS_5* are not included because the definition of the relative wave length yields negative unphysical numerical values. Yet it is assumed that the relative wave amplitude decreases for the remaining onshore sensors due to the fact that the kinetic energy of the incident wave is converted into potential energy.

In theory the energy flux of the wave remains constant along the beach under the assumption of an inviscid fluid and small bottom friction. This fact results in steepening of the waves until, as a limiting condition, the wave finally breaks. If no wave breaking occurs, the wave steepening is still limited by the energy consumption due to the transformation of kinetic into potential energy. The beach wedge region where decreasing relative wave amplitudes are observed coincides with the initially dry onshore region whereas constant relative wave amplitudes are associated with the distance to where the draw-down of the waves can be traced back.

5.1.3 Surface Elevation Profiles

Apart from the temporal behavior of the wave propagation along the wave flume for waves climbing up a plane undisturbed beach in the following, the qualitative influence of the macro-roughness element configuration to the spatial distribution of the water level at distinct time steps should be assessed.

Figs. 5.5 and 5.6 illustrate the development of the surface elevation profile along the beach wedge. The normalized surface elevation $\hat{\eta} = \eta/h_0$ is given as a function of the non-dimensional horizontal coordinate $\hat{x} = x/h_0$. Each of the panels shown in the figures depict a specific time step as a snapshot of the water surface elevation. For these illustrations the water depth is chosen for the normalization due to its invariant character for the entire set of experiments. The dimensionless time $\hat{t} = t\sqrt{g/h_0}$ is always given in the lower left corner of the panels to indicate the temporal evolution of the wave. The figure panels compare the normalized surface elevation for a case where macro-roughness elements are absent with the macro-roughness configuration

$\Gamma = 4$. This configuration is characterized by a staggered, rotated arrangement of the obstacles. Additionally, the smallest street width b_{st} is utilized for the plots in order to highlight the qualitative effects of the macro-roughness elements. The position and the height of the obstacle area is given by the dash-dotted gray lines while the beach surface is presented by the full gray line. A wave with a non-linearity of $\epsilon = 0.093$ is used. Out of the sequence of available time steps of the wave evolution along the beach wedge four specific times are presented in order to focus on the basic features. For the remaining time steps the reader is referred to the annex. The Figs. C.11 - C.21 present the remaining time steps of the snapshot sequence.

Generally three phases can be determined where differences occur. First of all the initial draw-back of the water, which is due to the leading depression wave character, characterizes the wave evolution. In this phase no significant differences can be found for the cases with and without macro-roughness elements. In a second phase when the water surface elevation is rising on the beach, in tendency higher water levels are determined for the involvement of macro-roughness elements. Thirdly, during the run-down of the long wave the situation inverts and the surface profile is lower for the macro-roughness elements. Also the back-rush of water which is in-between and behind the obstacles is retarded significantly.

The investigated waves are always leading depression waves with a wave trough at the beginning which results in an initial draw-back of the water from the coastline. The comparison between the two cases (with and without macro-roughness) does not show any difference because the obstacles are not touched in this phase of the wave evolution. This changes as soon as the water level rises and approaches the first line of macro-roughness elements in the wake of the positive amplitude.

Then an interesting feature is revealed, which is demonstrated in Fig. 5.5. The approaching wave tongue collides with the first macro-roughness element row and a shock wave is formed which propagates seawards. This feature is observable for all investigated street widths and for all different macro-roughness configurations. The height of the shock wave however is smaller due to the fact that lesser obstruction ratios and thus smaller reflective vertical surfaces are involved in these cases. The front of the initiated shock wave is comparable with a monoclinal rising wave which in contrast to the definition is rapidly varying during its seaward propagation. A similar phenomena in principle is present at the Chientang River also known as the Hangchow bore (cp. e.g. Chow, 1959). In the present case the surface gradient of the positive surge, whose front is initially steep, decreases rapidly and it flattens out noticeably. The increase of the hydraulic radius as a function of the beach

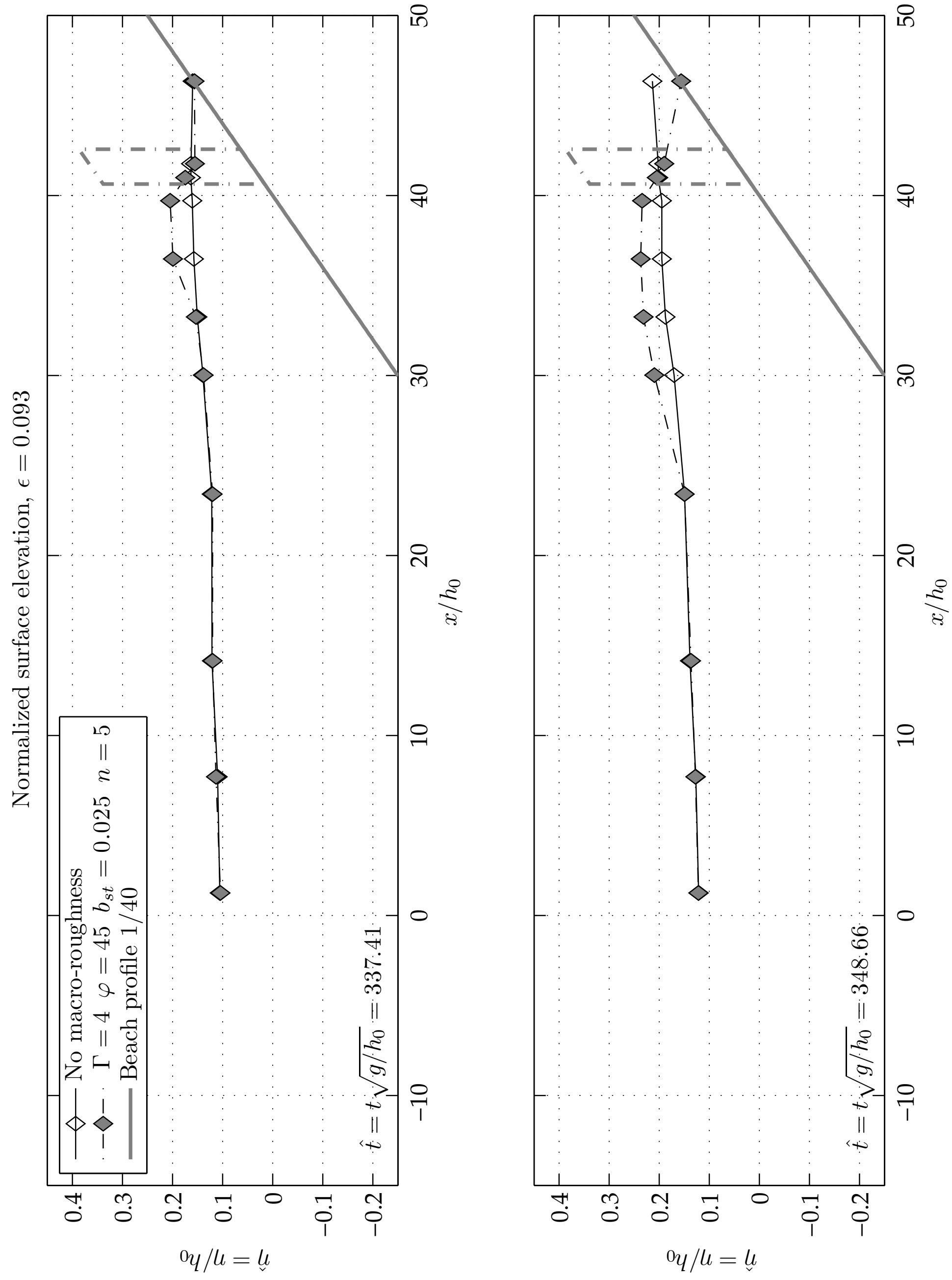

Figure 5.5 Comparison of the normalized surface elevation for a sinusoidal wave with $\epsilon = 0.093$ at $\hat{t} = 337.41$ and $\hat{t} = 348.66$ with and without the presence of macro-roughness elements. The macro-roughness element configuration is specified by $\Gamma = 4$, $\varphi = 45°$, $b_{st} = 0.025$ and $n = 5$. Surface elevation and spatial coordinates are normalized by the invariant water depth h_0. The dash-dotted line depicts the macro-roughness element area.

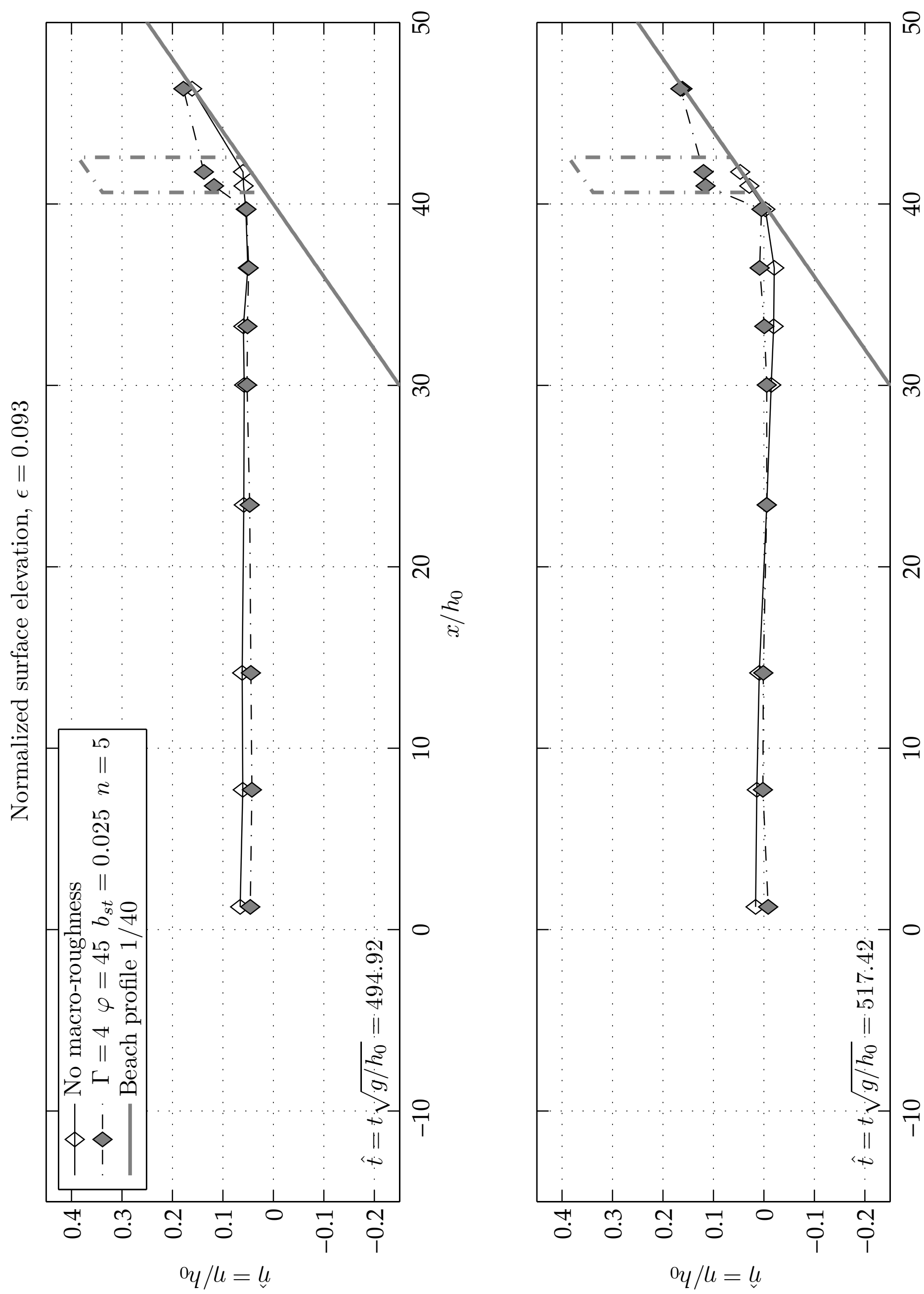

Figure 5.6 Comparison of the normalized surface elevation for a sinusoidal wave with $\epsilon = 0.093$ at $\hat{t} = 494.92$ and $\hat{t} = 517.42$ with and without the presence of macro-roughness elements. The macro-roughness element configuration is specified by $\Gamma = 4$, $\varphi = 45°$, $b_{st} = 0.025$ and $n = 5$. Surface elevation and spatial coordinates are normalized by the invariant water depth h_0. The dash-dotted line depicts the macro-roughness element area.

slope is responsible for this property. In the time course the cases with and without macro-roughness element differ in that the water levels remain increased for the macro-roughness present (cp. Figs. C.17 and C.18). Yet it is observable that these higher water levels in front of the macro-roughness elements slowly converge to the water levels when no obstacles are incorporated.

The situation inverts as soon as the long wave starts the draw-down (cp. Figs. C.19 - C.21). In the vicinity of the macro-roughness elements the undisturbed case faces higher water levels than the macro-roughness cases. This is a direct result of the macro-roughness effect causing decreasing maximum wave run-up. A detailed quantitative assessment of the macro-roughness influence is given in Section 5.4. The obstacles are found to partially reflect the shoreward transported energy back to the sea.

The water levels remain higher in front of the first element row for the remaining measured interval. Yet an additional feature shows up within the macro-roughness area. There, the water levels with macro-roughness elements in place are again higher. This is due to the fact that the volume of water which at this time is situated in-between and behind the obstacles is retarded significantly and is only displaced with a notable time lag. In the case of macro-roughness it is apparent that the negative, seaward directed surface gradient in the vicinity of the obstacles is considerably higher than that without obstacles. In consequence the flow velocities are qualitatively increased compared to the undisturbed run-up.

This qualitative description of the influence of macro-roughness elements on the run-up dynamics can be related to the cross-shore obstruction ratio ψ_{cs} in order to quantify the effects for the investigated macro-roughness configurations $\Gamma = 1 - 4$. The Figs. 5.7(a) and 5.7(b) reveal the functional relation of the maximum normalized surface elevation η to the cross-shore obstruction ratio ψ_{cs} for two sensor positions (cp. Fig. 3.9). The first position of sensor *PRS_5* is located directly in front of the macro-roughness elements whereas the second position of sensor *PRS_7* is in-between the macro-roughness elements. From the viewpoint of designing a building which might be exposed to a violent flow, the general question arises whether surrounding buildings are possibly influencing the design water levels of the new building. In this sense the maximum surface elevation over the entire time of inundation is plotted in relation to the cross-shore obstruction ratio. A value of $\psi_{cs} = 0$ indicates that no macro-roughness is present.

It is apparent that the maximum surface elevation is not significantly influenced by the presence of macro-roughness elements. Only a little decrease is observable which

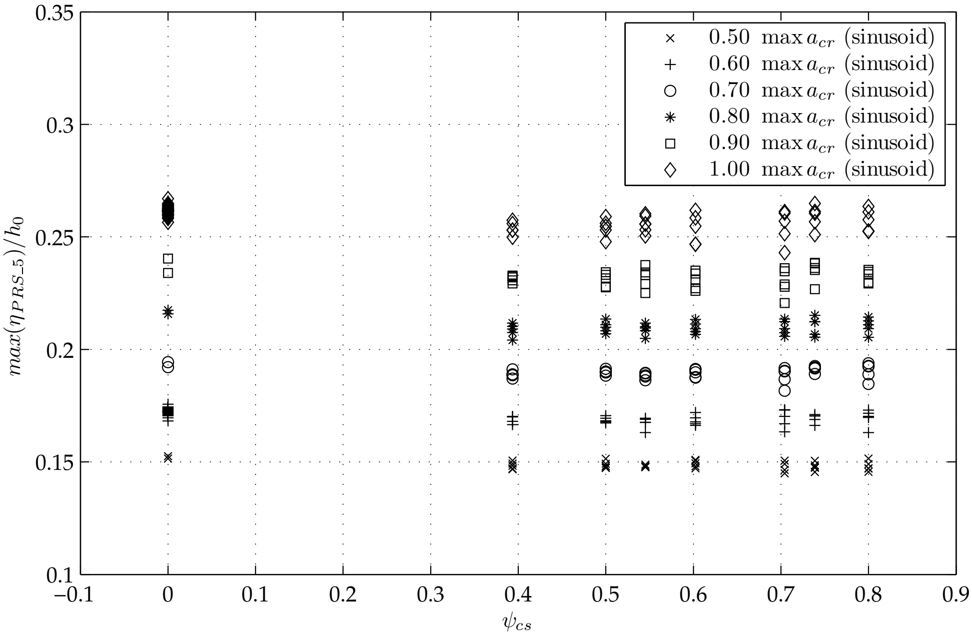

(a) Recorded sensor *PRS_5*, cp. Fig. 3.9 for the position

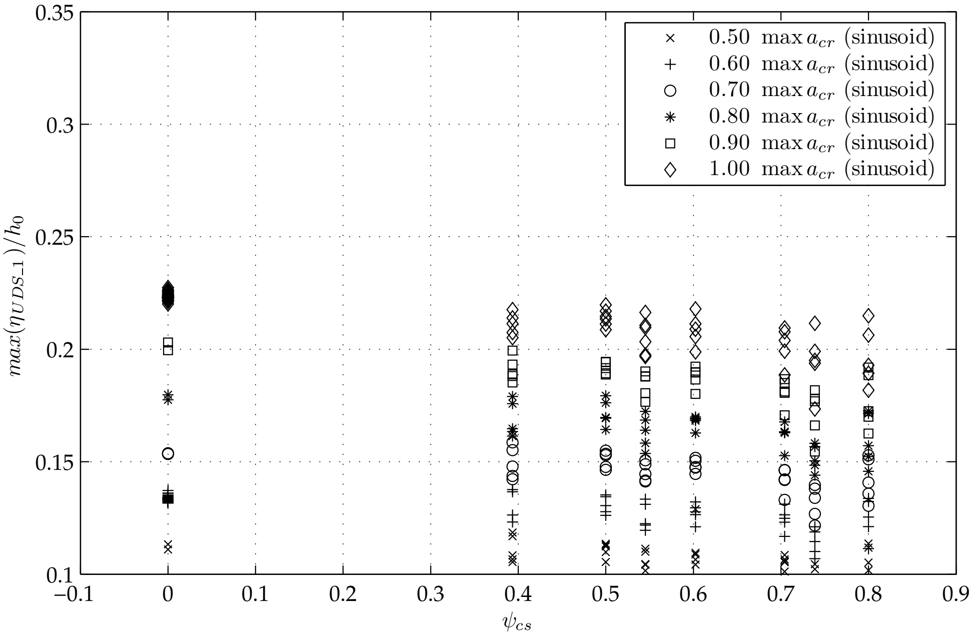

(b) Recorded sensor *PRS_7*

Figure 5.7 Functional relation of the maximum of the normalized surface elevation η to the cross-shore obstruction ratio ψ_{cs} for a position before the macro-roughness elements *PRS_5* and in-between *PRS_7*. The measurements are sorted by the positive amplitude at the wavemaker.

still lies in the range of the overall measured values. Hence in the context of building design it is recommendable to assume water levels equivalent to non-obstructed conditions at least for objects which are in the direct vicinity of the shoreline. In contrast to the aforementioned location the situation differs slightly when one interprets available data for a position which is located in-between the macro-roughness area. It has to be expected that a general decrease in the maximum water surface elevation is likely if macro-roughness elements are in place. In general this assumption holds true though the expected effect is not very predominant. Over the course of time water levels in the macro-roughness element area rise less than in the non-obstructed case. At first sight this fact could allow for the conclusion of smaller static pressure distributions on buildings walls and associated forces. Yet higher dynamic pressure is expected in reverse due to channelized flow acceleration in the streets. With increasing distance to the shoreline, higher differences in the maximum surface elevation between obstructed and non-obstructed configurations are concluded. This is the cause because a significant reduction of the relative wave run-up is found in relation with the macro-roughness elements, as will be shown in Section 5.4.

5.1.4 Velocity Profiles

An essential property of long waves is their velocity profile over the water depth. The shallow water character of long waves manifests from the formation in deep water until the inevitable arrival at a specific coast. A net volume flux associated with a pronounced uniform vertical velocity profile is deduced from the theory. The following subsection serves the dual purpose of substantiating the uniformity of the vertical velocity profile in the laboratory and proving that the lateral vertical velocities are negligibly small compared to the velocities in wave propagation direction. The wave run-up process could be negatively influenced because the bend of the flume could possibly induce radial-pointing velocity components. The positing of the EMS probe head is additionally depicted in Fig. A.1.

Fig. 5.8(a) illustrates the velocity profile at the position $x/h_0 = 2.58$ which is situated at the beginning of the beach wedge (cp. Fig. 3.10). The velocities are given in non-dimensional manner as $\hat{v}_x = v_x/\sqrt{gh_0}$ and $\hat{v}_y = v_y/\sqrt{gh_0}$. The subscripts denote the velocity direction in the coordinate system defined in Fig. 3.10. At this position detailed measurements were conducted with the focus of obtaining the vertical velocity profile. The depicted velocity profile consists of 15 individual measurements at three vertical levels and five distances in cross-shore direction. The chosen time step $\hat{t} = 281.16$, which is illustrated, marks a time of maximum flow velocity during the wave run-up to the beach. Additionally it is referred to Fig. C.22 in the annex where the time step $\hat{t} = 435.29$ is chosen to also elucidate the velocity distribution during the run-down phase of the long wave. In the presented figures some contour lines are also given. The colorbar indicates the range of velocities which were recorded and the overall mean velocity as well as the standard deviation are plotted additionally.

It becomes apparent that the velocity profiles in landward direction given in Figs. 5.8(a) and C.22 possess a good uniformity. The values of the standard deviation of the profiles are $\sigma = 0.0029$ and $\sigma = 0.0040$ respectively. The distribution of the velocities in the vertical does not exhibit a trend to smaller velocities either at the flume walls or the bottom. Only at the upper vertical limit of the velocity profile it comes to mind that slightly higher velocities are found, which is likely to stem from the electromagnetic probe. The sensor starts to be biased if the nominal water level above the sensor head is too small. Yet, an overall good agreement with the postulated uniformity, which is characteristic to a typical long wave, is achieved in the laboratory.

Secondly Fig. 5.8(b) depicts the cross-shore velocities at the cross-section under investigation. While the wave crest and the associated flow velocities in the landward direction are strong, it appears that the cross-shore velocities are an order of magnitude smaller. The average non-dimensional cross-shore velocity is $\bar{v}_y = -0.003$ and the related standard deviation amounts to $\sigma = 0.0028$. This indicates that on the one hand the velocities are negligibly small compared with the dominant onshore pointing wave motion. The average velocity and the standard deviation on the other hand is in the same range of values, which suggests the assumption that almost only signal noise is present. The cross-shore velocity components are therefore marginal. Hence it can be excluded that radial velocities are generated during the wave propagation along the flume bend and no effects are to be expectable in correlation with the wave run-up and run-down.

5.1.5 Summary and Conclusions

In this subsection the investigated long waves are presented. In general a notable reproducibility is found. The applicability of the volume-driven wavemaker is hence again confirmed. Secondly surface elevation time series and profiles are depicted in order to document the data for further usage. The presented data are suitable to serve as benchmark datasets to validate numerical models. The qualitative features of the approaching wave are also highlighted. It is obvious that significant changes in the surface elevation and the flow velocities are to be expected in the vicinity of the mimicked urban pattern. This leads to changed force and pressure distributions at

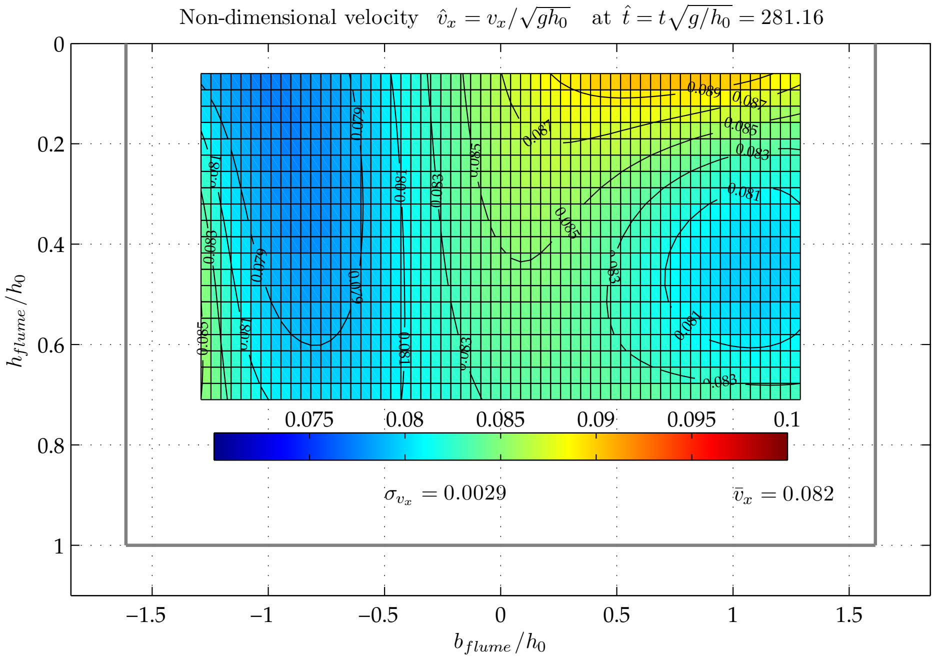

(a) Velocity profile $\bar{v}_x$

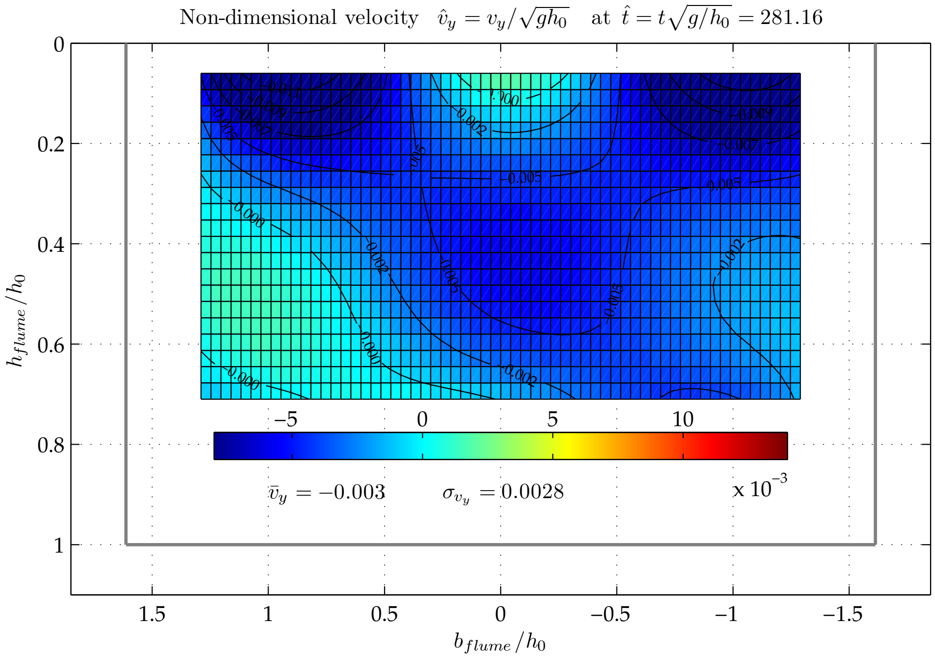

(b) Velocity profile $\bar{v}_y$

Figure 5.8 Non-dimensional velocities in a cross-shore profile at position $x/h_0 = 2.58$ involving measurements *EMS_1-EMS_7* and *EMS_15-EMS_22*. Velocities are interpolated and given in non-dimensional form $\hat{v}_x = v_x/\sqrt{gh_0}$ for the time step $\hat{t} = 281.16$ and a wave of non-linearity $\epsilon = 0.058$. Gray thick lines denote the flume walls.

obstacle walls and the adjacent bottom topography. In consequence to these observations, new conclusions in regard to forces on and design parameters for buildings in such environments are demanded.

Additionally it is shown that the velocity profiles at two different time steps of the approaching wave are satisfactorily uniform and the assumption of a valid representation of the laboratory-generated long waves with long waves in prototype holds true. Negative influences which might be guessed at first sight are excluded and in the region of the wave run-up no disturbing effects are found. The assumption of two-dimensionality is finally substantiated.

5.2 Reflection Analysis

5.2.1 General Considerations

Wave reflection is known from many physical phenomena, such as light being reflected in a mirror or sound waves producing echoes reflected at mountainsides. Even earthquake waves causatively interlinked with the wave motion, addressed herein, are reflected at crustal interfaces. In coastal engineering total reflections appear for example at vertical or near-vertical walls such as piers or quay walls, resulting in standing waves, whereas partial reflections are present at various other coastal measures such as dikes and sea walls. Apart from the general phenomenology and in the context of long incident waves, sloping beaches may also be interpreted as vertical walls when the ratio of the horizontal beach spread to the incoming wave length tends to zero or becomes very small. In analytical solutions of long wave run-up, a common assumption is to demand full reflection to derive describing run-up formula and standing wave solutions at the beach toe (e.g. Pelinovsky and Mazova, 1992; Madsen and Schäffer, 2010).

In experimental studies it is often essential to separate the incident and reflected wave spectra in order to deduce wave properties for example at or in the vicinity of a beach toe or a coastal structure. Various methods were developed and a valuable review could be found in Hughes (1993b). At this time, methods which adopted two-point measurements of wave height in a line parallel to the approaching waves were commonly utilized (Goda and Suzuki, 1976). Mansard and Funke (1980) developed a three-point method which overcame known limitations of the formerly applied two-point measurement method. The recorded wave height time series were decomposed by means of a least square analysis yielding greater accuracy over a wider range of frequencies. The method denoted an upgrade to that effect that then also wave spectra could be analyzed and not only periodic waves as was possible with existing methods. It was also recommended that the spacing between the wave gauges should be chosen according to fractional amounts of the wave lengths of the sea state or waves under consideration. Both methods described above yielded result in the frequency domain. While these methods rely on spatially separated wave gauges it would be erroneous to apply them to sloping bottoms because of shoaling and non-linear effects. Hence Hughes (1993a) presented a method with co-located instruments (wave gauge and velocimeter) in order to circumvent those error sources effectively and demonstrated the usefulness of the method along with recorded velocity measurements. This method is valid in the case of complete reflection.

Frigaard and Brorsen (1995) reported a method which also bases on a two-point measurement of wave height but yielding the resulting separated incident and reflected wave signals in the time-domain. Additionally the implementation of the method proved to function in real time by means of digital filters. The surface elevation of the wave can generally be written as a sum of incident and reflected waves. For monochromatic waves it reads

$$\begin{aligned}\eta\left(x,t\right)=\eta_I\left(x,t\right)+\eta_R\left(x,t\right)=&\\ &a_I\cos\left(\omega t-kx+\phi_I\right)+a_R\cos\left(\omega t+kx+\phi_R\right)\end{aligned}\qquad(5.2.1)$$

where $\omega=2\pi/T$, x, t denotes the spatial and temporal variables, k the wave number, $a=a\left(1/T\right)$ the amplitude, $\Phi=\Phi\left(1/T\right)$ the phase. The indices I and R denote the incident and reflected wave portions. At the two gauges it can be written

$$\eta\left(x_1,t\right)=a_I\cos\left(\omega t-kx_1+\phi_I\right)+a_R\cos\left(\omega t+kx_1+\phi_R\right)\qquad(5.2.2a)$$

$$\begin{aligned}\eta\left(x_2,t\right)=a_I\cos\left(\omega t-kx_2+\phi_I\right)+a_R\cos\left(\omega t+kx_2+\phi_R\right)=&\\ &a_I\cos\left(\omega t-kx_1+k\Delta x+\phi_I\right)+a_R\cos\left(\omega t+kx_1+k\Delta x+\phi_R\right)\end{aligned}\qquad(5.2.2b)$$

where $x_2=x_1+\Delta x$ and Δx denoting the distance between the two applied wave gauges. $\Delta\phi=k\Delta x$ can be seen as the phase shift between the incident and reflected wave signals. Without repeating the entire derivation the general idea is furthermore to phase-shift the signals in a way that the incident parts of the wave are in phase while the reflected parts are in mutual opposite phase. Finally a system of equations arise which yield the sought unknown phase shifts and an also unknown amplification factor C. Once the incident and reflected parts of the measured waves are found, the reflection coefficient K_r can be defined by

$$K_r = \frac{a_R}{a_I} \tag{5.2.3}$$

Baldock and Simmonds (1999) extended the method of Frigaard and Brorsen (1995) for waves over sloping bottoms under the assumption that bottom gradients are mild. Additionally assuming short distances or spacing between the wave gauges it was concluded that the sloping bottom can be accounted for by means of the linear shoaling coefficient in good approximation.

5.2.2 Reflection Characteristics

Analytically wave reflection had been treated by linear and non-linear theory for a range of different bottom variation settings. Dingemans (1997, § 2.6) outlined and reviewed many of the solutions to reflections arising from an unevenness of the sea bottom. However it is beyond the scope of the work at hand to repeat the derivations. Hence the addressed bottom settings refer to variations which could be compared to shelf regions. None of them are applicable to mild sloping beaches where strong non-linearity becomes significant. From an engineering perspective, again physical modeling is preferred over analytical approaches. Nevertheless, only little literature exists dealing with wave reflection of mild sloping beaches and the approach of long waves in the laboratory. This is partly due to missing suitable wavemakers, partly due also to limitations in laboratory space. A short review paper on the available experimental data on that special field was written by Sunamura and Okazaki (1996). The authors elaborated on the influence of the surf similarity parameter to the reflection coefficient and presented an empirical formula for beach slopes in the range of $1:2.5 - 1:15$ which reads

$$K_r = 0.84 \left(1 - e^{-12.8\tan(\beta)}\right) \tanh\left(0.11\xi_\infty^{0.24}\right) \tag{5.2.4}$$

where β is the beach slope and ξ_∞ is the offshore surf similarity parameter. The validity of the formula is strongly limited to the above mentioned beach slopes and it will be seen that much higher reflection coefficients were found than expected from the ratio of the beach spread to the wave length. It is also obvious that the wave properties in the laboratories utilized to fit the data empirically were reported to be rather short to be compared to the wave length addressed herein. The empirical relations by Sunamura and Okazaki (1996) are also plotted for a range of beach slopes in Fig. 5.9(a). It is apparent that the reflection coefficients tend to their maxima rather rapidly and are located between $\xi_\infty = 3.5 - 4.5$. Along with this observation it is also clear that given a fixed beach slope the reflection coefficient reduces with increasing offshore wave heights. The parametrized curve for a $1/40$ beach slope is given with the purpose of comparing it with the resulting reflection coefficient. However, it has to be brought to mind that strictly speaking the validity given in the original paper is violated.

Fig. 5.9(b) presents the resulting reflection coefficients of the experiments reported herein. At first, the 75 experiments were used for the graph, which excludes macro-roughness elements, in order to properly compare with results found in literature. The surf similarity parameter is referred to the deep water wave length in accordance with e.g. Madsen and Schäffer (2010) and is given by

$$\xi_\infty = \frac{\tan(\beta)}{\sqrt{H/L_\infty}} = \sqrt{\pi}\left(\frac{A_0}{h_0}\right)^{-1/2}\left(\frac{\Omega^2 h_0}{g\tan(\beta)^2}\right)^{-1/2} \tag{5.2.5}$$

where $L_\infty = gT^2/(2\pi)$ denotes the offshore wave length and under the assumption that the period T can be interpreted as a duration of the special wave event reading $T = 2\pi/\Omega$. The surf similarity parameter is calculated according to Eq. (5.2.5) and the reflection coefficients are calculated by means of the method of Baldock and Simmonds (1999). For the calculation two wave gauges were used in the even bottom section. For the first wave gauges the instantaneous pressure sensor is used *PRS_inst* and the second wave gauge is named *RWG_1*. For the sensor locations the reader is also referred to Fig. 3.9 and to Fig. A.2. The distance between the two gauges amounts to 19.465 m. Due to the fact that the methodology is in principle suitable to also capture reflections over sloping bathymetry, the bottom gradient is first adjusted at a very narrow angle for these calculations while it will be seen that the beach slope is used when the reflections over the beach are investigated. However the derivation of the methodology bases on the assumption of a small amplitude wave theory and on the assumption that reflectivity is concentrated on a rather short spread of the beach interacting with the approaching waves or the wave spectrum. Hence both assumptions do not fully apply to the given wave properties. As already mentioned the ratio of the wave length to the beach spread is high compared to short- or long crested wave spectra commonly applied to reflection analysis. Secondly the waves under investigation reveal non-linear properties. The Ursell parameter mentioned in

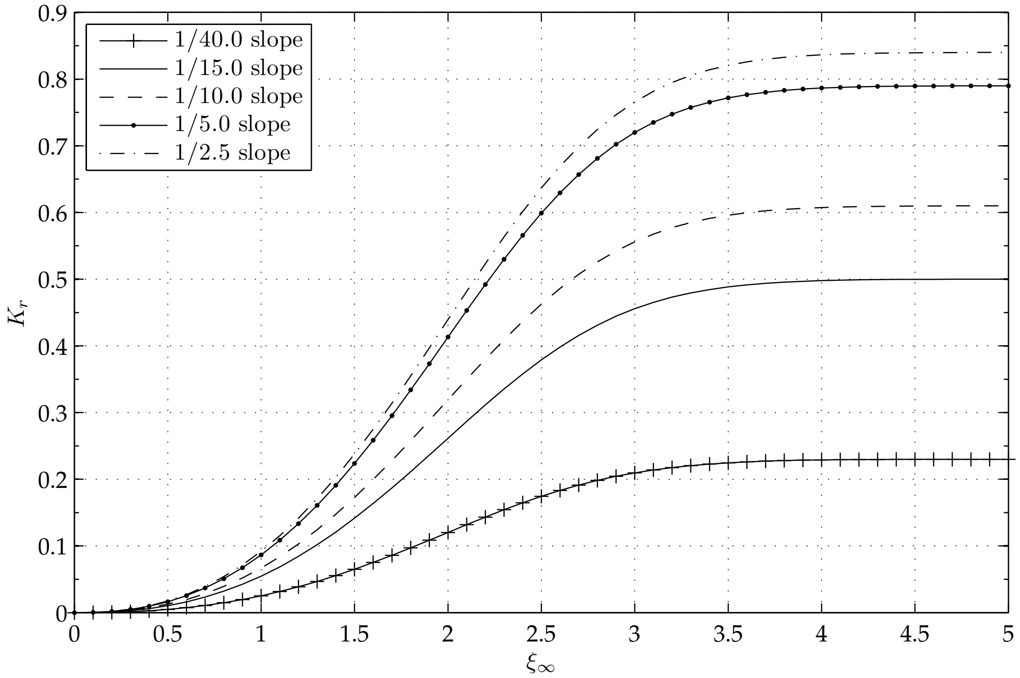

(a) Empirically fitted curves for different beach slopes according to Sunamura and Okazaki (1996)

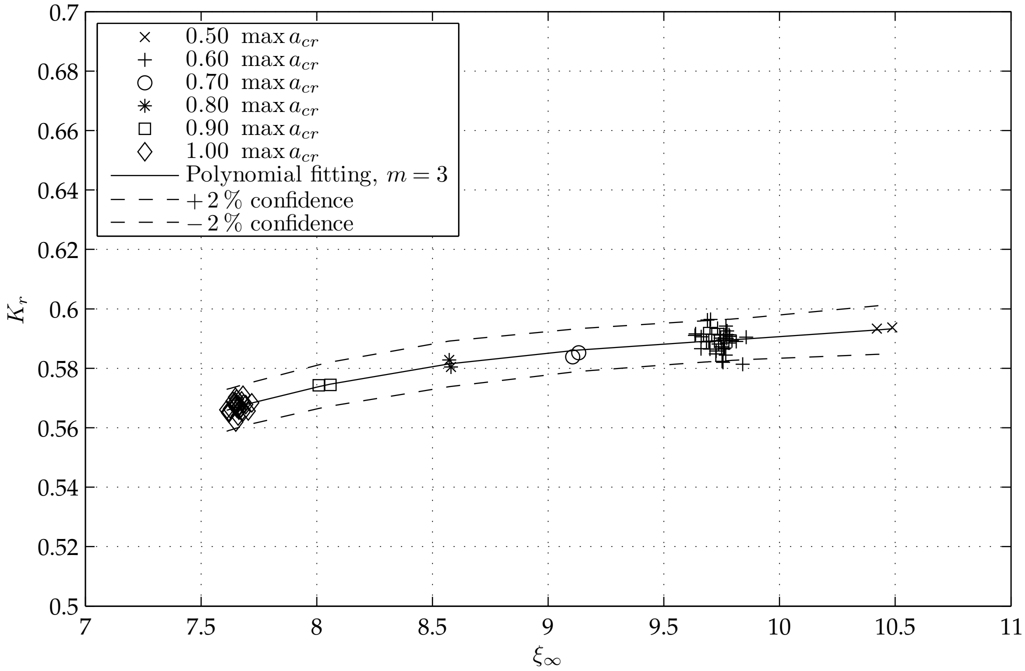

(b) Resulting reflection coefficients K_r in relation to the surf similarity parameter ξ_∞

Figure 5.9 Reflection of long waves at a mildly sloping beach of $1/40$ comparing to empirically fitted reflection relations for steeper beach slopes

Chapter 2.1 indicates how non-linear effects influence the wave motion ranges between $U = 10.7 \cdot 10^3$ and $U = 24.3 \cdot 10^3$ for the current study and thus calculations would generally benefit from the application of non-linear theory.

From Fig. 5.9(b) it is conveyed that the reflection coefficients are in the range of $K_r = 0.57$ to $K_r = 0.59$ for the experiments without investigating macro-roughness elements. The reflection coefficient decreases slightly with increasing wave heights as indicated by the factors given in the legend relating to the maximum amplitude used throughout the experiments. A curve fitting yields a polynomial of degree $n = 3$ fitting the data in a least square sense which reads for the data plotted in Fig. 5.9

$$\begin{aligned} p(x) = p_1 x^n + p_2 x^{n-1} + \ldots + p_n x + p_{n+1} = \\ -0.6605 + 0.3732x^1 - 0.0376x^2 + 0.0013x^3 \end{aligned} \quad (5.2.6)$$

Additionally, the 2% confidence intervalls of the described data set are plotted in order to demonstrate how well the data are distributed along the fitted curve. It is remarkable that most of the resulting reflection coefficients basing on the measurements are closely distributed in a tie, which in turn militates for a substantial quality of the wavemaker as well as for the suitability of the applied wave flume. A prerequisite is however, that one assumes that the reflectivity of the 180° bend plays a tangential role compared to the sloping beach investigated in the experiments. Important evidence to significant perturbations caused by the flume bend would be given when the velocity distribution in the cross-section directly at the end of the flume bend (which is also more or less at the toe of the beach wedge) would significantly deviate from uniformity at different time steps of single experiments. In this case one would have to conjecture that reflection and the general experimental behaviour could be biased by this specialty of the applied wave flume. Yet it has been clearly shown in Section 5.1.4 that the flow pattern for a distinct time step analysed over the flow depth and the cross-shore direction is homogenous and the velocity components perpendicular to the predominant flow directions are negligible. An influence of the flume bend can therefore be ruled out.

Furthermore it is also obvious that the reflection characteristics of mildly sloping beaches at least in the range of the surf similarity investigated in this study cannot be adequately described by means of existing empirical approaches. It is therefore vital for the process understanding to study the influence of the beach slope on the one hand and on the other hand a wider range of surf similarity has to be addressed in future studies. This includes inherently that experimental facilities which are able to cover the needed areal capacity and the adequate wavemakers are of immense importance.

Equivalently, analytical approaches commonly assume full reflectivity of the beach (e.g. Madsen and Schäffer, 2010). Obviously from an experimental point of view, if one maintains this assumption, it has to be exemplified why the analytically obtained solutions to a given run-up problem should hold true in real applications. It also has to be mentioned that the calculation of the reflection coefficient is generally linked to the assumption of absent bottom friction and dissipation of energy due to wave breaking. While the influence from the first assumption is kept to a minimum by using a PVC board as beach surface, the second assumption is uncritical because the waves of the utilized wave regime never broke during the experiments.

Once macro-roughness elements are placed on the beach the question arises how these elements affect the reflectivity of the shore and the resulting reflection coefficient in general. In order to answer this question a similar calculation was carried through to obtain the reflection coefficient with the remaining experimental data sets, consisting of 212 remaining runs. All of these data sets involve various macro-roughness element configurations. It appears that only the first macro-roughness element row contributes to the reflection process or when the configurations are in staggered arrangement then also the elements of the second row participate in the reflection. The main difference in the analyzed data is due to the fact that the cross-shore distances between the macro-roughness elements vary over the analyzed data set. Hence it is not detectable whether the reflection coefficients of configurations with high cross-shore obstruction ratios tend to be higher than those of lower cross-shore obstruction ratios. Fig. 5.10 reveals how the reflection coefficients are distributed according to the surf similarity.

The distribution in general follows the same trend that the results without the presence of macro-roughness elements show. The reflection coefficient increases with ascending surf similarity. Though the data are again fitted with a polynomial of degree $n = 3$ in a least square sense yielding the Eq. 5.2.7 below, it cannot be definitely concluded that the relation is by all means describable by a polynomial. For further insight it is strongly recommended to investigate the whole range of surf similarity, although this is beyond the scope of this work.

$$\begin{aligned} p\left(x\right) = p_1 x^n + p_2 x^{n-1} + \ldots + p_n x + p_{n+1} = \\ -0.1925 + 0.2368 x^1 - 0.0244 x^2 + 0.0008 x^3 \end{aligned} \qquad (5.2.7)$$

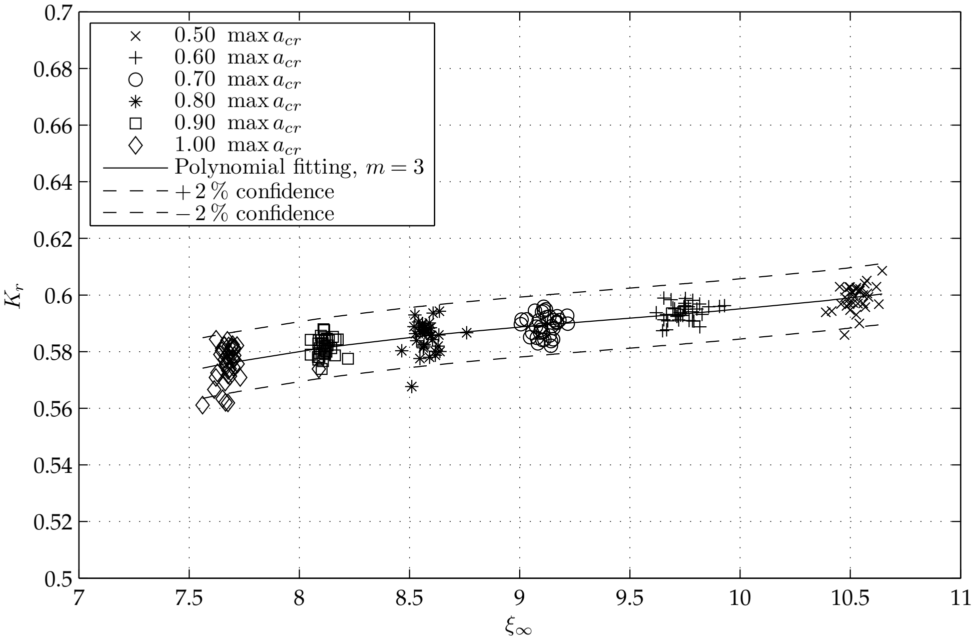

Figure 5.10 Resulting reflection coefficients K_r in relation to the surf similarity parameter ξ_∞ in regard to long waves at a mildly sloping beach of $1/40$ with reference to present macro-roughness elements on the shore

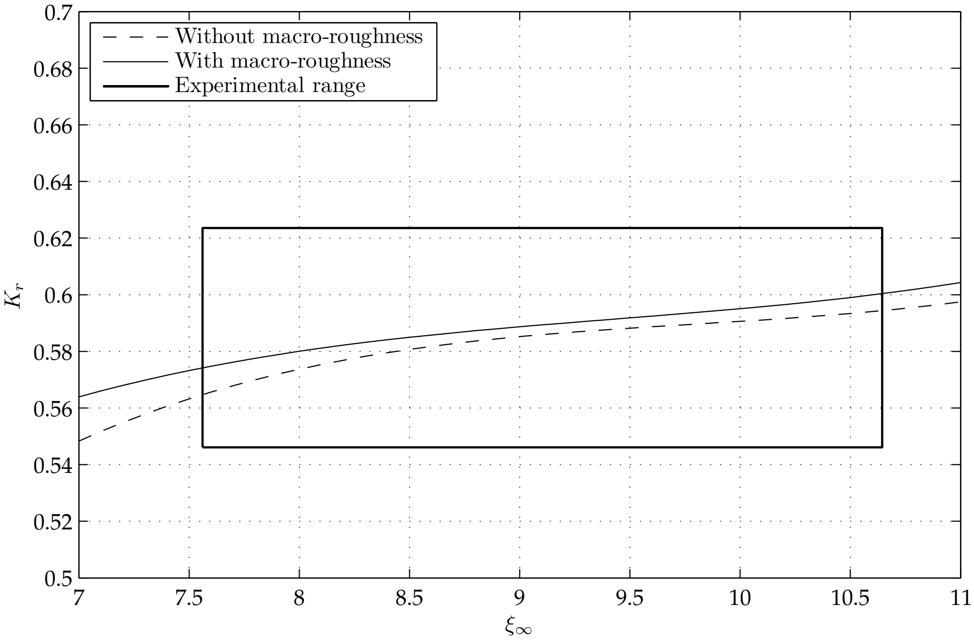

Figure 5.11 Comparison of the fitted polynomials with and without macro-roughness elements on the shore, K_r denotes the reflection coefficient and ξ_infty the surf similarity

The final comparison is on how the reflection coefficients differ when either macro-roughness elements are excluded from the run-up process or not. Fig. 5.11 depicts the polynomial fitting the reflection coefficient with and without macro-roughness elements for a $1/40$ shore. Additionally the experimental range is given by a box. It is apparent in principle that a difference exists. The difference increases the nearer the fitted curves are situated at the experimental range border, from which one might conclude that this is due to the polynomial fitting. A credible estimate of the influence which the macro-roughness element configurations add to the reflection coefficient can be drawn from the inner area of the experimental range. The difference amounts approximately to 1% of K_r. It becomes obvious that the difference is still within the calculated range of reflection coefficients. Consequently seen the influence of the macro-roughness elements tends to play only a minor role.

5.2.3 Summary and Conclusions

It was shown in the previous subsection that the calculated reflection coefficients for the conducted experiments range between $K_r = 0.57 - 0.62$ for the $1/40$ sloping beach under investigation. Furthermore no significant differences of the reflection coefficients were found originating from the presence of macro-roughness elements on the beach. The reflection coefficient was calculated by means of the method outlined by Baldock and Simmonds (1999). The assumption for the utilized methodology, which usually limits the applicability to short waves and wave spectra, however suggests that the resulting reflection coefficients have to be additionally justified by other means. The presented range of reflection coefficients is thus associated with the methodology and from the present knowledge it can not be eliminated that higher reflection coefficients are likely. For example, Madsen et al. (2008) show a reflection coefficient for a steep continental shelf region of $s = 1/5 - 1/20$ on the basis of a method by Mei et al. (2005) and calculate a reflection coefficient of $K_r = 0.68$ for a typical tsunami. This is already slightly higher than the values obtained for the reflectivity of the current beach. Higher values in the range of $K_r = 0.80$ are obtained when the threshold value accounting for singularities in the calculation is significantly decreased.

The marginal influence of the macro-roughness elements on the beach is unexpected and is clearly dedicated to the applied method. Without the experiments one could have reasoned that the macro-roughness elements onshore definitely contribute to the overall reflectivity of the beach. Hence a conclusive answer to this question is still pending. It firstly requires an accurate methodology to determine the reflection coefficient of long waves on mild sloping beaches. Secondly any other influences which are conceivably induced by the flume geometry have to be eliminated.

5.3 Long Wave Run-up on a Plane Beach

5.3.1 Run-up Results

In the following, the experimental run-up results are going to be presented. The objective of the section is to elucidate the run-up of long waves on a plane, $1/40$ sloping, impermeable beach. At first no macro-roughness elements are considered on the beach in order to evaluate the wave run-up without disturbing effects. The outcome of the analysis is then compared to existing theoretical approaches and to experimental results found in literature to assess the quality and to interlink the findings within the functional context.

The findings in Subsection 3.1.3 as an outcome of a dimensional analysis revealed the dependence of four non-dimensional terms to the plane long wave run-up. The focus of the current study first of all relates to the interaction of approaching long waves to macro-roughness elements on the beach. Hence it was not feasible to vary all the detected non-dimensional terms dealing with plane long wave run-up. In order to keep the task realizable the overall number of experiments was limited.

From Eq. (3.1.17), which lists the four dimensionless variables, the wave non-linearity and the wave steepness were varied. With reference to following statements, the three latter terms expressed in Eq. (3.1.17) can also be regarded as the surf similarity parameter, in which all dimensional terms are contained. It then reads

$$\frac{R}{a_0} = F\left(\frac{2a_0}{h_0}, \xi\right) \tag{5.3.1}$$

In the present study the wave period T and the beach slope β were not varied due to practical aspects of the experimental procedure. From the remaining non-dimensional terms at first the non-linearity of the wave should be related to the wave run-up. Fig. 5.12 depicts the maximum relative run-up R_{mean}/a_{cr} as a function of the non-linearity $\epsilon = a_{cr}/h_0$ of the investigated waves. Here the maximum relative run-up is defined as the average of the measured run-up outlined in Subsection 3.3.4. The general trend of the measured data set is expressed by the polynomial fit of the degree $n = 1$ which basically reduces to a linear function.

The maximum relative run-up is always given relatively to the amplitude of the wave crest a_{cr} at the positive pump-station inlet to assure comparability of the data. Though the measured run-up data show up in a certain range, the overall trend is inevitably present. The distribution of the measured run-up data indicates repeatability of the experiments in general although optimizations of the experimental procedure are surmisable, as already discussed in Section 4. It is also obvious that the relative run-up related to the positive crest amplitude is remarkably high. It ranges between $R_{mean}/a_{cr} = 3.1 - 3.4$. It will be seen in the following that on the one hand these values are far higher than previous experimental results derived for commonly applied solitary waves and on the other hand it agrees well with the analytical theory.

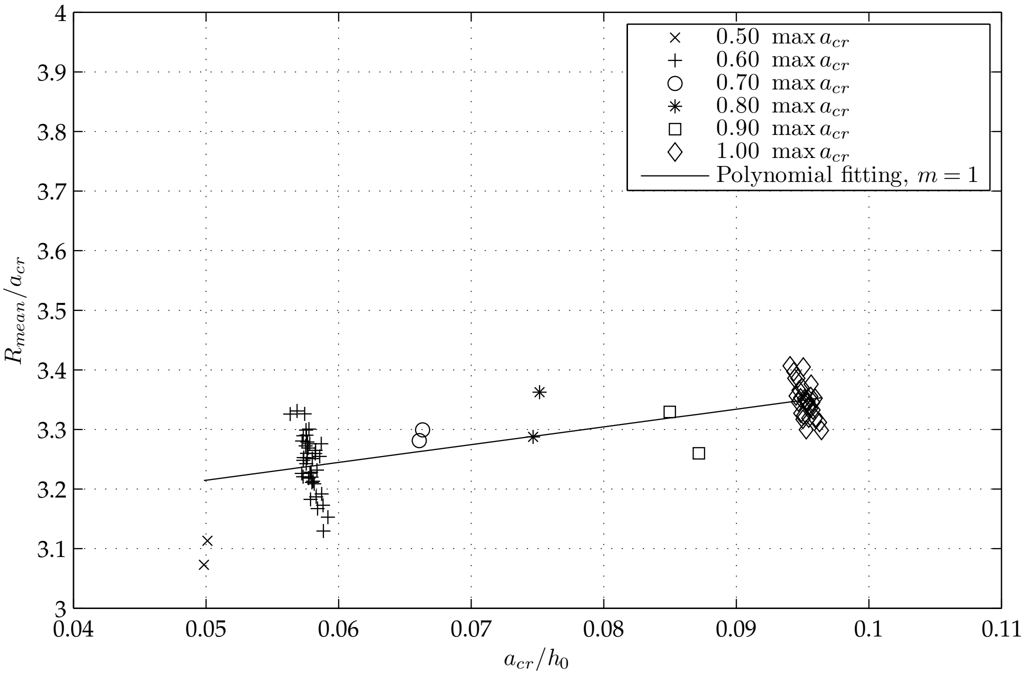

Figure 5.12 Maximum relative run-up as a function of the non-linearity ϵ of the waves depicted by the markers, a linear polynomial fit denotes the increase in maximum run-up with increasing non-linearity

Secondly, a similar function is found for the relation between the maximum relative run-up to the (local) wave steepness as presented in Fig. 5.13. In contrast to the wave length ξ_∞ used for the definition and the calculation of the surf similarity parameter, the local wave steepness derived from the conjugated wave length L_0 and the amplitude of the wave crest a_{cr} is related to the relative maximum wave run-up. On the basis of the underlying data set a linear functional relation is similarly given. Yet it is not clear if the relation holds true for a greater range of non-linearity or wave steepness because this is beyond the experimental data range. The answer to this specific question therefore remains unanswered.

The two remaining non-dimensional terms given by Eq. (5.3.1) cannot be related to the wave run-up without conducting additional experiments which vary the wave period and the beach slope. Yet Madsen and Schäffer (2010) analytically derived a theoretical formula which incorporates the non-dimensional terms found in the dimensional analysis delineated in Subsection 3.1.3. In the following a comparison with this existing theory should bring to light the validity of the theoretical approach in context with the experimental data.

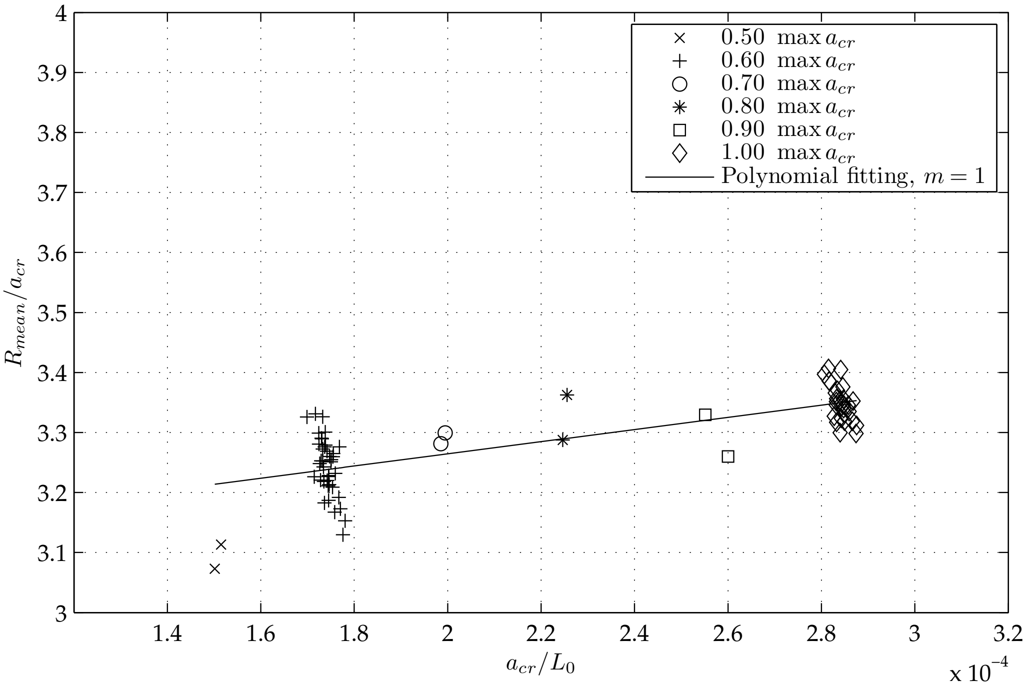

Figure 5.13 Maximum relative run-up as a function of the wave steepness s depicted by the markers, a linear polynomial fit denotes the increase in maximum run-up with increasing wave steepness

5.3.2 Past Experiments and Theoretical Approaches

Fig. 5.14 presents the maximum relative wave run-up in the framework of the surf similarity parameter, whose relation to the wave run-up was in principle already outlined by Hunt (1959). Eq. (2.1.28) represents a functional relation which suits the conditions claimed in Eq. (5.3.1) as a result of the dimensional analysis. The derivation of the functional analysis originates from Madsen and Schäffer (2010). In the following it will be shown that the experimental data of the long waves climbing up the investigated beach agree well with the analytical approach.

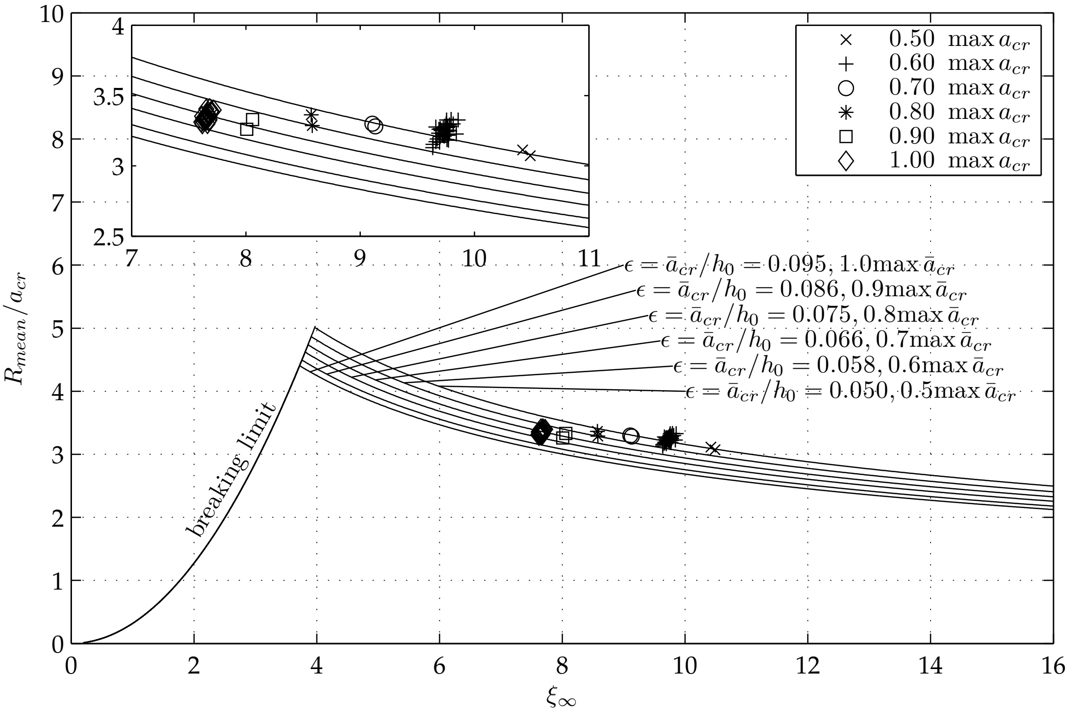

Figure 5.14 Maximum relative run-up as a function of the surf similarity parameter ξ_∞ depicted by the markers and according to the wave conditions applied, the theoretical breaking limit given by Eq. (5.3.2) and the theoretical run-up functions given by Eq. (2.1.28) (Madsen and Schäffer, 2010) basing on the non-linearity ϵ. The inset zooms to the experimental data.

As shown in Fig. 5.14 the maximum relative run-up, which is normalized by the positive amplitude at the wavemaker, decreases with an increasing surf similarity parameter ξ_∞. The increase in non-linearity, which can be expressed as the ratio of the applied wave amplitude of the crest a_{cr}/h_0, reduces the surf similarity of the applied wave condition at the beach under investigation. Higher non-linearity of the wave also indicates higher energy content. This finding underlines the statement of Madsen and Fuhrman (2008) where critical flow depth and flow velocities occur for surf similarity in the order of $\xi_\infty = 3 - 6$ and in turn require relatively mild beach slopes.

$$\frac{R^{limit}}{a_0} = \frac{\chi_{elev}\chi_{break}}{\pi}\xi_\infty^2 \tag{5.3.2}$$

Additionally, the theoretically derived formula by Madsen and Schäffer (2010) for the breaking limit and the functional relation of the surf similarity to the maximum relative run-up of sinusoids approaching a sloping beach is drawn to relate the experimental data to the theory. The breaking limit, which could be expressed by Eq. (5.3.2), occurs at the point of maximum run-down of the wave. The values of $\chi_{elev} = 2\sqrt{\pi}$ and $\chi_{break} = 2\sqrt{\pi}^{-1}$ are in accordance with the numerical values given in the original paper. The values of $\chi(\mu)$ are more generally a function of the amplitude ratio $\mu = a_2/a_1$ which for example is capable of incorporating N-waves as formerly introduced by Tadepalli and Synolakis (1994). The breaking limit increases parabolically with the surf similarity parameter.

The functional relation of surf similarity to the maximum relative run-up was computed on the basis of Eq. (2.1.28), where the non-linearity of the measured waves was averaged over the number of experiments classified in the six groups of waves (cp. Subsection 5.1.1). The resulting curves are in good agreement with the point clouds of the relative wave run-up found in the experiments. Yet it is apparent that the results do not perfectly fit the expected analytical behavior even though the results already indicate that the theory and the functional relation of the non-dimensional terms is well established. The analytical approach neglects the influence of roughness fully and the experiments aim at eliminating roughness influences to the greatest extent within the limitations of model and scale effects as illustrated in Subsection 3.1.3. Hence besides these possible biasing factors it also has to be considered that the theoretical approach reckons the approaching waves at the beach toe to be linear. But in fact it is obvious that non-linear effects are already most likely to contribute to the physical process to some extent not only because the Ursell parameter is $\mathcal{O}\left(10^4\right)$. Therefore non-linear effects also have to be taken into account.

For clarification of the general agreement between the analytical and experimental results, the theoretical maximum wave run-up can exemplarily be computed with the following parameters taken from an experiment with the smallest non-linearity. While the wave parameters were derived from experiments which are scaled in Froude similitude, for the computation and for the sake of compatibility to prototype, all wave parameters measured in the laboratory are subsequently transformed back into prototype scales. The following shall be considered: a water depth in the region of constant water depth of $h_0 = 30.0$ m, a beach slope of $\gamma = 1/40$, $c_0 = \sqrt{gh_0} = 17.2$ m/s. The waveform could be characterized as a sinusoidal wave with $A_0^{\text{trough}} = 1.5$ m, $A_0^{\text{crest}} = 1.5$ m and $T = 660$ s. The angular frequency defined as a duration according to Madsen and Schäffer (2010) yields $\Omega = 2\pi/T = \pi/330$ 1/s. The surf similarity parameter according to Eq. (2.1.27) (see Eq. 6.5 in Madsen and Schäffer, 2010) becomes

$$\xi = \sqrt{\pi}\left(\frac{1.5}{30}\right)^{-1/2}\left(\frac{\left(\frac{\pi}{330}\right)^2 30}{g\cdot(1/40)^2}\right)^{-1/2} = 11.9 \tag{5.3.3}$$

The theoretical run-up is then determined by assuming that $\chi_{elev} = 2\sqrt{\pi}$. (see Eq. 6.6 in Madsen and Schäffer, 2010). It reads

$$R_{\text{up}} = 1.5\cdot 2\sqrt{\pi}\pi^{1/4}\left(\frac{1.5}{30}\right)^{-1/4}\cdot 11.9^{-1/2} = 4.34 \text{ m} \tag{5.3.4}$$

Experimentally, the run-up according to the above outlined wave conditions was determined to be in the range of $R_{min} = 4.65 \text{ m} - R_{max} = 4.85 \text{ m}$ for the wave in prototype scale with a very good reproducibility (error $\approx 3-4\%$) when experiments were repeated. The amplification factor yields ≈ 2.89. Lower and upper bound of the maximum run-up is again due to cross-shore variations of the moving shoreline (cp. Subsection 3.3.4). Results of the analytics and the experimentals are therefore in good agreement however the experimental set-up overestimates the theoretical results by approximately 10%. In analogy to Li and Raichlen (e.g. 2001) for solitary wave run-up, it can additionally be concluded that non-linearity contributes to the maximum run-up, though only to second order.

$$\frac{R_{\text{up/down}}}{A_0} = \chi_{\text{elev}}\pi^{1/4}\left(\frac{A_0}{h_0}\right)^{-1/\left(4+\epsilon^{2/3}\right)}\xi^{-1/\left(2+\epsilon^{2/3}\right)2} \tag{5.3.5}$$

In a similar manner Eq. (5.3.5) relates the surf similarity parameter to the maximum relative run-up. As seen distinctly from the original equation of Madsen and Schäffer (2010), the non-linearity ϵ is now stronger influencing the relative run-up.

In Fig. 5.15 the modified functional relation of Eq. (5.3.5) is plotted. Again the breaking limit of Eq. (5.3.2) constitutes the lower bound of the surf similarity where non-breaking waves occur. In contrast to the original relation it is apparent that the experimental results are matched even closer to the theoretical predictions. The chosen modification of the run-up equation is yet found on the basis of trial and error in order to fit the predictive equation with the experiments. Further experiments and a derivation of the fundamental dependencies under consideration of non-linear waves at the beach toe could help facilitating further insight.

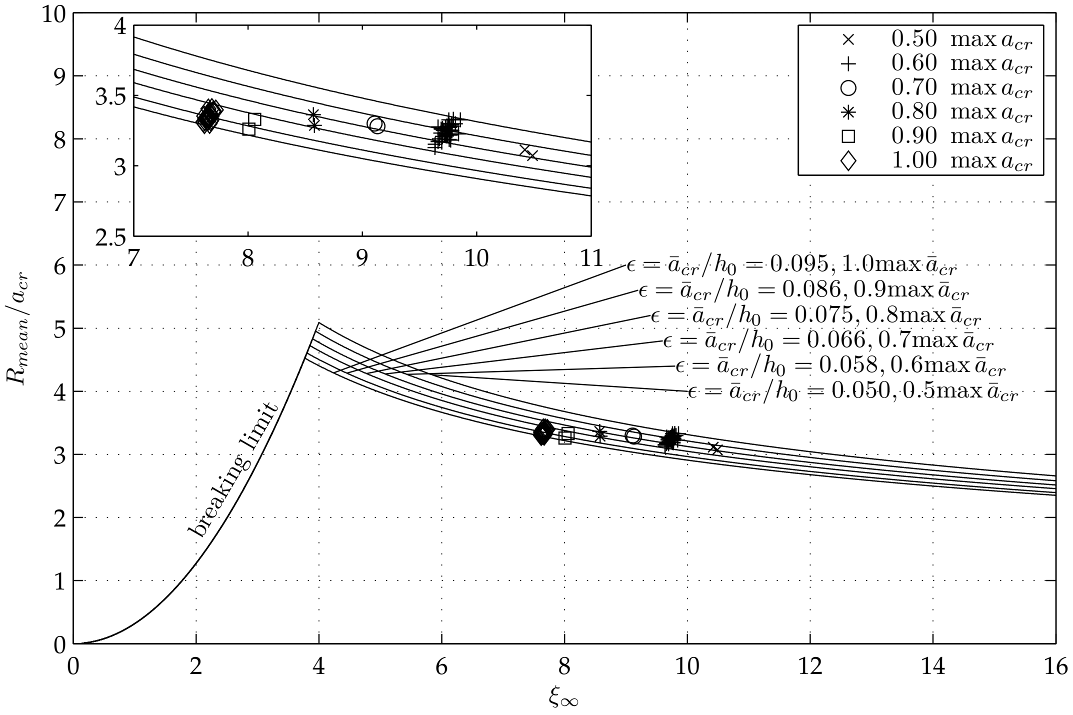

Figure 5.15 Maximum relative run-up as a varied function of the surf similarity parameter ξ_∞ depicted by the markers and according to the wave conditions applied, the theoretical breaking limit given by Eq. (5.3.2) and the theoretical run-up functions given by Eq. (5.3.5) basing on a variation of the original formula. The inset zooms to the experimental data.

Next a comparison of the run-up data with experimental results of Synolakis (1987), who utilized solitary waves, are presented. As proposed by a variety of researchers in the past, solitary waves are believed to adequately model disastrous effects of tsunami (cp. e.g. Goring, 1979; Li and Raichlen, 2001). In order to discuss solitary wave run-up and the run-up of periodic waves which are used in this thesis, the maximum relative run-up is related to both the non-linearity and to the relative wave length. This aims at comparing with the parameters ϵ, μ forming the Ursell parameter U.

Firstly, Fig. 5.16 shows the run-up results of periodic waves on a $1/40$ sloping beach in comparison to solitary wave run-up to a $1/19.85$ sloping beach published by Synolakis (1987) as well as the run-up of periodic waves to a beach slope of $1/20$ (Goseberg and Schlurmann, 2010) in relation to the non-linearity ϵ. While for the sinusoidal, periodic waves the maximum relative run-up is normalized by the positive wave amplitude at the wavemaker denoted by R_{mean}/a_{cr} it is common to use the wave height H for solitary waves. The numerical values for Synolakis (1987) experiments were digitized from the original tables and presented in the electronic version of the PhD thesis.

During the experiments addressing periodic long wave run-up either to a $1/20$ (Goseberg and Schlurmann, 2010) or $1/40$ sloping beach it becomes obvious that these waves never break during the experimental procedure whereas the solitary waves show a much earlier breaking limit, ranging around $\epsilon \leq 0.055$. Secondly, for the results compiled by Goseberg and Schlurmann (2010) a reasonable agreement with the breaking solitary waves can be determined. The few unique measurements of real tsunami in the prototype allow for the conclusion that the non-linearity of the waves is in the range of the investigated wave addressed in the cited laboratory studies. Yet it is problematic to solely tie the similitude of tsunami in the prototype to the non-linearity. A comparison of the experiments, incorporating $1/20$ beach slopes with the current $1/40$ experiments, further delineates the effect of the slope angle and appears to influence the wave run-up to first order. It seems that the relative run-up increases with decreasing beach slopes. From the narrow band of non-linearities investigated in the current study it can be concluded that the maximum relative wave run-up increases with increasing non-linearity for the $1/40$ beach slope. This is in contrast to the observation that solitary wave run-up in tendency decreases rapidly with increasing non-linearity due to wave breaking induced energy dissipation.

In the following, the relation between the relative run-up and the dimensionless wave length is assessed. Fig. 5.17 displays the same experimental data as presented before plus the currently presented data in relation to the relative wave length μ^{-1}. To be fair in all cases the local wave length L_0 was calculated. For the case of the solitary waves and in analogy to the wave length definition of short waves the solitary wave length, which is infinite by theory, can be specified sufficiently by Eq. (5.3.6)

$$L_s = \frac{2\cosh^{-1}(10)}{k} = \frac{2\cosh^{-1}(10)}{\left(\sqrt{\frac{3H_0}{4h_0^3}}\right)} \tag{5.3.6}$$

where the relative wave height is reduced to $h_0/H_0 = 0.01$ and where therefore the surface displacement is already reduced to a negligible numerical value. Similarly the wave length of the periodic waves is computed by means of the relation $L_0 = cT$, where the period T is taken from the measured time series at the wavemaker. In

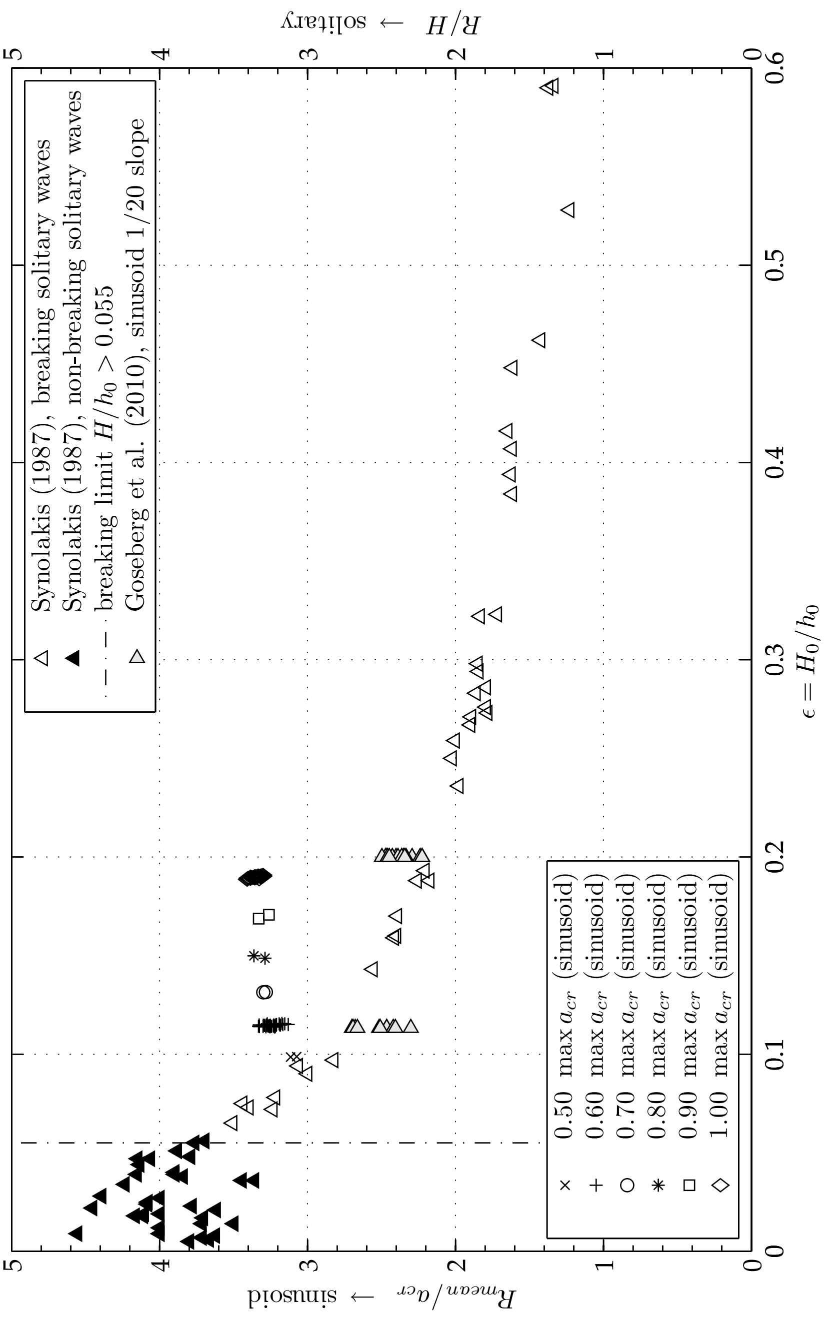

Figure 5.16 Maximum relative run-up as a function of the non-linearity $\epsilon = H_0/h_0$, own periodic wave run-up results are depicted by the markers given in the lower left legend while the solitary wave run-up is flagged by the upward pointing triangles, dash-dotted line denotes the breaking limit of solitary waves (Synolakis, 1987), the 1/20 beach slope experiments by Goseberg and Schlurmann (2010) are indicated by the rightward pointing triangles respectively.

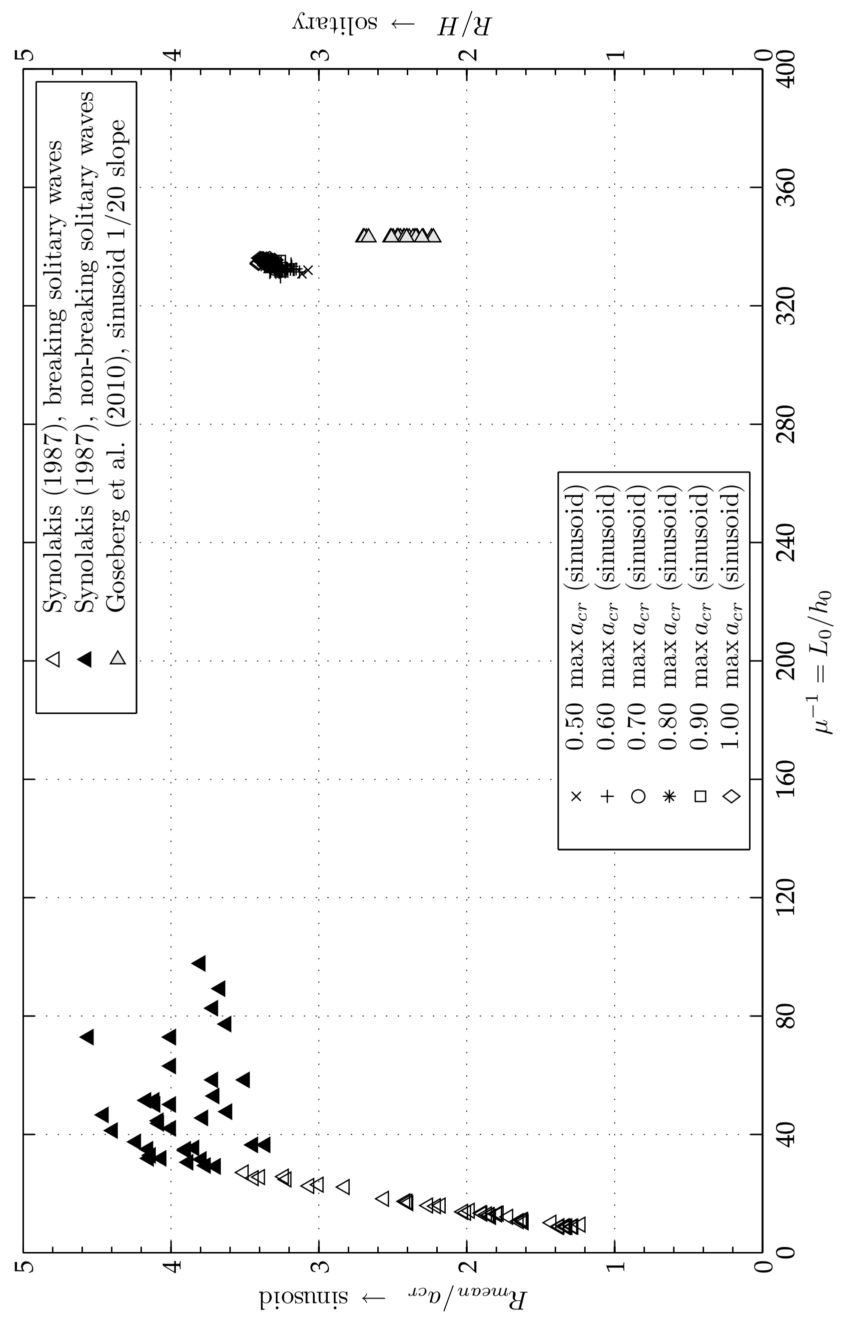

Figure 5.17 Maximum relative run-up as a function of the relative wave length $\mu^{-1} = L_0/h_0$, periodic wave run-up results on a $1/40$ beach are depicted by the markers given in the lower left legend while the solitary wave run-up is flagged by the upward pointing triangles (Synolakis, 1987), the $1/20$ beach slope experiments by Goseberg and Schlurmann (2010) are indicated by the rightward pointing triangles respectively.

contrast to the comparison basing on the non-linearity (Fig. 5.16), it turns out that the maximum relative run-up of the periodic waves is not associated with the resulting run-up of solitary waves even though the non-linearity is rather similar. The relative wave length of the periodic waves is a few times higher than the wave length of the solitary waves.

Wu (1981) described the characteristics of long waves in the ocean and in coastal waters. His argumentation bases on fundamental non-dimensional parameters such as the non-linearity of the wave, the non-dimensional wave length and the Ursell number. For tsunami in coastal water it hence becomes clear that the Ursell number, which is thought of to be smaller than unity in water depth of the deep ocean, rapidly increases to order of $\mathcal{O}\left(\geq 10^3\right)$ in coastal waters. Generally the Ursell number is proportional to $U \sim h^{-9/4}$. Actual echo soundings during the disastrous tsunami incident in the Indian ocean in the year 2004 recorded by the yacht Mercator, which anchored at the southwestern tip of Phuket, Thailand, offered the chance to estimate the local Ursell parameter in the region of interest ($h_0 = 14.0 \text{ m}$, $H_0 = 5.0 \text{ m}$, $T = 13.0 - 14.0 \text{ min}$). The local wave characteristics suggest Ursell parameter in the order of $\mathcal{O}\left(\geq 10^5\right)$, where e.g. $\mu = 14 \text{ m}/\left(\sqrt{9.81 \text{ m/s}^2 \cdot 14.0 \text{ m}} \cdot 840 \text{ s}\right) = 1.42 \cdot 10^{-3}$ denotes the dimensionless wave length and $\epsilon = 2.5 \text{ m}/14.0 \text{ m} = 0.18$ yielding a Ursell number of $U \approx 8.8 \cdot 10^5$. With reference to the Fig. 5.16 and 5.17 it can be shown that the usage of the solitary wave type is questionable at least for the purpose to model near-shore effects of tsunami generated by sudden displacements of the sea floor. The local Ursell parameter of the solitary waves usually generated in the laboratory is in $\mathcal{O}\left(\geq 10^2 - 10^3\right)$. Solitary waves exhibit a far too small Ursell parameter to be adequately compared with tsunami in the prototype. In contrast the applied sinusoids are found to be $\mathcal{O}\left(\geq 10^4 - 10^5\right)$ and are therefore genuinely capable of mimicking the impact of tsunami in shallow coastal waters and to coastal urban areas.

5.3.3 Summary and Conclusions

The run-up of long waves on a plane, $1/40$ sloping beach has been addressed in this section. The relative run-up appears to be a linear function of both the non-linearity and the steepness of the wave. By means of the proposed wave generation technique, repeatable and plausible run-up results are obtained.

Moreover, it turns out that the experimental run-up data agree well with the theoretical formula derived by Madsen and Schäffer (2010) which relate the relative run-up to the surf similarity parameter ξ_∞. For the first time, it becomes possible to validate this theoretical approach to deal with long wave run-up. It depicts a paradigmatic change in the field of long wave and tsunami research. This theory overcomes the solitary wave paradigm towards arbitrary long wave representations and hereby adequately models the geophysical time and length scales of prototype tsunami incidents more adequately.

The validation reveals that the theoretical approach holds true for the experimentally investigated case of sinusoidal long waves climbing up a beach of constant slope. Furthermore, with increasing non-linearity of the waves a supplement to the exponents of the Eq. (5.3.5) was found, which empirically fits the recorded run-up data even better.

In contrast to solitary waves, the applied sinusoidal waves are found to mimic tsunami in prototype much more realistically. While the non-linearity of commonly applied solitary waves is in a similar range compared to the analyzed sinusoidal waves, the dimensionless wave length μ of solitary waves underestimates the dominant character of real tsunami by an order of magnitude. It appears that the applied sinusoidal waves addressed herein do not break at all, whereas the solitary waves of similar non-linearity always break during the wave run-up process. Wave breaking is known to result in an effective energy dissipation. In turn, breaking waves exhibit less energy for the run-up process. The run-up of the utilized sinusoidal waves therefore contains much more energy because no wave breaking occurs. Hence the sinusoidal waves are more likely to reveal the prototype conditions in terms of near-shore flow velocities and forces. Additionally, the effective duration of the wave run-up process is far longer than for solitary waves of the same non-linearity, which in turn also argues for the utilization of the applied sinusoidal waves.

5.4 Long Wave Run-up Influenced by Macro-Roughness

The following section is going to analyze the given objective of the interaction of long tsunami-like waves with the proposed macro-roughness element configurations and the alleged reduction of the relative run-up due to the obstruction imposed by the macro-roughness elements. From the dimensional analysis four non-dimensional terms were determined which contribute to the interaction of long wave run-up in the presence of macro-roughness elements. It is therefore essential to analyze the run-up reduction which is a priori assumed with regard to the variable Γ, the ratio of cross-shore obstruction ψ_{cs}, the ratio of long-shore obstruction ψ_{ls} and the ratio of obstructed height ψ_{mr}. Therefrom it can be deduced how significant each of the terms is to the wave run-up reduction. During the analysis it became apparent that a holistic approach describing all of the studied macro-roughness configurations is not possible. Hence the analysis bases on the assumption that characteristic urban pattern results in associated wave-structure interaction. Tab. 5.3 lists the labeled macro-roughness configurations $\Gamma = 1 - 4$.

Table 5.3 Macro-roughness element configurations investigated with respect to the run-up of long waves

Γ	Arrangement	Element angle φ
1	aligned	$0°$
2	aligned	$45°$
3	staggered	$0°$
4	staggered	$45°$

5.4.1 Cross-Shore Obstruction Ratio

The relative run-up of long waves normalized by the positive wave amplitude at the wavemaker is shown in the Figs. 5.18, 5.19, 5.20 and 5.21 as a function of the cross-shore obstruction ratio according to the macro-roughness element configurations listed in Tab. 5.3. The cross-shore obstruction ratio is given by Eq. (3.1.11a) and an obstruction ratio of unity denotes full cross-shore obstruction. The entire set of tested configurations is given in the Annex B.

The first configuration $\Gamma = 1$ (Fig. 5.18) comprises macro-roughness elements in aligned arrangement with non-rotated elements. The resulting run-up reduction can generally be described by a downward opening parabolic function. Two of the experiments belonging to the macro-roughness configuration presented in Fig. 5.18 were excluded from the analysis because the deviation from the average run-up appeared to be unphysical. The experiments with $\Gamma = 1$ were comprised of four different cross-shore obstruction ratios. The long wave run-up diminishes with increasing ψcs. Tendentially it can be seen that the influence of the incident wave amplitude indicated by the marker symbols increases with a growth of the cross-shore obstruction ratio. Higher wave amplitudes at the wavemaker automatically result in higher water levels in the vicinity of the macro-roughness area. The reason for the greater influence of the wave amplitude, with increasing cross-shore obstruction ratios, could be that higher velocities in the streets result in subsequently higher energy exchange between the predominant flow in the streets and the calmed areas in the back of the macro-roughness elements. Acceleration between wooden pillars and eddies in the back of the pillars were similarly reported and described by Goto and Shuto (1983) who investigated the effects of wooden pillars exposed to a steady flow. A comparison between the three different numbers of macro-roughness rows is presented after the remaining three macro-roughness element configurations are presented and discussed.

The second configuration $\Gamma = 2$ (Fig. 5.19) comprises macro-roughness elements which are again in aligned arrangement, but in this case the elements are rotated. According to the definition of the cross-shore obstruction ratio (Eq. (3.1.11a)), the macro-roughness element angle φ increases the obstruction ratio for a fixed distance of the macro-roughness elements. It ranges between $\psi_{cs} = 0.38 - 0.74$. Also it is obvious that only three street widths are feasible due to the limitation of the flume width. In contrast to the previous configuration $\Gamma = 1$ the polynomials, which are fitted in a least square sense to the experimental data, are less curved. Generally the run-up is reduced more in the case of rotated macro-roughness elements than in the non-rotated case. This observation can be related to the fact that oblique reflections occur at the front faces of the macro-roughness elements. The reflected flow directly interferes with the flow which has to pass the remaining space in-between the elements. This feature is also discussed in the context of the flow measurements described in Sec. 5.5.

This interaction between the main flow and the reflected flow portions results in greater energy loss. It is apparent also - again due to the interaction of main and reflected flow portions - that the influence of the wave amplitude increases with increasing cross-shore obstruction.

The third configuration $\Gamma = 3$ (Fig. 5.20) comprises macro-roughness elements in staggered arrangement with non-rotated elements. The cross-shore obstruction ratio ranges, similar to the aligned case, between $\psi_{cs} = 0.5 - 0.8$. Staggered arrangements are by definition only possible for more than one macro-roughness row $n > 1$. Hence only the variations with $n = 5, 10$ are presented in Fig. 5.20. In general, the run-up of long waves interacting with staggered macro-roughness configurations is reduced compared to aligned configurations. The run-up reduction again increases with increasing wave amplitude of the investigated long waves. The measured range of relative wave run-up, with reference to the wave amplitudes, is essentially greater when compared to the aligned configurations with either $\varphi = 0°$ or $45°$. A reason for this observation could be the circumstance that the maximum run-up extent the beach can only be reached by the flow after it was multiply redirected and decelerated by the macro-roughness elements. An increase in energy loss is hence the consequence. Whereas in the case of the aligned configuration at least a portion of the cross-shore

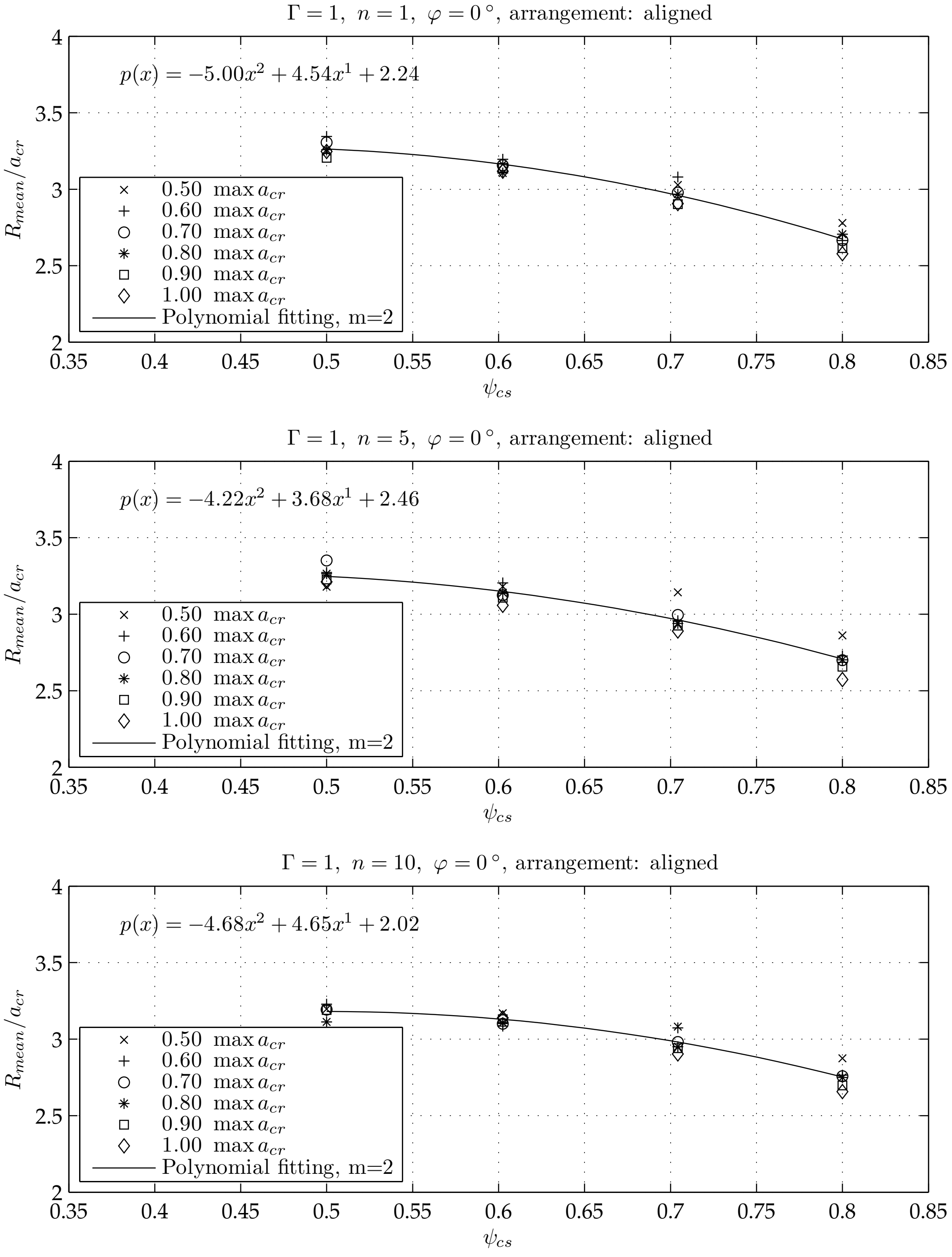

$\Gamma = 1,\ n = 1,\ \varphi = 0\,^{\circ}$, arrangement: aligned

$p(x) = -5.00x^2 + 4.54x^1 + 2.24$

$\Gamma = 1,\ n = 5,\ \varphi = 0\,^{\circ}$, arrangement: aligned

$p(x) = -4.22x^2 + 3.68x^1 + 2.46$

$\Gamma = 1,\ n = 10,\ \varphi = 0\,^{\circ}$, arrangement: aligned

$p(x) = -4.68x^2 + 4.65x^1 + 2.02$

Figure 5.18 The relative wave run-up R_{mean} as a function of the cross-shore obstruction ratio ψ_{cs}, $\Gamma = 1$. The experimental data are fitted to a polynomial of degree $m = 2$ and the equations are given according to the investigated number of macro-roughness rows $n = 1, 5, 10$

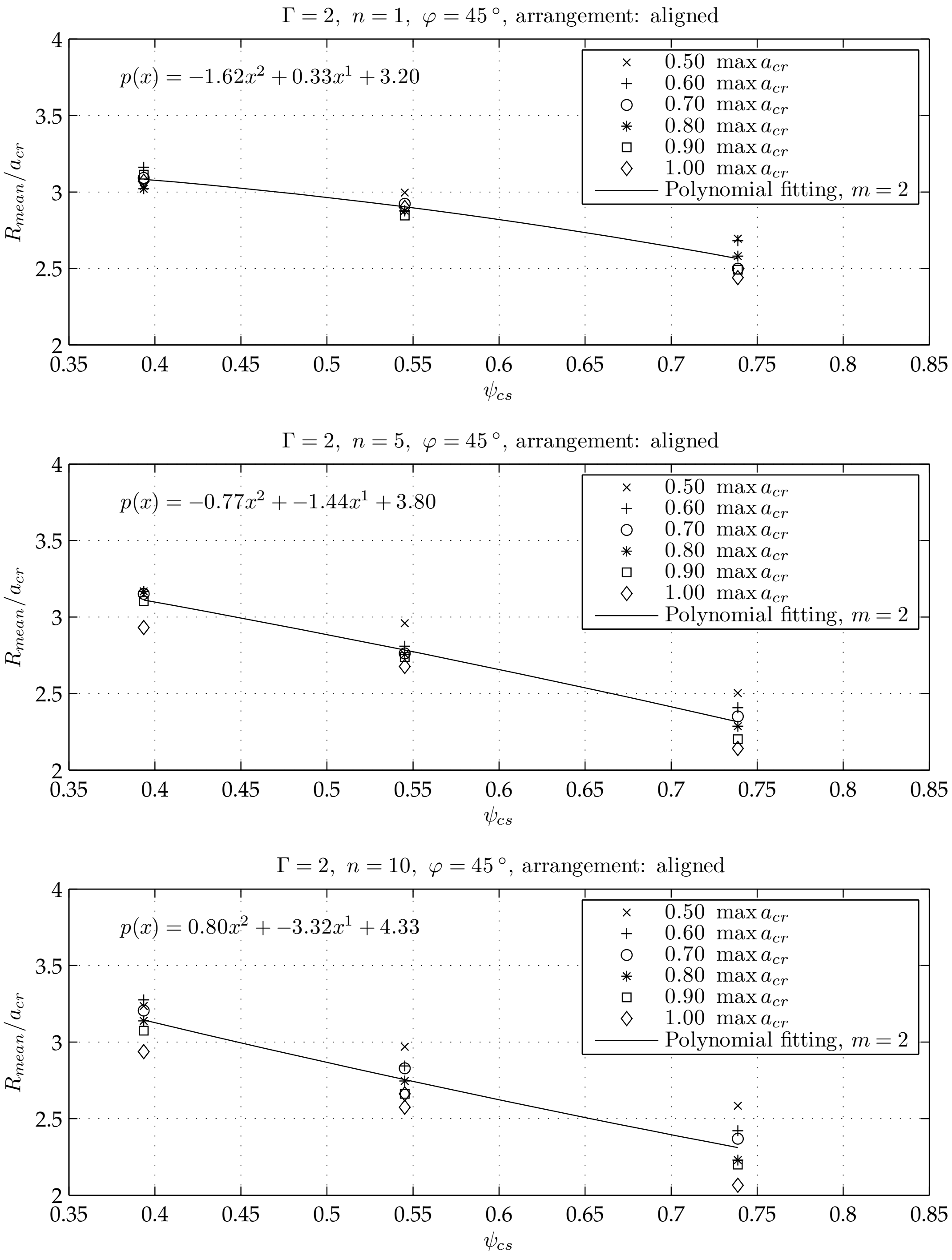

Figure 5.19 The relative wave run-up R_{mean} as a function of the cross-shore obstruction ratio ψ_{cs}, $\Gamma = 2$. The experimental data are fitted to a polynomial of degree $m = 2$ and the equations are given according to the investigated number of macro-roughness rows $n = 1, 5, 10$

distance is always left open where the flow can propagate onshore, disturbed only by the sudden narrowing and widening.

Soares-Frazão et al. (2008) qualitatively found the same flow pattern (sudden narrowing, widening and deceleration) in the case of a flood wave impinging a urban settlement of houses which are arranged in aligned and staggered configuration.

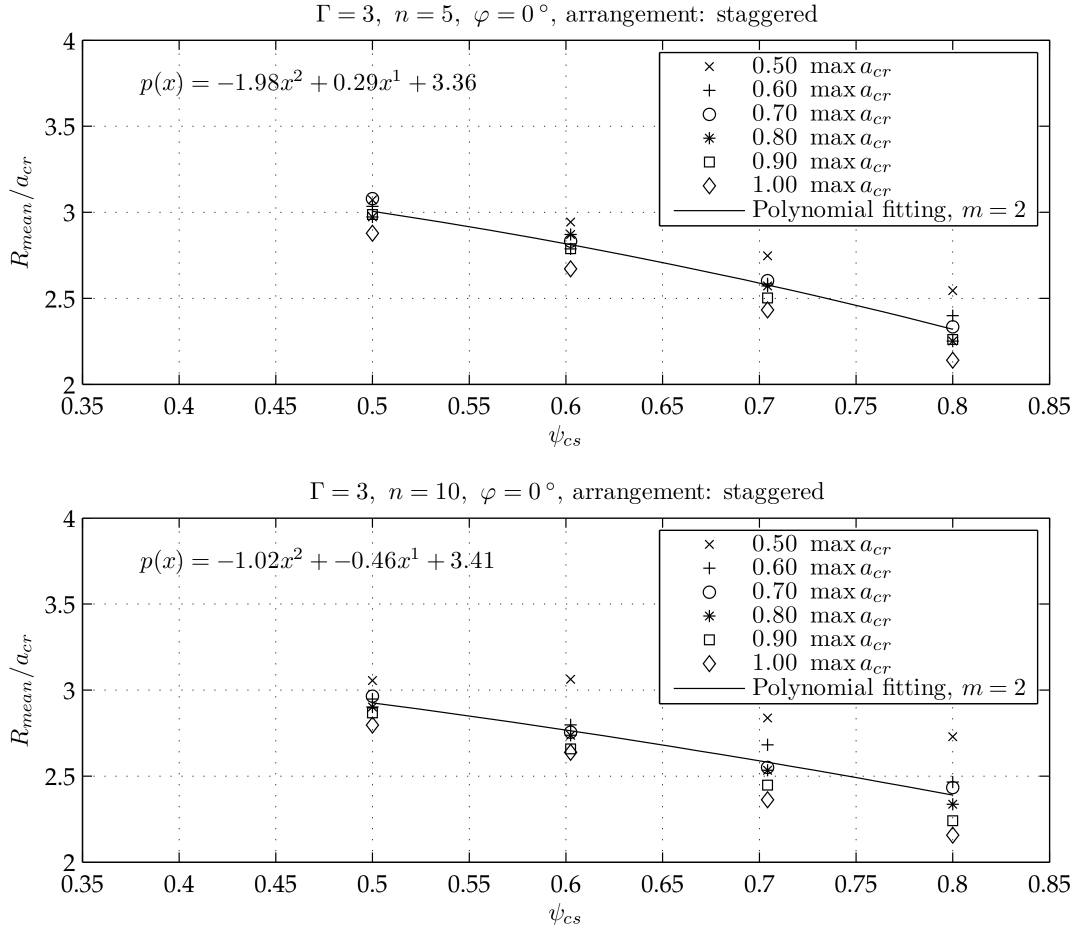

Figure 5.20 The relative wave run-up R_{mean} as a function of the cross-shore obstruction ratio ψ_{cs}, $\Gamma = 3$. The experimental data are fitted to a polynomial of degree $m = 2$ and the equations are given according to the investigated number of macro-roughness rows $n = 5, 10$

The fourth configuration $\Gamma = 4$ (Fig. 5.21) comprises macro-roughness elements which are again in staggered arrangement, but in this case the elements are rotated by the angle $\varphi = 45°$. The functional dependency is similar to the three previously discussed configurations. A parabolic polynomial is suitable to fit the measured data. The run-up reduction is higher than in the staggered, non-rotated case. An explanation for the higher run-up reduction is the oblique reflection of the approaching wave and the associated flow at the front walls of the macro-roughness elements which interacts with the main portion of the flow.

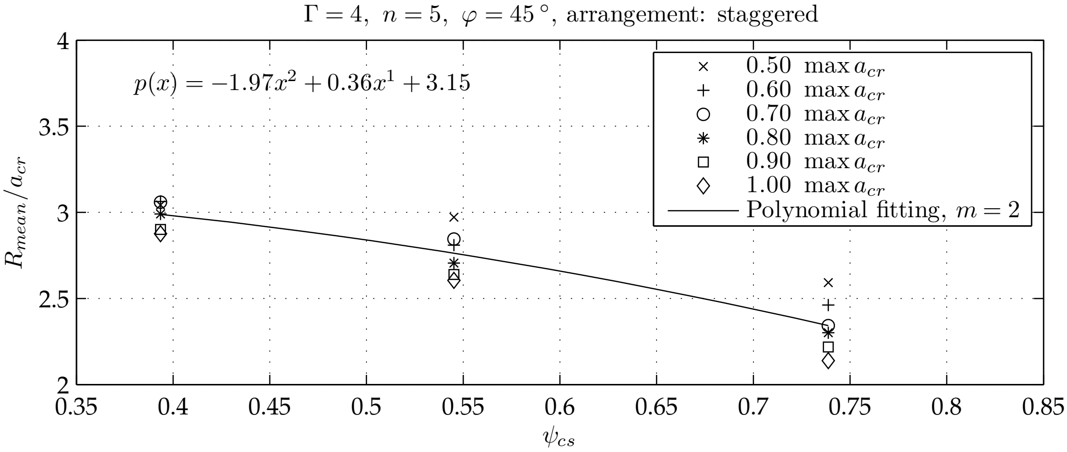

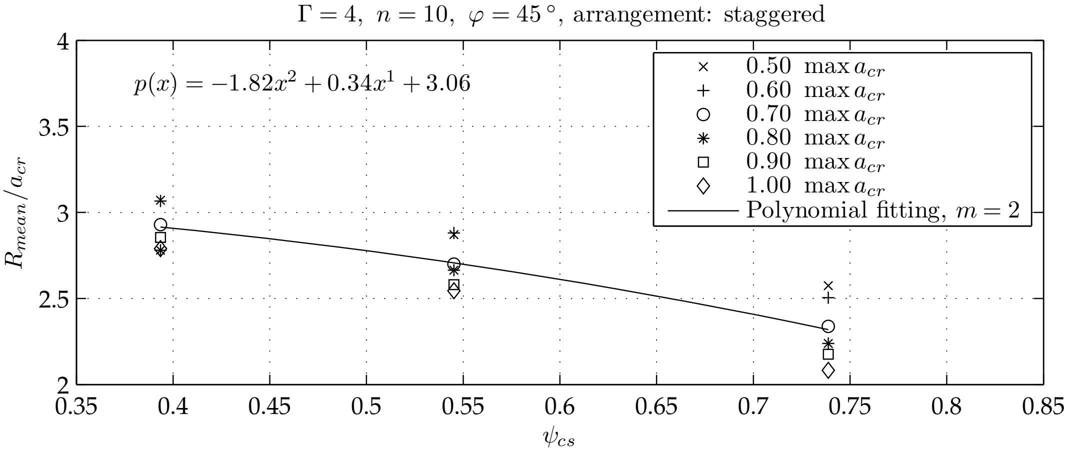

Figure 5.21 The relative wave run-up R_{mean} as a function of the cross-shore obstruction ratio ψ_{cs}, $\Gamma = 4$. The experimental data are fitted to a polynomial of degree $m = 2$ and the equations are given according to the investigated number of macro-roughness rows $n = 5, 10$

In order to compare the four macro-roughness configurations according to the cross-shore obstruction ratio and to estimate the effects induced by an increase in the number of macro-roughness rows, the polynomials fitted in the experimental data are in recapitulation presented in Fig. 5.22 and 5.23. When considering the aligned configurations in Fig. 5.22 it is obvious that the non-rotated cases are not significantly influenced by the number of macro-roughness rows. At the lowest obstruction ratio $\psi_{cs} = 0.5$ the difference between the cases $n = 1$ and $n = 10$ only amounts to

$0.05 \cdot R_{mean}/a_{cr}$ while the polynomial fit predicts a converse unphysical difference of $-0.05 \cdot R_{mean}/a_{cr}$. The apparently insignificant influence of the number of macro-roughness rows in the case of $\Gamma = 1$ is attributed to inevitable measurement errors. A greater number of individual experiment repetitions could enhance the results at this point. A more pronounced situation is given for $\Gamma = 2$ where the elements are rotated by $\varphi = 45°$ with respect to the incident wave direction. The run-up reduction is slightly increased when the cases $n = 1$ and $n = 5$ are compared. But on the other hand no significant deviations are detectable if the number of macro-roughness elements is further increased to $n = 10$. The maximum difference between the cases $n = 1$ and $n = 5$ amounts roughly to $0.25 \cdot R_{mean}/a_{cr}$. A comparison between the rotated and non-rotated, aligned case yields more interesting findings. For the comparable range of cross-shore obstruction ratios the difference in the relative run-up more or less constantly reaches a value of $0.4 \cdot R_{mean}/a_{cr}$. Hence in the case of aligned macro-roughness configurations, the effect of the macro-roughness element angle is superior to the number of macro-roughness element rows.

In contrast, the comparison of the two staggered configurations $\Gamma = 3, 4$ results in smaller differences. At first, the effects attributed to the number of macro-roughness element rows is detectable but ranges in the order of the measurement error so that the effect can be interpreted to be small, at least for the cases $n = 5$ and $n = 10$. If rotated macro-roughness elements are considered the differences are far below the findings of aligned configurations. The differences only amount to $0.05 - 0.10 R_{mean}/a_{cr}$. Obviously in this case the complicated exchange of momentum and the redirected flow at the front of the obstacles within the macro-roughness area allow the conclusion that in staggered configurations a distinction between rotated and non-rotated elements is not of primary importance. Equally the number of macro-roughness elements is of subordinate concern when compared to the cross-shore obstruction ratio. This aforementioned ratio to the greatest extent contributes to the run-up reduction of approaching long waves.

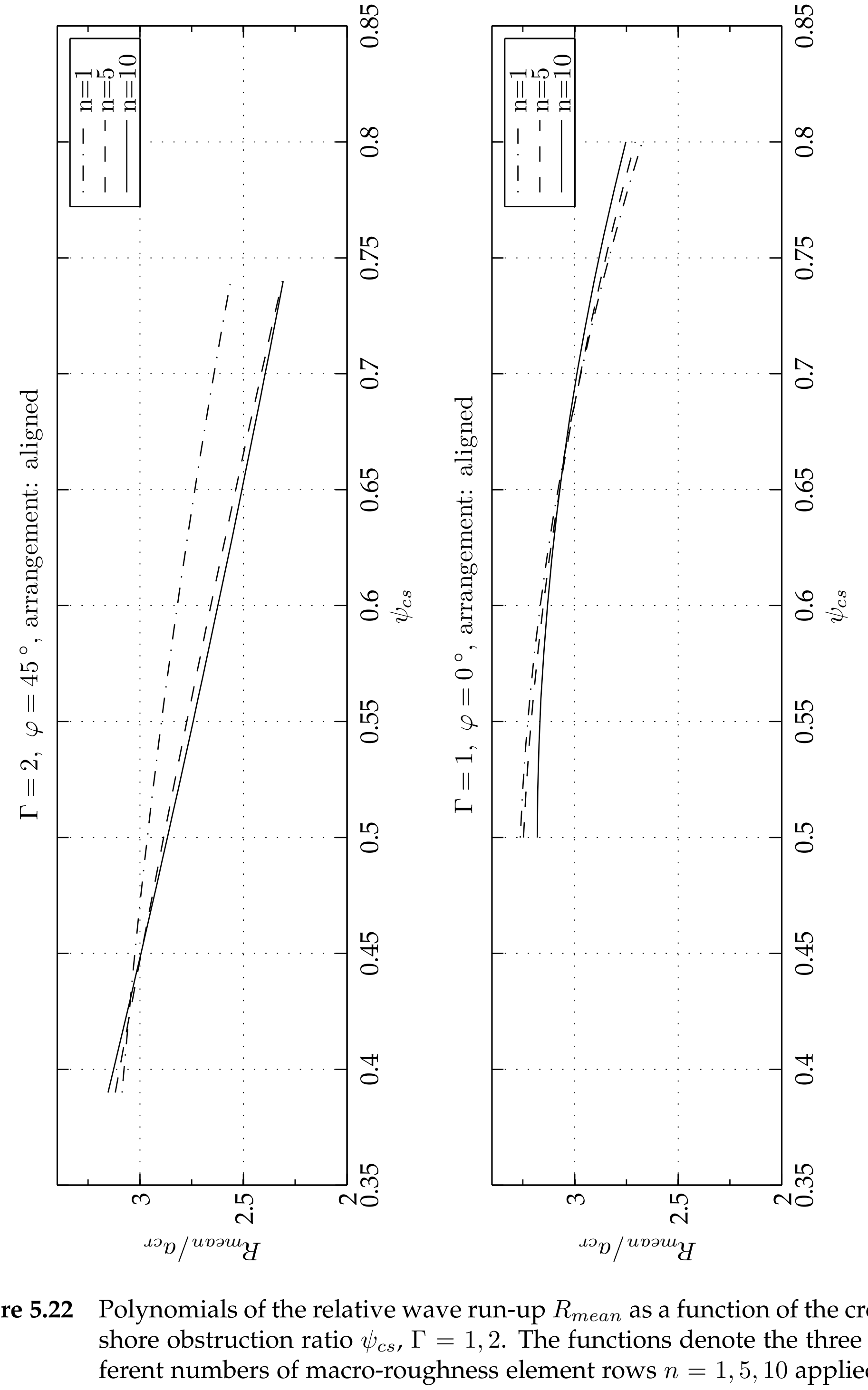

Figure 5.22 Polynomials of the relative wave run-up R_{mean} as a function of the cross-shore obstruction ratio ψ_{cs}, $\Gamma = 1, 2$. The functions denote the three different numbers of macro-roughness element rows $n = 1, 5, 10$ applied in the experiments.

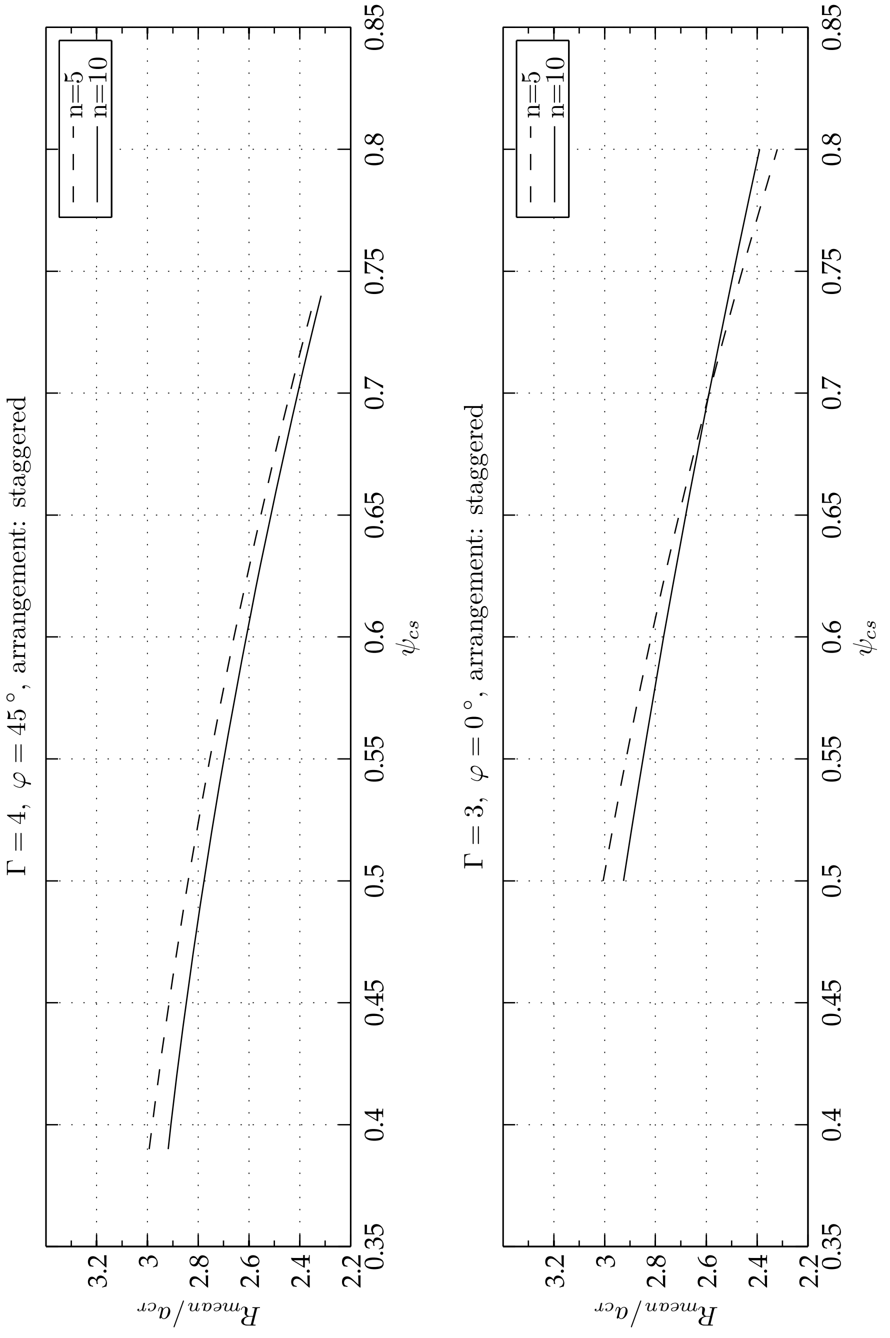

Figure 5.23 Polynomials of the relative wave run-up R_{mean} as a function of the cross-shore obstruction ratio ψ_{cs}, $\Gamma = 3, 4$. The functions denote the two different numbers of macro-roughness element rows $n = 5, 10$ applied in the experiments.

5.4.2 Long-Shore Obstruction Ratio

The long-shore obstruction ratio ψ_{ls} is defined by Eq. (3.1.11b). It relates the obstructed shore length of the macro-roughness area (cp. Eq. (3.1.10a)) to the length occupied by the macro-roughness elements in long-shore direction. By definition the long-shore obstruction ratio reaches unity if only one macro-roughness row is considered and decreases with a growing number of macro-roughness element rows.

$$\psi_{2d} = \psi_{cs}\psi_{ls} \tag{5.4.1}$$

Yet in relation with the cross-shore obstruction ratio it describes the two-dimensional obstruction of the onshore area given by Eq. (5.4.1). Consistently, for one macro-roughness row the product of ψ_{cs} and ψ_{ls} reduces to the cross-shore obstruction ratio ψ_{cs} whereas it grows with an increasing number of element rows. The two-dimensional obstruction is linear in the cross-shore direction. It has to be noted that the two-dimensional obstruction ratio and the results presented in the following base on the assumption that the street widths in the cross- and long-shore direction are equal. For cases where this assumption does not hold true, other results are conceivable. The convention of two-dimensional obstruction is not yet designed to describe the long-shore obstruction linearly. Analogously the effect on the backmost macro-roughness element rows is found to be lower than the effect on the frontmost rows. In this context, the definition of the two-dimensional obstruction ratio is physically reasonable. In accordance with the illustration in the previous subsection the relative run-up normalized by the wave amplitude at the wave maker is presented as a function of the two-dimensional obstruction ratio ψ_{2d} for the investigated macro-roughness configurations.

The resulting relative run-up for the configuration $\Gamma = 1$ as a function of the two-dimensional obstruction ratio is presented in Fig. 5.24 for the three different numbers of macro-roughness rows $n = 1, 5, 10$. The upper graph is identical with the results presented in Fig. 5.18 while the lower two graphs reveal the functional dependency on the two-dimensional obstruction ratio in the range of values as defined by Eq. (5.4.1). The qualitative course of the results is similar to the result of the cross-shore obstruction ratio. As was already outlined in the previous subsection, the influence of the number of macro-roughness rows and therewith the influence of the non-dimensional term ψ_{ls} is of lower order of significance for most of the macro-roughness configurations.

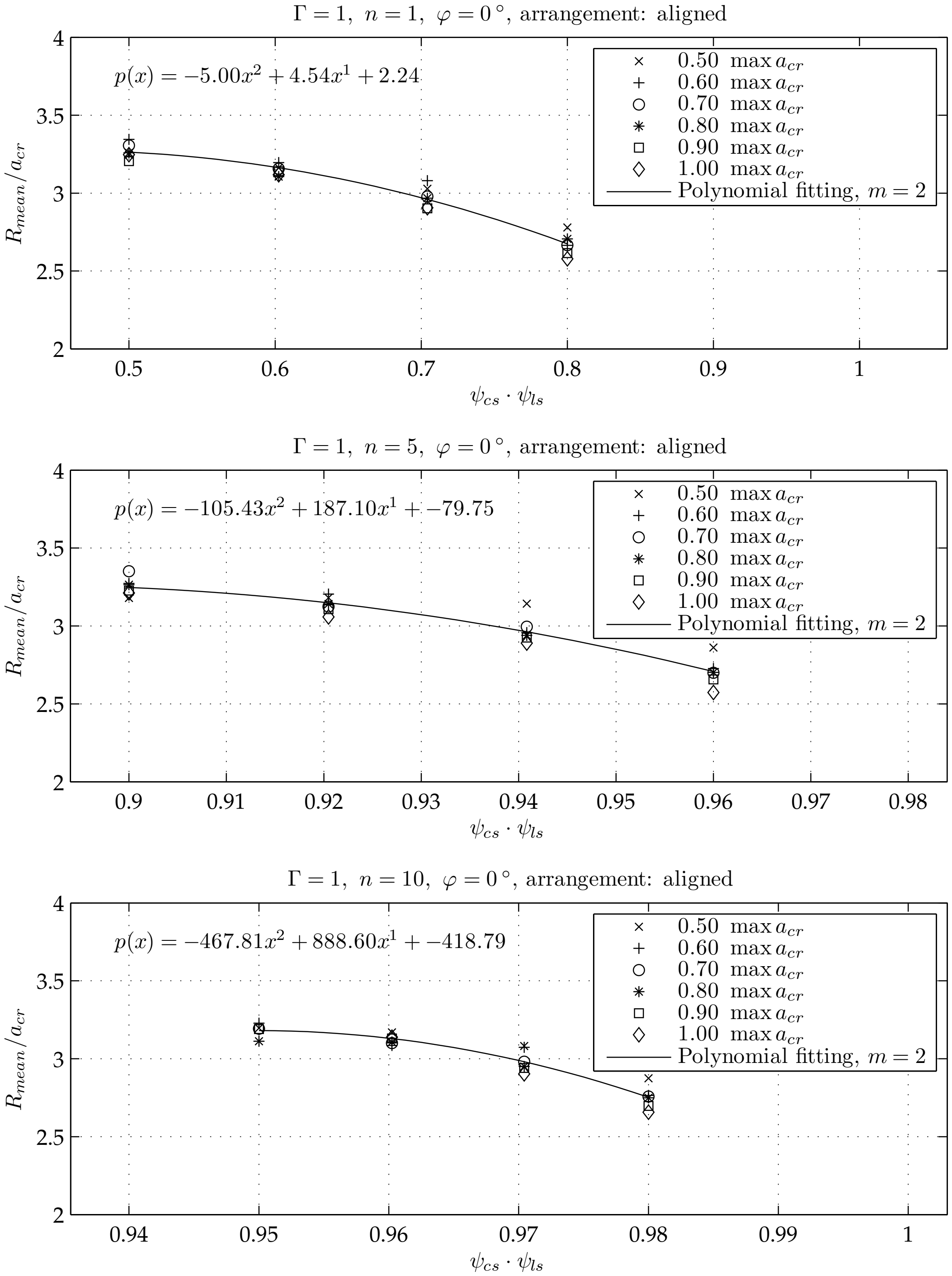

Figure 5.24 The relative wave run-up R_{mean} as a function of the cross-shore obstruction ratio ψ_{cs} times the long-shore obstruction ratio ψ_{ls}, $\Gamma = 1$. The experimental data are fitted to a polynomial of degree $m = 2$ and the equations are given according to the investigated number of macro-roughness rows $n = 1, 5, 10$

However it is not fully negligible, especially in the cases of $\Gamma = 1, 2$, those results are still presented. The remaining diagrams are placed in the annex for the sake of completeness. Fig. 5.25 presents the resulting relative run-up in relation to the two-dimensional obstruction ratio ψ_{2d} for the case of $\Gamma = 2$ with rotated elements in an aligned arrangement. The functional relation in principle follows the results presented in Fig. 5.19, though now the two lower diagrams relate the relative run-up directly to the two-dimensional obstruction ratio. For the cases $\Gamma = 3, 4$, the reader is referred to the Figs. C.1 and C.2 in the Annex. In the following the influence of the obstructed beach height is discussed.

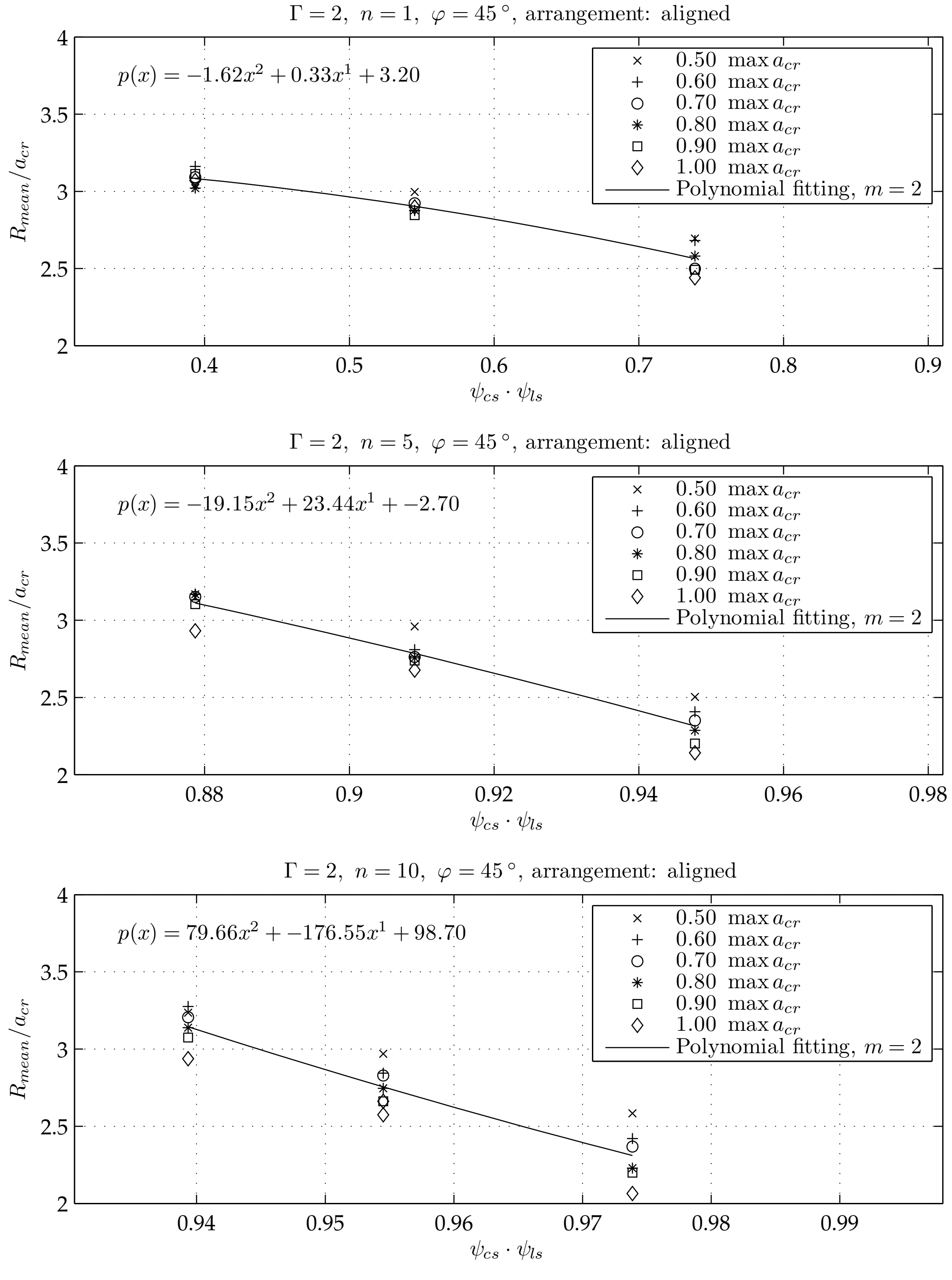

Figure 5.25 The relative wave run-up R_{mean} as a function of the cross-shore obstruction ratio ψ_{cs} times the long-shore obstruction ratio ψ_{ls}, $\Gamma = 2$. The experimental data are fitted to a polynomial of degree $m = 2$ and the equations are given according to the investigated number of macro-roughness rows $n = 1, 5, 10$

5.4.3 Obstructed Height

The non-dimensional obstructed height ψ_{mr} of the beach is expressed by Eq. (3.1.10b). It relates the geometrical vertical properties of the macro-roughness length obstructing the beach to the positive wave amplitude at the wavemaker. A growth of the beach slope $\tan\beta$ increases the non-dimensional obstructed height. A smaller number of macro-roughness element rows or a smaller street/element width decreases the ratio ψ_{mr}.

In the current investigation the beach slope was fixed to $\tan\beta = 1/40$. Only the street width b_{st} and the wave amplitude can therefore alter the non-dimensional obstruction ratio. It is hence clear that the wave amplitudes are inversely proportional to the non-dimensional obstructed heights.

Fig. 5.26 shows the results of the relative run-up R_{mean}/a_{cr} in regard to the obstructed height ψ_{mr} for the cases $n = 5, 10$. Firstly it becomes apparent that the polynomials for the two cases are similar in the course of the graphs while obviously the numerical range of the abscissa is shifted in accordance with the increase in the number of macro-roughness rows.

This fact substantiates the findings in Subsection 5.4.1 that especially for the cases $n = 5, 10$ in the staggered configuration the influence of the number of macro-roughness rows is less pronounced. With reference to the interlink between the wave amplitude and the obstructed length L_{mr} the relative run-up results of the higher amplitudes belong to smaller values of ψ_{mr}.

The remaining figures which depict the three other configurations of the macro-roughness can be found in the annex, Fig. C.3 and C.4, C.5.

5.4.4 Macro-roughness Influence

The previous three subsections elucidate the influence of the dimensionless terms ψ_{cs}, ψ_{ls} and ψ_{mr} detected by means of the dimensional analysis. While the cross-shore obstruction ratio ψ_{cs} is found to be very dominant, the long-shore obstruction ratio and the obstructed height are of minor importance. It also becomes clear that the relative run-up reduction significantly varies with the given macro-roughness configuration Γ. On that basis it is convenient to focus on the dominating cross-shore obstruction ratio ψ_{cs} to deduce conclusions from the experimental findings. From an engineering perspective it is preferable to either yield empirical equations or nomograms which are suitable to predict the reduced run-up due to a given macro-roughness combination in comparison with an undisturbed case.

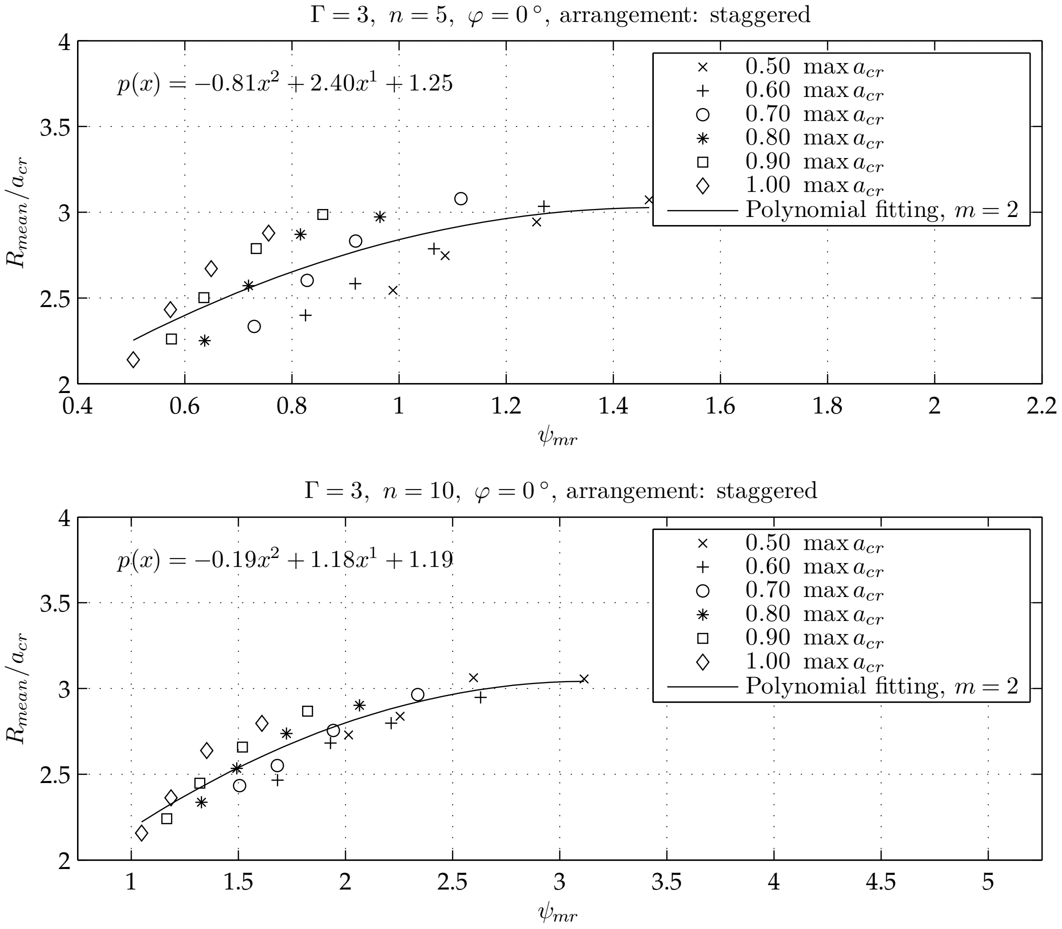

Figure 5.26 The relative wave run-up R_{mean} as a function of the cross-shore obstruction ratio ψ_{cs} times the long-shore obstruction ratio ψ_{ls}, $\Gamma = 3$. The experimental data are fitted to a polynomial of degree $m = 2$ and the equations are given according to the investigated number of macro-roughness rows $n = 5, 10$

The following Figs. 5.27 – 5.30 illustrate the relation of the relative run-up R_{mean}/a_{cr} to the surf similarity parameter ξ_∞. The parameters of the macro-roughness configuration and the label are given in the figure title. The reduced relative run-up according to the cross-shore obstruction ratio is plotted as a error bar line where the line denotes the averaged run-up of the cases $n = 1$, $n = 5$ and $n = 10$. The error bars mark the standard deviation to the plotted average values. Generally a smaller relative run-up is associated with a higher number of macro-roughness element rows. The relative run-up associated with the cross-shore obstruction ratio decreases slightly with an increasing non-linearity of the applied waves, which is contributed to greater momentum exchange within the macro-roughness element area. The six error bars for each cross-shore obstruction ratio always assign the six applied wave conditions described in Subsection 5.1.1. The labels which indicate the non-linearity of the waves refer to all error bars arranged in the vertical.

Fig. 5.27 represents the macro-roughness configuration $\Gamma = 1$. Two experiments with a non-linearity of $a_{cr}/h_0 = 0.095$ were excluded in this figure. The reduction of the relative run-up decreases slightly with decreasing surf similarity. The reduction of the relative run-up is less significant for a cross-shore obstruction ratio of $\psi_{cs} = 0.5$. It is located slightly below the analytical results given by Eq. (5.3.5). Yet, a notable reduction of approximately 21.0 % can be read as the highest non-linearity. The standard deviation, which indicates the differences due to the variation of the parameter n, is fairly low which is in good agreement with the findings outlined in Subsection 5.4.2 and 5.4.3.

Next, Fig. 5.28 illustrates the same functional relation but focuses on the macro-roughness configuration $\Gamma = 2$ with aligned arrangement and rotated macro-roughness elements. In comparison to $\Gamma = 1$ a higher reduction is found over the whole range of non-linearity. A distinct reduction of the relative run-up is already traceable for a cross-shore obstruction ratio of $\psi_{cs} = 0.393$, whereas almost no influence was found for the aligned, non-rotated configuration. Further it appears that the differences due to the number of macro-roughness elements expressed by the error bars show a noteworthy increase for this configuration, especially for $\psi_{cs} = 0.739$. The reduction of the relative run-up compared to the undisturbed case yields approximately 33.0 % in the case of the highest non-linearity.

Fig. 5.29 shows the relative run-up results for the configuration $\Gamma = 3$. The general run of the curves is similar to the one previously presented for the configurations $\Gamma = 1, 2$. It can be observed that in tendency the relative run-up again decreases with an increase in non-linearity, which is contributed to the growth in momentum exchange when a wave of higher non-linearity interacts with the macro-roughness elements. Also, the influence of the number of macro-roughness element rows is of less importance than conveyed in case $\Gamma = 2$. In contrast to the aligned, non-rotated configuration a reduction of the relative run-up can already be detected for the smallest investigated non-linearity $a_{cr} = 0.05$. For the highest non-linearity, the reduction of the relative run-up also comprises approximately 3.0 % which is similar to the aligned, rotated configuration.

Finally, the staggered, rotated configuration $\Gamma = 4$ is addressed in Fig. 5.30. In contrast to the comparable aligned configuration, the standard deviation according to the variation of the number of macro-roughness element rows is much smaller. Yet, the trend in the relative run-up to increase not only proportionally to the cross-shore obstruction ratio, but also to the increasing non-linearity, is clearly present. The maximum reduction of the relative run-up for a cross-shore obstruction ratio of $\psi_{cs} = 0.839$ amounts approximately to 36.0 %.

It is apparent that the influence of the cross-shore obstruction ratio to the reduction of the relative wave run-up is not linear. This also depends on the non-linearity of the applied waves resulting in higher energy loss for stronger non-linearity due to an increase in energy dissipation during the highly turbulent interaction process with the macro-roughness elements.

With the aid of the results presented in Figs. 5.27 – 5.30 it is consequently possible to have estimations of the relative run-up reduction on the basis of the given diagrams. For instance, if a certain wave height in shallow water is assumed, it is possible in principle to deduce the relative run-up reduction induced by a given macro-roughness configuration onshore. Of course the results are only valid under the assumption that the chosen parameters agree with the investigated range of surf similarities, the beach slope and the non-linearity of the waves. It is not recommended to apply the nomograms in other cases until further investigations come up which substantiate the generality of the findings presented herein.

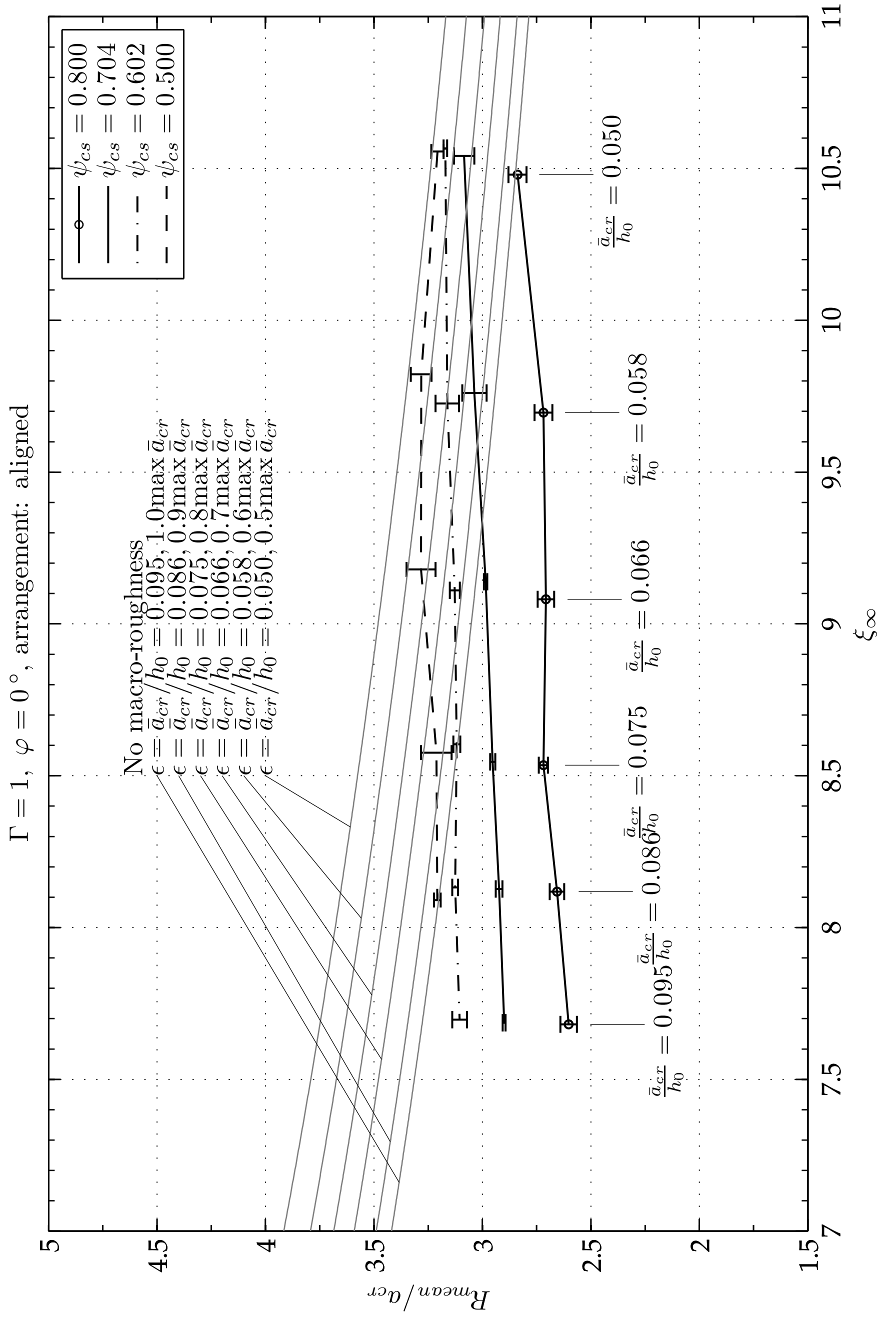

Figure 5.27 The relative wave run-up R_{mean}/a_{cr} as a function of the surf similarity parameter ξ_∞, $\Gamma = 1$. The experimental data are plotted according to the individual cross-shore obstruction ratio. The error bars indicate the variation of the number of macro-roughness element rows. The gray parallel graphs indicate the relative run-up without the interaction with macro-roughness. The non-linearity of the applied waves is indicated as text which always refers to all error bars in the vertical above.

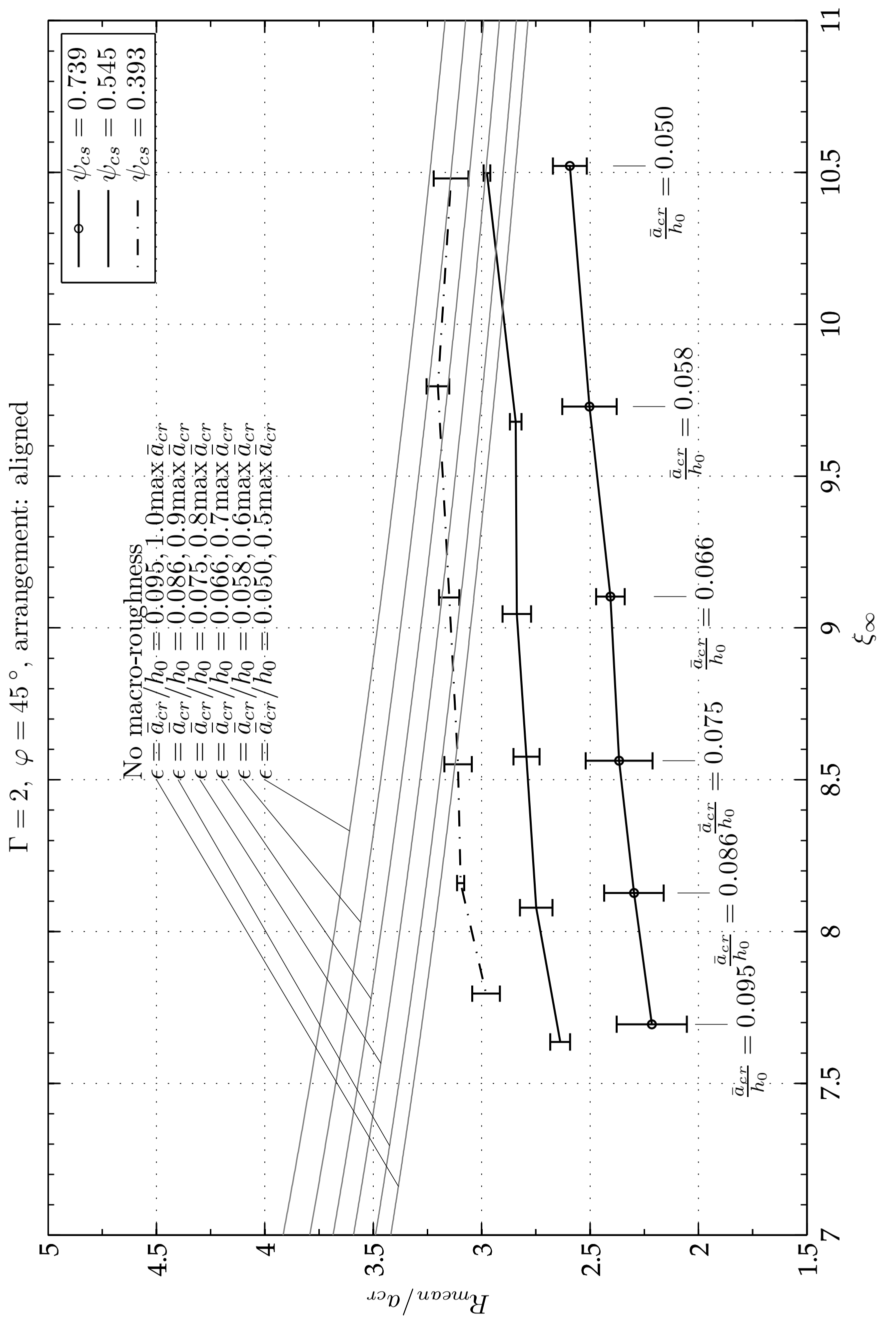

Figure 5.28 The relative wave run-up R_{mean}/a_{cr} as a function of the surf similarity parameter ξ_∞, $\Gamma = 2$. The experimental data are plotted according to the individual cross-shore obstruction ratio. The error bars indicate the variation of the number of macro-roughness element rows. The gray parallel graphs indicate the relative run-up without the interaction with macro-roughness. The non-linearity of the applied waves is indicated as text which always refers to all error bars in the vertical above.

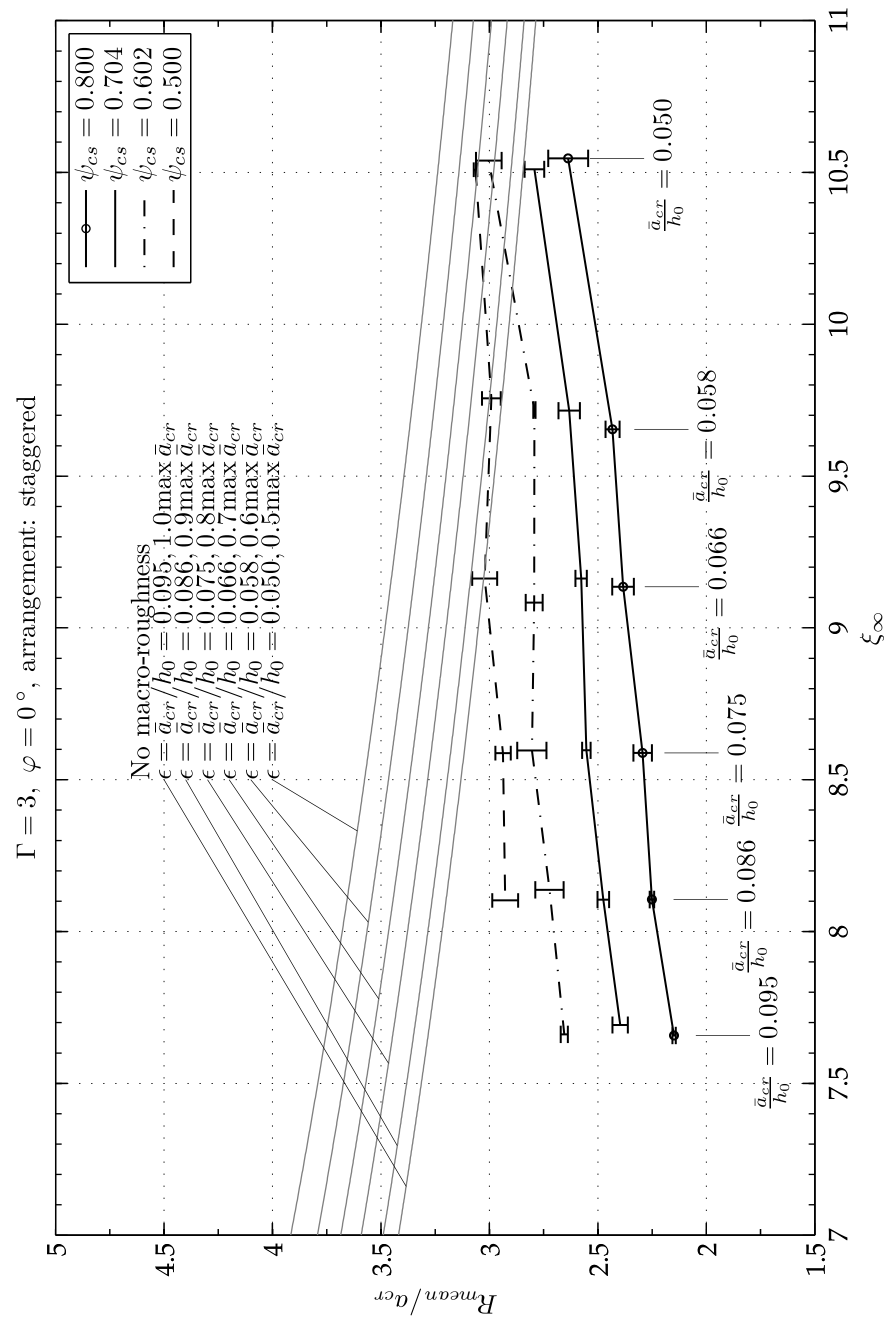

Figure 5.29 The relative wave run-up R_{mean}/a_{cr} as a function of the surf similarity parameter ξ_∞, $\Gamma = 3$. The experimental data are plotted according to the individual cross-shore obstruction ratio. The error bars indicate the variation of the number of macro-roughness element rows. The gray parallel graphs indicate the relative run-up without the interaction with macro-roughness. The non-linearity of the applied waves is indicated as text which always refers to all error bars in the vertical above.

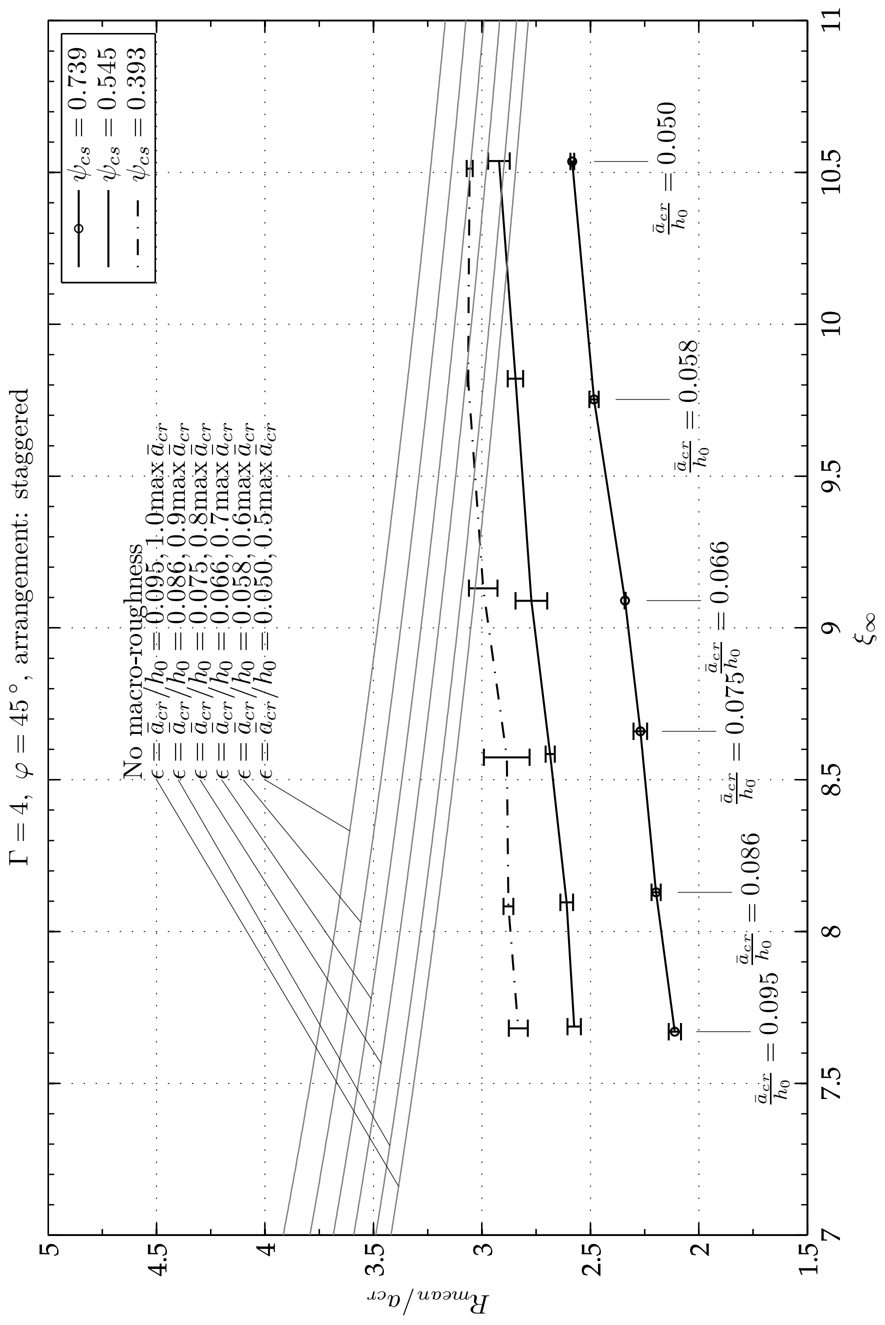

Figure 5.30 The relative wave run-up R_{mean}/a_{cr} as a function of the surf similarity parameter ξ_∞, $\Gamma = 4$. The experimental data are plotted according to the individual cross-shore obstruction ratio. The error bars indicate the variation of the number of macro-roughness element rows. The gray parallel graphs indicate the relative run-up without the interaction with macro-roughness. The non-linearity of the applied waves is indicated as text which always refers to all error bars in the vertical above.

5.4.5 A Case Study

The properties of the investigated macro-roughness configurations are guided by realistic, prototype-like obstruction ratios of densely populated, coastal urban settlements. However for laboratory investigations, such a settlement situation has to be abstracted from the very diverse real situations to idealized laboratory conditions in order to deepen the insight into the phenomenology.

One of the most imperiled regions worldwide is the city of Padang, which is situated on the western coast of Sumatra. A potential tsunami originating from a sub-oceanic earthquake at the Sunda arc subduction zone could reach the coastline in a time frame of $20 - 30\ \mathrm{min}$. The city of Padang is densely populated and most of the developed areas of the city stretch along the flat, low-lying coast. These near-shore areas exhibit almost the highest population densities in the city (Taubenböck et al., 2009). An analysis of extracts of the building footprint of the city of Padang reveals cross-shore obstruction ratios of approximately $\psi_{cs} = 0.5 - 0.7$. A sample map of building footprints directly at the coast of Padang is given by Fig. C.6 at the coastline. This map was used as a basis for the estimation of the cross-shore obstruction ratio according to Eq. (3.1.11a). A total number of 173 houses directly at the coast were selected for the calculation (colored dark gray). Subsequently the cross-shore obstruction ratio was determined with the aid of a geographic information system software.

Recently, Muhari et al. (2010) investigated tsunami mitigation efforts for the West Sumatra province in Indonesia by pure numerical means. The obstruction due to building features, which is unquestionably present in the city of Padang, was modeled threefold in order to assess the occurring differences. Besides the detailed modeling with solid obstacles as real buildings in the model, a similar roughness approach and a distributed roughness approach were applied. Similar to the findings in this thesis, a building density of $0.6 - 0.8$ was reported for the coastline of Padang. In line with the findings from the laboratory, the approach utilizing solid obstacles in the numerical model yielded a reduction of the maximum inundated area, though unfortunately this reduction was not decidedly quantified.

Jakeman et al. (2010) assesses the quality of tsunami inundation models in terms of the spatial distribution of the inundation. The impact of the 2004 Indian Ocean tsunami at the city of Patong, Thailand is taken into focus for this study. Especially the influence of buildings and other structures was analyzed. It turned out that the influence can only be incorporated into numerical investigations adequately when those obstructing structures are included one-to-one as in the actual development situation. Besides the reported significant influence of the built-up areas to the maximum run-up, the authors moreover stressed the demand for calibration and validation of the numerical tools. The study utilized field data of Patong to assess the quality of the numerical model. This was only possible because extensive data before and after the tsunami as well as additional field surveys are available. In other, less well documented cases this method will likely fail. Then the application of physical scale experiments is more recommendable because experiments are generally repeatable and they can more readily be suited to the investigator's need.

Schlurmann et al. (2010) also analyzed the impact of potential tsunami threat for the city of Padang by numerical means. At first, a digital elevation model was used which only contained elevation data of the bare ground. Secondly, a digital surface model was also applied for the modeling, comprising buildings and other vertical structures with realistic obstacle heights, on the basis of highly-resolved datasets stemming from a stereo-camera flight campaign. A comparison of the numerical results obtained from the different geometrical models for a physically sound tsunami incident revealed that these macro-roughness elements reduced the maximum inundated area by approximately $36\ \%$ when obstacles are involved. The non-linearity of the investigated potential tsunami can be deduced from the surface elevation time series at the numerical boundary and the associated water depth of $h_0 \approx 80.0\ \mathrm{m}$ taken from hydrographic charts. The positive wave amplitude is stated to be $a_{cr} = 3.9\ \mathrm{m}$ which yields a non-linearity of $\epsilon = 0.049$ (Schlurmann et al., 2010, cp. their Fig. 9a).

From the given example in literature the question arises if the results from the experiments are in principle comparable to that particular case study at Padang. A validation with Fig. 5.29 comprising the results for a staggered, non-rotated configuration does not agree well with the reported reduction of the inundation by Schlurmann et al. (2010). However the tendency to bring a reduction of inundation about is definitely implicated and the reason for this is clearly due to the obstructed onshore area. From laboratory experiments of a $1/40$ sloping beach the reduction of the relative run-up is $\approx 7 - 8\ \%$ for the comparable non-linearity (cp. Fig. 5.29 or Fig. 5.30).

Yet in contrast, the assumptions made for the experimental results are not fully valid for the Padang case study. Neither the bottom gradient in the near-shore area of Padang ($\tan\beta \approx 1/125$) nor the onshore gradient ($\tan\beta \approx 1/500$) are fully comparable to the numerical results, which are only valid for ($\tan\beta \sim 1/40$). From the theoretical point of view, much higher wave run-up is expected for such mild sloping beaches and the influence of the interaction with macro-roughness conceivably increases due to the fact that the temporal timespan and the spatial length of interaction is significantly increased. Hence it is concluded that care must be taken when the experimental results are related to realistic case studies. Furthermore it is of paramount importance to broaden the experimental data basis and to focus on the beach slope and the wave length/period influence in future investigations.

5.4.6 Summary and Conclusions

The influence of macro-roughness elements on the run-up of long sinusoidal waves is investigated. Four different macro-roughness element configurations are chosen and various distances between the single macro-roughness elements are considered. In general it turns out that the macro-roughness elements onshore, which are modeled as solid cubic concrete blocks mimicking urban developments, are capable of reducing the long wave run-up significantly. The reduction of the relative run-up depends primarily on the cross-shore obstruction ratio ψ_{cs} while the influence of the long-shore obstruction ratio is generally less pronounced. The influence of the macro-roughness elements grows according to the macro-roughness element configuration. Aligned configurations are less effective in the run-up reduction than staggered element configurations. Moreover, the angle of the single obstacles is equally found to influence the overall run-up reduction significantly. For aligned and staggered configurations, rotated obstacle arrangement results in a greater reduction of the relative run-up.

Additionally, a case study for the city of Padang reveals that the transferability of the experimental results is still deficient though the general mechanism of the macro-roughness elements is already present in numerical models. As a first further step the demand arises to validate the existing numerical models against the results from the experiments in order to elucidate how well the numerical models agree. Secondly it has to be investigated how the macro-roughness element effects can numerically best be modeled. It seems advisable to transfer the utilization of those numerical models to realistic problems on the basis of laboratory-founded validations only if major discrepancies can be accepted by the modelers.

5.5 PIV-based Description of the Wave Motion

The characteristic flow pattern of the long wave interaction with macro-roughness configurations is going to be presented in this section. Besides the essential findings regarding the run-up reduction of long waves approaching a $1/40$ sloping beach it is important to understand how the run-up induced flow is diverted, accelerated and decelerated in-between the obstacles in principle. Hence a partial coverage of the obstructed onshore area is regarded in the following to highlight the basic behavior of the flow. Section 5.5.1 depicts the flow pattern in a top view perspective qualitatively and quantitatively whereas Section 5.5.2 analyses a virtual gauge at an exposed position in the flow to highlight the velocity differences which are generated under the variation of macro-roughness configurations in general.

5.5.1 Velocity Fields

First of all the flow pattern is presented in a top view perspective. In this connection the camera coverage of the field of view is delineated in Fig. 3.12 where the wave is approaching from the right to the left. The coordinate system can be found in Fig. 3.9. Generally, two points in time were chosen for the presented results. The first one is at the dimensionless time $\hat{t} \approx 340 - 342$ which coincides with strong flow velocities during the run-up phase of the wave while the second time step relates to the run-down phase of the wave at $\hat{t} \approx 441 - 456$. In addition, at the first chosen time the wave front is visible in the left half of the illustration. It has to be noted, that differences of absolute dimensionless time occur during individual experiments after a distinct number of images. This is caused by the buffering and storage of the grabbed images on the software side leading to time lags. Yet it does not make a significant difference for the flow pattern description.

Figs. 5.31 and 5.32 outline how the flow interacts with the four investigated macro-roughness configurations. In these figures always every second vector arrow was plotted. The arrows are however not plotted on a distinct velocity scale because the foremost aim is of a qualitative description of the flow pattern. In Fig. 5.31 the aligned arrangements are presented. The non-dimensional cross-shore obstruction ratio is in a comparable range of values. In the case of non-rotated macro-roughness elements given in Fig. 5.31(a) it is apparent that the velocity fields in-between the macro-roughness elements is uniformly pointing in the direction of wave run-up. Yet as soon as the flow widens, after the constriction due to the macro-roughness elements, it indicates that the channelized flow expands into the spaces in the back of the obstacles. This tendency is still small because the spatial consumption to fully expand is too small. The following row of obstacles again forces the flow to contract. Eddies are formed in the spaces between the obstacles in wave propagation direction. Most of the flow in the case of $\Gamma = 1$ is directed onshore and it can be assumed that only a small amount of energy is dissipated during the run-up process. This assumption blends in well with the observation that the run-up reduction is smallest for this configuration (cp. Section 5.4).

In Fig. 5.31(b) the typical run-up flow pattern features stronger transverse velocity components than the previous case. As already conjectured in Subsection 5.4.4, the constricted flow in the narrowest space between the obstacles immediately widens after passing through. This observation is in line with the law of continuity. In this context a decrease in water level was clearly visible behind the narrowest distance which was yet not tracked and recorded during the experiments. The observed flow pattern reminds of the propagation of dam-break induced flood waves which were frequently investigated for example by Fraccarollo and Toro (1995) and Briechle (2006).

Figs. 5.32(a) and 5.32(b) display the flow pattern for the two staggered macro-roughness element configurations. Again every second vector arrow is plotted. In the non-rotated case given in Fig. 5.32(a) it turns out that high flow velocities occur especially in the constrictions at the moving wave front. High velocities are apparent where the approaching surge is diverted through $90°$ after passing through the constrictions which were already passed by the wave front. The flow vectors are orientated at $45°$ with respect to the run-up direction and they primarily agglomerate at the corners of the wave-facing front of the obstacles. In the back of the obstacles eddies and back currents are formed. Interestingly, in the constrictions of the second rows with respect to the moving wave front, flow velocities are significantly smaller than in the following widenings. This fact is probably associated with a change from sub- to supercritical flow and vice-versa. Final proof for this assumption cannot be given because water level measurements for a Froude number calculation were not conducted.

Finally Fig. 5.32(b) depicts the configuration $\Gamma = 4$ with staggered and rotated arrangement of the macro-roughness elements. The wave front propagates in a similar pattern as in the case $\Gamma = 2$ and it widens, but the staggered arrangement causes an earlier deceleration of the flow in the widening section. In the back of the rotated macro-roughness elements a backwater area is found on both back faces where almost no flow velocity is present. Similar to the non-rotated case $\Gamma = 3$ the direction of the flow velocities in the front of the obstacles is $45°$ with respect to the run-up direction but it is supposed that the energy loss is smaller because the surge flow does not collide with the obstacle front faces head-on but under the bisected angle.

In the following the wave run-down should be discussed on the basis of the full coverage of the velocity field which is given for a wave of non-linearity $\epsilon = 0.058$ (cp. Section 5.1.1 for details of the generation of the wave and the resulting surge flow).

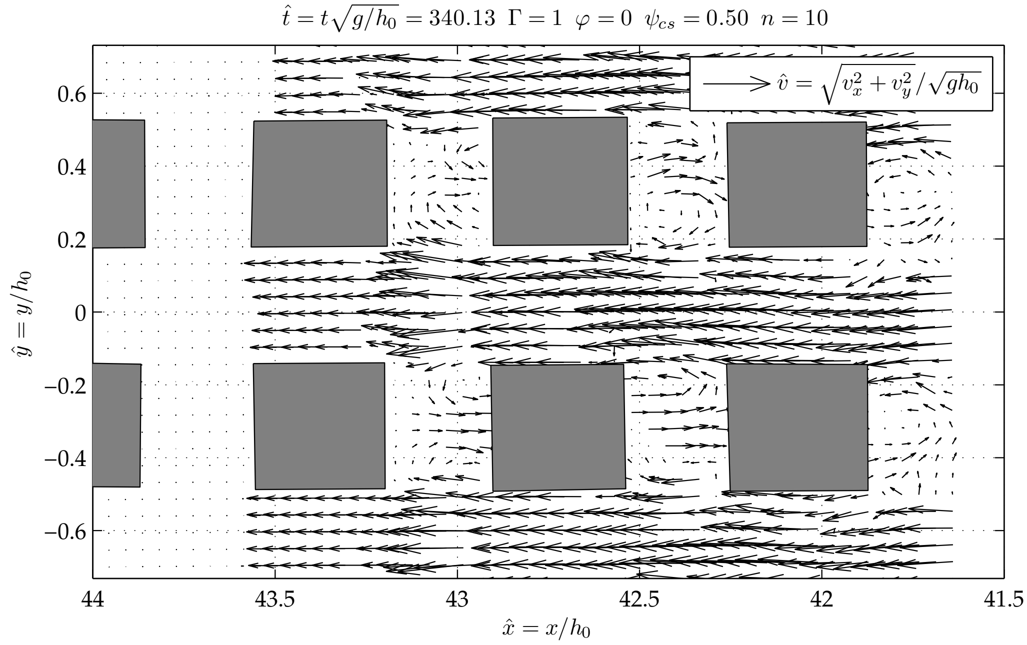

(a) Aligned, non-rotated configuration $\Gamma = 1$

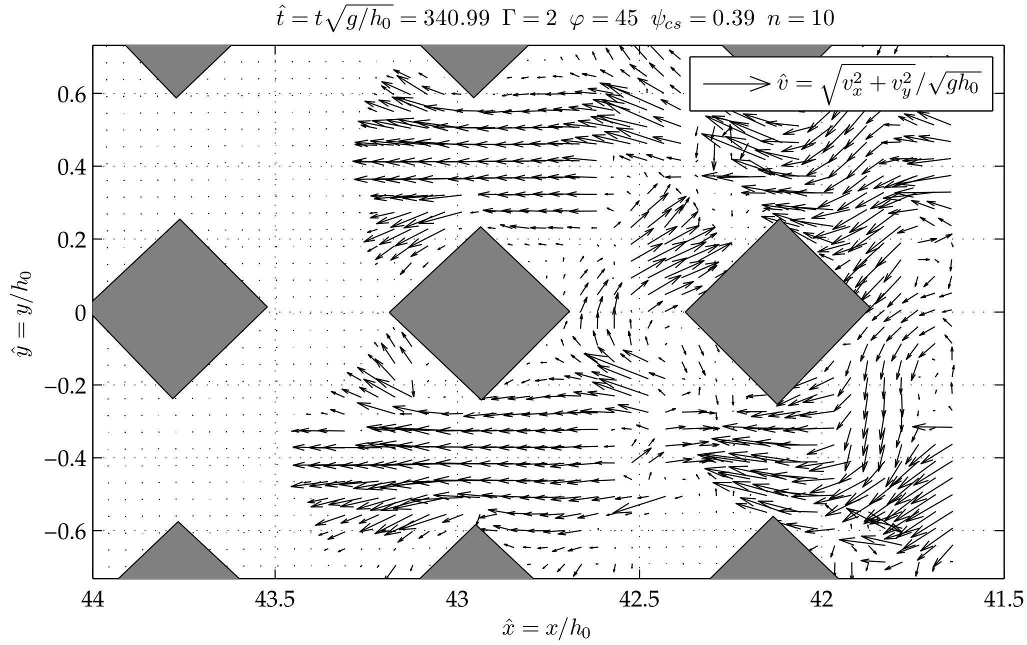

(b) Aligned, rotated configuration $\Gamma = 2$

Figure 5.31 Top-view perspective of the detailed velocity field around aligned macro-roughness element configurations, the wave run-up direction is from the right to the left.

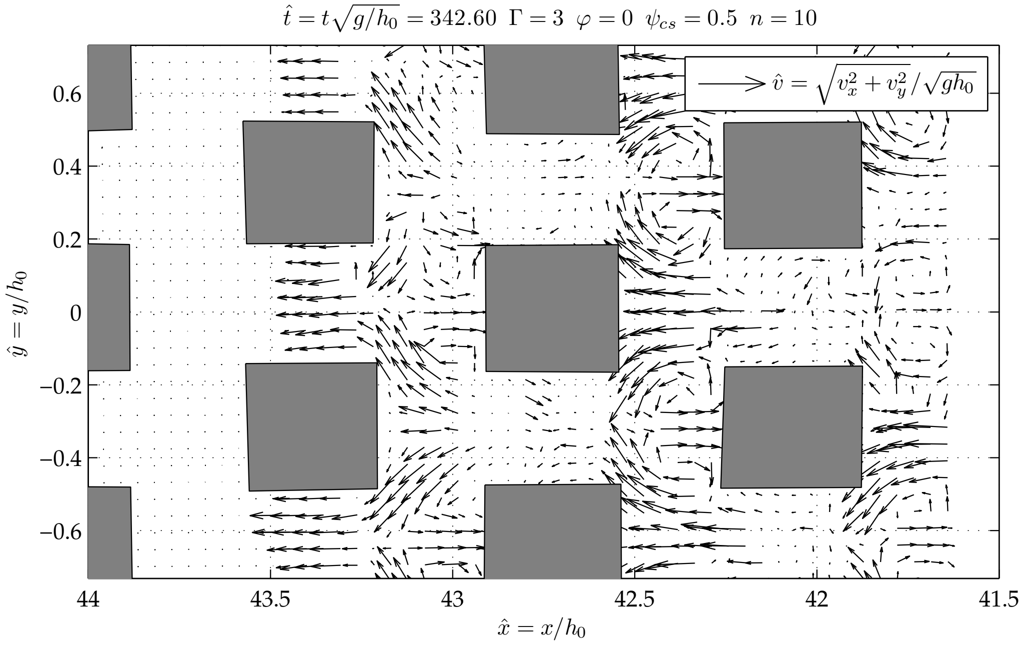

(a) Staggered, non-rotated configuration $\Gamma = 3$

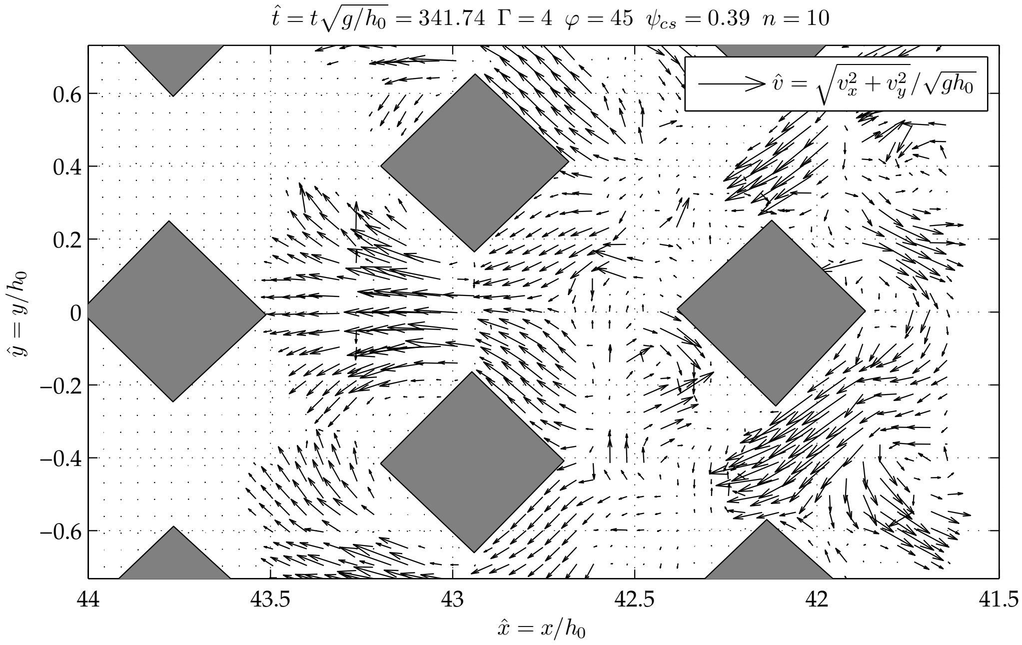

(b) Staggered, rotated configuration $\Gamma = 4$

Figure 5.32 Top-view perspective of the detailed velocity field around staggered macro-roughness element configurations, the wave run-up direction is from the right to the left.

The remaining velocity field results were analyzed quantitatively for the dimensionless time at $\hat{t} \approx 441 - 456$ in Figs. 5.33 and 5.34. The thick gray lines in these figures indicate the flume walls for the reader's orientation. For the sake of completeness, the qualitative results for a step during the run-up phase at $\hat{t} \approx 340 - 342$ are also given in the annex (Figs. C.23, C.24, C.25). In these illustrations of the top-view perspective of velocity fields only every 20th vector is plotted with an additional colour-coding basing on the velocity magnitude.

Figs. 5.33(a) and 5.33(b) display the top-view perspective of the velocity fields which appear for the aligned macro-roughness configurations during the run-down phase. The comparison of these two macro-roughness configurations in Section 5.4 yielded a greater run-up reduction for the case $\Gamma = 2$. This is partly contributed to the fact that different cross-shore obstruction ratios are found for the displayed cases. However, in addition it is also associated to smaller velocities in the main flow of run-up and run-down (Figs. C.24(a) and C.24(b)) in-between the obstacles. For the considered time step it appears that the velocities in case $\Gamma = 2$ are approximately reduced by $25\ \%$ compared to case $\Gamma = 1$.

Further reductions in the maximum occurring velocity are found in the Figs. 5.34(a) and 5.34(b) where the cases $\Gamma = 3$ and $\Gamma = 4$ are depicted in the full coverage view. During the run-down phase higher velocities occur in-between the obstacles associated with the law of continuity. After this acceleration the flow generally bifurcates in the vicinity of the next obstacle reached. The bifurcation is more pronounced for the case $\Gamma = 3$ because the flow collides head-on with the obstacle whereas a smoother diversion of the flow is realized by the rotated orientation of the obstacles in case $\Gamma = 4$.

The velocity magnitudes found in the cases $\Gamma = 1 - 4$ are mostly higher than the undisturbed case where macro-roughness elements are absent onshore. Fig. C.23 finally indicated the velocity conditions during the run-up and run-down of the long wave in the observed section of the beach. The run-up behavior given in Fig. C.23(a) suggests lower velocities directly at the wave front while substantially higher velocities occur behind the wave front. This observation is congruent with eye-witness reports stating that victims could firstly walk slowly at the pace of the front velocity but later with increasing water levels the fluid velocity increased rapidly (Fritz et al., 2006).

The spatial deviation at the foremost tip of the run-up tongue is an interesting phenomenon. Already Yeh et al. (1989) observed similar variations for different time steps of the experiments. Equally it was apparent in various repeated experimen-

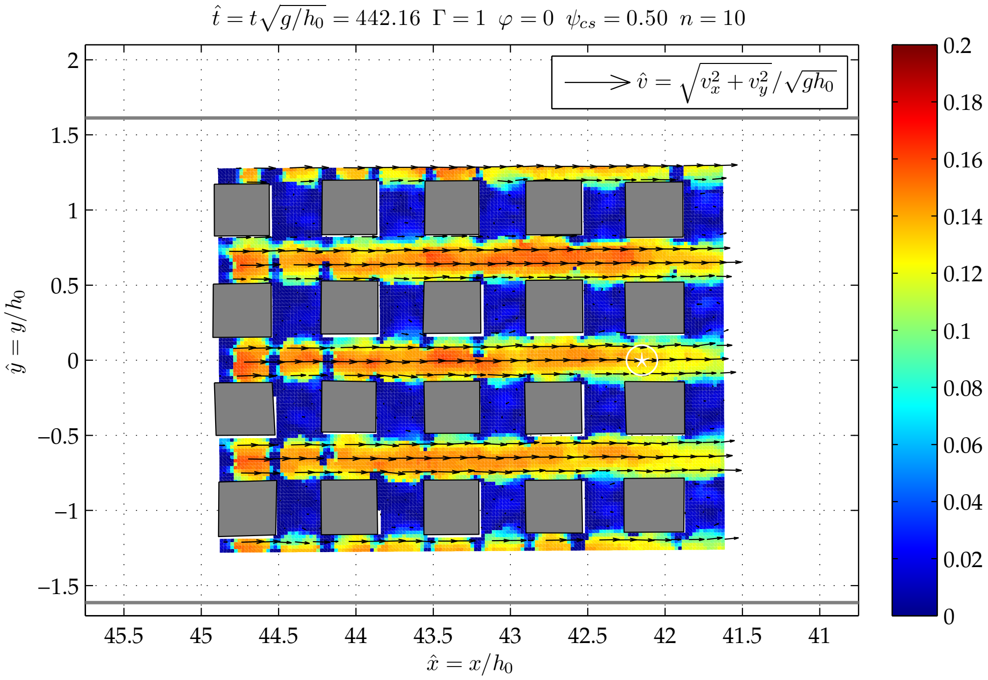

(a) Aligned, non-rotated configuration $\Gamma = 1$

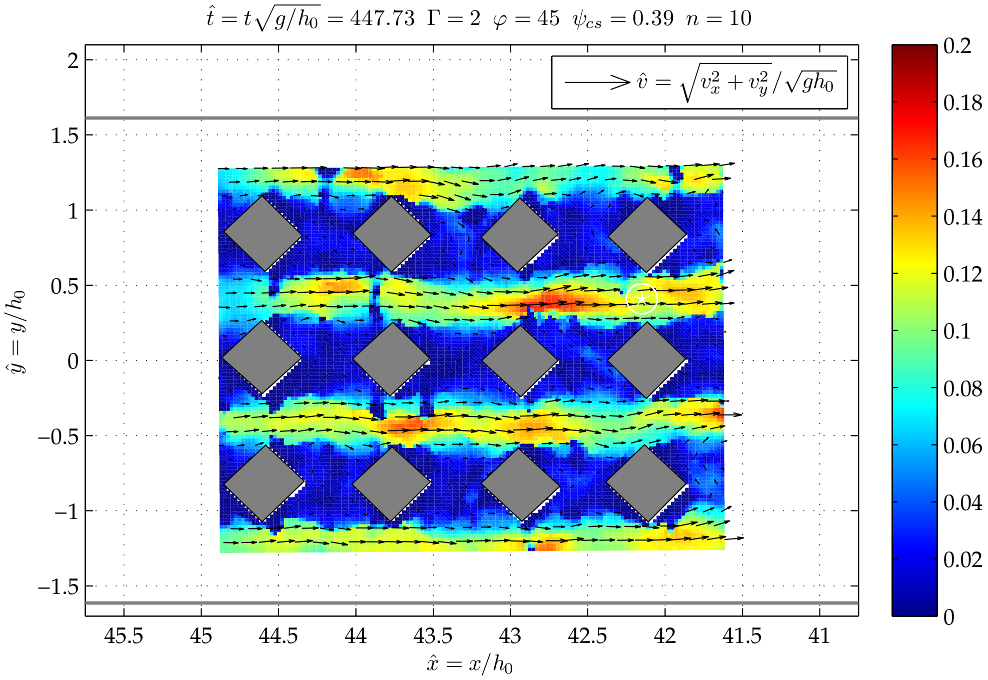

(b) Aligned, rotated configuration $\Gamma = 2$

Figure 5.33 Top-view perspective of the full coverage velocity field around aligned macro-roughness element configurations, the wave run-up direction is from the right to the left.

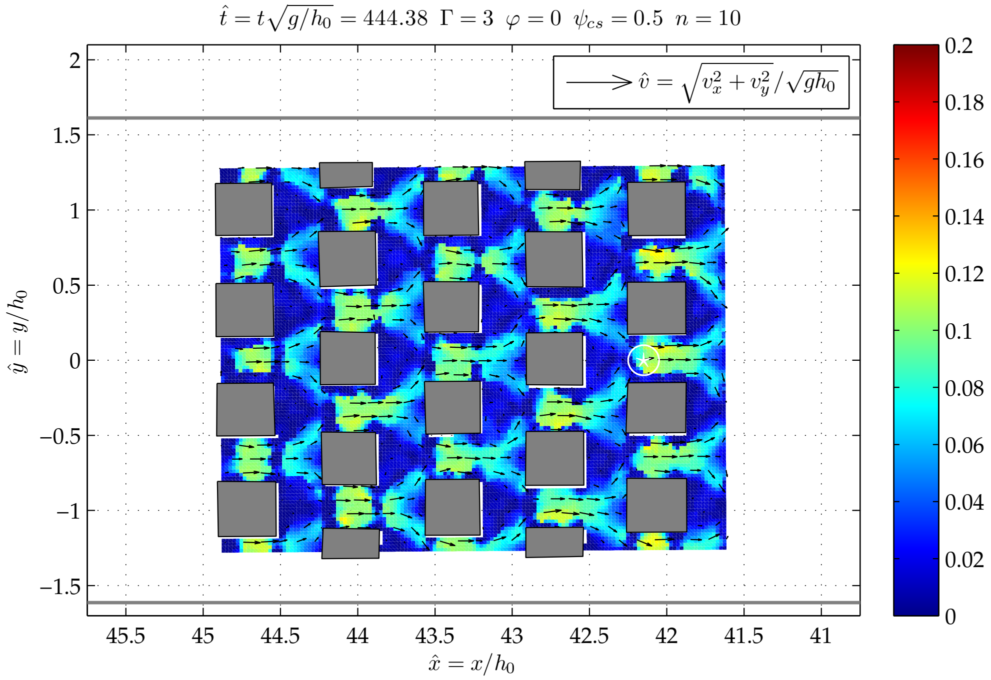

(a) Staggered, non-rotated configuration $\Gamma = 3$

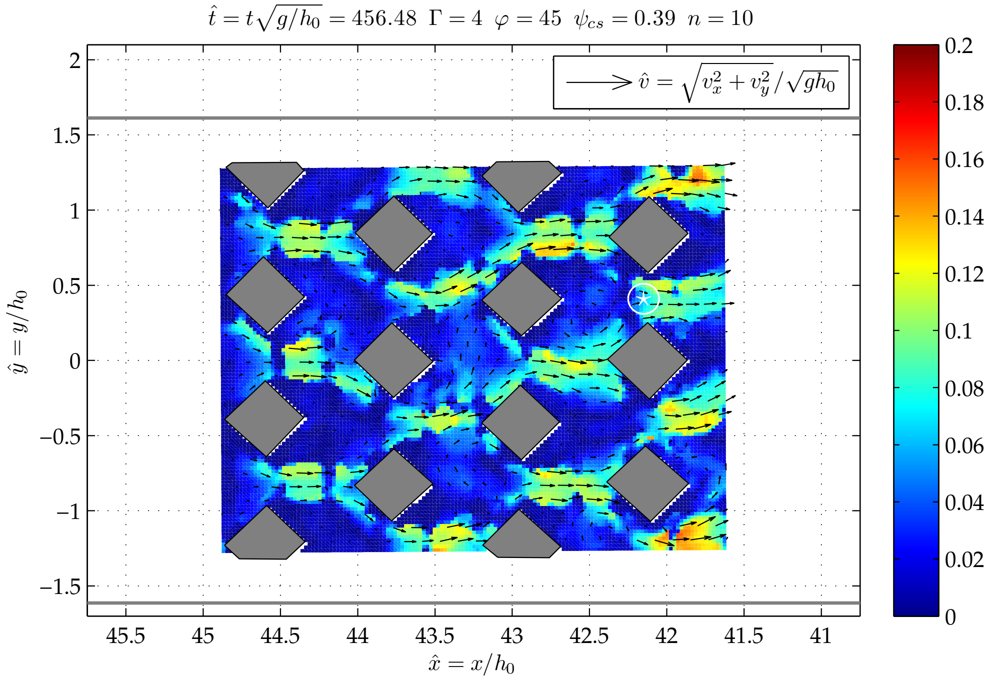

(b) Staggered, rotated configuration $\Gamma = 4$

Figure 5.34 Top-view perspective of the full coverage velocity field around staggered macro-roughness element configurations, the wave run-up direction is from the right to the left.

tal runs that the run-up tongue varied intermittently. This also finds expression in the maximum run-up spread, which is reported herein as a mean of the lowest and highest maximum run-up (cp. also Annex D).

One could conjecture that the front variations are due to the flume geometry and the $180°$, but two facts contradict this assumption. Firstly, the velocity profiles given in Subsection 5.1.4 measured at the beach toe show remarkable uniform characteristics and secondly the variations were not limited to one side of a flume wall but changed from experiment to experiment. A reason for the run-up tongue variations have to be seen instead in the complex interaction at the air-water-beach contact line.

5.5.2 Velocity Time Series

In order to highlight the velocity increase in-between the obstacles onshore Figs. 5.35(a) and 5.35(b) compare the time series of the dimensionless velocity magnitude for a virtual onshore gauge. The comparison groups the cases according to the rotation angle φ of the obstacles. As a reference, the undisturbed case without the presence of macro-roughness elements is chosen. The virtual gauge locations are also indicated in Figs. 5.33 and 5.34. It should be mentioned that the different lengths of the time series result from instabilities of the PIV method. These instabilities have their origin in reflections on the water surface due to fast flow velocities.

It is observed that the velocity gradient or the acceleration is greater for the cases $\Gamma = 1, 3$ in comparison to the undisturbed beach at the considered virtual gauge. In the cases $\Gamma = 1, 3$ the differences associated with the aligned or staggered arrangement of the obstacle configurations are rather small. It turns out that the velocity magnitude constantly decreases with advanced time. The turning point of the velocity direction, which is indicated by zero velocity with an ensuing increase in velocity, is almost identical for all displayed cases no matter if obstacles are present onshore. in the non-rotated cases. A little yet notable time shift is found for these cases $\Gamma = 2, 4$. A clearer time shift is detectable for the staggered, rotated case. Again the gradient of the velocity magnitude is more pronounced once obstacles are involved onshore.

5.5.3 Summary and Conclusions

The velocity fields were deduced by means of standard particle image velocimetry. The interaction of the flow induced by the approaching wave climbing the $1/40$ beach was studied in detail around the obstacles for four different macro-roughness configurations. In general, it was found that an increase in flow velocities is anticipated

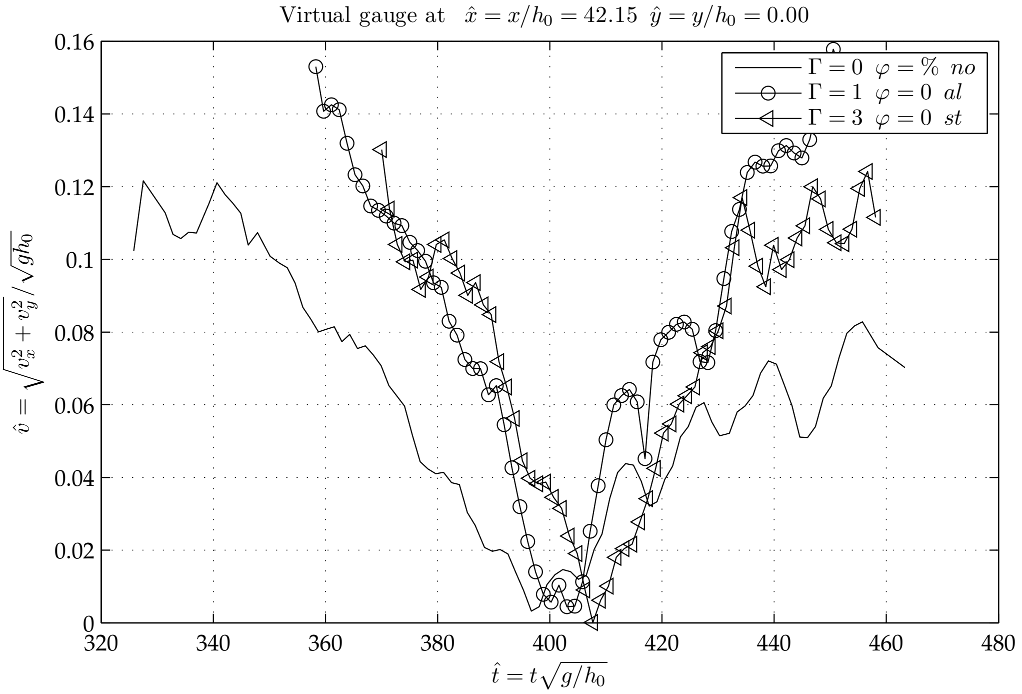

(a) No macro-roughness compared with $\Gamma = 1, 3$

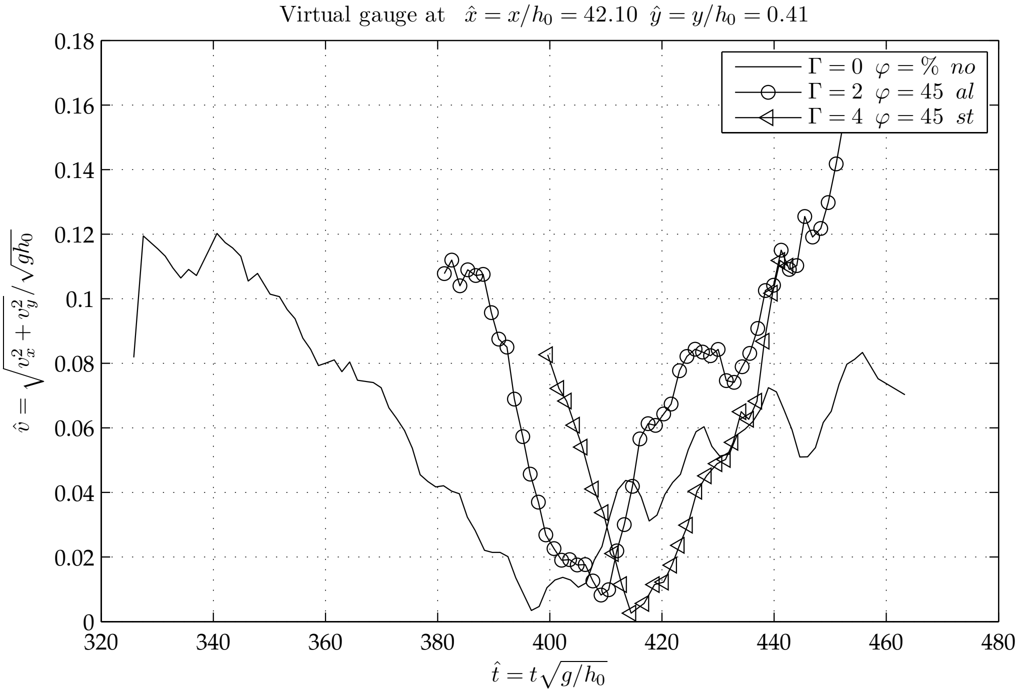

(b) No macro-roughness compared with $\Gamma = 2, 4$

Figure 5.35 Time series comparisons of the dimensionless velocity magnitude at a virtual onshore gauges for the cases $\Gamma = 1 - 4$ with the undisturbed condition without macro-roughness elements once a significant cross-shore obstruction ratio is present onshore. An aligned, non-rotated configuration allows for the highest increase in flow velocity whereas with staggered and additionally rotated configurations the tendency to high velocities significantly decreases. This is caused by the transversal interactions of the predominant flow colliding on the obstacle faces.

The velocities in the laboratory reach a maximum value of approximately $\hat{t} = 0.2$. Under laboratory conditions including the given water level of $h_0 = 0.31$ m, the acceleration due to gravity and the applied Froude scaling law prototype velocities of approximately $v_P = 3.5$ m/s are likely for the presented wave condition of $\epsilon = 0.058$. Higher velocities are anticipated in cases of higher non-linearity due to steeper water surface gradients which however are not presented in this thesis. As a justification of these values only two publications should be mentioned which deal with flow velocity distributions in densely developed built-up areas.

The former, Fritz et al. (2006) presented an investigation considering the flow dynamics of the inundation in the city of Banda Aceh during the 2004 Indian Ocean tsunami. The authors reported flow velocities which are in the range of $v_P = 2.0 - 5.0$ m/s. This range of indicated flow velocities agrees well with the velocities found in this laboratory study although it is not analyzed in detail how the incident wave non-linearity was for the specific event nor how the bottom gradient at the investigated area was. Nevertheless it appears that the prototype velocities during a realistic tsunami event can be adequately reproduced in the laboratory with the proposed wave generation scheme.

The latter, Matsutomi et al. (2006) analyzed the 2004 Indian Ocean tsunami in the regions of southern Thailand and northern Sumatra. The authors estimated the flow velocities by means of an empirical formula which relates the specific velocities around houses to the water levels at the front and the back of the obstacles. The range of velocities which were reported in their paper were generally higher than those of Fritz et al. (2006). Yet it was not explicitly stated if the applied empirical formula was already validated against commonly accepted benchmark data sets. Overall the agreement with the higher velocities reported in this second piece of literature resides in a similar range, which is notable. Remaining variations should be contributed to the various differences between the prototype situation and the academic setting of the study of idealized macro-roughness configurations.

6 Summary and Outlook

6.1 Summary

The objective of this study was the analysis of the interaction between the long wave run-up on a plane beach and coastal urban structures. Long quasi-periodic waves of a single period were utilized to study the wave motion, in contrast to many previous studies in literature which adopted solitary waves to represent tsunami in downscaled laboratory models. The interaction of macro-roughness elements, mimicking coastal urban settlements, with these waves is the focal point of the study. Additionally, the behavior of the long waves was also investigated when climbing up a plane beach fully undisturbed. Generally the application of solitary waves was discarded because the temporal and spatial scales of these waves are in most cases not suitable to adequately represent tsunami impact to coasts. Yet the generation of more suitable long waves or wave trains was determined to lack sufficient stroke capacity. No wavemaker design was investigated to serve the purpose of generating waves which represent wave motions with periods of $6-30\ \mathrm{min}$ in the prototype and in a water depth of $\approx h_0 = 30\ \mathrm{m}$.

The investigation of the above described objective attained several main results. There from, the following basic conclusions can be drawn:

1. A novel volume-driven wave generation methodology is proposed. The generation of arbitrary long waves is achieved by means of pipe pumps which accelerate or decelerate a volume of water in horizontal direction under the control of a feedback loop system. It accounts for the fact that tsunami are basically shallow water waves where the particle velocity is homogeneously distributed over the water depth. The experimental reproduction of numerically deduced surface elevation time series proved the applicability of the novel wave generation technique.

2. The reflection of sinusoidal waves of different wave amplitudes was studied for a $1/40$ sloping beach. The calculated reflection coefficients in the range of

$K_r = 0.57 - 0.62$ are found to be smaller than expected. The analysis of reflectivity bases on the assumption that the waves are short compared to the beach spread and that the reflection occurs at a specific point on a beach or a coastal structure. The climb of long waves on mild sloping beaches violates this assumption. The reflection coefficient slightly increases under the presence of macro-roughness elements although it is not clear if the applied approach allows for the correct determination.

3. The experimentally determined relative run-up of sinusoidal waves on a plane beach without macro-roughness elements agrees well with an analytical theory by Madsen and Schäffer (2010). For the first time this theoretical approach is successfully validated by experimental means.

4. An empirical supplement to the theoretical formula by Madsen and Schäffer (2010) is determined which improves the fit of the experimental data to the analytical approach. It allows for the prediction of the run-up of long waves without the common tie of solitary waves between the non-linearity and the effective duration of the wave. It reads

$$\frac{R_{\text{up/down}}}{A_0} = \chi_{\text{elev}} \pi^{1/4} \left(\frac{A_0}{h_0} \right)^{-1/\left(4+\epsilon^{2/3}\right)} \xi^{-1/\left(2+\epsilon^{2/3}\right)2} \tag{6.1.1}$$

5. The relative run-up of long sinusoidal waves is significantly influenced by the presence of macro-roughness elements onshore. Nomograms are designed to allow for the determination of the relative run-up reduction for four different macro-roughness element configurations, various distances between the single obstacles and a range of wave non-linearities. Simple yet idealized predictions of the reduction of long waves due to macro-roughness element configurations are therewith made possible.

6. The differences in the water levels in front of the first macro-roughness row with regard to an undisturbed run-up case are significant and they vary in time in relation to the phases of the wave dynamics. Additionally, a shock wave is generated as soon as the wave tongue reaches the first row of macro-roughness elements and it propagates seawards.

7. The study includes the qualitative analysis of the temporal variation of the flow field around macro-roughness element configuration. The comparison of the hydrodynamic features associated with the properties of the macro-roughness

configurations allows for conclusions on the energy loss during the interaction of the wave and the obstacles. What is more, for one wave condition quantitative results are presented to highlight the increase of velocities in-between the obstructed area compared with the undisturbed run-up case. This velocity increase is found to be significant. Hence the impact of long waves on the investigated, idealized urban area would also increase. This finding substantiates the demand for further investigations in the field of building resistance and adaptations of existing building codes.

8. Finally the experimental datasets are of paramount importance for future numerical models to be validated and calibrated in order to increase the reliability of their numerical results. In this context it is also important to assess the correct numerical reproduction of the vertically orientated obstacle faces. Only after a careful calibration, numerical models are then in principle able to model greater coastal stretches to develop inundation and hazard maps.

6.2 Outlook

Idealized urban settlement configurations in the interaction with the run-up of long waves are addressed in this thesis, which are represented by means of solid, cubic blocks. In the first approximation the idealization validly represents coastal urban settlements which are frequently affected by tsunami incidents. Yet from the analysis of model and scale effects it is apparent that limitations exist due to the chosen length scale of the down-scaled model. Physical models at a greater scale are therefore preferable although it is acknowledged that laboratory space is a limiting factor.

It belongs to the character of laboratory idealizations that some aspects of the prototype process are neglected. Among these aspects are influences stemming from the collapse of buildings, the transport of sediment and debris, the volumetric disequilibrium between solid blocks (in the present model) and common buildings (in prototype), three-dimensional influences of river estuaries or heterogeneous existing developments, different building orientations and dimensions, the overflow of developments and spatially or temporally varying surface gradients. Some of these sub-processes are most likely to alter the findings of this thesis. These sub-processes imply the demand to enhance future physical modeling attempts.

Nevertheless, the demand for the prediction of the inundation spread and the vertical run-up of tsunami remains unchanged because the implications for human beings are still serious. In this context the current finding depicts an important step towards a better understanding of the underlying physical processes and the influence of energy dissipation stemming from macro-roughness elements. In the following an outlook to subsequent research objectives is given in order to point to further research demand.

1. The developed volume-driven wave generation technique has to be applied to the generation of even longer and shorter waves in order to demonstrate and justify the capabilities and limits.
2. The influence of the beach slope $\tan\beta$ and the duration of the waves to the relative wave run-up over the entire range of surf similarity parameters has to be elaborated on in further studies to fully substantiate the validity of the theory.
3. The volumetric disequilibrium between solid blocks (in the present model) and common buildings (in prototype) remains unclear. On the one hand it is important to assess the effects to the relative wave run-up whereas on the other hand it has to be questioned if such a influence can be correctly studied with a length scale of say $1:100$.
4. The estimation of the head loss of the macro-roughness area in the long-shore direction might be possibly accomplished by means of the Borda-Carnot equation in accordance with the findings of Soares-Frazão et al. (2008). The energetic view of the run-up process through the macro-roughness element area could yield further insight into the physical process.

7 Bibliography

Abadie, S., Morichon, D., Grilli, S., and Glockner, S. (2008). VOF/Navier-Stokes numerical modeling of surface waves generated by subaerial landslides. *Houille Blanche*, 1(1):21–26.

Allen, R., Davies, T., and Horn, C. (1992). The design of a control system for small hydraulic models. *Measurement Science and Technology*, 3:1098–1102.

Allsop, W., Rossetto, T., Robinson, D., Charvet, I., and Bazin, P.-H. (2008). A unique tsunami generator for physical modeling of violent flows and their impact. In *Proceedings of the 14th World Conference on Earthquake Engineering*, Beijing, China.

Ang, K., Chong, G., and Li, Y. (2005). PID control system analysis, design, and technology. *IEEE Transactions on Control Systems Technology*, 13(4):559–576.

Arnason, H. (2005). *Interactions between an incident bore and a freestanding coastal structure*. PhD thesis, Univ. of Washington, Seattle.

Åström, K. J. and Hägglund, T. (1995). *PID Controllers: Theory, Design, and Tuning*. Instrument Socitey of Amerika, 2nd edition.

Baldock, T. E. and Simmonds, D. J. (1999). Separation of incident and reflected waves over sloping bathymetry. *Coastal Engineering*, 38(3):167 – 176.

Battjes, J. A. (1974). Surf similarity. In *Proceedings of the 14th International Conference on Coastal Engineering*, volume 1, pages 466–480. ASCE.

Battjes, J. A. and Roos, A. (1971). Characteristics of flow in the run-up of periodic waves. Technical Report 75-3, Dept. of Civil Engineering, Delft University of Technology. 160 pp.

Bernard, E., Mofjeld, H., Titov, V., Synolakis, C., Gonzalez, F., Purvis, M., Sharpe, J., Mayberry, G., and Robertson, R. (2006). Tsunami: Scientific frontiers, mitigation, forecasting and policy implications. *Philosophical Transactions of the Royal Society A: Mathematical, Physical and Engineering Sciences*, 364(1845):1989–2007.

Biesel, F. (1949). Calcul de l'ammortissement d'une houle dans un liquide visqueux de profondeur finie. *La Houille Blanche*, 4.

Bollrich, G. (2000). *Technische Hydromechanik*. Verlag für Bauwesen, Berlin, 4^{th} edition.

Born, M. and Wolf, E. (2002). *Principles of Optics: Electromagnetic Theory of Propagation, Interference and Diffraction of Light*. Cambridge University Press, 7th edition.

Borrero, J. C., Sieh, K., Chlieh, M., and Synolakis, C. E. (2006). Tsunami inundation modeling for western Sumatra. *Proceedings of the National Academy of Science of the United States of America*, 103(52):19673–19677.

Briechle, S. R. (2006). *Die Fächenhafte Ausbreitung der Flutwelle nach Versagen von Hochwasserschutzeinrichtungen an Fliessgewässern*. PhD thesis, Rheinisch-Westfälischen Technischen Hochschule Aachen.

Briggs, M., Synolakis, C., Harkins, G., and Green, D. (1995a). Laboratory experiments of tsunami runup on a circular island. *Pure and applied geophysics*, 144(3-4):569–593.

Briggs, M. J., Synolakis, C. E., Harkins, G. S., , and Hughes, S. A. (1995b). Large-scale, three-dimensional laboratory measurements of tsunami. In *Tsunamis: Progress in prediction, disaster prevention and warning*, pages 129–149. Kluwer Academic, Dordrecht, The Netherlands.

Briggs, M. J., Synolakis, C. E., and Hughes, S. A. (1993). Laboratory measurements of tsunami runup. In *Tsunami '93 Proceedings*, pages 585–598, Wakayama, Japan.

Bronštein, I. and Semendjaev, K. (2001). *Taschenbuch der Mathematik*. Verlag Harri Deutsch, 5th edition.

Bryant, E. (2008). *Tsunami - The Underrated Hazard*. Springer, Berlin Heidelberg New York, 2nd edition.

Bung, D. (2009). *Zur selbstbelüfteten Gerinneströmung auf Kaskaden mit gemäßigter Neigung*. PhD thesis, Bergische Universität Wuppertal, Aachen. Bericht Nr. 16, Shaker Verlag.

Camfield, F. and Street, R. (1969). Shoaling of solitary waves on small slopes. *Journal of the Waterways and Harbour division*, 1:1–22.

Carrier, G. F. and Greenspan, H. P. (1958). Water waves of finite amplitude on a sloping beach. *Journal of Fluid Mechanics*, 4(1):97–109.

CEM U.S. Army Corps (2002). *U.S. Army Corps of Engineers Coastal Engineering Manual*. U.S. Army Corps of Engineers, Washington, D.C. Engineer Manual 1110-2-1100 (in 6 volumes).

Chanson, H. (2006). Tsunami surges on dry coastal plains: Application of dam break wave equations. *Coastal Engineering Journal*, 48(4):355–370.

Chanson, H., Aoki, S.-I., and Maruyama, M. (2003). An experimental study of tsunami runup on dry and wet horizontal coastlines. *Science of Tsunami Hazards*, 20(5):278–293.

Chow, V. T. (1959). *Open-channel hydraulics*. McGraw-Hill Book Company, Inc. New York, Toronto, London.

Cox, D., Tomita, T., Lynett, P., and Holman, R. (2009). Tsunami inundation with macroroughness in the constructed environment. In Smith, J. M., editor, *Proceedings of the International Conference on Coastal engineering*, volume 2, pages 1421–1432. World Scientific.

Cuypers, K. (2004). Breakwater stability under tsunami attack for a site in nicaragua. Master's thesis, Technical University of Delft.

Dalrymple, R. A. (1989). Directional wavemaker theory with sidewall reflection. *Journal of Hydraulic Research*, 27(1):23–34.

Dean, R. and Dalrymple, R. (1991). *Water Wave Mechanics for Engineers and Scientists*. World Scientific.

Dingemans, M. W. (1997). *Water wave propagation over uneven bottom*, volume Part 1 - Linear wave propagation of *Advanced Series on Ocean Engineering - Vol. 13*. World Scientific, Singapore, New Jersey, London, Hong Kong.

Doyle, J., Francis, B., and Tannenbaum, A. (1990). *Feedback Control Theory*. Macmillan Publishing Co.

Fenton, J. and Rienecker, M. (1982). A fourier method for solving nonlinear water-wave problems: application to solitary-wave interactions. *J. of Fluid Mechanics*, 118:411–443.

Flandrin, P., Rilling, G., and Gonçalvés, P. (2004). Empirical mode decomposition as a filter bank. *IEEE Signal Processing Letters*, 11(2 PART I):112–114.

Fraccarollo, L. and Toro, E. F. (1995). Experimental and numerical assessment of the shallow water model for two-dimensional dam-break type problems. *Journal of Hydraulic Research*, 33(6):843 – 864.

Freeman, J. and Le Méhauté, B. (1964). Wave breakers on a beach and surges on a dry bed. *Journal of Hydraulics Div.*, 90:187–216. ASCE.

Frigaard, P. and Brorsen, M. (1995). A time-domain method for separating incident and reflected irregular waves. *Coastal Engineering*, 24(3-4):205 – 215.

Fritz, H. M., Borrero, J. C., Synolakis, C. E., and Yoo, J. (2006). 2004 Indian Ocean tsunami flow velocity measurements from survivor videos. *Geophysical Research Letters*, 33:L24605.

Fuhrman, D. R. and Madsen, P. A. (2008). Surf similarity and solitary wave runup. *Journal of Waterway, Port, Coastal, and Ocean Engineering*, 134(3):195–198.

Fujima, K. (2001). Long wave propagation on large roughness. In Whitney, R. L., editor, *Proceedings of the International Tsunami Symposium*, pages 891–895.

Fujita, I., Muste, M., and Kruger, A. (1998). Large-scale particle image velocimetry for flow analysis in hydraulic engineering applications. *Journal of Hydraulic Research*, 36(3):397–414.

Galvin, C. J. (1964). Wave-height prediction for wave generators in shallow waters. Technical Memorandum 4, U.S. Army, Coastal Engineering Research Center.

Gedik, N., Irtem, E., and Kabdasli, S. (2005). Laboratory investigation on tsunami run-up. *Ocean Engineering*, 32(5-6):513 – 528.

Goda, Y. and Suzuki, Y. (1976). Estimation of incident and reflected waves in random wave experiments. In *Proceedings of the 15th Conference on Coastal Engineering*, volume 1, pages 828–845, Honolulu.

Goldstein, R. J., editor (1996). *Fluid mechanics measurements*. Taylor & Francis, 2 edition.

Gomez-Gesteira, M. and Dalrymple, R. A. (2004). Using a three-dimensional smoothed particle hydrodynamics method for wave impact on a tall structure. *Journal of Waterway, Port, Coastal, and Ocean Engineering*, 130(2):63–69.

Goring, D. G. (1979). *Tsunamis–the propagation of long waves onto a shelf.* PhD thesis, California Institute of Technology, Pasadena, California.

Goseberg, N. and Schlurmann, T. (2008). Relevant factors on the extent of inundation based on tsunami scenarios for the city of padang, west sumatra. In *Proceedings of the International Conference on Tsunami Warning (ICTW)*, Bali, Indonesia.

Goseberg, N. and Schlurmann, T. (2009). Enhanced hazard mapping on a medium-resolved numerical grid for the city of padang, west sumatra. *Journal of Ship Technology*, 5(2):13–21.

Goseberg, N. and Schlurmann, T. (2010). Numerical and experimental study on tsunami run-up and inundation influenced by macro roughness elements. In Lynett, P. and Smith, J. M., editors, *Proceedings of the International Conference on Coastal Engineering*.

Goto, C. and Shuto, N. (1983). Effects of large obstacles on tsunami inundations. In Iida, K. and Iwasaki, T., editors, *Tsunamis: Their Science and Engineering*, chapter Tsunami Run-up, pages 551–525. Terra Science Pub. Co., Tokyo/Reidel, Dordrecht.

Grace, R. (1978). Surface wave heights from pressure records. *Coastal Engineering*, 2(C):55–67.

Guinot, V. and Soares-Frazão, S. (2006). Flux and source term discretization in two-dimensional shallow water models with porosity on unstructured grids. *International Journal for Numerical Methods in Fluids*, 50(3):309–345.

Hall, J. V. and Watts, J. W. (1953). Laboratory investigation of the vertical rise of solitary waves on impermeable slopes. Tech. memo. 33, Beach erosion board, USACE.

Hammack, J. L. (1972). *Tsunamis – A model of their generation and propagation*. PhD thesis, California Institute of Technology, Pasadena, California.

Hammack, J. L. (1973). A note on tsunamis : Their generation and propagation in an ocean of uniform depth. *Journal of Fluid Mechanics*, 60(4):769–800.

Hashimoto, H. and Park, K. (2008). *Flood Recovery, Innovation and Response I*, chapter Two-dimensional urban flood simulation: Fukuoka flood disaster in 1999, pages 369–384. WIT press.

Heinrich, P. (1992). Nonlinear water waves generated by submarine and aerial landslide. *Journal of Waterways, Port, Coast and Ocean Engineering*, 118(3):249–266.

Heitner, K. and Housner, G. (1970). Numerical model for tsunami run-up. *J. Waterw. Harbors Coastal Eng. Div.*, 93(3):701–719. ASCE.

Heller, V. (2007). Massstabseffekte im Hydraulischen Modell. *Wasser Energie Luft*, 99(2):153–160.

Huang, N., Shen, Z., Long, S., Wu, M., Snin, H., Zheng, Q., Yen, N.-C., Tung, C., and Liu, H. (1998). The empirical mode decomposition and the Hilbert spectrum for nonlinear and non-stationary time series analysis. *Proceedings of the Royal Society A: Mathematical, Physical and Engineering Sciences*, 454(1971):903–995.

Hughes, A. (1993a). Laboratory wave reflection analysis using co-located gauges. *Coastal Engineering*, 20:223–247.

Hughes, S. A. (1993b). *Physical Models and Laboratory Techniques in Coastal Engineering*, volume 7 of *Advances in Ocean Engineering*. World Scientific, Scientific Publishing Co. Pte. Ltd., Singapore.

Hughes, S. A. (2004). Estimation of wave run-up on smooth, impermeable slopes using the wave momentum flux parameter. *Coastal Engineering*, 51(11-12):1085 – 1104.

Hunt, I. A. (1959). Design of seawalls and breakwaters. *Journal of Waterways and Harbour Division, ASCE*, 85(3):123–152.

Ippen, A. (1966). *Estuary and coastal hydrodynamics*. Engineering Society monographs. McGraw-Hill Book Company, New York.

Iwasaki, S. (1987). On the estimation of a tsunami generated by underwater landslide. In *Proceedings of the International Tsunami Symposium*, pages 134–138, Vancouver, B.C.

Jakeman, J., Nielsen, O., Putten, K., Mleczko, R., Burbidge, D., and Horspool, N. (2010). Towards spatially distributed quantitative assessment of tsunami inundation models. *Ocean Dynamics*, 60(5):1115–1138.

Kaplan, K. (1955). Generalized laboratory study of tsunami run-up. Technical report, Beach Erosion Board. U.S. Army Corps of Engineers, Tech. Memo 60.

Kinsman, B. (1965). *Wind Waves, Their Generation and Propagation on the Ocean Surface*. Prentice Hall, Inc., Englewood Cliffs, N.J.

Kishi, T. and Saeki, H. (1966). The shoaling, breaking and runup of the solitary wave on impermeable rough slopes. In *Proceedings of the 10th Conference on Coastal Engineering*, volume 1, pages 322–348.

Kobayashi, N. and Karjadi, E. A. (1994). Surf-similarity parameter for breaking solitary-wave runup. *Journal of Waterway, Port, Coastal, and Ocean Engineering*, 120(6):645–650.

Kobus, H. (1974). Anwendung der Dimensionsanalyse in der experimentellen Forschung des Bauingenieurwesens. *Die Bautechnik*, 3:88–94.

Lange, D., W.P., Prasetya, G., and Healy, T. (2001). Modelling of tsunamis generated by pyroclastic flows (ignimbrites). *Natural Hazards*, 24(3):251–266.

Le Méhauté, B. (1976). *An Introduction to Hydrodynamics & Water Waves*. Springer-Verlag New York, Heidelberg, Berlin.

Li, Y. (2000). *Tsunamis: Non-Breaking and Breaking Solitary Wave Run-Up*. PhD thesis, California Institute of Technology, Pasadena, California.

Li, Y. and Raichlen, F. (2001). Solitary wave runup on plane slopes. *Journal of Waterway, Port, Coastal and Ocean Engineering*, 127(1):33–44.

Liu, P. L.-F. (2008). *Advanced numerical models for simulating tsunami waves and runup*, volume 10 of *Advances In Coastal And Ocean Engineering*. World Scientific Publishing Co.

Liu, P. L.-F., Cho, Y.-S., Briggs, M. J., and Synolakis, C. E. (1995). Runup of solitary waves on a circular island. *Journal of Fluid Mechanics*, 302:259–285.

Liu, P. L.-F., Synolakis, C. E., and Yeh, H. H. (1991). Report on the international workshop on long-wave run-up. *Journal of Fluid Mechanics*, 229:675–688.

Lynett, P. J. (2007). Effect of a shallow water obstruction on long wave runup and overland flow velocity. *Journal of Waterway, Port, Coastal and Ocean Engineering*, 133(6):455–462.

Madsen, P. A. and Fuhrman, D. R. (2008). Run-up of tsunamis and long waves in terms of surf-similarity. *Coastal Engineering*, 55(3):209 – 223.

Madsen, P. A., Fuhrman, D. R., and Schäffer, H. A. (2008). On the solitary wave paradigm for tsunamis. *Journal of Geophysical Research C: Oceans*, 113(12):1–22.

Madsen, P. A., Fuhrman, D. R., and Schäffer, H. A. (2009). A critical discussion of the solitary wave paradigm for tsunamis. In Smith, J. M., editor, *Proceedings of the International Conference on Coastal engineering*, volume 2, pages 1262–1274. World Scientific.

Madsen, P. A. and Schäffer, H. A. (2010). Analytical solutions for tsunami runup on a plane beach: single waves, n-waves and transient waves. *Journal of Fluid Mechanics*, 645:27–57.

Mansard, E. and Funke, E. (1980). The measurement of incident and reflected spectra using a least square method. *Proceedings of the 17th Conference on Coastal Engineering*, page 154–172. Reston VA, USA.

Martin, H. and Pohl, R., editors (2009). *Technische Hydromechanik 4 (Hydraulische und numerische Modelle)*. huss-Medien GmbH, 2 edition.

Matsutomi, H., Sakakiyama, T., Nugroho, S., and Matsuyama, M. (2006). Aspects of inundated flow due to the 2004 Indian Ocean tsunami. *Coastal Engineering Journal*, 48(2):167–195.

Mei, C. C., Stiassnie, M., and Yue, D. K.-P. (2005). *Theory and application of ocean surface waves*, volume 23 of *Advanced Series on Ocean Engineering*. Wolrd Scientific.

Monaghan, J. J. and Kos, A. (2000). Scott russell's wave generator. *Physics of Fluids*, 12(3):622–630.

Moronkeji, A. (2007). Physical modelling of tsunami induced sediment transport and scour. In *Proceedings of the 2007 Earthquake Engineering Symposium for Young researchers*.

Muhari, A., Imamura, F., Natawidjaja, D. H., Diposaptono, S., Latief, H., Post, J., and Ismail, F. A. (2010). Tsunami mitigation efforts with pTA in West Sumatra province, Indonesia. *Journal of Earthquake and Tsunami*, 4:341 – 368.

Müller, D. R. (1995). *Auflaufen und Überschwappen von Impulswellen an Talsperren*. Mitteilungen des Instituts, Versuchsanstalt für Wasserbau, Hydrologie und Glaziologie der Eidgenössischen Hochschule Zürich, Zürich. D. Vischer, Editor.

Nakamura, M., Shiraishi, H., and Sasaki, Y. (1969). Hydraulic characteristic of tsunami acting on dikes. In *Proceedings of the 13th IAHR congress*, Japan.

Nistor, I., Palermo, D., al Faesly, T., and Cornett, A. (2009). Modelling of tsunami-induced hydrodynamic forces on buildings. In *33rd IAHR Congress: Water Engineering for a Sustainable Environment*.

Novak, P. and Cabelka, J. (1981). *Models in Hydraulic Engineering - Physical principles and Design Applications*. Pitman, Boston.

Okal, E.A.a, S. C. (2004). Source discriminants for near-field tsunamis. *Geophysical Journal International*, 158(3):899–912.

Oumeraci, H., Schüttrumpf, H., Möller, J., Zimmermann, C., Daemrich, K.-F., and Ohle, N. (2001). Influence of oblique wave attack on wave run-up and wave overtopping - 3D model tests at NRC/Canada with long and short crested waves -. Technical report, Coastal Research Center (FZK), Hannover, Germany. FI Report No. 643 and LWI Report No. 859.

Pagliara, S. and Chiavaccini, P. (2006). Flow resistance of rock chutes with protruding boulders. *Journal of Hydraulic Engineering*, 132(6):545–552.

Peakall, J. and Warburton, J. (1996). Surface tension in small hydraulic river models - the significance of the Weber number. *Journal of Hydrology*, 53(2):199–212.

Pedro, H., Leung, K.-W., Kobayashi, M., and Riggs, H. (2007). Numerical study of the wave impact on a square column using large eddy simulation. In *Proceedings of the International Conference on Offshore Mechanics and Arctic Engineering - OMAE*, volume 3, pages 1015–1021.

Pelinovsky, E. N. and Mazova, R. K. (1992). Exact analytical solution of the nonlinear problems of tsunami wave run-up on slopes with different profiles. *Natural Hazards*, 6:227 – 249.

Plafker, G. (1997). Catastrophic tsunami generated by submarine slides and backarc thrusting during the 1992 earthquake on eastern flores island, indonesia. *Geol. Soc. Am. Cordill. Sect.*, 29(5):57. (Abstract with programme).

Raichlen, F. (1970). Tsunamis: Some laboratory and field observations. In *Proceedings of the 12th Coastal Engineering Conference*, volume 3, pages 2103–2122. American Society of Civil Engineering.

Ramsden, J. (1996). Forces on a vertical wall due to long waves, bores, and dry-bed surges. *Journal of Waterway, Port, Coastal and Ocean Engineering*, 122(3):134–141.

Ramsden, J. D. (1993). *Tsunamis: Forces On A Vertical Wall Caused By Long Waves, Bores, And Surges On A Dry Bed*. PhD thesis, California Institute of Technology, Pasadena, California.

Ramsden, J. D. and Raichlen, F. (1990). Forces on vertical wall caused by incident bores. *Journal of Waterway, Port, Coastal and Ocean Engineering*, 116(5):592–613.

Rehbock, T. (1921). Brückenstau und Walzenbildung. *Der Bauingenieur*, 2(13). Berlin.

Reynolds, O. (1887). On certain laws relating to the regime of rivers and estuaries, and on the possibility of experiments on a small scale. Technical report, British Association Report, United Kingdom.

Riggs, H., Robertson, I. N., Cheung, K. F., Pawlak, G., Young, Y. L., and Yim, S. C. (2008). Experimental simulation of tsunami hazards to buildings and bridges. In *Proceedings of 2008 NSF Engineering Research and Innovation Conference*, Knoxville, Tennessee.

Robertson, I., Riggs, H., and Mohamed, A. (2008). Experimental results of tsunami bore forces on structures. In *Proceedings of the* 27^{th} *International Conference on Offshore Mechanics and Sctic Engineering*, Estoril, Portugal.

Rossetto, T., Allsop, W., Robinson, D., Chavet, I., and Bazin, R.-H. (2009). Analysis of tsunami hazard by modelling tsunami wave effects. In Samuels, P., Huntington, S., Allsop, W., and Harrop, J., editors, *Proceedings of Flood risk Management: Research and Practice*, pages 515–521. Taylor & Francis Group, London.

Russell, J. S. (1845). Report on waves. In *Report of the 14th Meeting of the British Association for the Advancement of Science*, pages 311–390. John Murray, London.

Schlurmann, T. (2005). *Time-Frequency Analysis Methods in Hydrology and Hydraulic Engineering*. Habilitationsschrift, Fachbereich D - Bauingenieurwesen, Bergische Universität Wuppertal.

Schlurmann, T., Kongko, W., Goseberg, N., Natawidjaja, D. H., and Sieh, K. (2010). Near-field tsunami hazard map padang, west sumatra: utilizing high resolution geospatial data and reseasonable source scenarios. In Lynett, P. and Smith, J. M., editors, *Proceedings of the International Conference on Coastal Engineering*.

Schmidt-Koppenhagen, R., Grüne, J., and Oumeraci, H. (2007). Tsunami wave decay in near- and onshore areas. In Smith, J. M., editor, *Proceedings of the International Conference on Coastal engineering*, volume 2, pages 1664–1676. World Scientific.

Schulz, K.-P. (1992). *Maßstabseffekte beim Wellenauflauf auf glatten und rauhen Böschungen*. PhD thesis, Technische Universität Braunschweig, Braunschweig.

Schüttrumpf, H. (2001). *Wellenüberlaufströmung bei Seedeichen - Experimentelle und theoretische Untersuchungen*. PhD thesis, Technischen Universität Carolo-Wilhelmina, Braunschweig.

Schüttrumpf, H. and Oumeraci, H. (2005). Layer thicknesses and velocities of wave overtopping flow at seadikes. *Coastal Engineering*, 52(6):473–495.

Segur, H. (2007). *Tsunami and Nonlinear Waves*. Springer, Berlin Heidelberg New York.

Small, C. and Nicholls, R. J. (2003). A global analysis of human settlement in coastal zones. *Journal of Coastal Research*, 19(3):pp. 584–599.

Soares-Frazão, S., Lhomme, J., Guinot, V., and Zech, Y. (2008). Two-dimensional shallow-water model with porosity for urban flood modelling. *Journal of Hydraulic Research*, 46(1):45–64.

Soares-Frazão, S. and Zech, Y. (2008). Dam-break flow through an idealised city. *Journal of Hydraulic Research*, 46(5):648–658.

Sobey, R. J. (2009). Wetting and drying in coastal flows. *Coastal Engineering*, 56(5-6):565 – 576.

SPM (1977). *Shore Protection Manual*. U.S. Army Corps of Engineers, Washington, D.C., 4 edition. In 2 volumes.

Sunamura, T. and Okazaki, S.-i. (1996). Breaker types and wave reflection coefficient: Laboratory relationships. *Journal of Coastal Research*, 12(1):240–245.

Sveen, J. K. (2004). An introduction to matpiv v.1.6.1. Eprint no. 2, ISSN 0809-4403, Dept. of Mathematics, University of Oslo. http://www.math.uio.no/˜jks/matpiv.

Sveen, J. K. and Cowen, E. A. (2004). *PIV and Water Waves*, chapter Quantitative imaging techniques and their application to wavy flow, pages 1–50. World Scientific.

Svendsen, I. A. (2006). *Introduction to nearshore hydrodynamics*, volume 24 of *Advanced series on ocean engineering*. World Scientific, New Jersey London Singapure.

Synolakis, C. E. (1987). *The runup of long waves*. Dissertation, W. M. Keck Laboratory of Hydraulics and Water Resources, California Institute of Technology.

Synolakis, C. E. (1990). Generation of long waves in laboratory. *Journal of Waterway, Port, Coastal, and Ocean Engineering*, 116(2):252–266.

Synolakis, C. E. and Bernard, E. N. (2006). Tsunami science before and beyond boxing day 2004. *Phil. Trans. R. Soc. A*, 364:2231–2265.

Synolakis, C. E. and Kanoglu, U. (2009). *Nonlinear wave dynamics*. World Scientific Publishing Co. Pte. Ltd., Singapore.

Tadepalli, S. and Synolakis, C. E. (1994). The Run-Up of N-Waves on Sloping Beaches. *Proceedings: Mathematical and Physical Sciences*, 445(1923):99–112.

Taubenböck, H., Goseberg, N., Setiadi, N., Lämmel, G., Moder, F., Oczipka, M., Klüpfel, H., Wahl, R., Schlurmann, T., Strunz, G., Birkmann, J., Nagel, K., Siegert, F., Lehmann, F., Dech, S., Gress, A., and Klein, R. (2009). Last-mile preparation to a potential disaster - interdisciplinary approach towards tsunami early warning and an evacuation information system for the coastal city of padang, indonesia. *Natural Hazards and Earth System Sciences (NHESS)*, 9(4):1509–1528.

Teng, M. H., Feng, K., and Liao, T. I. (2000). Experimental study on long wave run-up on plane beaches. In *Proceedings of the Tenth International Offshore and Polar Engineering Conference*, volume 3, pages 660–664, Seattle, USA.

Testa, G. and, Z. D., Alcrudo, F., Mulet, J., and Soares-Frazão, S. (2007). Flash flood flow experiment in a simplified urban district. *Journal of Hydraulic Research*, 45(SPEC. ISS.):37–44.

Tomita, T. and Honda, K. (2007). Tsunami estimation including effects of coastal structures and buildings by 3d model. In *Proceedings of Coastal Structures*.

Tomita, T., Honda, K., and Kakinuma, T. (2007). Application of three-dimensional tsunami simulator to estimation of tsunami behaviour around structures. In Smith, J. M., editor, *Proceedings of the International Conference on Coastal engineering*, volume 2, pages 1677–1688. World Scientific.

Ursell, F. (1953). The long-wave paradox in the theory of gravity waves. *Mathematical Proceedings of the Cambridge Philosophical Society*, 49:685 – 694.

Ward, S. N. and Day, S. (2008). Tsunami balls: A granular approach to tsunami runup and inundation. *Communications in Computational Physics*, 3(1):222–249.

Watts, P. (2000). Tsunami features of solid block underwater landslides. *Journal of Waterways, Port, Coast and Ocean Engineering*, 126(3):144–152.

Weiss, R., Wünnemann, K., and Bahlburg, H. (2006). Numerical modelling of generation, propagation and run-up of tsunamis caused by oceanic impacts: model strategy and technical solutions. *Geophysical Journal International*, 167(1):77–88.

Weitbrecht, V., Kühn, G., and Jirka, G. (2002). Large scale piv-measurements at the surface of shallow water flows. *Flow Measurement and Instrumentation*, 13(5-6):237–245.

Westerweel, J. (1993). *Digital Particle Image Velocimetry - Theory and Application*. PhD thesis, Delft University of Technology, The Netherlands.

Wiegel, R. (1964). *Oceanographical Engineering*. International Series in Theoretical and applied Mechanics. Prentice-Hall Inc., Englewood Cliffs, N.J.

Wiegel, R. L. (1955). Laboratory studies of gravity waves generated by the movement of a submarine body. *Transactions of the American Geophysical Union*, 36(5):759–774.

Wilkie, M. J. and Young, G. A. J. (1992). Pneumatic tide generator. *The engineer*, 11:133ff.

Wu, T. Y. (1981). Long waves in ocean and coastal waters. *Journal of the Engineering Mechanics Division, Proceedings of the American Society of Civil Engineers*, 107(EM 3):501 – 523.

Wu, Z. and Huang, N. E. (2009). Ensemble empirical mode decomposition: A noise-assisted data analysis method. *Advances in Adaptive Data Analysis*, 1(1):1–41.

Xiao, H. and Huang, W. (2008). Numerical modeling of wave runup and forces on an idealized beachfront house. *Ocean Engineering*, 35(1):106–116.

Yalin, M. (1971). *Theory of Hydraulic Models*. The Macmillan Press Ltd., London and Basingstoke.

Yeh, H. (2006). Maximum fluid forces in the tsunami runup zone. *Journal of Waterway, Port, Coastal, and Ocean Engineering*, 132(6):496–500.

Yeh, H., Ghazali, A., and Marton, I. (1989). Experimental study of bore run-up. *Journal of Fluid Mechanics*, 206:563–578.

Yeh, H., Liu, P., Briggs, M., and Synolakis, C. (1994). Propagation and amplification of tsunamis at coastal boundaries. *Nature*, 372(6504):353–355.

Yeh, H., Liu, P. L. F., and Synolakis, C. (1995). *Long-wave runup models*. World Scientific, Singapore, River Edge, New York.

Zelt, J. A. and Raichlen, F. (1991). Overland flow from solitary waves. *Journal of Waterway, Port, Coastal, and Ocean Engineering*, 117(3):247–263.

Appendices

A General Technical Drawings

The annex is provided in order to highlight the technical design and the equipment of the applied wave flume. Furthermore a circuit layout of the software based portion of the long wave control is given. An extra drawing of the positioning of the EMS probe at the beach toe is also attached.

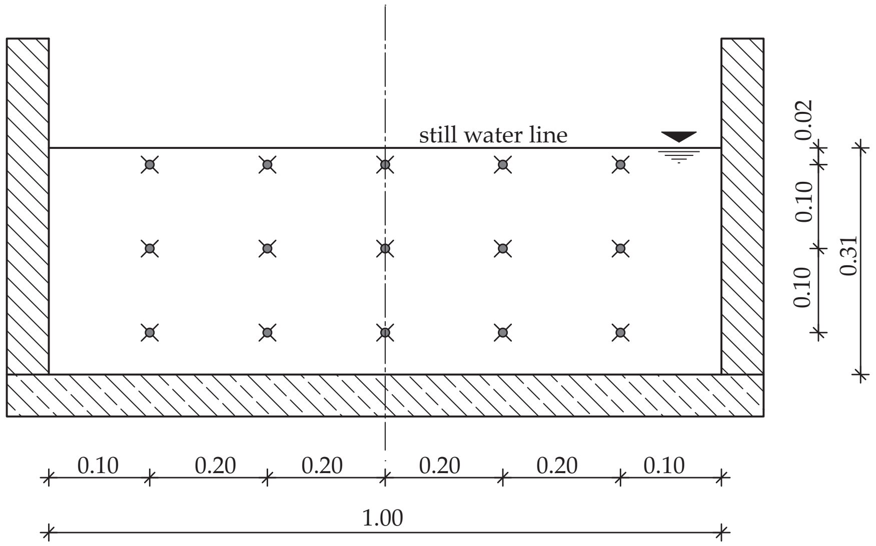

Figure A.1 Detailed positioning of the EMS probe at the beach toe for the analysis of the velocity distribution after the flume bend

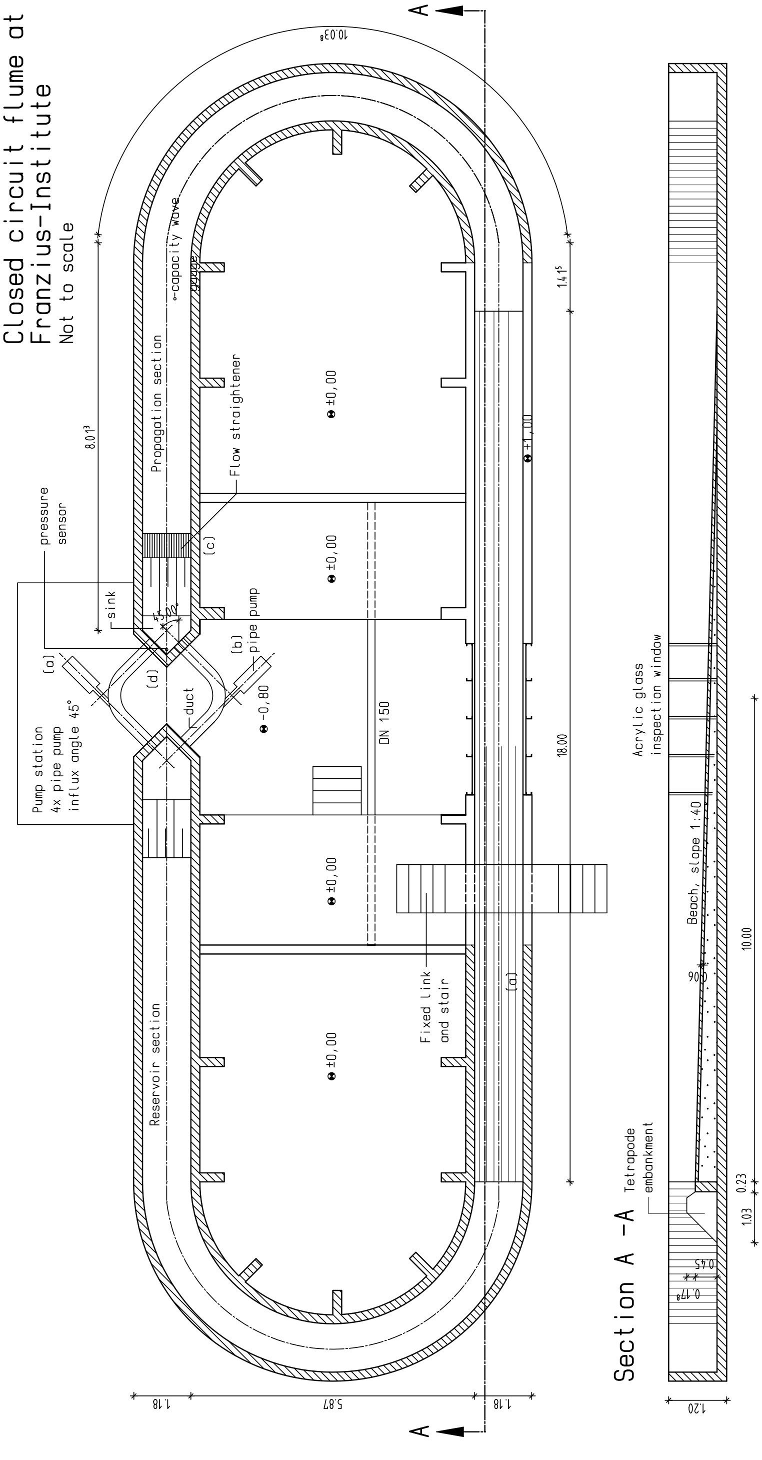

Figure A.2 Technical drawing of the closed-circuit flume, plan view of the facility and a cross section of the ramp

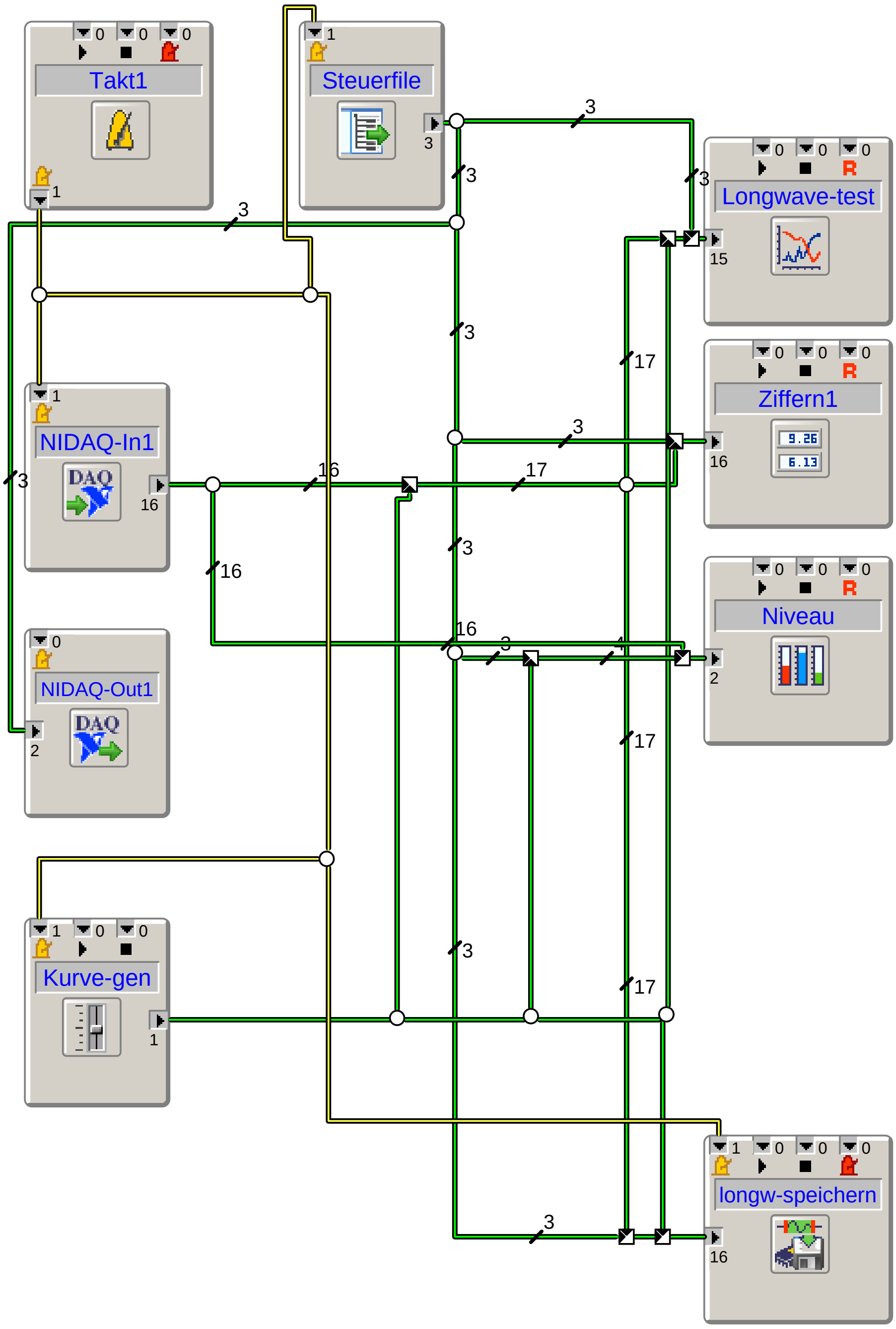

Figure A.3 Circuit layout of the software based portion of the long wave control with yellow channels for clock frequency transmission and green channels depicting data stream, circuit blocks for input/output, data storage, clock generation and visualisation

B Macro-Roughness Element Configurations

In total 35 different macro-roughness element configurations were used for the experiments. The variation of the single concrete blocks on the shore was determined by the distance b_{st} of the elements to each other, the number of element rows n, the angle of the macro-roughness elements to the approaching wave φ and the choice whether the rows were arranged staggered or aligned. For the sake of completeness these 35 configurations were drawn to $1/40$ scale in order to facilitate the perception of the macro-roughness configuration.

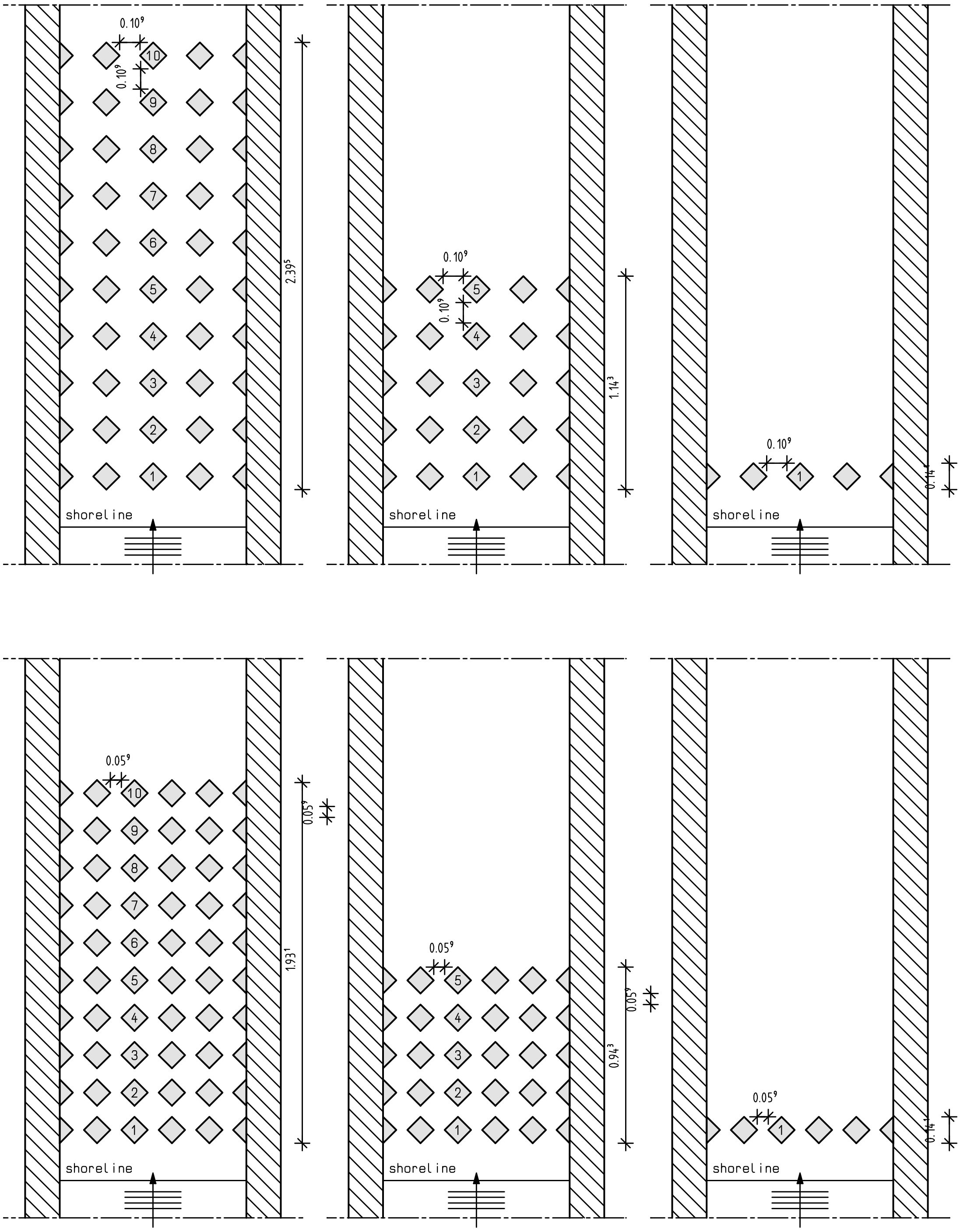

Figure B.1 Utilized macro-roughness configurations with aligned, rotated element arrangement for cases with 10.9 cm and 5.9 cm street width, 10, 5 and 1 macro-roughness element rows, configuration drawn to scale 1/40

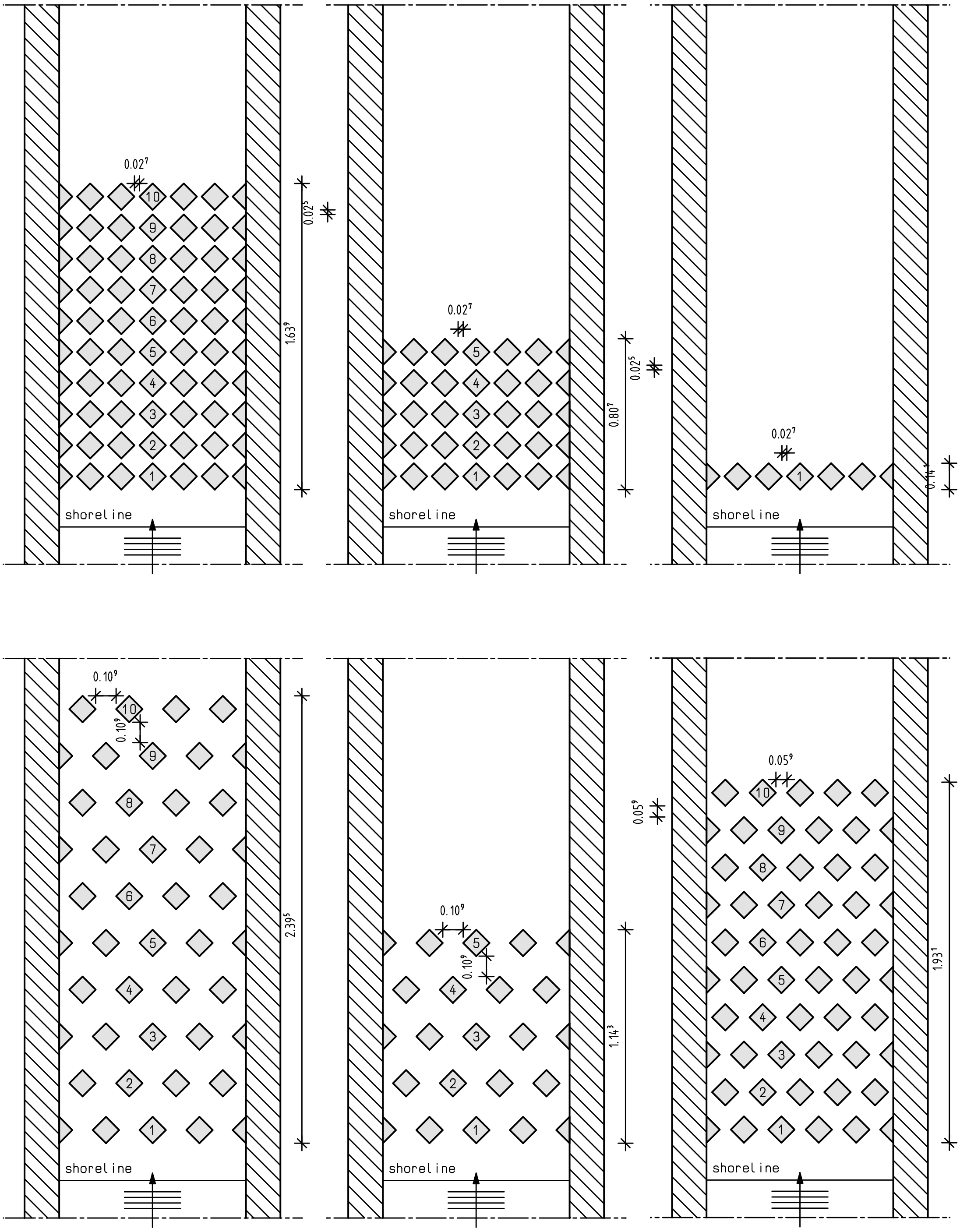

Figure B.2 Utilized macro-roughness configurations with aligned/staggered, non-rotated element arrangement for the cases with 2.5 cm, 5.9 cm and 10.9 cm street width, 10, 5 and 1 macro-roughness element rows, configuration drawn to scale 1/40

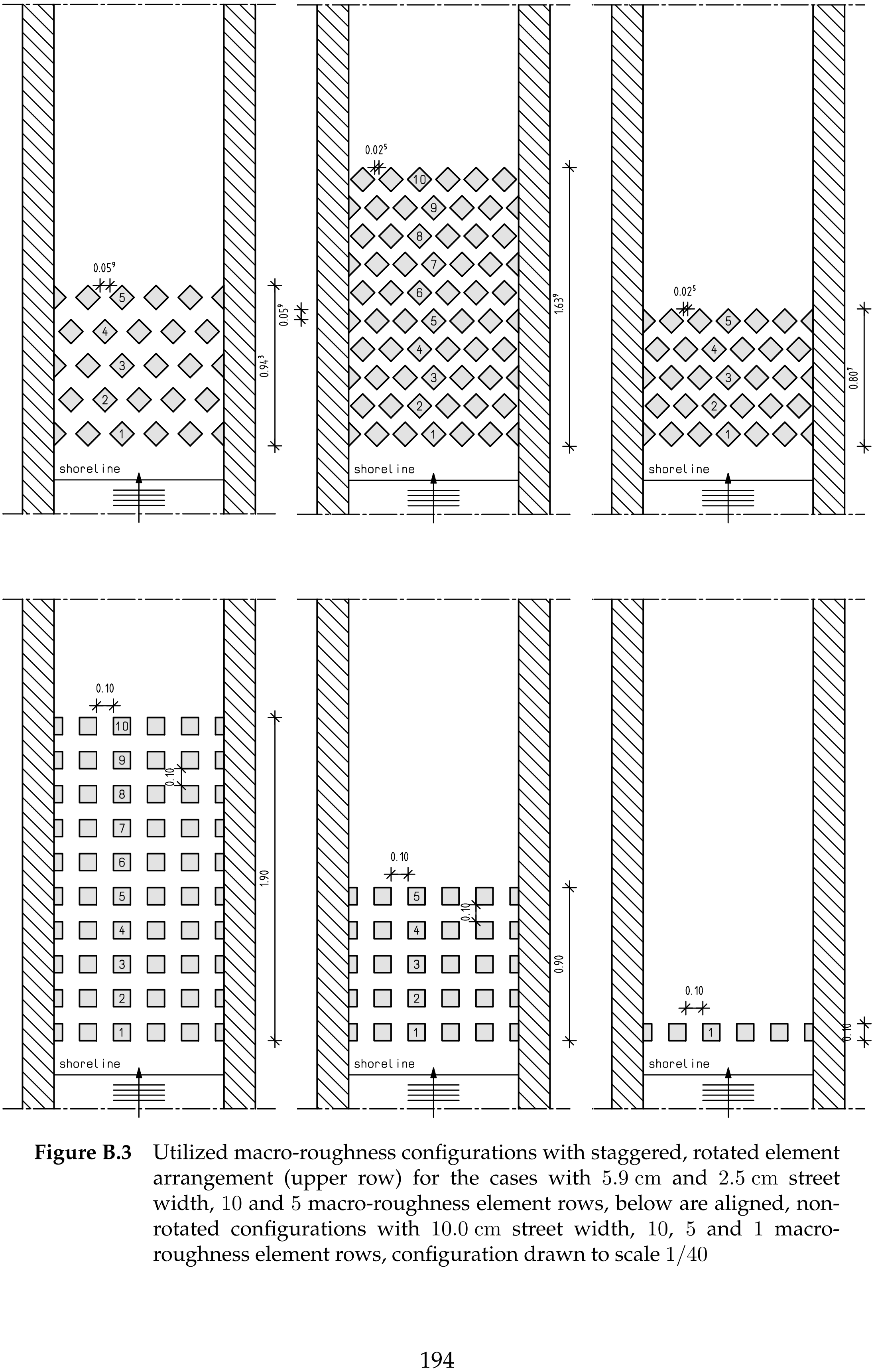

Figure B.3 Utilized macro-roughness configurations with staggered, rotated element arrangement (upper row) for the cases with $5.9\,\mathrm{cm}$ and $2.5\,\mathrm{cm}$ street width, 10 and 5 macro-roughness element rows, below are aligned, non-rotated configurations with $10.0\,\mathrm{cm}$ street width, 10, 5 and 1 macro-roughness element rows, configuration drawn to scale $1/40$

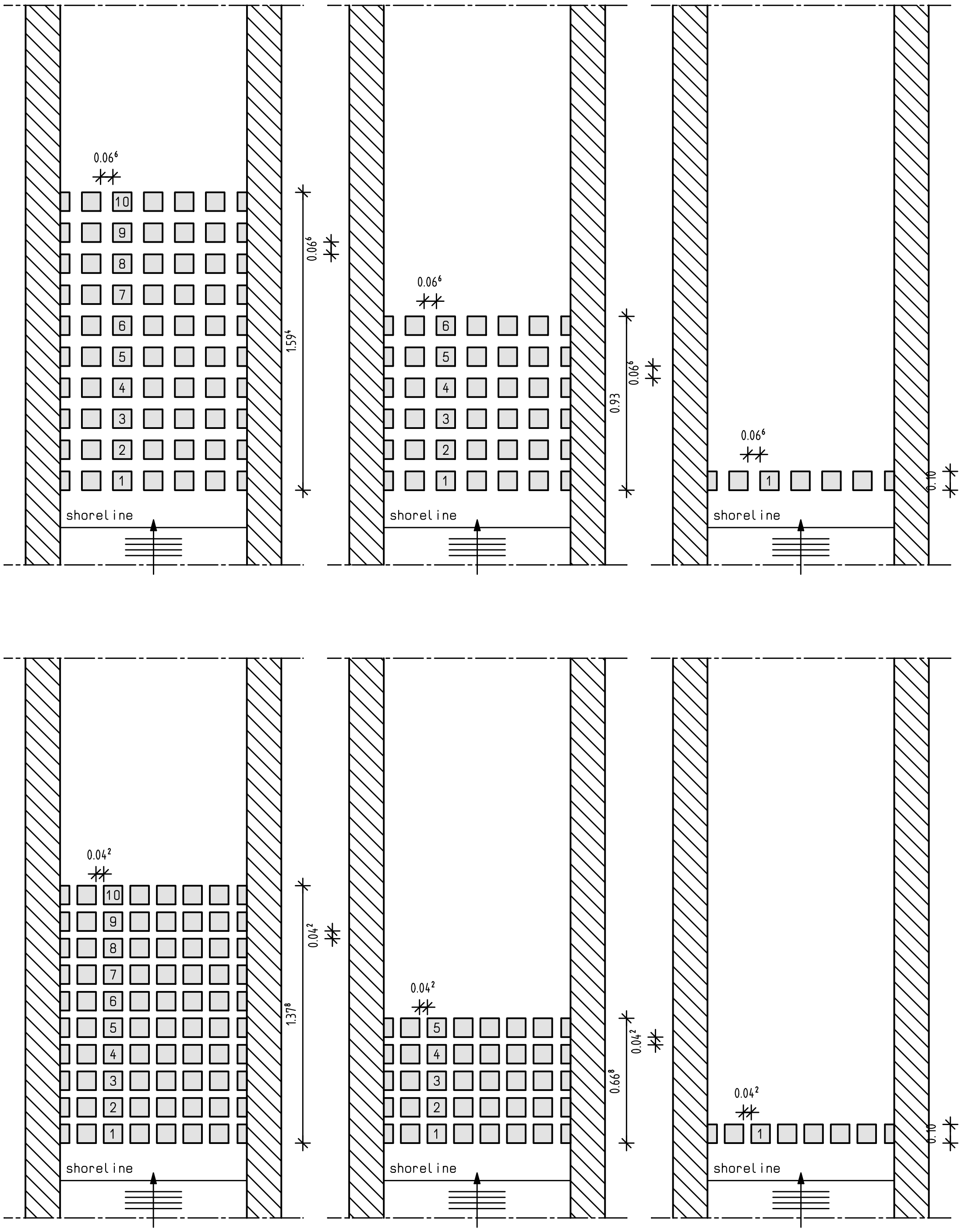

Figure B.4 Utilized macro-roughness configurations with aligned, non-rotated element arrangement for the cases with 6.6 cm (above) and 4.2 cm (below) street width, 10, 5 and 1 macro-roughness element rows

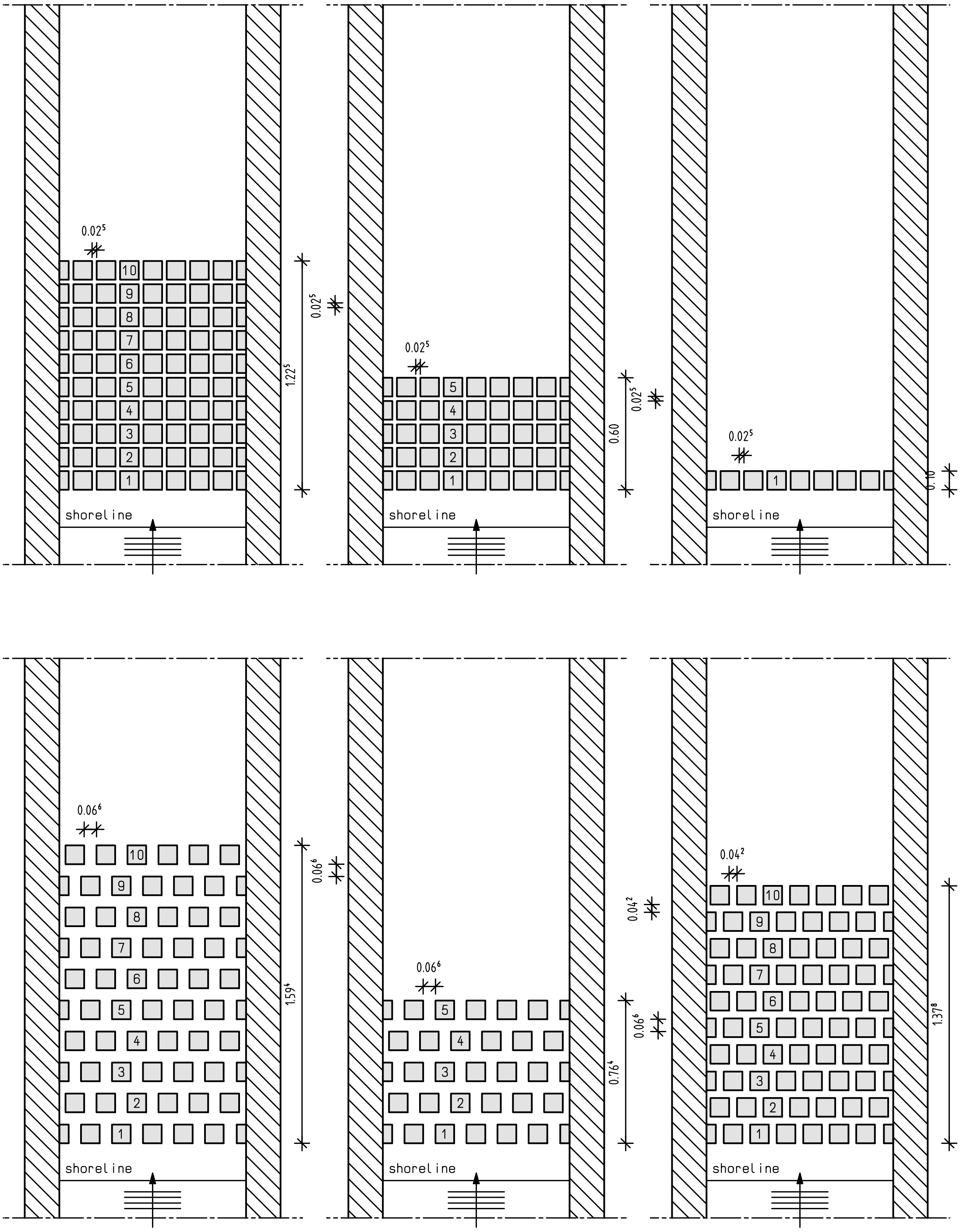

Figure B.5 Utilized macro-roughness configurations with aligned, non-rotated element arrangement (upper row) for the case with 2.5 cm street width, 10, 5 and 1 macro-roughness element rows, below are staggered, non-rotated configurations with 6.6 cm and 4.2 cm street width, 10 and 5 macro-roughness element rows, configuration drawn to scale $1/40$

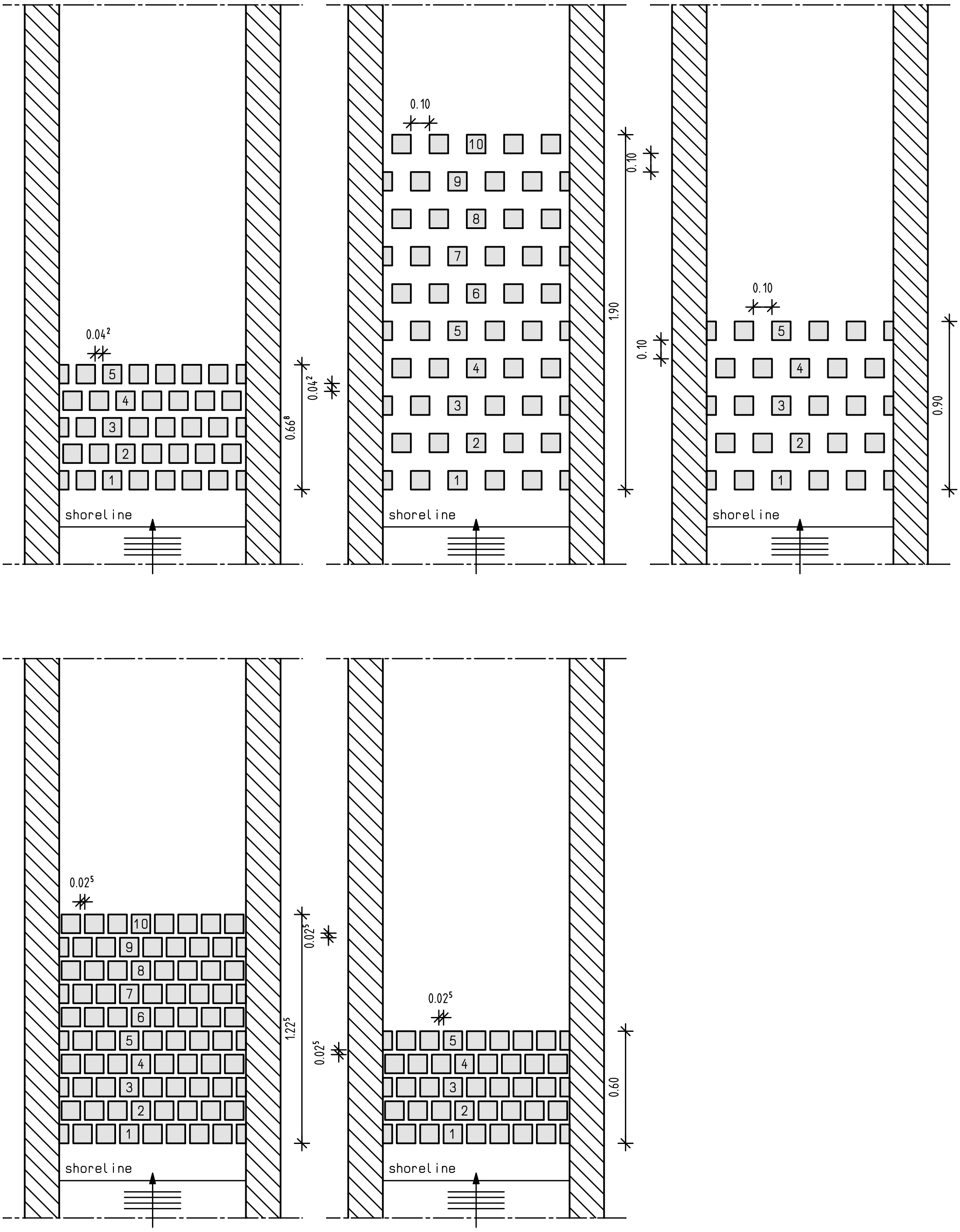

Figure B.6 Utilized macro-roughness configurations with staggered, non-rotated element arrangement for the cases with 4.2 cm and 10.0 cm street width, 10 and 5 macro-roughness element rows, configuration drawn to scale 1/40

C Supplementary illustrations

This chapter is meant to provide additional illustrations which were excluded from the main text of the thesis. Additional figures show the functional relation between the relative run-up $R_{mean}(a_{cr}$ to the long-shore obstruction ratio ψ_{ls} (Figs. C.1, C.2). Next, supplementary illustrations depict the influence of the obstructed height to the relative run-up (Figs. C.3, C.4, C.5).

A typical urban, coastal settlement is mapped in Fig. C.6 for the city of Padang, Indonesia to show how buildings could be arranged in a prototype city. This map was also used to estimate the cross-shore obstruction ratio ψ_{cs} for that particular case study. In Figs. C.7, C.8, C.9 and C.10 the time series of the surface elevation at various distances to the beach toe are drawn.

Additional surface elevation profiles are presented in Figs. C.11-C.21 for various time steps. Further cross-sections of the velocity distribution parallel and perpendicular to the wave run-up direction are given in Fig. C.22. Also additional top-view perspectives of the full coverage velcocity fields deduced with the PIV-method are given in Figs. C.23-C.25.

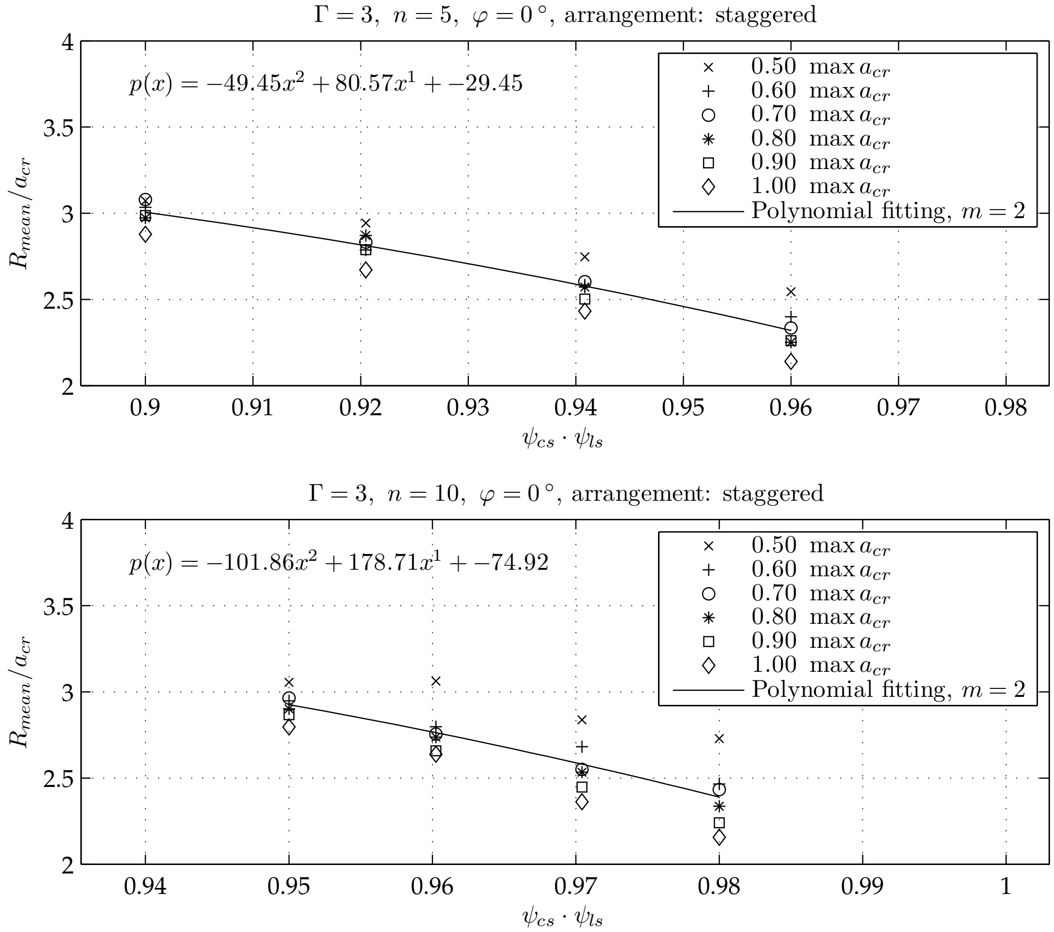

Figure C.1 The relative wave run-up R_{mean} as a function of the cross-shore obstruction ratio ψ_{cs} times the long-shore obstruction ratio ψ_{ls}, $\Gamma = 3$. The experimental data are fitted to a polynomial of degree $m = 2$ and the equations are given according to the investigated number of macro-roughness rows $n = 5, 10$

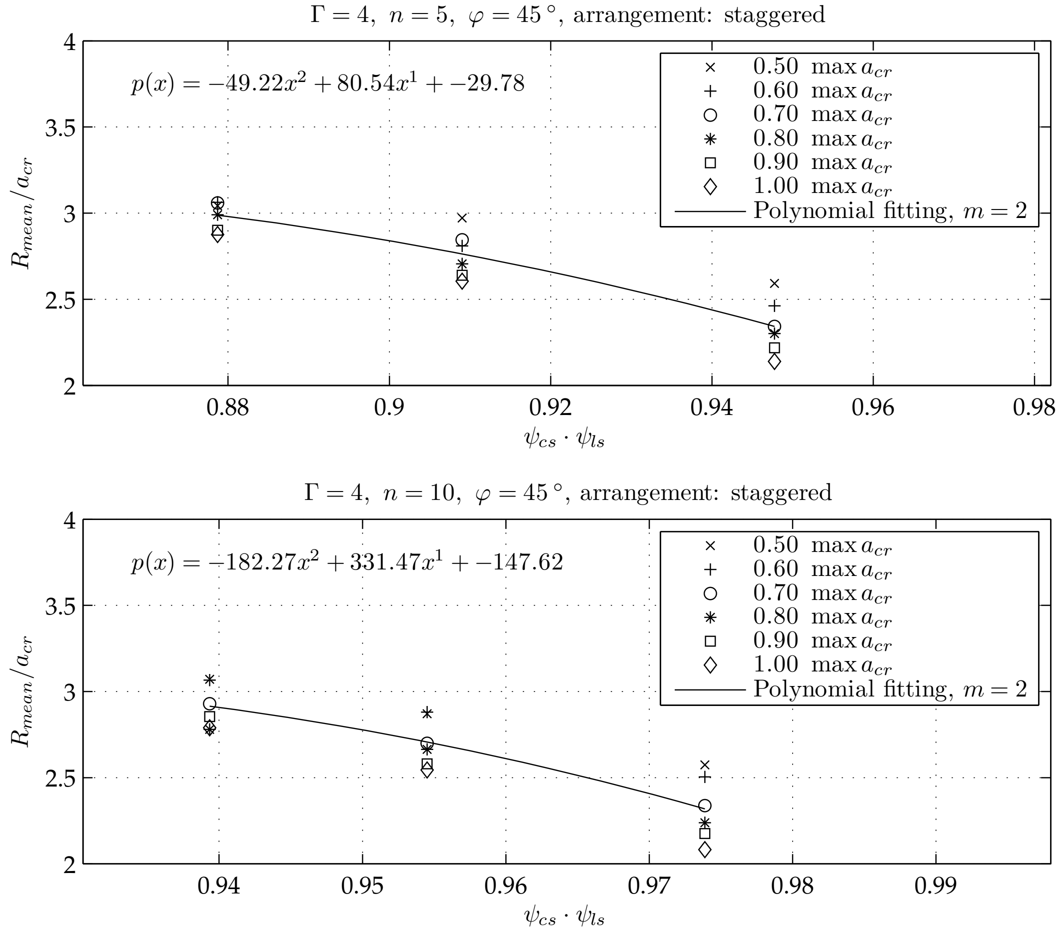

Figure C.2 The relative wave run-up R_{mean} as a function of the cross-shore obstruction ratio ψ_{cs} times the long-shore obstruction ratio ψ_{ls}, $\Gamma = 4$. The experimental data are fitted to a polynomial of degree $m = 2$ and the equations are given according to the investigated number of macro-roughness rows $n = 5, 10$

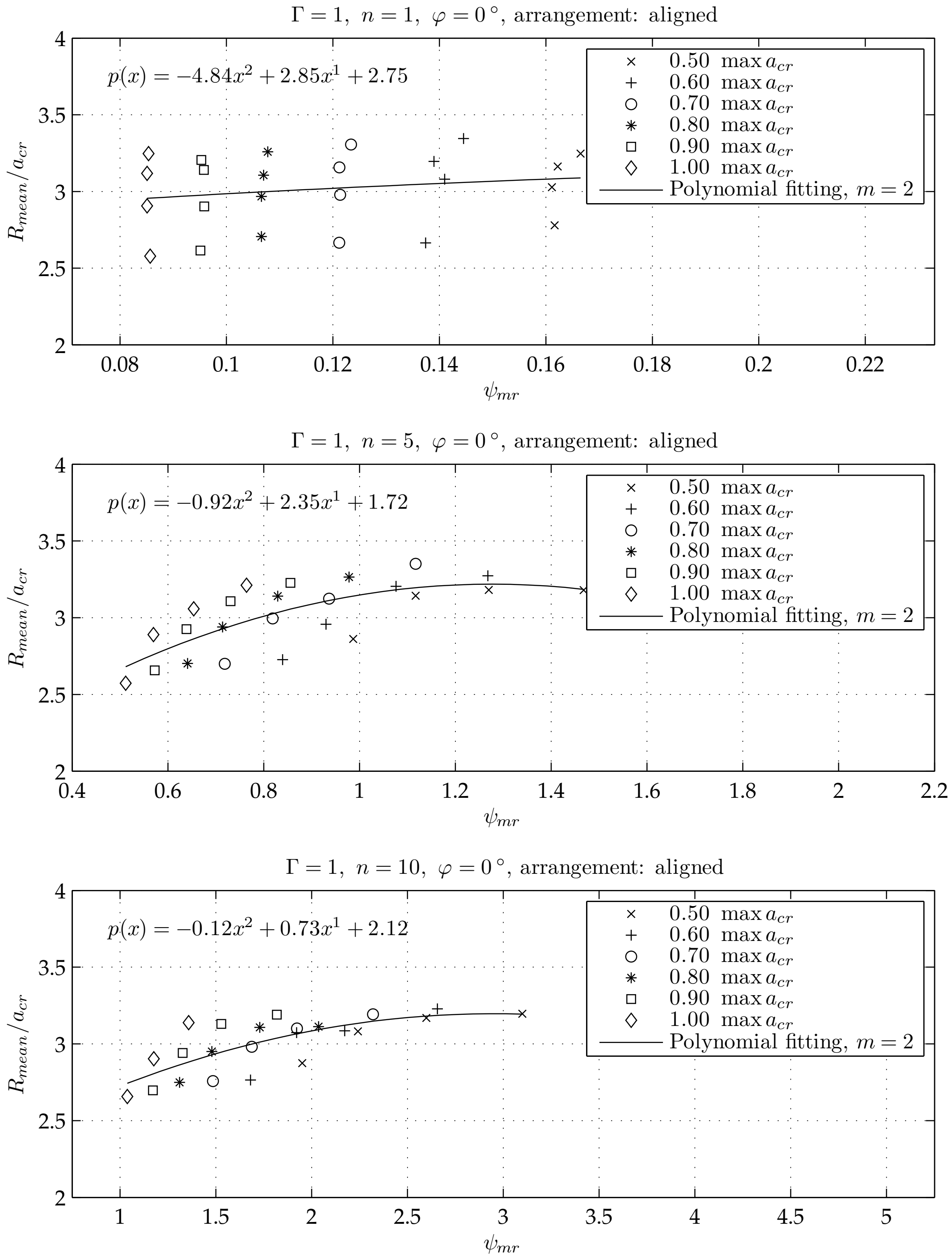

Figure C.3 The relative wave run-up R_{mean} as a function of the cross-shore obstruction ratio ψ_{cs} times the long-shore obstruction ratio ψ_{ls}, $\Gamma = 1$. The experimental data are fitted to a polynomial of degree $m = 2$ and the equations are given according to the investigated number of macro-roughness rows $n = 1, 5, 10$

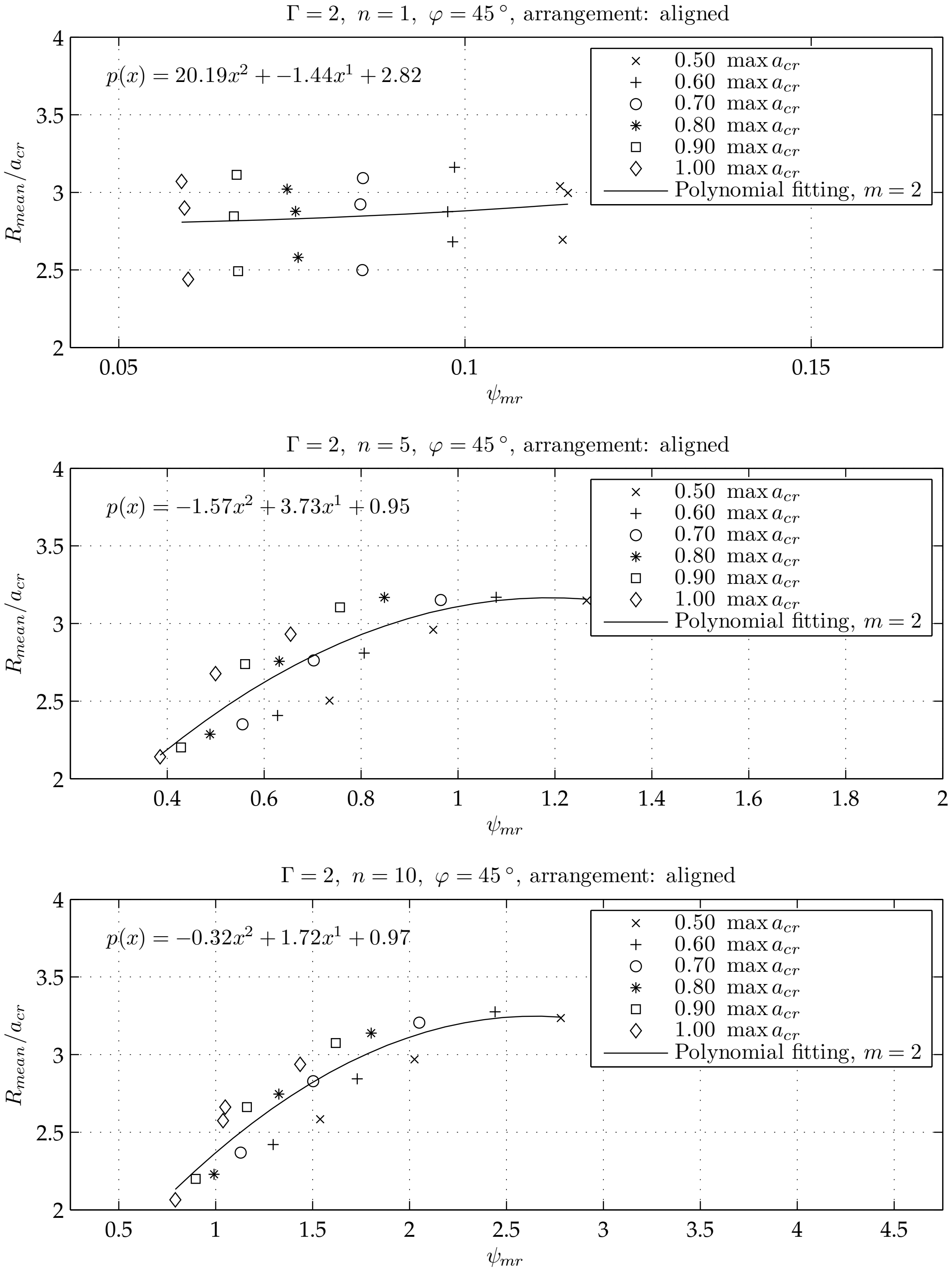

Figure C.4 The relative wave run-up R_{mean} as a function of the cross-shore obstruction ratio ψ_{cs} times the long-shore obstruction ratio ψ_{ls}, $\Gamma = 2$. The experimental data are fitted to a polynomial of degree $m = 2$ and the equations are given according to the investigated number of macro-roughness rows $n = 1, 5, 10$

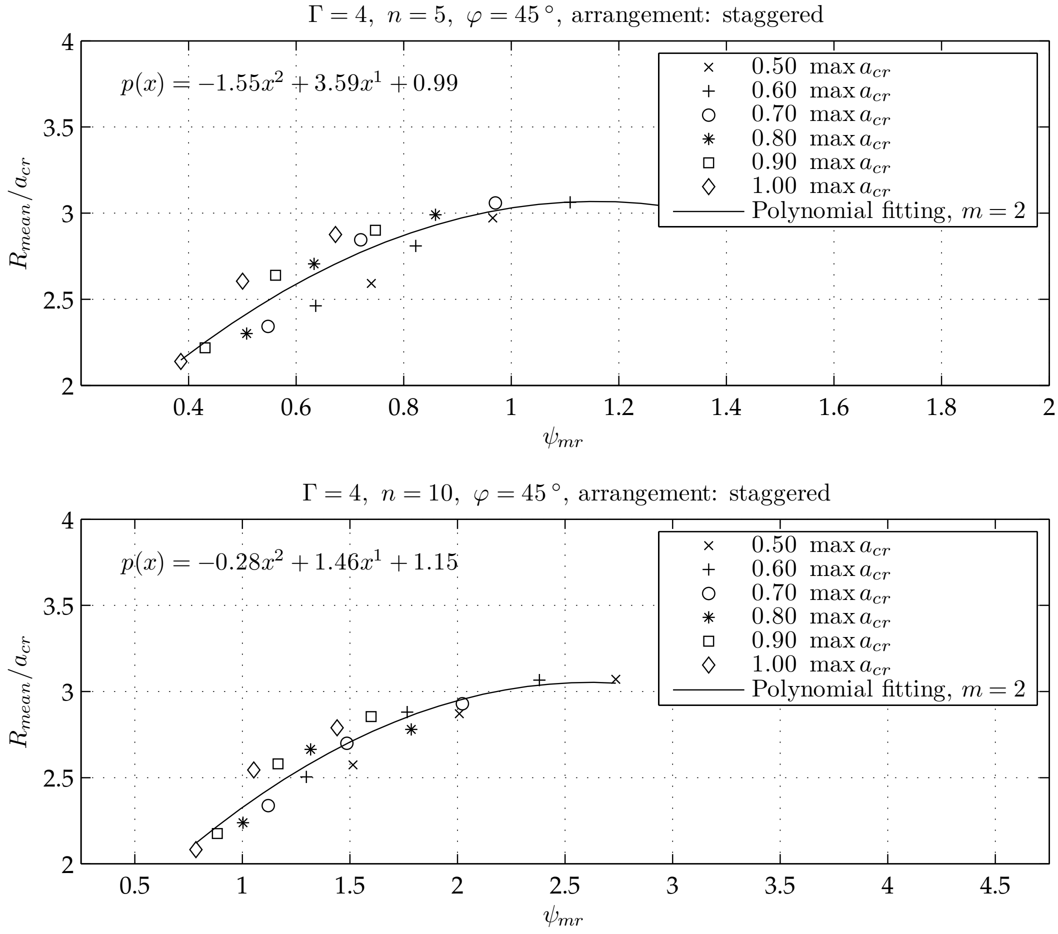

Figure C.5 The relative wave run-up R_{mean} as a function of the cross-shore obstruction ratio ψ_{cs} times the long-shore obstruction ratio ψ_{ls}, $\Gamma = 4$. The experimental data are fitted to a polynomial of degree $m = 2$ and the equations are given according to the investigated number of macro-roughness rows $n = 5, 10$

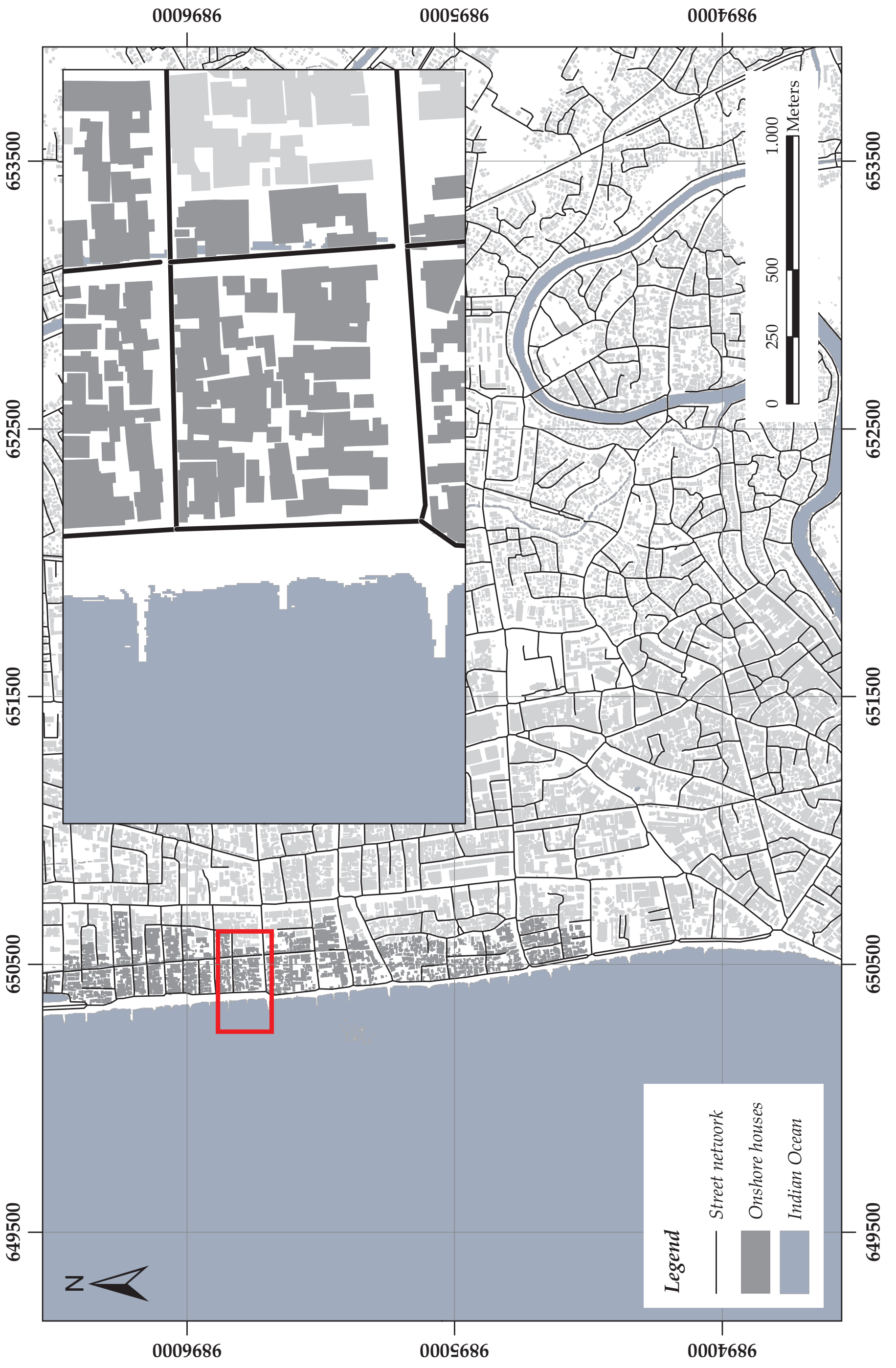

Figure C.6 Onshore coastal settlement pattern at Padang, Indonesia. The dark grey coloured polygons depict a selection of building footprints to estimate the cross-shore obstruction ratio for that particular coastal stretch.

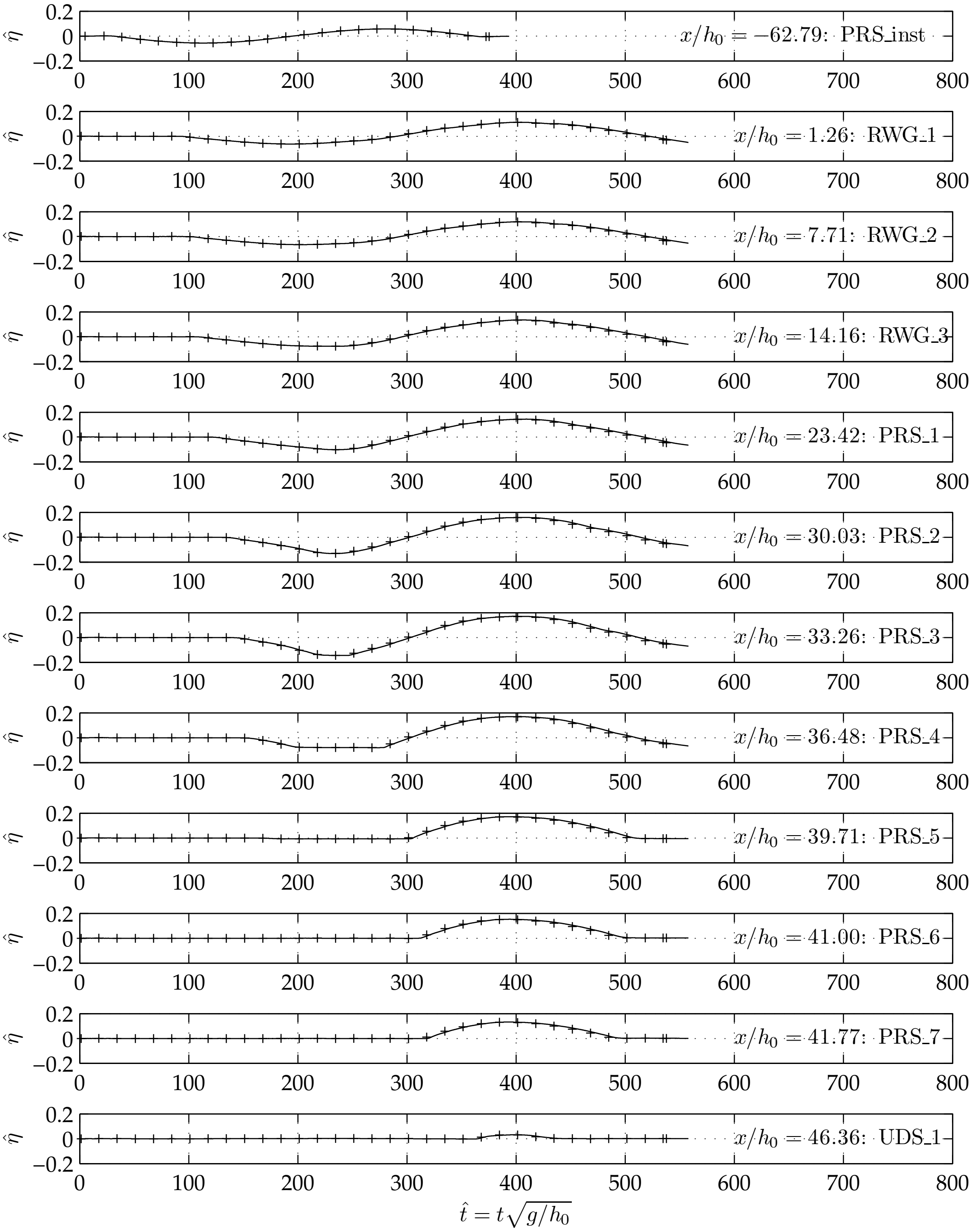

Figure C.7 Time series of the surface elevation $\hat{\eta}$ for a wave with a non-linearity of $\epsilon = 0.058$ at different positions x/h_0 as a function of the non-dimensional time $\hat{t} = t\sqrt{g/h_0}$.

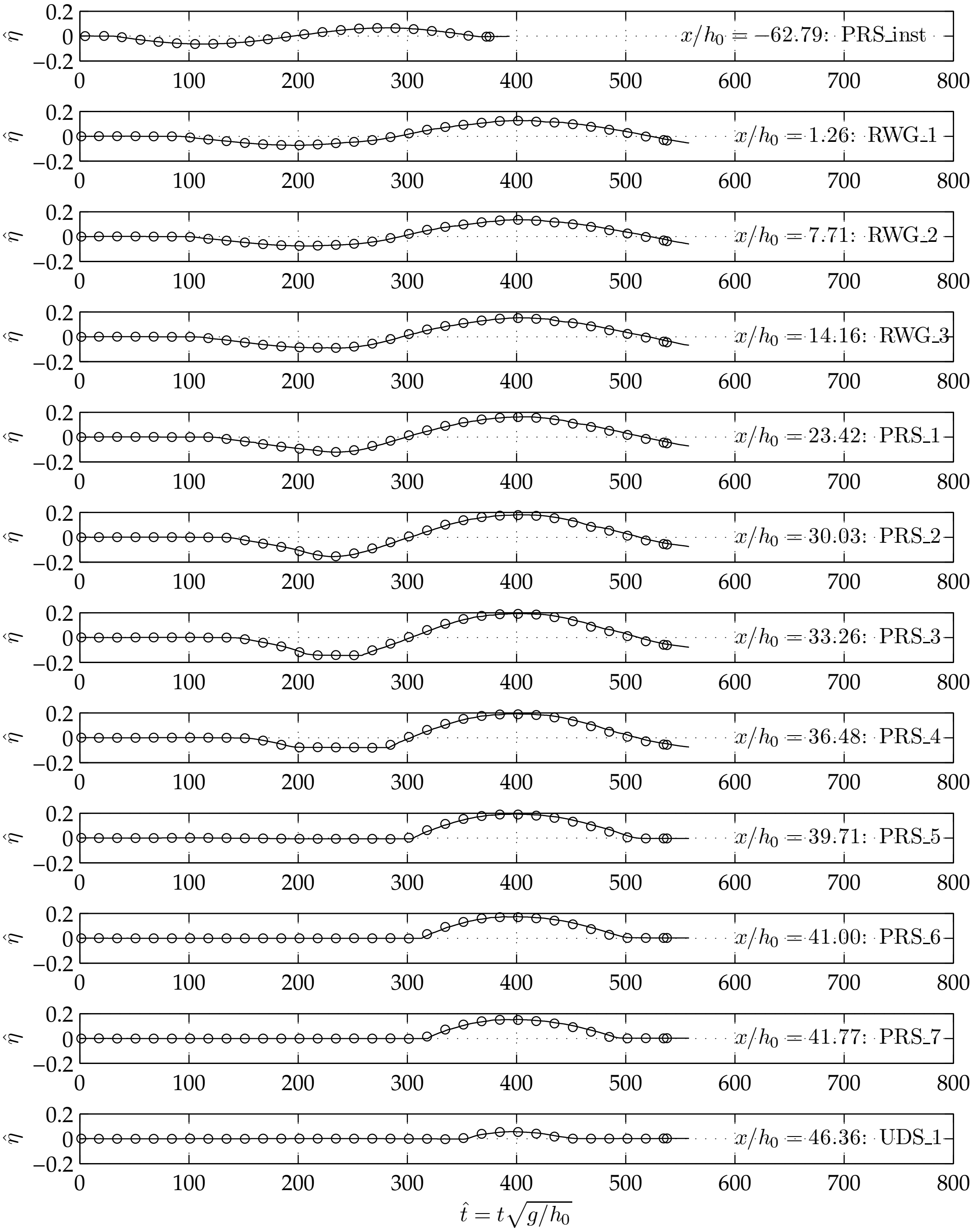

Figure C.8 Time series of the surface elevation $\hat{\eta}$ for a wave with a non-linearity of $\epsilon = 0.066$ at different positions x/h_0 as a function of the non-dimensional time $\hat{t} = t\sqrt{g/h_0}$.

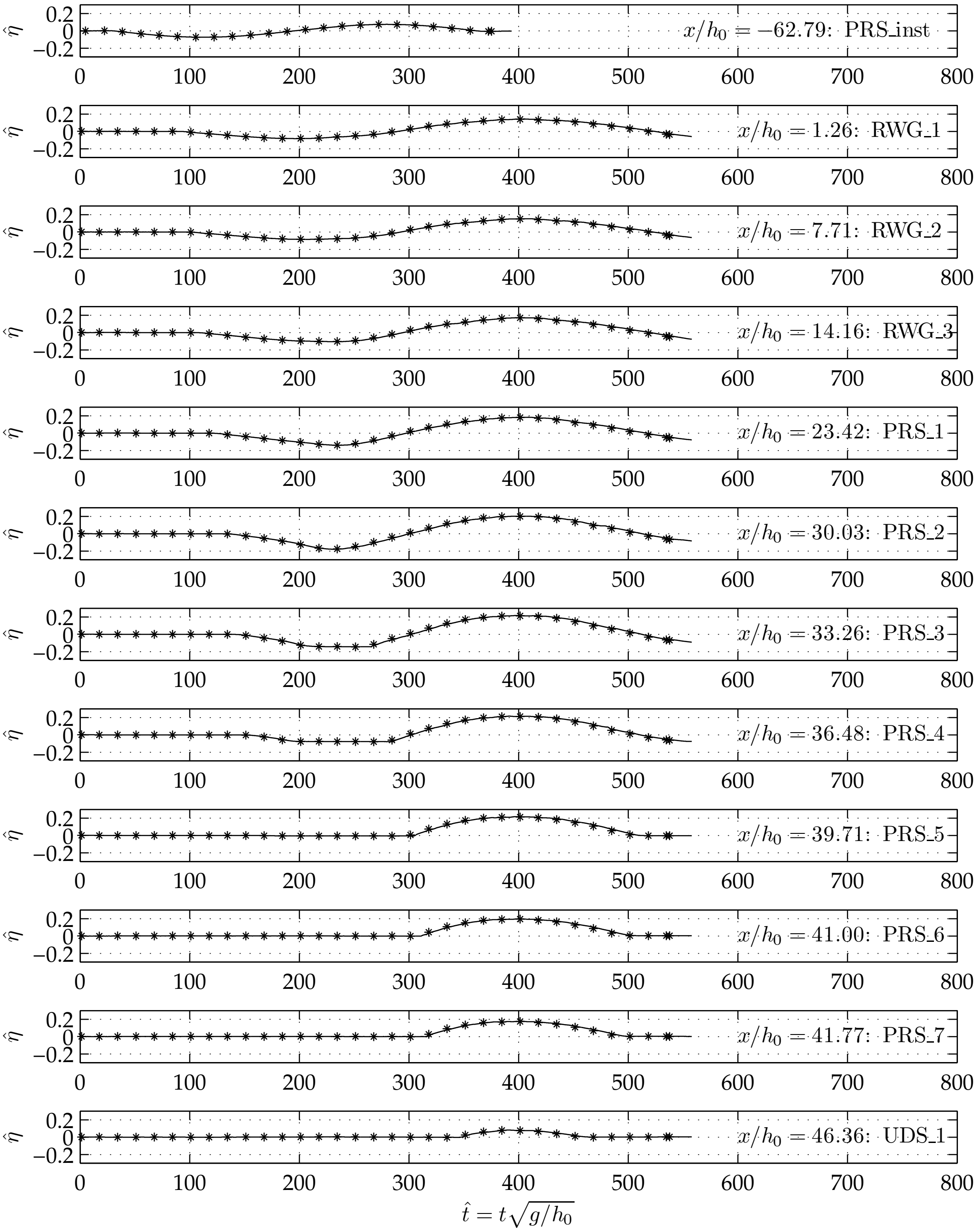

Figure C.9 Time series of the surface elevation $\hat{\eta}$ for a wave with a non-linearity of $\epsilon = 0.075$ at different positions x/h_0 as a function of the non-dimensional time $\hat{t} = t\sqrt{g/h_0}$.

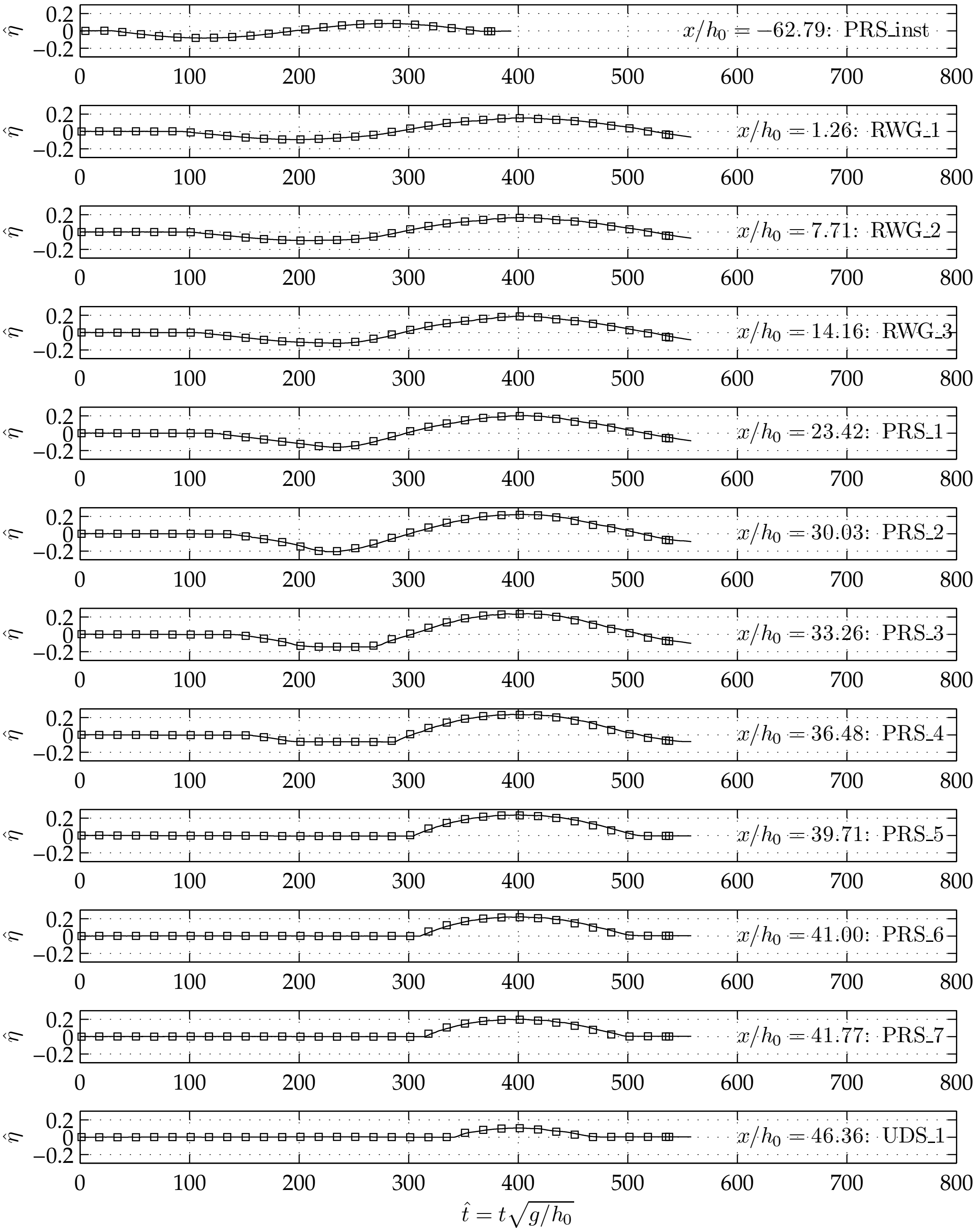

Figure C.10 Time series of the surface elevation $\hat{\eta}$ for a wave with a non-linearity of $\epsilon = 0.086$ at different positions x/h_0 as a function of the non-dimensional time $\hat{t} = t\sqrt{g/h_0}$.

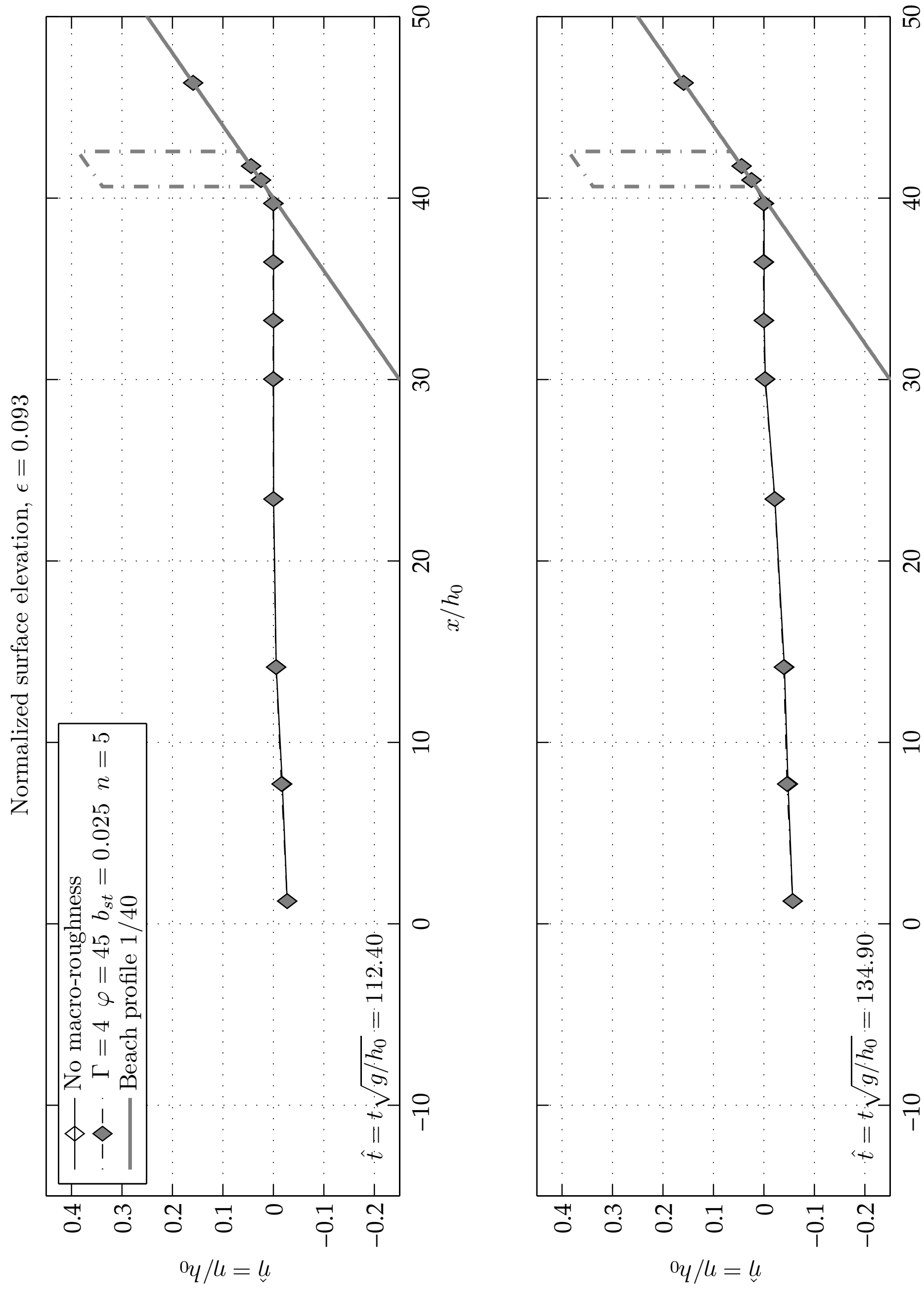

Figure C.11 Comparison of the normalized surface elevation for a sinusoidal wave with $\epsilon = 0.093$ at $\hat{t} = 112.40$ and $\hat{t} = 134.90$ with and without the presence of macro-roughness elements. The macro-roughness element configuration is specified by $\Gamma = 4$, $\varphi = 45°$, $b_{st} = 0.025$ and $n = 5$. Surface elevation and spatial coordinates are normalized by the invariant water depth h_0. The dash-dotted line depicts the macro-roughness element area.

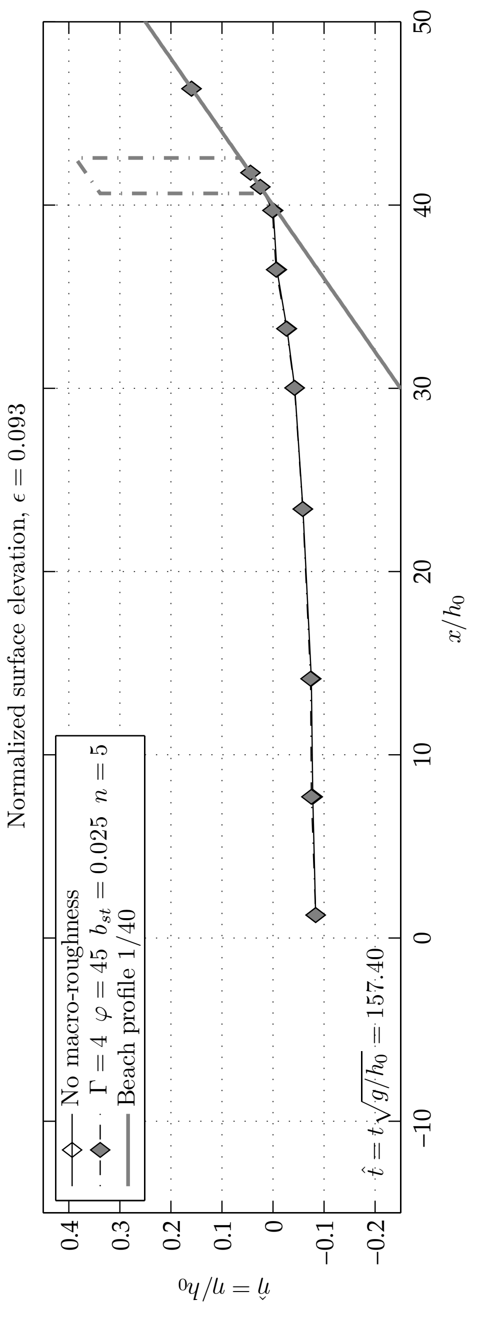

Figure C.12 Comparison of the normalized surface elevation for a sinusoidal wave with $\epsilon = 0.093$ at $\hat{t} = 157.40$ and $\hat{t} = 179.90$ with and without the presence of macro-roughness elements. The macro-roughness element configuration is specified by $\Gamma = 4$, $\varphi = 45°$, $b_{st} = 0.025$ and $n = 5$. Surface elevation and spatial coordinates are normalized by the invariant water depth h_0. The dash-dotted line depicts the macro-roughness element area.

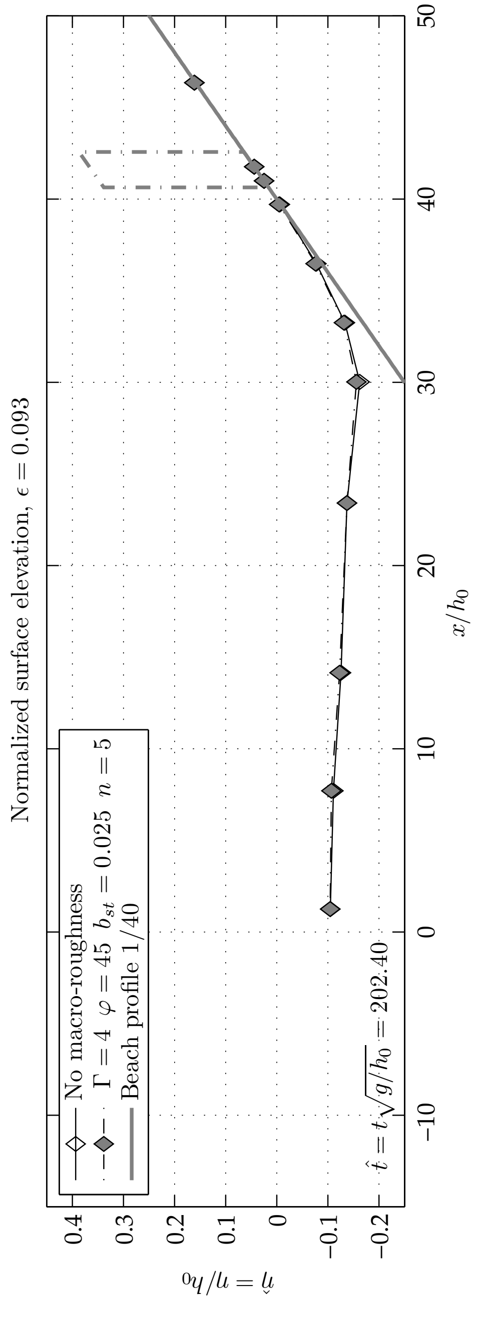

Figure C.13 Comparison of the normalized surface elevation for a sinusoidal wave with $\epsilon = 0.093$ at $\hat{t} = 202.40$ and $\hat{t} = 224.90$ with and without the presence of macro-roughness elements. The macro-roughness element configuration is specified by $\Gamma = 4$, $\varphi = 45°$, $b_{st} = 0.025$ and $n = 5$. Surface elevation and spatial coordinates are normalized by the invariant water depth h_0. The dash-dotted line depicts the macro-roughness element area.

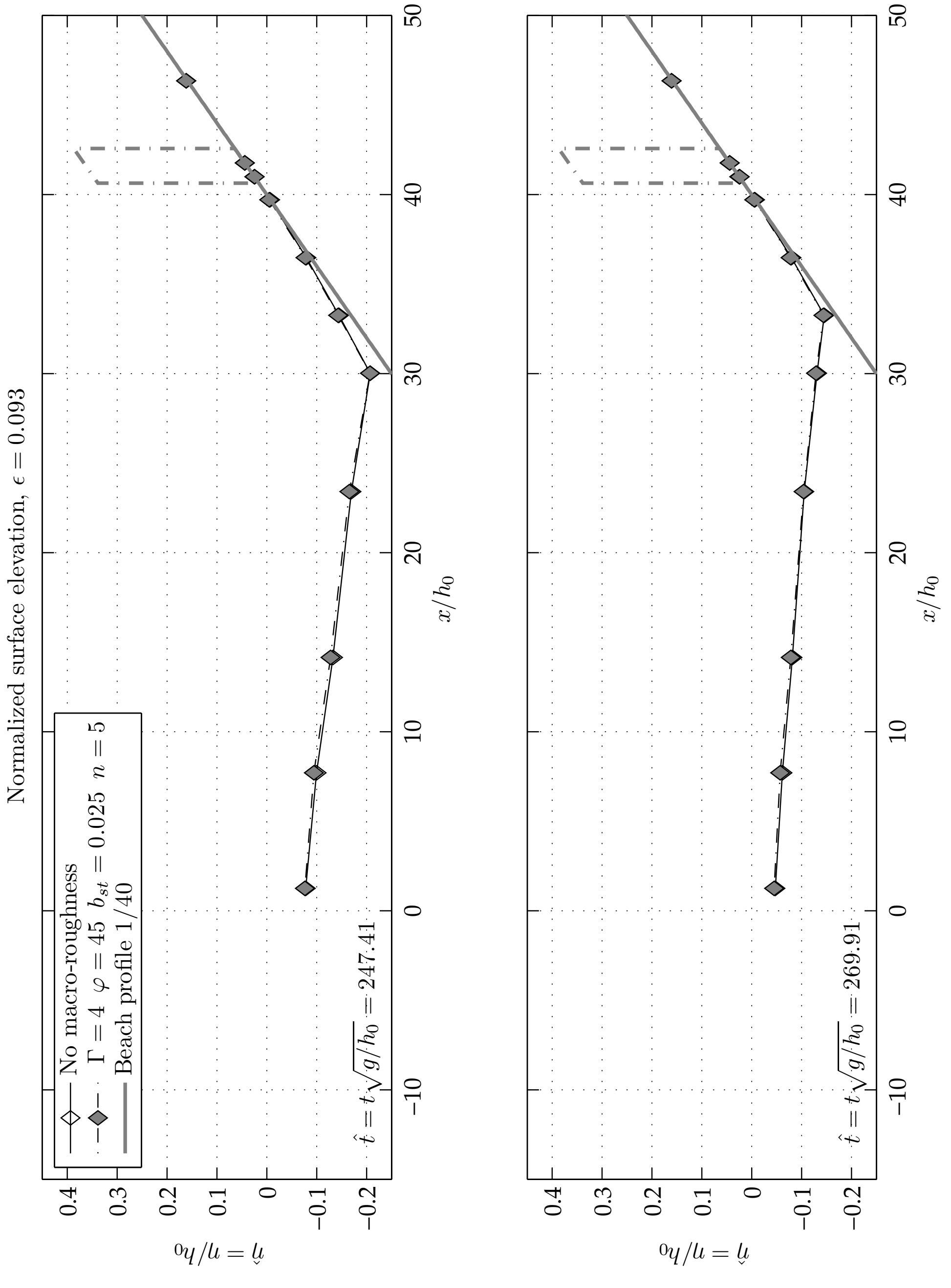

Figure C.14 Comparison of the normalized surface elevation for a sinusoidal wave with $\epsilon = 0.093$ at $\hat{t} = 247.41$ and $\hat{t} = 269.91$ with and without the presence of macro-roughness elements. The macro-roughness element configuration is specified by $\Gamma = 4$, $\varphi = 45°$, $b_{st} = 0.025$ and $n = 5$. Surface elevation and spatial coordinates are normalized by the invariant water depth h_0. The dash-dotted line depicts the macro-roughness element area.

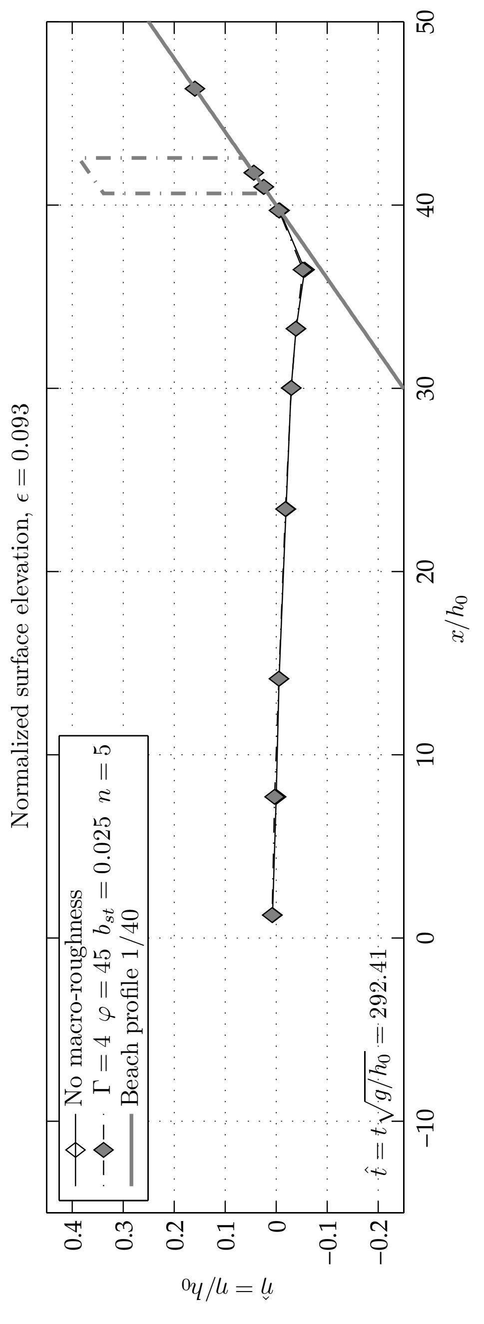

Figure C.15 Comparison of the normalized surface elevation for a sinusoidal wave with $\epsilon = 0.093$ at $\hat{t} = 292.41$ and $\hat{t} = 303.66$ with and without the presence of macro-roughness elements. The macro-roughness element configuration is specified by $\Gamma = 4$, $\varphi = 45°$, $b_{st} = 0.025$ and $n = 5$. Surface elevation and spatial coordinates are normalized by the invariant water depth h_0. The dash-dotted line depicts the macro-roughness element area.

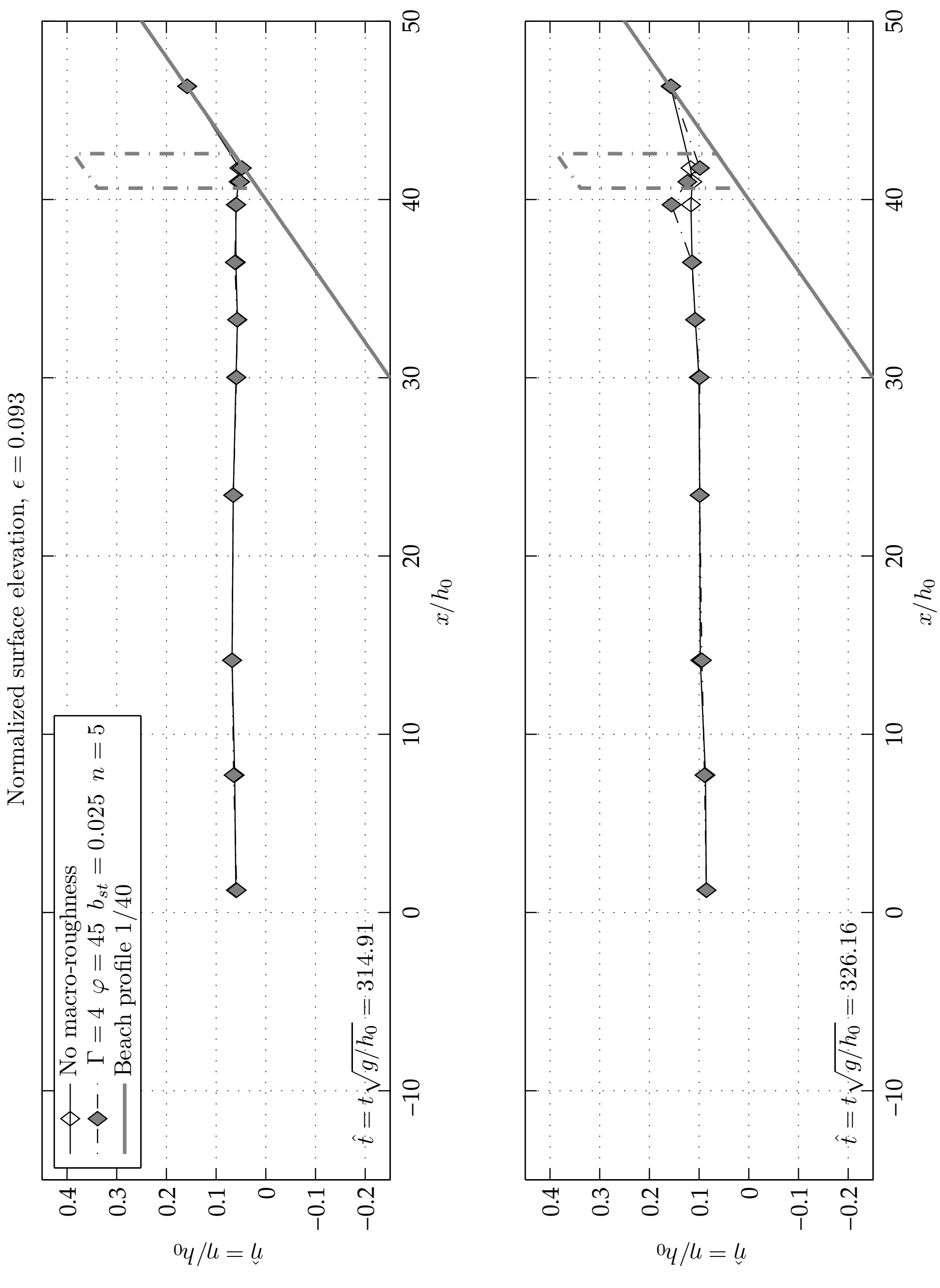

Figure C.16 Comparison of the normalized surface elevation for a sinusoidal wave with $\epsilon = 0.093$ at $\hat{t} = 314.91$ and $\hat{t} = 326.16$ with and without the presence of macro-roughness elements. The macro-roughness element configuration is specified by $\Gamma = 4$, $\varphi = 45°$, $b_{st} = 0.025$ and $n = 5$. Surface elevation and spatial coordinates are normalized by the invariant water depth h_0. The dash-dotted line depicts the macro-roughness element area.

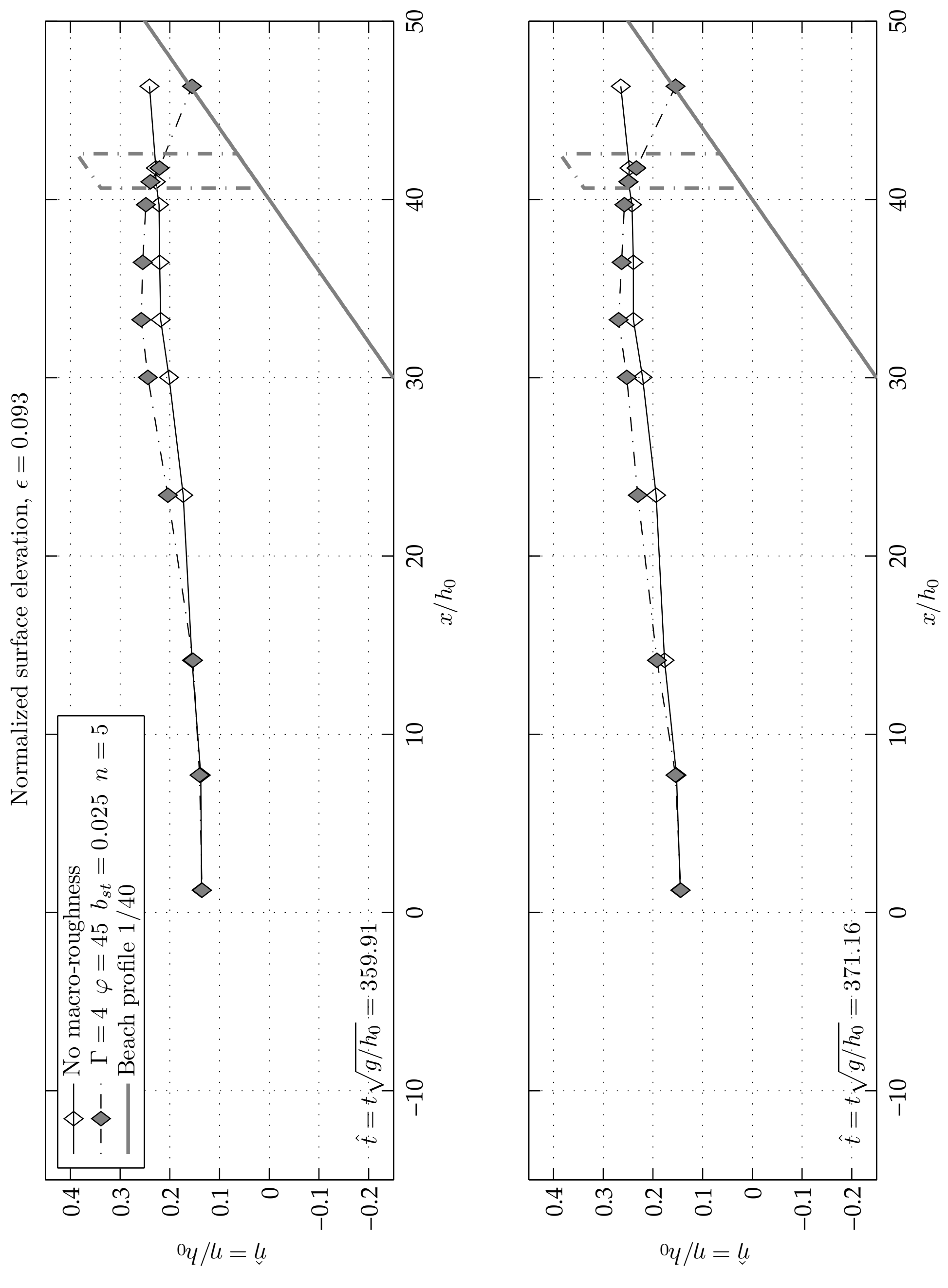

Figure C.17 Comparison of the normalized surface elevation for a sinusoidal wave with $\epsilon = 0.093$ at $\hat{t} = 359.91$ and $\hat{t} = 371.16$ with and without the presence of macro-roughness elements. The macro-roughness element configuration is specified by $\Gamma = 4$, $\varphi = 45°$, $b_{st} = 0.025$ and $n = 5$. Surface elevation and spatial coordinates are normalized by the invariant water depth h_0. The dash-dotted line depicts the macro-roughness element area.

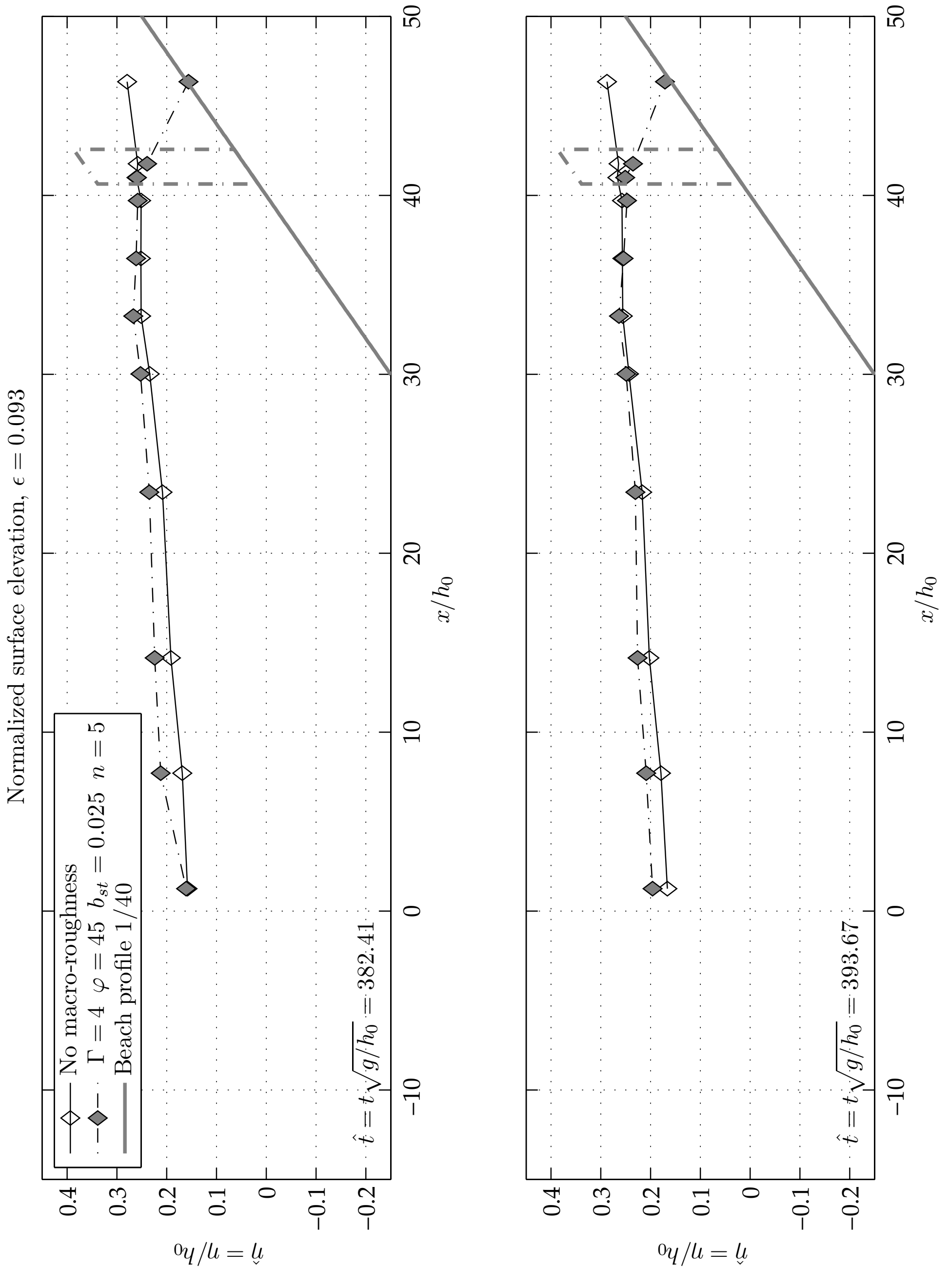

Figure C.18 Comparison of the normalized surface elevation for a sinusoidal wave with $\epsilon = 0.093$ at $\hat{t} = 382.41$ and $\hat{t} = 393.67$ with and without the presence of macro-roughness elements. The macro-roughness element configuration is specified by $\Gamma = 4$, $\varphi = 45°$, $b_{st} = 0.025$ and $n = 5$. Surface elevation and spatial coordinates are normalized by the invariant water depth h_0. The dash-dotted line depicts the macro-roughness element area.

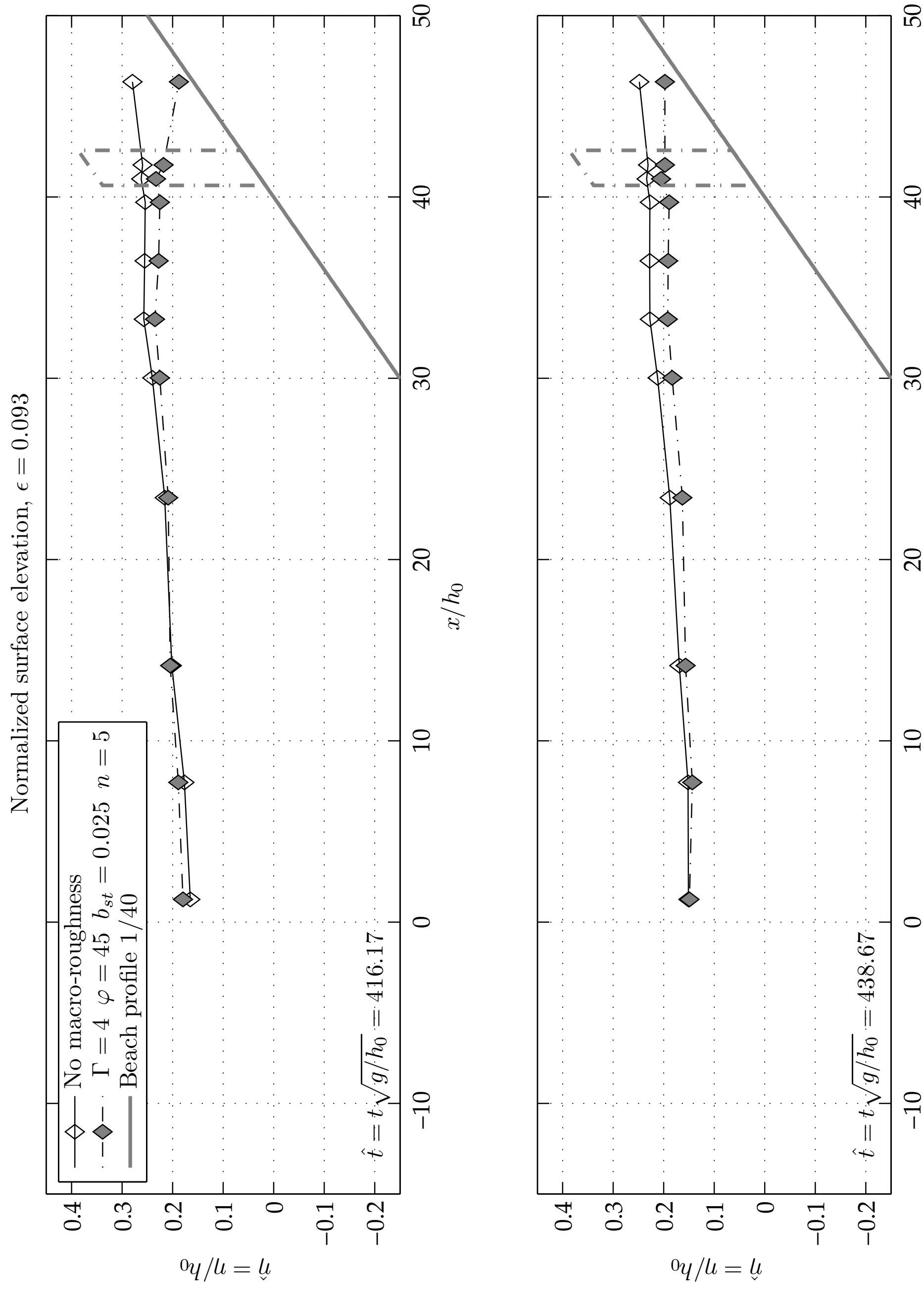

Figure C.19 Comparison of the normalized surface elevation for a sinusoidal wave with $\epsilon = 0.093$ at $\hat{t} = 416.17$ and $\hat{t} = 438.67$ with and without the presence of macro-roughness elements. The macro-roughness element configuration is specified by $\Gamma = 4$, $\varphi = 45°$, $b_{st} = 0.025$ and $n = 5$. Surface elevation and spatial coordinates are normalized by the invariant water depth h_0. The dash-dotted line depicts the macro-roughness element area.

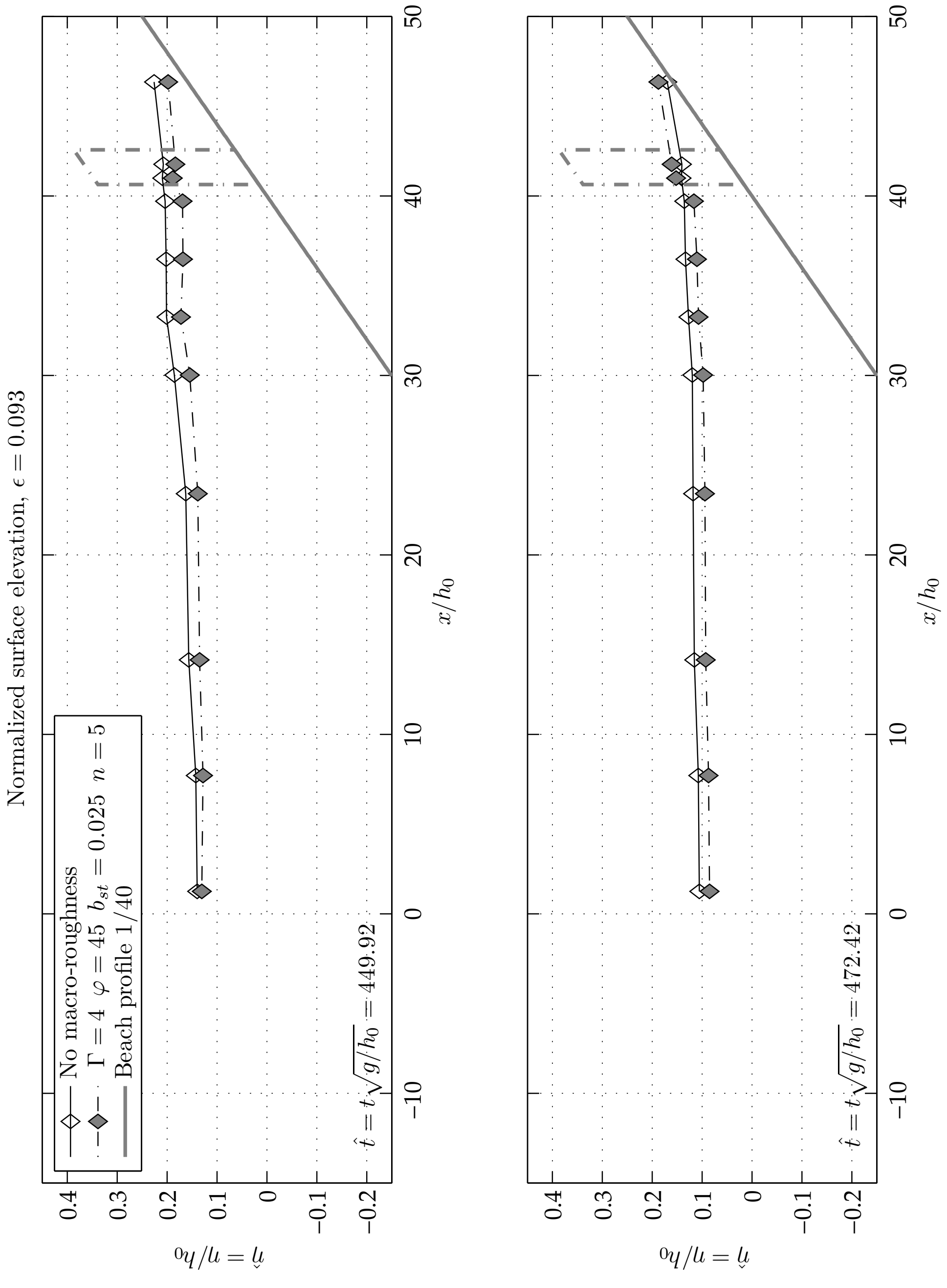

Figure C.20 Comparison of the normalized surface elevation for a sinusoidal wave with $\epsilon = 0.093$ at $\hat{t} = 449.92$ and $\hat{t} = 472.42$ with and without the presence of macro-roughness elements. The macro-roughness element configuration is specified by $\Gamma = 4$, $\varphi = 45°$, $b_{st} = 0.025$ and $n = 5$. Surface elevation and spatial coordinates are normalized by the invariant water depth h_0. The dash-dotted line depicts the macro-roughness element area.

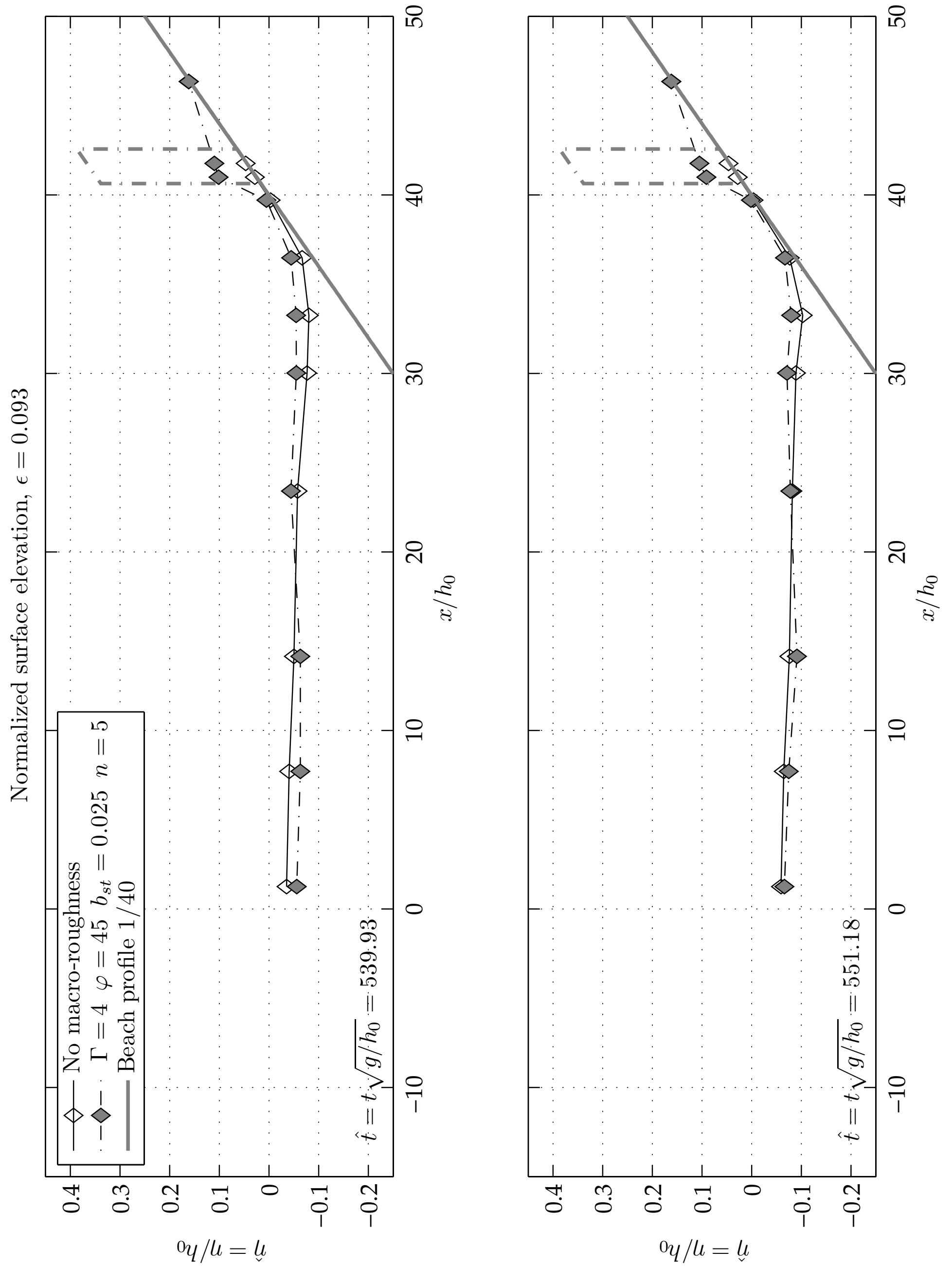

Figure C.21 Comparison of the normalized surface elevation for a sinusoidal wave with $\epsilon = 0.093$ at $\hat{t} = 539.93$ and $\hat{t} = 551.18$ with and without the presence of macro-roughness elements. The macro-roughness element configuration is specified by $\Gamma = 4$, $\varphi = 45°$, $b_{st} = 0.025$ and $n = 5$. Surface elevation and spatial coordinates are normalized by the invariant water depth h_0. The dash-dotted line depicts the macro-roughness element area.

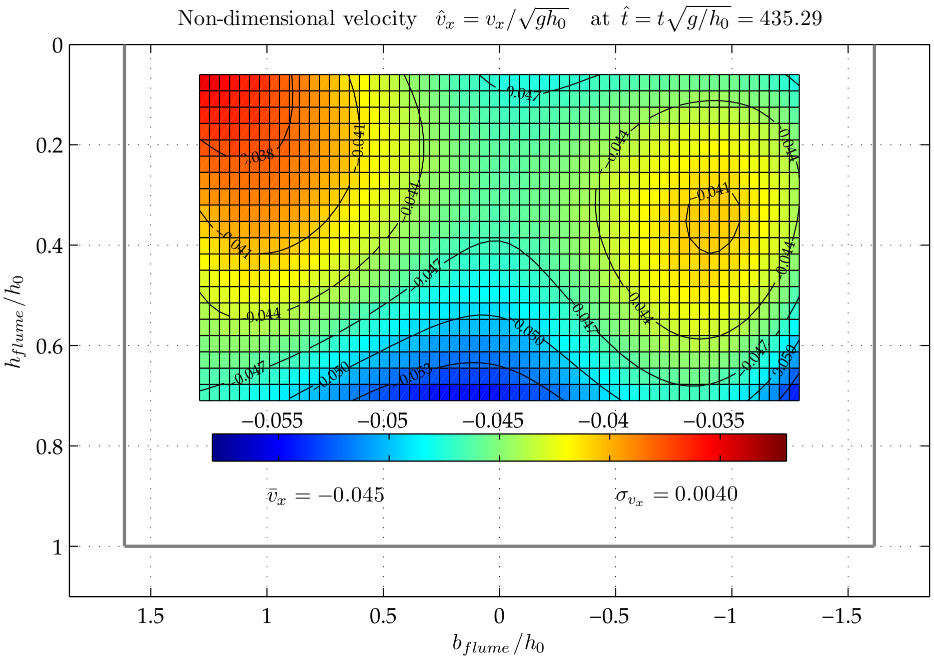

(a) Velocity profile $\bar{v}_x$

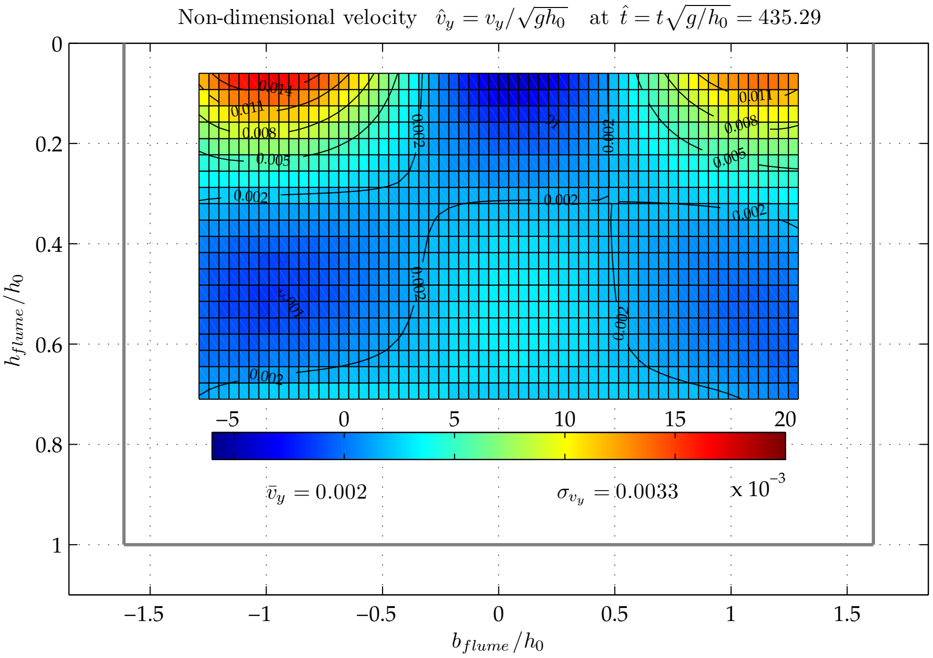

(b) Velocity profile $\bar{v}_y$

Figure C.22 Non-dimensional velocities in a cross-shore profile at position $x/h_0 = 2.58$ involving measurements *EMS_1-EMS_7* and *EMS_15-EMS_22*. Velocities are interpolated and given in non-dimensional form $\hat{v}_x = v_x/\sqrt{gh_0}$ for the time step $\hat{t} = 435.29$ and a wave of non-linearity $\epsilon = 0.058$. Gray thick lines denote the flume walls.

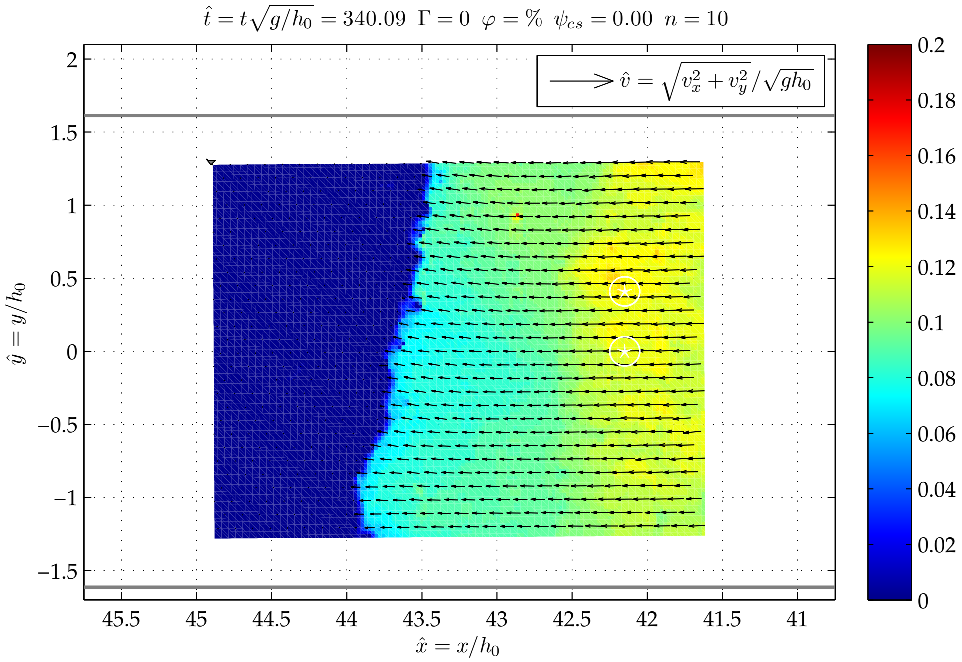

(a) No macro-roughness elements during run-up at $\hat{t} = 340.09$

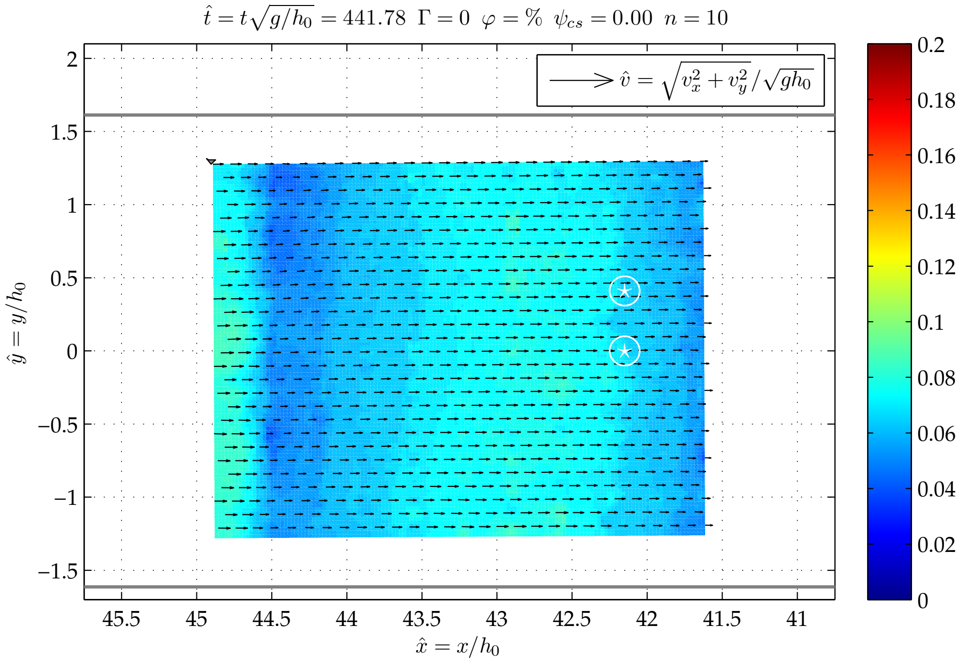

(b) No macro-roughness elements during run-down at $\hat{t} = 441.78$

Figure C.23 Top-view perspective of the full coverage velocity field for the undisturbed case where no macro-roughness elements are present onshore, the wave run-up direction is from the right to the left.

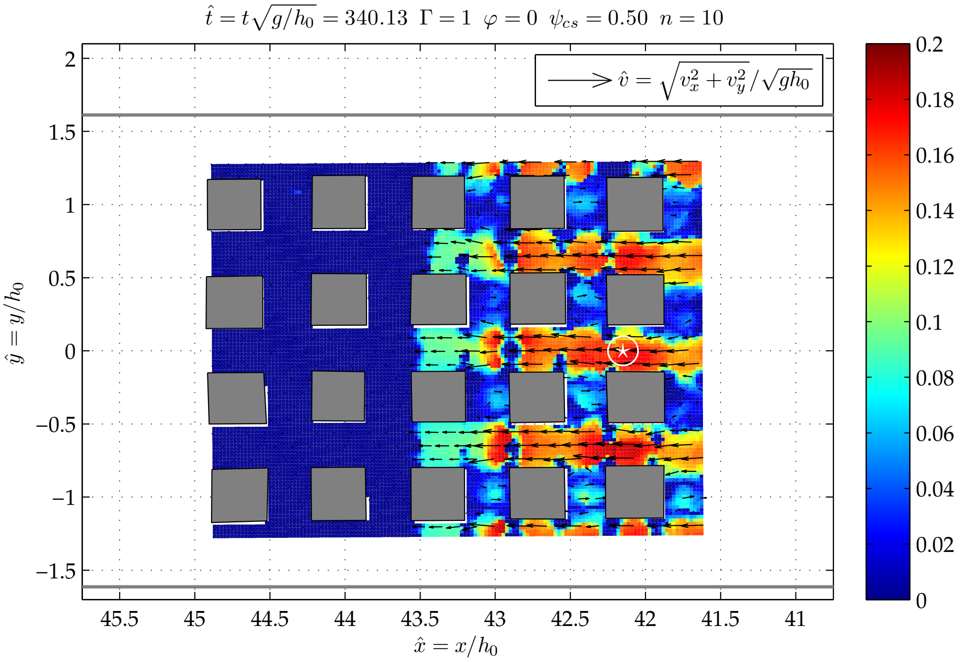

(a) Staggered, non-rotated configuration $\Gamma = 1$

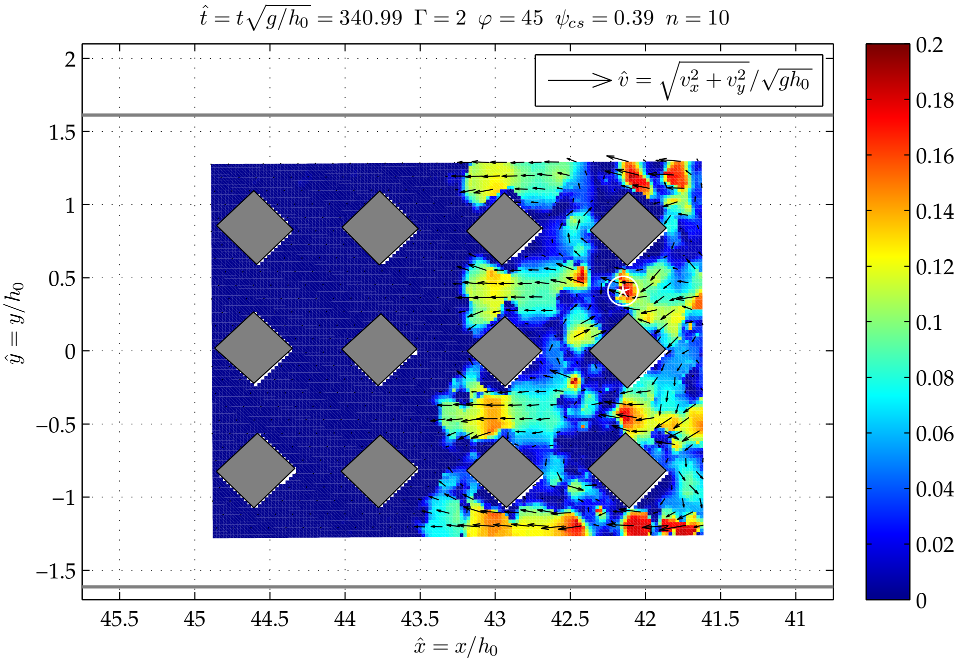

(b) Staggered, rotated configuration $\Gamma = 2$

Figure C.24 Top-view perspective of the full coverage velocity field around aligned macro-roughness element configurations, the wave run-up direction is from the right to the left.

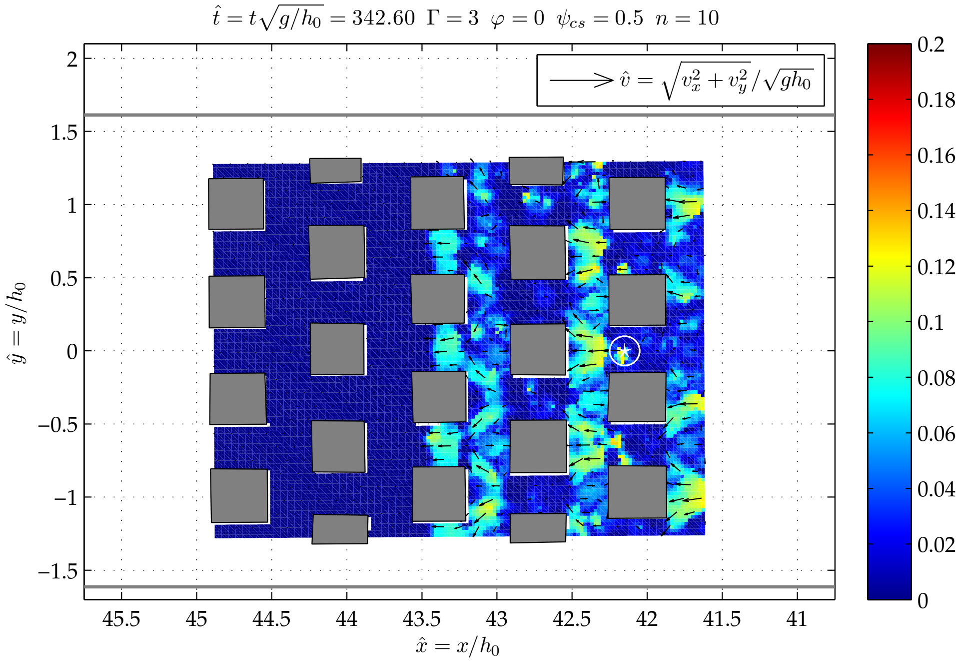

(a) Staggered, non-rotated configuration $\Gamma = 3$

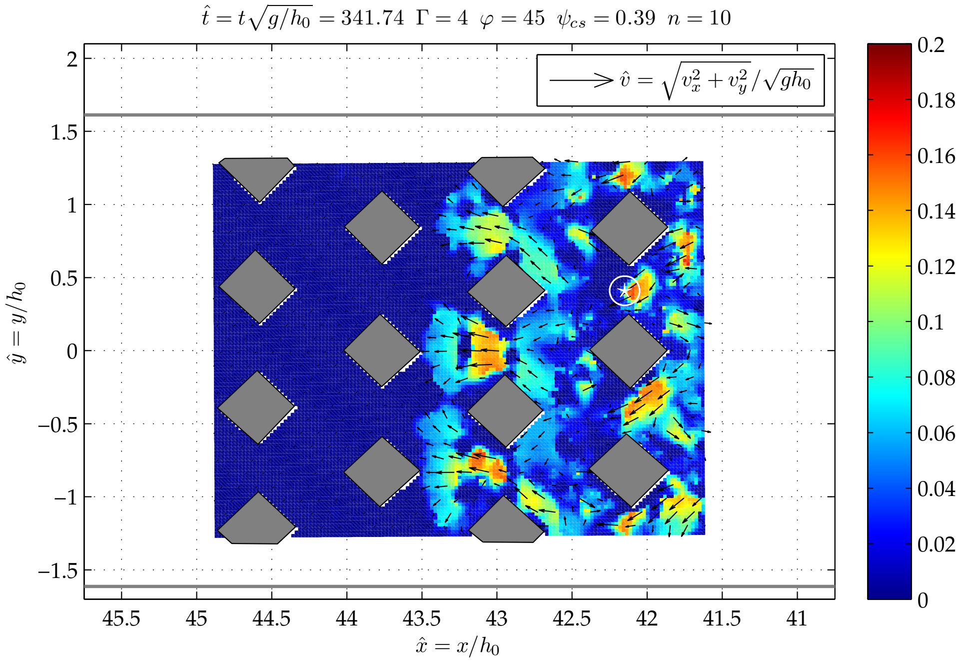

(b) Staggered, rotated configuration $\Gamma = 4$

Figure C.25 Top-view perspective of the full coverage velocity field around staggered macro-roughness element configurations, the wave run-up direction is from the right to the left.

D Tabulated experiment data for a 1/40 sloping beach

The essential experimental run-up results derived in the laboratory are tabulated below. The experiments are sequentially numbered after their conduction in the laboratory. The individual name contains the important parameters of the experiment. Each experiment parameter is separated by an underscore. In particular, the separated experiment parameter connote in their order of appearance:

- "ph": physical model
- "a,b,c. . . ,f": experiment repetition
- "e + number": position of the EMS probe (cp. also Fig.3.10)
- "a + number": percentage of the incident wave amplitude (cp. subsection 5.1.1)
- "no,al,st": **no** macro-roughness, **al**igned or **st**aggered configuration
- "hw + number": width of the macro-roughness element in [cm]
- "nom + number": number of macro-roughness element rows
- "sw + number": cross-shore distance of individual obstacles in [cm]
- "sl + number": long-shore distance of individual obstacles in [cm]
- "angl + number": rotation angle φ of the obstacle in [°]
- "slo + number": beach slope

No.	Name	$R_{min}[m]$	$R_{max}[m]$
1	ph_a_e01_a06_no_hw00_nom00_sw0_sl0_angl00_slo_0025	0.059	0.060
2	ph_a_e01_a10_no_hw00_nom00_sw0_sl0_angl00_slo_0025	0.097	0.098
3	ph_a_e02_a06_no_hw00_nom00_sw0_sl0_angl00_slo_0025	0.059	0.060
4	ph_a_e02_a10_no_hw00_nom00_sw0_sl0_angl00_slo_0025	0.097	0.099
5	ph_a_e03_a06_no_hw00_nom00_sw0_sl0_angl00_slo_0025	0.058	0.059
6	ph_a_e03_a10_no_hw00_nom00_sw0_sl0_angl00_slo_0025	0.100	0.100
7	ph_a_e04_a06_no_hw00_nom00_sw0_sl0_angl00_slo_0025	0.058	0.059
8	ph_a_e05_a06_no_hw00_nom00_sw0_sl0_angl00_slo_0025	0.058	0.059
9	ph_a_e06_a06_no_hw00_nom00_sw0_sl0_angl00_slo_0025	0.058	0.059
10	ph_a_e07_a06_no_hw00_nom00_sw0_sl0_angl00_slo_0025	0.057	0.058
11	ph_b_e01_a06_no_hw00_nom00_sw0_sl0_angl00_slo_0025	0.059	0.059
12	ph_b_e01_a10_no_hw00_nom00_sw0_sl0_angl00_slo_0025	0.098	0.100
13	ph_b_e02_a06_no_hw00_nom00_sw0_sl0_angl00_slo_0025	0.059	0.059
14	ph_b_e02_a10_no_hw00_nom00_sw0_sl0_angl00_slo_0025	0.099	0.100
15	ph_b_e03_a06_no_hw00_nom00_sw0_sl0_angl00_slo_0025	0.057	0.059
16	ph_b_e04_a06_no_hw00_nom00_sw0_sl0_angl00_slo_0025	0.058	0.059
17	ph_b_e05_a06_no_hw00_nom00_sw0_sl0_angl00_slo_0025	0.058	0.059
18	ph_b_e06_a06_no_hw00_nom00_sw0_sl0_angl00_slo_0025	0.057	0.059
19	ph_b_e07_a06_no_hw00_nom00_sw0_sl0_angl00_slo_0025	0.058	0.060
20	ph_a_e04_a10_no_hw00_nom00_sw0_sl0_angl00_slo_0025	0.097	0.098
21	ph_a_e05_a10_no_hw00_nom00_sw0_sl0_angl00_slo_0025	0.098	0.100
22	ph_a_e06_a10_no_hw00_nom00_sw0_sl0_angl00_slo_0025	0.098	0.100
23	ph_a_e07_a10_no_hw00_nom00_sw0_sl0_angl00_slo_0025	0.098	0.099

Continued on next page

continued from previous page

No.	Name	$R_{min}[m]$	$R_{max}[m]$
24	ph_b_e03_a10_no_hw00_nom00_sw0_sl0_angl00_slo_0025	0.097	0.100
25	ph_b_e04_a10_no_hw00_nom00_sw0_sl0_angl00_slo_0025	0.097	0.100
26	ph_b_e05_a10_no_hw00_nom00_sw0_sl0_angl00_slo_0025	0.097	0.099
27	ph_b_e06_a10_no_hw00_nom00_sw0_sl0_angl00_slo_0025	0.098	0.100
28	ph_b_e07_a10_no_hw00_nom00_sw0_sl0_angl00_slo_0025	0.098	0.100
29	ph_a_e08_a06_no_hw00_nom00_sw0_sl0_angl00_slo_0025	0.057	0.058
30	ph_a_e08_a10_no_hw00_nom00_sw0_sl0_angl00_slo_0025	0.098	0.100
31	ph_a_e09_a06_no_hw00_nom00_sw0_sl0_angl00_slo_0025	0.057	0.058
32	ph_a_e09_a10_no_hw00_nom00_sw0_sl0_angl00_slo_0025	0.098	0.100
33	ph_a_e10_a10_no_hw00_nom00_sw0_sl0_angl00_slo_0025	0.098	0.099
34	ph_a_e11_a10_no_hw00_nom00_sw0_sl0_angl00_slo_0025	0.098	0.099
35	ph_a_e12_a10_no_hw00_nom00_sw0_sl0_angl00_slo_0025	0.099	0.100
36	ph_a_e13_a06_no_hw00_nom00_sw0_sl0_angl00_slo_0025	0.057	0.059
37	ph_a_e13_a10_no_hw00_nom00_sw0_sl0_angl00_slo_0025	0.098	0.100
38	ph_b_e08_a06_no_hw00_nom00_sw0_sl0_angl00_slo_0025	0.057	0.059
39	ph_b_e08_a10_no_hw00_nom00_sw0_sl0_angl00_slo_0025	0.097	0.099
40	ph_b_e09_a10_no_hw00_nom00_sw0_sl0_angl00_slo_0025	0.097	0.098
41	ph_b_e10_a10_no_hw00_nom00_sw0_sl0_angl00_slo_0025	0.100	0.101
42	ph_b_e11_a10_no_hw00_nom00_sw0_sl0_angl00_slo_0025	0.098	0.099
43	ph_b_e12_a10_no_hw00_nom00_sw0_sl0_angl00_slo_0025	0.098	0.100
44	ph_b_e13_a06_no_hw00_nom00_sw0_sl0_angl00_slo_0025	0.057	0.058
45	ph_b_e13_a10_no_hw00_nom00_sw0_sl0_angl00_slo_0025	0.098	0.100
46	ph_a_e10_a06_no_hw00_nom00_sw0_sl0_angl00_slo_0025	0.057	0.058
47	ph_a_e11_a06_no_hw00_nom00_sw0_sl0_angl00_slo_0025	0.058	0.059
48	ph_a_e12_a06_no_hw00_nom00_sw0_sl0_angl00_slo_0025	0.057	0.058

Continued on next page

continued from previous page

No.	Name	$R_{min}[m]$	$R_{max}[m]$
49	ph_a_e14_a05_no_hw00_nom00_sw0_sl0_angl00_slo_0025	0.046	0.048
50	ph_a_e14_a06_no_hw00_nom00_sw0_sl0_angl00_slo_0025	0.057	0.059
51	ph_a_e14_a07_no_hw00_nom00_sw0_sl0_angl00_slo_0025	0.066	0.069
52	ph_a_e14_a08_no_hw00_nom00_sw0_sl0_angl00_slo_0025	0.076	0.080
53	ph_a_e14_a09_no_hw00_nom00_sw0_sl0_angl00_slo_0025	0.087	0.089
54	ph_a_e14_a10_no_hw00_nom00_sw0_sl0_angl00_slo_0025	0.098	0.100
55	ph_b_e09_a06_no_hw00_nom00_sw0_sl0_angl00_slo_0025	0.058	0.059
56	ph_b_e10_a06_no_hw00_nom00_sw0_sl0_angl00_slo_0025	0.057	0.057
57	ph_b_e11_a06_no_hw00_nom00_sw0_sl0_angl00_slo_0025	0.057	0.057
58	ph_b_e12_a06_no_hw00_nom00_sw0_sl0_angl00_slo_0025	0.058	0.059
59	ph_b_e14_a05_no_hw00_nom00_sw0_sl0_angl00_slo_0025	0.047	0.049
60	ph_b_e14_a06_no_hw00_nom00_sw0_sl0_angl00_slo_0025	0.057	0.058
61	ph_b_e14_a07_no_hw00_nom00_sw0_sl0_angl00_slo_0025	0.066	0.068
62	ph_b_e14_a08_no_hw00_nom00_sw0_sl0_angl00_slo_0025	0.077	0.075
63	ph_b_e14_a09_no_hw00_nom00_sw0_sl0_angl00_slo_0025	0.086	0.090
64	ph_b_e14_a10_no_hw00_nom00_sw0_sl0_angl00_slo_0025	0.098	0.100
65	ph_f_e14_a05_al_hw10_nom10_sw66_sl66_angl00_slo_0025	0.047	0.050
66	ph_f_e14_a05_st_hw10_nom10_sw66_sl66_angl00_slo_0025	0.046	0.048
67	ph_f_e14_a06_al_hw10_nom10_sw66_sl66_angl00_slo_0025	0.056	0.057
68	ph_f_e14_a06_st_hw10_nom10_sw66_sl66_angl00_slo_0025	0.049	0.051
69	ph_f_e14_a07_al_hw10_nom10_sw66_sl66_angl00_slo_0025	0.063	0.065
70	ph_f_e14_a07_st_hw10_nom10_sw66_sl66_angl00_slo_0025	0.056	0.057
71	ph_f_e14_a08_al_hw10_nom10_sw66_sl66_angl00_slo_0025	0.071	0.072
72	ph_f_e14_a08_st_hw10_nom10_sw66_sl66_angl00_slo_0025	0.062	0.064
73	ph_f_e14_a09_al_hw10_nom10_sw66_sl66_angl00_slo_0025	0.081	0.082

Continued on next page

continued from previous page

No.	Name	$R_{min}[m]$	$R_{max}[m]$
74	ph_f_e14_a09_st_hw10_nom10_sw66_sl66_angl00_slo_0025	0.069	0.070
75	ph_f_e14_a10_al_hw10_nom10_sw66_sl66_angl00_slo_0025	0.091	0.093
76	ph_f_e14_a10_st_hw10_nom10_sw66_sl66_angl00_slo_0025	0.076	0.079
77	ph_f_e14_a05_al_hw10_nom10_sw10_sl10_angl00_slo_0025	0.048	0.050
78	ph_f_e14_a05_st_hw10_nom10_sw10_sl10_angl00_slo_0025	0.045	0.048
79	ph_f_e14_a06_al_hw10_nom10_sw10_sl10_angl00_slo_0025	0.057	0.058
80	ph_f_e14_a06_st_hw10_nom10_sw10_sl10_angl00_slo_0025	0.052	0.054
81	ph_f_e14_a07_al_hw10_nom10_sw10_sl10_angl00_slo_0025	0.064	0.066
82	ph_f_e14_a07_st_hw10_nom10_sw10_sl10_angl00_slo_0025	0.059	0.061
83	ph_f_e14_a08_al_hw10_nom10_sw10_sl10_angl00_slo_0025	0.072	0.073
84	ph_f_e14_a08_st_hw10_nom10_sw10_sl10_angl00_slo_0025	0.065	0.068
85	ph_f_e14_a09_al_hw10_nom10_sw10_sl10_angl00_slo_0025	0.083	0.084
86	ph_f_e14_a09_st_hw10_nom10_sw10_sl10_angl00_slo_0025	0.074	0.075
87	ph_f_e14_a10_al_hw10_nom10_sw10_sl10_angl00_slo_0025	0.066	0.094
88	ph_f_e14_a10_st_hw10_nom10_sw10_sl10_angl00_slo_0025	0.081	0.084
89	ph_g_e14_a10_al_hw10_nom10_sw10_sl10_angl00_slo_0025	0.068	0.094
90	ph_f_e14_a05_al_hw10_nom10_sw42_sl42_angl00_slo_0025	0.046	0.048
91	ph_f_e14_a05_st_hw10_nom10_sw42_sl42_angl00_slo_0025	0.043	0.044
92	ph_f_e14_a06_al_hw10_nom10_sw42_sl42_angl00_slo_0025	0.054	0.056
93	ph_f_e14_a06_st_hw10_nom10_sw42_sl42_angl00_slo_0025	0.047	0.049
94	ph_f_e14_a07_al_hw10_nom10_sw42_sl42_angl00_slo_0025	0.060	0.061
95	ph_f_e14_a07_st_hw10_nom10_sw42_sl42_angl00_slo_0025	0.051	0.053
96	ph_f_e14_a08_al_hw10_nom10_sw42_sl42_angl00_slo_0025	0.068	0.069
97	ph_f_e14_a08_st_hw10_nom10_sw42_sl42_angl00_slo_0025	0.058	0.059
98	ph_f_e14_a09_al_hw10_nom10_sw25_sl25_angl00_slo_0025	0.069	0.071

Continued on next page

continued from previous page

No.	Name	$R_{min}[m]$	$R_{max}[m]$
99	ph_f_e14_a09_al_hw10_nom10_sw42_sl42_angl00_slo_0025	0.075	0.077
100	ph_f_e14_a09_st_hw10_nom10_sw42_sl42_angl00_slo_0025	0.063	0.064
101	ph_f_e14_a10_al_hw10_nom10_sw25_sl25_angl00_slo_0025	0.077	0.079
102	ph_f_e14_a10_al_hw10_nom10_sw42_sl42_angl00_slo_0025	0.084	0.086
103	ph_f_e14_a10_st_hw10_nom10_sw42_sl42_angl00_slo_0025	0.068	0.069
104	ph_f_e14_a05_al_hw10_nom10_sw25_sl25_angl00_slo_0025	0.044	0.046
105	ph_f_e14_a05_st_hw10_nom10_sw25_sl25_angl00_slo_0025	0.040	0.042
106	ph_f_e14_a06_al_hw10_nom10_sw25_sl25_angl00_slo_0025	0.050	0.051
107	ph_f_e14_a06_st_hw10_nom10_sw25_sl25_angl00_slo_0025	0.044	0.046
108	ph_f_e14_a07_al_hw10_nom10_sw25_sl25_angl00_slo_0025	0.056	0.057
109	ph_f_e14_a07_st_hw10_nom10_sw25_sl25_angl00_slo_0025	0.048	0.050
110	ph_f_e14_a08_al_hw10_nom10_sw25_sl25_angl00_slo_0025	0.064	0.064
111	ph_f_e14_a08_st_hw10_nom10_sw25_sl25_angl00_slo_0025	0.053	0.054
112	ph_f_e14_a09_st_hw10_nom10_sw25_sl25_angl00_slo_0025	0.058	0.059
113	ph_f_e14_a10_st_hw10_nom10_sw25_sl25_angl00_slo_0025	0.063	0.063
114	ph_f_e14_a05_al_hw10_nom05_sw10_sl10_angl00_slo_0025	0.048	0.049
115	ph_f_e14_a06_al_hw10_nom05_sw10_sl10_angl00_slo_0025	0.057	0.059
116	ph_f_e14_a07_al_hw10_nom05_sw10_sl10_angl00_slo_0025	0.067	0.068
117	ph_f_e14_a08_al_hw10_nom05_sw10_sl10_angl00_slo_0025	0.074	0.076
118	ph_f_e14_a05_al_hw10_nom01_sw10_sl10_angl00_slo_0025	0.047	0.050
119	ph_f_e14_a05_st_hw10_nom05_sw10_sl10_angl00_slo_0025	0.047	0.047
120	ph_f_e14_a06_al_hw10_nom01_sw10_sl10_angl00_slo_0025	0.057	0.058
121	ph_f_e14_a06_st_hw10_nom05_sw10_sl10_angl00_slo_0025	0.052	0.055
122	ph_f_e14_a07_al_hw10_nom01_sw10_sl10_angl00_slo_0025	0.066	0.068
123	ph_f_e14_a07_st_hw10_nom05_sw10_sl10_angl00_slo_0025	0.062	0.062

Continued on next page

continued from previous page

No.	Name	$R_{min}[m]$	$R_{max}[m]$
124	ph_f_e14_a08_al_hw10_nom01_sw10_sl10_angl00_slo_0025	0.074	0.077
125	ph_f_e14_a08_st_hw10_nom05_sw10_sl10_angl00_slo_0025	0.069	0.070
126	ph_f_e14_a09_al_hw10_nom01_sw10_sl10_angl00_slo_0025	0.083	0.085
127	ph_f_e14_a09_al_hw10_nom05_sw10_sl10_angl00_slo_0025	0.084	0.086
128	ph_f_e14_a09_st_hw10_nom05_sw10_sl10_angl00_slo_0025	0.077	0.079
129	ph_f_e14_a10_al_hw10_nom01_sw10_sl10_angl00_slo_0025	0.094	0.096
130	ph_f_e14_a10_al_hw10_nom05_sw10_sl10_angl00_slo_0025	0.094	0.095
131	ph_f_e14_a10_st_hw10_nom05_sw10_sl10_angl00_slo_0025	0.085	0.086
132	ph_f_e14_a05_al_hw10_nom05_sw66_sl66_angl00_slo_0025	0.047	0.049
133	ph_f_e14_a05_st_hw10_nom05_sw66_sl66_angl00_slo_0025	0.043	0.046
134	ph_f_e14_a06_al_hw10_nom05_sw66_sl66_angl00_slo_0025	0.056	0.057
135	ph_f_e14_a06_st_hw10_nom05_sw66_sl66_angl00_slo_0025	0.049	0.051
136	ph_f_e14_a07_al_hw10_nom05_sw66_sl66_angl00_slo_0025	0.063	0.064
137	ph_f_e14_a08_al_hw10_nom05_sw66_sl66_angl00_slo_0025	0.072	0.073
138	ph_f_e14_a09_al_hw10_nom05_sw66_sl66_angl00_slo_0025	0.081	0.081
139	ph_f_e14_a10_al_hw10_nom05_sw66_sl66_angl00_slo_0025	0.088	0.090
140	ph_f_e14_a05_al_hw10_nom01_sw66_sl66_angl00_slo_0025	0.048	0.050
141	ph_f_e14_a06_al_hw10_nom01_sw66_sl66_angl00_slo_0025	0.057	0.058
142	ph_f_e14_a07_al_hw10_nom01_sw66_sl66_angl00_slo_0025	0.064	0.066
143	ph_f_e14_a07_st_hw10_nom05_sw66_sl66_angl00_slo_0025	0.058	0.060
144	ph_f_e14_a08_al_hw10_nom01_sw66_sl66_angl00_slo_0025	0.072	0.073
145	ph_f_e14_a08_st_hw10_nom05_sw66_sl66_angl00_slo_0025	0.065	0.069
146	ph_f_e14_a09_st_hw10_nom05_sw66_sl66_angl00_slo_0025	0.072	0.073
147	ph_f_e14_a10_st_hw10_nom05_sw66_sl66_angl00_slo_0025	0.077	0.080
148	ph_f_e14_a05_al_hw10_nom05_sw42_sl42_angl00_slo_0025	0.046	0.048

Continued on next page

continued from previous page

No.	Name	$R_{min}[m]$	$R_{max}[m]$
149	ph_f_e14_a06_al_hw10_nom05_sw42_sl42_angl00_slo_0025	0.052	0.054
150	ph_f_e14_a07_al_hw10_nom05_sw42_sl42_angl00_slo_0025	0.060	0.062
151	ph_f_e14_a08_al_hw10_nom05_sw42_sl42_angl00_slo_0025	0.068	0.069
152	ph_f_e14_a09_al_hw10_nom01_sw66_sl66_angl00_slo_0025	0.081	0.082
153	ph_f_e14_a09_al_hw10_nom05_sw42_sl42_angl00_slo_0025	0.076	0.077
154	ph_f_e14_a10_al_hw10_nom01_sw66_sl66_angl00_slo_0025	0.091	0.092
155	ph_f_e14_a10_al_hw10_nom05_sw42_sl42_angl00_slo_0025	0.084	0.085
156	ph_f_e14_a05_al_hw10_nom01_sw42_sl42_angl00_slo_0025	0.046	0.048
157	ph_f_e14_a05_st_hw10_nom05_sw42_sl42_angl00_slo_0025	0.041	0.043
158	ph_f_e14_a06_al_hw10_nom01_sw42_sl42_angl00_slo_0025	0.054	0.055
159	ph_f_e14_a06_st_hw10_nom05_sw42_sl42_angl00_slo_0025	0.046	0.048
160	ph_f_e14_a07_st_hw10_nom05_sw42_sl42_angl00_slo_0025	0.052	0.053
161	ph_f_e14_a08_st_hw10_nom05_sw42_sl42_angl00_slo_0025	0.059	0.060
162	ph_f_e14_a09_st_hw10_nom05_sw42_sl42_angl00_slo_0025	0.065	0.066
163	ph_f_e14_a10_st_hw10_nom05_sw42_sl42_angl00_slo_0025	0.070	0.072
164	ph_f_e15_a06_no_hw00_nom00_sw0_sl0_angl00_slo_0025	0.058	0.059
165	ph_f_e16_a06_no_hw00_nom00_sw0_sl0_angl00_slo_0025	0.057	0.058
166	ph_f_e17_a06_no_hw00_nom00_sw0_sl0_angl00_slo_0025	0.057	0.058
167	ph_f_e18_a06_no_hw00_nom00_sw0_sl0_angl00_slo_0025	0.057	0.058
168	ph_f_e19_a06_no_hw00_nom00_sw0_sl0_angl00_slo_0025	0.058	0.059
169	ph_f_e20_a06_no_hw00_nom00_sw0_sl0_angl00_slo_0025	0.057	0.058
170	ph_f_e21_a06_no_hw00_nom00_sw0_sl0_angl00_slo_0025	0.057	0.057
171	ph_f_e22_a06_no_hw00_nom00_sw0_sl0_angl00_slo_0025	0.057	0.058
172	ph_f_e23_a06_no_hw00_nom00_sw0_sl0_angl00_slo_0025	0.057	0.058
173	ph_f_e24_a06_no_hw00_nom00_sw0_sl0_angl00_slo_0025	0.057	0.058

Continued on next page

continued from previous page

No.	Name	$R_{min}[m]$	$R_{max}[m]$
174	ph_f_e25_a06_no_hw00_nom00_sw0_sl0_angl00_slo_0025	0.058	0.058
175	ph_f_e14_a05_al_hw10_nom05_sw25_sl25_angl00_slo_0025	0.042	0.044
176	ph_f_e14_a06_al_hw10_nom05_sw25_sl25_angl00_slo_0025	0.048	0.049
177	ph_f_e14_a07_al_hw10_nom01_sw42_sl42_angl00_slo_0025	0.061	0.062
178	ph_f_e14_a07_al_hw10_nom05_sw25_sl25_angl00_slo_0025	0.056	0.057
179	ph_f_e14_a08_al_hw10_nom01_sw42_sl42_angl00_slo_0025	0.069	0.070
180	ph_f_e14_a08_al_hw10_nom05_sw25_sl25_angl00_slo_0025	0.063	0.064
181	ph_f_e14_a09_al_hw10_nom01_sw42_sl42_angl00_slo_0025	0.075	0.076
182	ph_f_e14_a09_al_hw10_nom05_sw25_sl25_angl00_slo_0025	0.068	0.071
183	ph_f_e14_a10_al_hw10_nom01_sw42_sl42_angl00_slo_0025	0.085	0.086
184	ph_f_e14_a10_al_hw10_nom05_sw25_sl25_angl00_slo_0025	0.074	0.076
185	ph_f_e14_a05_st_hw10_nom05_sw25_sl25_angl00_slo_0025	0.038	0.039
186	ph_f_e14_a06_st_hw10_nom05_sw25_sl25_angl00_slo_0025	0.042	0.045
187	ph_f_e14_a07_st_hw10_nom05_sw25_sl25_angl00_slo_0025	0.047	0.049
188	ph_f_e14_a08_st_hw10_nom05_sw25_sl25_angl00_slo_0025	0.052	0.053
189	ph_f_e14_a09_st_hw10_nom05_sw25_sl25_angl00_slo_0025	0.058	0.059
190	ph_f_e14_a10_st_hw10_nom05_sw25_sl25_angl00_slo_0025	0.063	0.064
191	ph_f_e14_a05_al_hw10_nom01_sw25_sl25_angl00_slo_0025	0.042	0.044
192	ph_f_e14_a06_al_hw10_nom01_sw25_sl25_angl00_slo_0025	0.048	0.049
193	ph_f_e14_a07_al_hw10_nom01_sw25_sl25_angl00_slo_0025	0.054	0.056
194	ph_f_e14_a08_al_hw10_nom01_sw25_sl25_angl00_slo_0025	0.063	0.064
195	ph_f_e14_a09_al_hw10_nom01_sw25_sl25_angl00_slo_0025	0.068	0.069
196	ph_f_e14_a10_al_hw10_nom01_sw25_sl25_angl00_slo_0025	0.075	0.076
197	ph_f_e14_a05_st_hw10_nom05_sw11_sl11_angl45_slo_0025	0.045	0.048
198	ph_f_e14_a05_st_hw10_nom10_sw11_sl11_angl45_slo_0025	0.046	0.048

Continued on next page

continued from previous page

No.	Name	$R_{min}[m]$	$R_{max}[m]$
199	ph_f_e14_a06_st_hw10_nom05_sw11_sl11_angl45_slo_0025	0.054	0.055
200	ph_f_e14_a06_st_hw10_nom10_sw11_sl11_angl45_slo_0025	0.053	0.055
201	ph_f_e14_a07_st_hw10_nom05_sw11_sl11_angl45_slo_0025	0.061	0.064
202	ph_f_e14_a07_st_hw10_nom10_sw11_sl11_angl45_slo_0025	0.061	0.061
203	ph_f_e14_a08_st_hw10_nom05_sw11_sl11_angl45_slo_0025	0.067	0.070
204	ph_f_e14_a08_st_hw10_nom10_sw11_sl11_angl45_slo_0025	0.065	0.066
205	ph_f_e14_a09_st_hw10_nom05_sw11_sl11_angl45_slo_0025	0.076	0.077
206	ph_f_e14_a09_st_hw10_nom10_sw11_sl11_angl45_slo_0025	0.075	0.076
207	ph_f_e14_a10_st_hw10_nom05_sw11_sl11_angl45_slo_0025	0.084	0.085
208	ph_f_e14_a10_st_hw10_nom10_sw11_sl11_angl45_slo_0025	0.081	0.082
209	ph_f_e14_a05_al_hw10_nom05_sw11_sl11_angl45_slo_0025	0.047	0.051
210	ph_f_e14_a05_al_hw10_nom10_sw11_sl11_angl45_slo_0025	0.048	0.050
211	ph_f_e14_a06_al_hw10_nom05_sw11_sl11_angl45_slo_0025	0.056	0.060
212	ph_f_e14_a06_al_hw10_nom10_sw11_sl11_angl45_slo_0025	0.056	0.057
213	ph_f_e14_a07_al_hw10_nom05_sw11_sl11_angl45_slo_0025	0.063	0.066
214	ph_f_e14_a07_al_hw10_nom10_sw11_sl11_angl45_slo_0025	0.065	0.067
215	ph_f_e14_a08_al_hw10_nom05_sw11_sl11_angl45_slo_0025	0.072	0.075
216	ph_f_e14_a08_al_hw10_nom10_sw11_sl11_angl45_slo_0025	0.072	0.075
217	ph_f_e14_a09_al_hw10_nom05_sw11_sl11_angl45_slo_0025	0.079	0.082
218	ph_f_e14_a09_al_hw10_nom10_sw11_sl11_angl45_slo_0025	0.079	0.081
219	ph_f_e14_a10_al_hw10_nom05_sw11_sl11_angl45_slo_0025	0.086	0.091
220	ph_f_e14_a10_al_hw10_nom10_sw11_sl11_angl45_slo_0025	0.085	0.087
221	ph_f_e14_a10_al_hw10_nom10_sw59_sl59_angl45_slo_0025	0.075	0.078
222	ph_g_e14_a10_al_hw10_nom10_sw59_sl59_angl45_slo_0025	0.077	0.080
223	ph_f_e14_a05_al_hw10_nom05_sw59_sl59_angl45_slo_0025	0.044	0.047

Continued on next page

continued from previous page

No.	Name	$R_{min}[m]$	$R_{max}[m]$
224	ph_f_e14_a05_al_hw10_nom10_sw59_sl59_angl45_slo_0025	0.045	0.046
225	ph_f_e14_a06_al_hw10_nom05_sw59_sl59_angl45_slo_0025	0.051	0.052
226	ph_f_e14_a06_al_hw10_nom10_sw59_sl59_angl45_slo_0025	0.050	0.052
227	ph_f_e14_a07_al_hw10_nom05_sw59_sl59_angl45_slo_0025	0.057	0.059
228	ph_f_e14_a07_al_hw10_nom10_sw59_sl59_angl45_slo_0025	0.058	0.058
229	ph_f_e14_a08_al_hw10_nom05_sw59_sl59_angl45_slo_0025	0.063	0.066
230	ph_f_e14_a08_al_hw10_nom10_sw59_sl59_angl45_slo_0025	0.063	0.065
231	ph_f_e14_a09_al_hw10_nom10_sw59_sl59_angl45_slo_0025	0.069	0.072
232	ph_f_e14_a05_st_hw10_nom05_sw59_sl59_angl45_slo_0025	0.044	0.046
233	ph_f_e14_a05_st_hw10_nom10_sw59_sl59_angl45_slo_0025	0.043	0.045
234	ph_f_e14_a06_st_hw10_nom05_sw59_sl59_angl45_slo_0025	0.049	0.051
235	ph_f_e14_a06_st_hw10_nom10_sw59_sl59_angl45_slo_0025	0.050	0.051
236	ph_f_e14_a07_st_hw10_nom05_sw59_sl59_angl45_slo_0025	0.056	0.060
237	ph_f_e14_a07_st_hw10_nom10_sw59_sl59_angl45_slo_0025	0.055	0.057
238	ph_f_e14_a08_st_hw10_nom05_sw59_sl59_angl45_slo_0025	0.062	0.064
239	ph_f_e14_a08_st_hw10_nom10_sw59_sl59_angl45_slo_0025	0.061	0.064
240	ph_f_e14_a09_al_hw10_nom05_sw59_sl59_angl45_slo_0025	0.070	0.073
241	ph_f_e14_a09_st_hw10_nom05_sw59_sl59_angl45_slo_0025	0.068	0.070
242	ph_f_e14_a09_st_hw10_nom10_sw59_sl59_angl45_slo_0025	0.067	0.069
243	ph_f_e14_a10_al_hw10_nom05_sw59_sl59_angl45_slo_0025	0.077	0.081
244	ph_f_e14_a10_st_hw10_nom05_sw59_sl59_angl45_slo_0025	0.076	0.077
245	ph_f_e14_a10_st_hw10_nom10_sw59_sl59_angl45_slo_0025	0.073	0.076
246	ph_f_e14_a05_al_hw10_nom01_sw11_sl11_angl45_slo_0025	0.046	0.048
247	ph_f_e14_a05_al_hw10_nom01_sw59_sl59_angl45_slo_0025	0.045	0.047
248	ph_f_e14_a06_al_hw10_nom01_sw11_sl11_angl45_slo_0025	0.056	0.058

Continued on next page

continued from previous page

No.	Name	$R_{min}[m]$	$R_{max}[m]$
249	ph_f_e14_a06_al_hw10_nom01_sw59_sl59_angl45_slo_0025	0.051	0.053
250	ph_f_e14_a07_al_hw10_nom01_sw11_sl11_angl45_slo_0025	0.063	0.065
251	ph_f_e14_a07_al_hw10_nom01_sw59_sl59_angl45_slo_0025	0.060	0.062
252	ph_f_e14_a08_al_hw10_nom01_sw11_sl11_angl45_slo_0025	0.070	0.073
253	ph_f_e14_a08_al_hw10_nom01_sw59_sl59_angl45_slo_0025	0.068	0.067
254	ph_f_e14_a09_al_hw10_nom01_sw11_sl11_angl45_slo_0025	0.080	0.084
255	ph_f_e14_a09_al_hw10_nom01_sw59_sl59_angl45_slo_0025	0.074	0.076
256	ph_f_e14_a10_al_hw10_nom01_sw11_sl11_angl45_slo_0025	0.091	0.092
257	ph_f_e14_a10_al_hw10_nom01_sw59_sl59_angl45_slo_0025	0.085	0.087
258	ph_f_e14_a05_st_hw10_nom05_sw25_sl25_angl45_slo_0025	0.039	0.040
259	ph_f_e14_a05_st_hw10_nom10_sw25_sl25_angl45_slo_0025	0.039	0.040
260	ph_f_e14_a06_st_hw10_nom05_sw25_sl25_angl45_slo_0025	0.043	0.045
261	ph_f_e14_a06_st_hw10_nom10_sw25_sl25_angl45_slo_0025	0.043	0.047
262	ph_f_e14_a07_st_hw10_nom05_sw25_sl25_angl45_slo_0025	0.047	0.050
263	ph_f_e14_a07_st_hw10_nom10_sw25_sl25_angl45_slo_0025	0.047	0.050
264	ph_f_e14_a08_st_hw10_nom05_sw25_sl25_angl45_slo_0025	0.050	0.053
265	ph_f_e14_a08_st_hw10_nom10_sw25_sl25_angl45_slo_0025	0.051	0.053
266	ph_f_e14_a09_st_hw10_nom05_sw25_sl25_angl45_slo_0025	0.058	0.059
267	ph_f_e14_a09_st_hw10_nom10_sw25_sl25_angl45_slo_0025	0.057	0.058
268	ph_f_e14_a10_st_hw10_nom05_sw25_sl25_angl45_slo_0025	0.062	0.064
269	ph_f_e14_a10_st_hw10_nom10_sw25_sl25_angl45_slo_0025	0.061	0.062
270	ph_f_e14_a05_al_hw10_nom01_sw25_sl25_angl45_slo_0025	0.041	0.043
271	ph_f_e14_a05_al_hw10_nom05_sw25_sl25_angl45_slo_0025	0.037	0.040
272	ph_f_e14_a06_al_hw10_nom01_sw25_sl25_angl45_slo_0025	0.047	0.049
273	ph_f_e14_a06_al_hw10_nom05_sw25_sl25_angl45_slo_0025	0.043	0.044

Continued on next page

continued from previous page

No.	Name	$R_{min}[m]$	$R_{max}[m]$
274	ph_f_e14_a07_al_hw10_nom05_sw25_sl25_angl45_slo_0025	0.047	0.049
275	ph_f_e14_a08_al_hw10_nom05_sw25_sl25_angl45_slo_0025	0.052	0.054
276	ph_f_e14_a09_al_hw10_nom05_sw25_sl25_angl45_slo_0025	0.058	0.059
277	ph_f_e14_a10_00_hw00_nom00_sw00_sl00_angl00_slo_0025	0.095	0.097
278	ph_f_e14_a10_al_hw10_nom05_sw25_sl25_angl45_slo_0025	0.062	0.063
279	ph_g_e14_a10_00_hw00_nom00_sw00_sl00_angl00_slo_0025	0.096	0.098
280	ph_h_e14_a10_00_hw00_nom00_sw00_sl00_angl00_slo_0025	0.096	0.097
281	ph_f_e14_a05_al_hw10_nom10_sw25_sl25_angl45_slo_0025	0.038	0.040
282	ph_f_e14_a06_al_hw10_nom10_sw25_sl25_angl45_slo_0025	0.043	0.044
283	ph_f_e14_a07_al_hw10_nom01_sw25_sl25_angl45_slo_0025	0.051	0.053
284	ph_f_e14_a07_al_hw10_nom10_sw25_sl25_angl45_slo_0025	0.048	0.050
285	ph_f_e14_a08_al_hw10_nom01_sw25_sl25_angl45_slo_0025	0.060	0.060
286	ph_f_e14_a08_al_hw10_nom10_sw25_sl25_angl45_slo_0025	0.051	0.053
287	ph_f_e14_a09_al_hw10_nom01_sw25_sl25_angl45_slo_0025	0.065	0.066
288	ph_f_e14_a09_al_hw10_nom10_sw25_sl25_angl45_slo_0025	0.056	0.058
289	ph_f_e14_a10_al_hw10_nom01_sw25_sl25_angl45_slo_0025	0.071	0.072
290	ph_f_e14_a10_al_hw10_nom10_sw25_sl25_angl45_slo_0025	0.060	0.061

E Curriculum Vitae

Personal Data

Name	Nils René Goseberg
Date of Birth	October 12, 1978
Place of Birth	Iserlohn / Germany
Nationality	German
Personal Status	Married
Email	goseberg@fi.uni-hannover.de
Phone	+49 511 762-4295

Work Experience

05/2007 - current	Research Engineer at Franzius-Institute for Hydraulics, Waterways and Coastal Engineering, Leibniz University Hannover Projects: "Numerical *Last-mile* Tsunami Early Warning and Evacuation Information System" (www.last-mile-evacuation.de), "Physical modeling of break water stability and cube armor layer system with iron silicate aggregate", "In-situ measurement of flow velocities at the Weser river"
06/2006 – 12/2006	Student assistant at Franzius-Institute for Hydraulics, Waterways and Coastal Engineering, Leibniz University Hannover Coupled 1D-2D hydrodynamic modeling of the lower Mississippi River
07/2004 – 06/2005	Student assistant at Institute of Hydraulic Engineering and Technical Hydromechanics, Dresden University of Technology Project assistance "Entwicklung und Erprobung neuer, innovativer Verbundrohre (Kunststoff-Textilbeton-Verbundsystem) einschließlich ihrer Herstellungstechnologie"
07/2004 – 03/2005	Student assistant at Geotechnical Engineering Institute, Dresden University of Technology

01/2001 – 09/2001	Carpenter, Carpentry Ross

Education

10/2001 – 03/2007	University education in Civil Engineering at Dresden University of Technology Degree: Diplomingenieur (equivalent to Master Degree) Specialization: Geotechnical and hydraulic engineering Thesis: "Einfluss steuerbarer Hochwasserschutzbauwerke auf Wasserstand und Abfluss während extremer Hochwasserereignisse im Mississippidelta"
08/1999 – 01/2001	Vocational training in carpentry Degree: Apprenticeship diploma
08/1989 – 06/1998	School education at the Burg Gymnasium Altena, Germany Graduated with German Abitur (equivalent to A-levels)

Languages

German	Mother tongue
English	Fluent
French	Basic skills
Spanish	Basic skills

Hannover, 20th May 2011

F Previously Published Issues

A list of previously published issues and – if available – the additional electronic document is also available at `http://www.fi.uni-hannover.de/franzius-mitteilungen.html`. Printed copies are available upon request at:

Leibniz Universität Hannover
Franzius-Institut für Wasserbau und Küsteningenieurwesen
Sekretariat
Nienburger Str. 4, D–30167 Hannover
Tel.: +49 511 762-2573
Fax.: +49 511 762-4002
Mail: sekretariat@fi.uni-hannover.de

Issue	Year	Author and Title
97	2011	**Goseberg, N.** The Run-up of Long Waves – Laboratory-scaled Geophysical Reproduction and Onshore Interaction with Macro-Roughness Elements
96	2008	**Spekker, H.** Steuerung von Küstenschutzelementen an Tideflüssen als Grundlage für ein Hochwasser- und Risikomanagement
95	2007	**Matheja, A., Zimmermann, C., Krabbe, H.** Application Architecture and System Technology for LDP (Logistical Data Platform) and FASTCORS (Fast Transport of Containers outside Regular Services)
		Matheja, A., Schweter, L., Zimmermann, C. Naturmessungen zur Bestimmung schiffsinduzierter Belastungen im Hafen eines Tideflusses
		Zimmermann, C., Zimmermann, G. Getting Music out of the Waves
94	2007	**Matheja, A., Schweter, L., Spekker, H., Zimmermann, C., Pohl, C.** Hydrodynamische numerische Simulation von Hochwasserereignissen und von Hochwasserschutzmaßnahmen für ein Tidegebiet
		Matheja, A., Spekker, H., Zimmermann, C., Brencher, J., Elsner, A. Risiko und Risikominderung in einer Tideregion
93	2007	**Scheffermann, J.** Instationäre Strömungssimulationen bei Öffnungsvorgängen mit und ohne freier Oberläche am Beispiel beweglicher Schütze

Continued on next page

Continued from previous page

Issue	Year	Author and Title
		Matheja, A., Zimmermann, C., Bach, F.-W., Barcikowski, S., Bunte, J., Haferkamp, J.-D., Scheer, C., Reimche, W., Scheffermann, J., Walter, J. Stationäres 3D-Strömungsmesssystem für hochturbulente Strömungszustände unter Tide-, Strömungs- und Welleneinfluss
92	2006	**Zimmermann, C., Ohle, N., Elsner, A.** Deichüberwachung unter Einsatz der Fernerkundung
		Paesler, C. Bau, Ausrüstung und Betrieb eines Labordeiches im Naturmaßstab
		Zimmermann, C., Penchev, V., Scheffermann, J., Shukrieva, S. Evaluation of Reef Breakwater Efficiency from Physical and Numerical Simulations
91	2004	**Mai, S.** Klimafolgenanalyse und Risiko für eine Küstenzone am Beispiel der Jade-Weser-Region
90	2004	**Stoschek, O.** Sedimentation und Gegenmaßnahmen in tide- und brackwasserbeeinflussten Häfen: eine Analyse mit Hilfe 3-dimensionaler Simulationen
		Mai, S., Paesler, C., Zimmermann, C. Wellen und Seegang an Küsten und Küstenschutzbauwerken
89	2003	**Scheffermann, J., Matheja, A., Zimmermann, C., Linke, T.** 5th Framework Programme of the European Comission: Enhancing Access to Research Infrastructures Action. 'Fundamental Hydraulic Research for Coastal Areas by Using Large Scale Facilities of the Hydro-Lab-Cluster North Germany'
		Stoschek, O., Matheja, A., Zimmermann, C. Entwicklung von Unterwasserstrukturen zur Verminderung von Sedimentation und Baggermengen am Liegeplatz eines Segelschiffes in einem Tidefluss
		Scheffermann, J., Linke, T. Numerische 3D-Simulationen und physikalische Modellversuche von Ablösezonen und Drehwirbeln im Wasserbau
		Mai, S., Daemrich, K.-F., Zimmermann, C. Wahrscheinlichkeit des Wellenüberlaufes an der Kaje eines geplanten Containerterminals
		Ohle, N., Daemrich, K.-F., Zimmermann, C., Möller, J., Schüttrumpf, H., Oumeraci, H. Schräger Wellenauflauf an Seedeichen
		Ohle, N., Zimmermann, C. Untersuchungen zu den Ursachen von Deckwerksverwerfungen am Nordufer der Elbe
88	2002	**Grier, D.** Binnenschifffahrt in den Vereinigten Staaten
		Scheerlinck, E. Elektronische Anbindung von Binnenhäfen und -schiffen an Seehäfen
		Burkert, P. Telematische Anbindung von Hinterlandverkehren mit Containern im Hamburger Hafen
		Doerre, H. Logistische Anforderungen an Seehäfen für den Hinterlandtransport auf Binnenwasserstraßen
		Matheja, A., Zimmermann, C., Miska, M., Bernard, M. BIDIS - Ein integriertes Software-Tool für Betrieb und Management von Binnenhäfen
		v. Dijk, M. Wirtschaftlichkeit von Binnenschiffstransporten mit schnelleren Schiffseinheiten
		Linke, T., Scheffermann, J., Zimmermann, C. Grenzen der Geschwindigkeitszunahme infolge hydrodynamischer Belastungen auf Sohle und Deckwerk
		Abdel-Maksoud, M., Heinke, C. Schnelle Schiffseinheiten - Hydrodynamische Modellierung und ökonomische Aspekte
		Heibaum, M., Soyeaux, R. Belastung von Sohle und Deckwerk durch schnellere Binnenschiffe bei Anwendung heutiger Bemessungsansätze
		Willems, C. Flussinformationssysteme im europäischen Vergleich
		Gevers, K. Produktion und Validierung von Inland-ECDIS Karten
		Matheja, A., Zimmermann, C., Miska, M., Bernard, M. Modellierung gemischter Verkehre innerhalb eines Flussinformationssystems

Continued on next page

Continued from previous page

Issue	Year	Author and Title
		Vetterlein, H.-U. Verkehrsüberwachung und Verkehrssteuerung auf Binnenwasserstraßen
		Wittmüss, D. Künftige Verkehrsüberwachung und Verkehrssteuerung im modernisierten Verkehrssicherungssystem Nord-Ostsee-Kanal (VSS-NOK)
		Kerstgens, H. Logistische Dienstleistungen einer Reederei für die Erhöhung der Wertschöpfung von Containertransporten mit Binnenschiffen
		Rekers, N. Die Rolle der Häfen als Systemoperateure und Logistikzentren
		Waldmüller, T. Intermodaler Verkehr oder Verkehrschaos
87	2002	**Linke, T., Müller, A.** Entwicklung eines Einleitungsbauwerkes an einer Binnenwasserstraße
		Matheja, A., Wurpts, A. Bestimmung von Überschwemmungsgrenzen durch Kopplung von hydrodynamischer Simulation und geografischem Informationssystem am Beispiel der Unteraller
		Miska, M. Entwicklung und Implementierung eines integrierten Hafensystems
		Bernard, M. Konzeption und objektorientierte Modellierung eines Simulationsverfahrens auf der Basis zellularer Automaten für den Verkehrsablauf auf Binnenwaserstraßen
		Mai, S. Seegangsausbreitung in Hever und Heverstrom
		Linke, T., Scheffermann, J., Stocksmeyer, M. Numerische Simulation des Strömungsfeldes um Binnenschiffe mittels Computational Fluid Dynamics (CFD)
86	2001	**Ohle, N., Dunker, S.** Konstruktive Maßnahmen zur Stabilisierung von Deichen
		Stoschek, O., Matheja, A. Simulation von Sedimenttransportprozessen in tidebeeinflussten Hafengebieten
		Zimmermann, C., v. Lieberman, N. Folgen von klimabedingten Wasserstands- und Windänderungen für den Küstenschutz an der Unterweser
		Mai, S. Anwendbarkeit kommerzieller Radar-Wasserstandspegel zur Seegangsmessung
85	2000	**Plate, E.-J.** Risikoanalyse im Hochwasserschutz, Risk Analysis for Protection and Coastal Defense
		Huber, K. Hochwasserstände an Nord- und Ostseeküsten, High Water-levels at North Sea and Baltic Sea Coasts
		Mai, S., v. Lieberman, N. Belastung der Seedeiche durch Wasserstände und Wellen, Loads on Dikes from Water-levels and Waves
		Jensen, J. Extremereignisse an Nord- und Ostseeküsten - Ermittlung von Bemessungsereignissen, Extreme Events at North Sea and Baltic Sea Coasts - Estimation of Design Criteria
		Starke, W.-D. Schäden und Vorsorgemöglichkeiten im Küsten- und Deichschutz, Damages and Mitigation for Dike Protection and Coastal Defence
		Krause, G. Generalplanung für den Küstenschutz in Niedersachsen, Regional Planning for Coastal Defence in Lower Saxony
		Probst, B. Generalplanung für den Küstenschutz in Schleswig-Holstein, Regional Planning for Coastal Defence in Schleswick-Holstein
		Jorissen, R.-E. Coastal Flood-Risk Management in the Netherlands, Management des Sturmflutrisikos an den Küsten der Niederlande
		Laustrup, C. Probabilistic Design for Coastal Defence in Denmark, Probabilistische Bemessung im Küstenschutz in Dänemark
		Mai, S., v. Lieberman, N. Risikopotentiale für Nutzflächen und Infrastruktur, Risk Potential for Settlement Areas and Infrastructures
		Hofstede, J., Hamann, M. Wertermittlung sturmflutgefährdeter Gebiete in Schleswig-Holstein, Appraisal for Areas Endangered by Storm Surges in Schleswick Holstein

Continued on next page

Continued from previous page

Issue	Year	Author and Title
		Remmers, I. Risiken aus Sicht des Natur- und des Umweltschutzes, Risk to Environmental Protection and Nature Conservation
		Wiedemann, M. Rechtliche Grundlagen für Hochwasser- und Küstenschutz, Legal Basis for Flood Protection and Coastal Defence
		Heiß, G. Katastrophenschutz, Disaster Management
		Kron, W. Occure and Insurance of Natural Disasters, Auftreten und Versicherbarkeit von Elementarereignissen
84	2000	**Linke, T., Zimmermann, C., Hüsig, A.** Schnelle Schiffe für Combiverkehre und Containertransport
		Mai, S., Zimmermann, C. Konzepte und Techniken im Küstenschutz im Land Niedersachsen
		Matheja, A., Lichy, C. Grundlagen für den Aufbau verteilter agierender Umweltinformationssysteme
83	1999	**v. Lieberman, N.** Leitbildmodell für den Küstenschutz der Nordseeküste am Beispiel der Vorländer
		Mai, S., v. Lieberman, N. Untersuchungen zum Risikopotential einer Küstenregion
		Mai, S., Zimmermann, C. Safty of Coastal Defense Systems - An Assessment of the Reliability of Coastal Systems in the Event of Rising Water Levels due to Climate Change
82	1998	**Matheja, A., Zimmermann, C., v. Lieberman, N., Schwarze, H.** Optimierung von Küstensicherungsarbeiten im Küstenvorfeld der Nordseeküste, Untersuchungen zur Wirksamkeit von Lahnungen durch Simulation der Hydromechanisch-Morphodynamischen Wechselwirkungen in physikalischen und numerischen Modellen
		Streich, G., Zimmermann, C., Schwarze, H. Hydraulische Modellversuche für die geplante Hafenerweiterung Altenwerder im Hamburger Hafen - Untersuchungen zur Anordnung und Gestaltung der Kaianlage und der Wendebereiche im Hinblick auf die Schlickfallminimierung im Hafenbereich
81	1998	**Kunz, H.** Wärmeeinleitung in Tidegewässern und deren Begrenzung durch fach-technische Behördenentscheidungen
80	1997	**Dursthoff, W., Mazurkiewicz, B.** Soil Water Pipeline Interaction - Review and Resulting Program for Further Investigations
		Schöttler, J. Zur Simulation des Betriebsablaufs auf Binnenwasserstraßen und ihre Anwendung auf den Containertransport mit Binnenschiffen
79	1997	**Beyersdorf, J.** Verhalten von Luftblasen und Sedimenten in Blasensäulen in Abhängigkeit vom Salzgehalt im Wasser
		Hüsig, A. Wiederherstellung der linearen Durchgängigkeit an Staustufen (Fischaufstiegshilfen) - Stand des Wissens - und hydraulische Modelluntersuchungen für ein naturnahes Parallelgewässer am Schnellen Graben in Hannover
78	1996	**Zhan, L.** Sekundäre Geschwindigkeitskomponenten im Wellenfeld
		Schulz, N. Aufspülmaßnahmen zum Schutz des Strandes und der Siedlung von Copacabana in Rio de Janeiro
		Woltering, S. Baggergutentsorgung der Hafengruppe Bremen
		Fiege, M., Hagmeier, H., Schulz, N. Lahnungsbauwerke: Entwicklung, Ausführungsvarianten und Entwässerungssysteme
		Zimmermann, C., Schulz, N. Morphological Effects from Waves and Tides on Artificially Stabilized Forelands in the Wadden Sea
77	1996	**Woltering, S.** Eine LAGRANGEsche Betrachtungsweise des Seeganges
		Deppe, M., Roddewig, K. Entwicklung der Aller als Wasserstraße von Celle bis Verden - Vergangenheit und Perspektive

Continued on next page

Continued from previous page

Issue	Year	Author and Title
		Machens, U. Binnenwasserstraßen im Hinblick auf die Erfordernisse von Transportketten
76	1995	**Wu, N.-T.** Numerische Simulation der Druckschlagbelastung durch brechende Wellen auf senkrechte Bauwerke
		Zimmermann, C., Schwarze, H., Schulz, N., Henkel, S. Modelluntersuchungen zu propellerstrahlinduzierten Strömungen an Schiffsliegeplätzen mit unterschiedlichen Maßnahmen zum Erosionsschutz
75	1994	**Kunz, H.** Die Einwirkungen des Meeres und des Menschen auf das Küstengebiet - Küstenschutz und Ökologie: Ein Widerspruch? - Aufgaben und Strategien
		Probst, B. Überlegungen für einen Küstenschutz der Zukunft
		Zander, R. Nationalpark und Küstenschutz als Gemeinschaftsaufgabe von Ökologen und Ingenieuren
		Otto, H.-J. Küstenschutz in Hamburg - Deichbau und Ökologie
		Moutzouris, C.-I., Daniil, E.-I. Oxygenation on a Sloping Beach Under Breaking Waves
		Zimmermann, C., Schöttler, J. Technische und logistische Voraussetzungen und Konzepte für eine Verknüpfung von Binnenschiff und Lkw
		Zimmermann, C., Damian, R.-M., Beyersdorf, J. Air Bubble Sizes in Aqueous NaCl Solutions
		Zimmermann, C. Forschungsvorhaben des Franzius-Instituts im Wasserbau und Küsteningenieurwesen ab 1993 (Stand: März 1994)
		Zimmermann, C. Projektstudien des Franzius-Instituts im Wasserbau und Küsteningenieurwesen ab 1993 (Stand: März 1994)
		Zimmermann, C. Verabschiedung des alten Vorstandes und Vorstellung des neuen Vorstandes der GESELLSCHAFT DER FÖRDERER DES Franzius-Instituts e.V. anläßlich der 31. Mitgliederversammlung und Vortragsveranstaltung am 24. März 1994 in Hannover
74	1993	**Zhu, J.** Numerische Simulation der Vorlandentwicklung im Tidebereich
		Schröder, D. Chancen und Grenzen der Erhöhung der Verkehrsleistungen auf den Binnenwasserstraßen in Deutschland
		Muller-Zwartepoorte, C.-M. Administrative Maßnahmen und Techniken zur verbesserten Nutzung von Binnenwasserstraßen in den Niederlanden und Europa
		Hecke, R. Chancen, Voraussetzungen und notwendige Anpassungen für den kombinierten Ladungsverkehr im Standort Binnenhafen
		Kaul, S. Neue Antriebe für Binnenschiffe und ihre Bedeutung für die Schifffahrt und die Wasserstraße
73	1992	**Preser, F.** Belastung horizontaler Rohrkörper in Meeresbodennähe durch Seegang im Übergangsbereich
		Rodiek, W. Der 14 m-Ausbau der Außenweser: Maßnahmen und Berücksichtigung der Umweltverträglichkeitsuntersuchungen
		Daemrich, K.-F., Osterthun, M., Hinsch, J. Einfluß von Baumaßnahmen auf Strömungs- und Seegangsverhältnisse der Außenweser als Grundlage der Beurteilung zur Umweltverträglichkeit
		Vollstedt, H.-W. Die Erweiterung des Containerterminals Bremerhaven (CT III): Umweltverträglichkeit und notwendige Ersatzmaßnahmen
		Corsmann, M., Elverich, L. Landschaftspflegerische Begleitplanung im Rahmen der Ersatzmaßnahmen für die Erweiterung des Containerterminals Bremerhaven (CT III)
		Zimmermann, C., Osterthun, M., Schwarze, H. Berücksichtigung des Küstenschutzes im Rahmen der Landschaftspflegerischen Begleitplanung für die Erweiterung des Containerterminals Bremerhaven (CT III)

Continued on next page

Continued from previous page

Issue	Year	Author and Title
		Hinsch, J. Hydraulische Modellversuche zur Entwicklung umweltrelevanter Planungsalternativen für eine Wasserstraße: Beispiel Mosel bei Fankel
		Liebenstein, H. Ausgleichsmaßnahmen und landschaftspflegerische Begleitplanung beim Ausbau einer Wasserstraße: Beispiel Mosel
		Nestmann, F. Aerodynamische Modelle - eine strömungsmechanische Untersuchungsmethode zur Planung wasserbaulicher Maßnahmen
		Gaumert, T. Anforderungen an Fischaufstiegshilfen in Fließgewässern
		Berkenkamp, G., Zimmermann, C., Schwarze, H. Lösungsvorschläge und Modellversuche für die ökologische Durchgängigkeit zwischen einer Wasserstraße und einem Zufluß am Beispiel der Weser in Nienburg
72	1991	**Saathoff, F.** Geokunststoffe in Dichtungssystemen - Laboruntersuchungen zum Verhalten von Geotextilien und Kunststoffdichtungsbahnen -
		Wilckens, F. Forschungsförderung im Küsteningenieurwesen
		Kunz, H. Klimaänderungen, Meeresspiegelanstieg, Auswirkungen auf die niedersächsische Küste
		Daemrich, K.-F. Modellversuche zum Wellenüberlauf an Polderwänden
		Osterthun, M., Partenscky, H.-W. Vorlandbildung an Deichen und SicherungsdämmenTeil 1: Morphologische Analyse der Vorlandentwicklung
		Zhu, J., Partenscky, H.-W. Vorlandbildung an Deichen und Sicherungsdämmen Teil 2: Numerische Modellierung der Vorlandentwicklung
71	1991	**Schade, D.** Untersuchungen über das Wellenklima an einer Brandungsküste unter Einschluß der Richtungsstruktur des Seegangs, dargestellt am Beispiel der Insel Sylt
70	1990	**Brinkmann, B.** Ein Beitrag zur Bestimmung des Wasseraustausches zwischen Fluß und Hafen in Tidegebieten
		Klinge, U. Zur Energie von Tidewellen in Ästuaren mit einem Beispiel für die Unterweser
		Römisch, K. Hydromechanische Effekte fahrender Schiffe in Binnenkanälen
69	1989	**Bobzin, H.** Praktische Naßbaggerei
		Mühring, W. Über die Anwendung porenmäßig abgestufter Vliesstoffe beim Ausbau von künstlichen Wasserstraßen
		Lüken, J. Hochwasserschutz in Hamburg. Darstellung der Entwicklung seit der Februarsturmflut 1962
68	1989	**Mühring, W.** Entwicklung und Stand der Deckwerksbauweisen im Bereich der Wasser- und Schiffahrtsdirektion Mitte
		Bartnik, H. Entwicklung und Stand der Deckwerksbauweisen im Bereich der WSD West
		Paul, W. Deckwerksbauweisen an Rhein, Neckar, Saar
		Paul, H.-J. Herstellen von Deckwerken unter ausführungstechnischen Gesichtspunkten
		Möbius, W. Abrollen von Geotextilien unter Wasser
		Saggau, W. Küstenschutzmaßnahmen in der Nordstrander Bucht
		Laustrup, C. Deckwerke an der dänischen Nordseeküste
		de Groot, M.-B. Allgemeine Grundlagen zur Standsicherheit des Untergrundes unter Deckwerken
		Oumeraci, H. Beanspruchung von Betonplattendeckwerken und ihre Berücksichtigung bei der Bemessung

Continued on next page

Continued from previous page

Issue	Year	Author and Title
		Richwien, W. Seegang und Bodenmechanik - Geotechnische Versagensmechanismen von Seedeichen
		Köhler, H.-J. Messung von Porenwasserüberdrücken im Untergrund
		Bezuijen, A. Wasserüberdrücke unter Betonsteindeckwerken
		Sparboom, U. Naturmaßstäbliche Untersuchungen an Deckwerken im Großen Wellenkanal
		Heerten, G. Analogiebetrachtungen zu Filtern
		Hallauer, O. Baustoffe für Deckwerke
		Saathoff, F. Prüfungen an Geotextilien
		Schulz, H. Überblick über neue nationale und internationale Empfehlungen
67	1988	**Riebensahm, R.** Dimensionierung von Container-Terminals in Binnenhäfen - Untersuchung der Einflußfaktoren für die betriebliche Bemessung
		Daemrich, K.-F., Scheffer, H.-J., Schwarze, H., Partenscky, H.-W., Kohlhase, S. Theoretische Vorstudie zur wellendämpfenden Wirkung des Riffs und zum seegangserzeugten Feststofftransport an der Westküste der Insel Sylt
		Brinkmann, B., Schoreder, E. Untersuchung der Abflußverhältnisse an einem im Nieuwe Waterweg geplanten Sturmflutsperrwerk
		Fittschen, T. Modellversuche für den Dollarthafen
		Müller, K.-D. Maßnahmen zur Reduzierung der Walzenströmung am Beispiel der Modellversuche für den Hamburger Hafen
		Osterthun, M. Vorlandbildung an Deichen und Sicherungsdämmen - ein BMFT-Forschungsprojekt -
		Salzmann, H. Planung und Bau des Emstunnels
66	1988	**Partenscky, H.-W.** Ausrüstungselemente von Binnenschiffs-Schleusen - Bemessung und konstruktive Ausbildung
		Oumeraci, H. Funktionelle Hafenplanung unter Berücksichtigung der Schiffsbewegungen infolge Wellenunruhe im Hafen
		Moutzouris, C.-I. Longshore Sediment Transport Computations: The Wave Power Equation and the Bijker Formula
65	1987	**Rupert, D.** Kontinuierliche Durchflußermittlung in Tideflüssen zur Bestimmung des Wasserhaushaltsparameters 'Abfluß'
		Ohling, J. Dollarthafen - Leidensweg einer Hafenplanung
		Brinkmann, B. Sedimentation in Hafenbecken
		Ricke, M. Gestaltung von Fischereihäfen
		Schwarze, H. Hydraulisches Tidemodell des See- und Lagunengebietes um Abu Dhabi
		Daemrich, K.-F., Schade, D. Seegangsmessungen vor Sylt mit einem Wellenrichtungsmeßsystem
		Saathoff, F. Filterwirksamkeit gedehnter Geotextilien
		Saathoff, F. Untersuchungen zum Langzeit-Filterverhalten von Geotextilien
		Holtorff, G. Entwicklung natürlicher alluvialer Abflußgerinne
		Müller, J. Verkehrsprobleme im Duisburger Hafen
		Passlack, G. Vom Lehrgebiet Wasserbau zum Franzius-Institut für Wasserbau und Küsteningenieurwesen der Universität Hannover (1847 bis 1987)
64	1987	**Hartung, W.** Über den Einfluß der Komponenten des Wasserverkehrssystems auf die Sicherheit des Seeschiffsverkehrs

Continued on next page

Continued from previous page

Issue	Year	Author and Title
		Saathoff, F. Marktformen und Grundsätzliches zur Wirkungsweise von Geotextilien
		Zanke, U. Sedimenttransportformeln für Bed-Load im Vergleich
63	1986	**Xiao, Z.** Ein neuer Weg der Fördertechnik für den Rohrleitungstransport von grobkörnigen Feststoffen
62	1986	**Partenscky, H.-W.** Zum 65. Geburtstag von Professor Dr.-Ing. F.-F. Zitscher
		Kniess, H.-G. Historische Entwicklung der Bauweisen für Auskleidungen von Binnenwasserstraßen
		Meyer, H. Durchlässige Böschungsbefestigungen am Mittellandkanal - einst und heute
		Mühring, W. Über die Entwicklung der Hartdichtungen beim Ausbau von Kanälen
		Schönian, E. Langzeitverhalten von Asphaltdichtungen im Wasserbau
		Hoffmann, H.-G. Asphaltdichtungen im Wasserbau
		Beckmann, J. Erneuerung der Versiegelung der Oberflächendichtung auf der wasserseitigen Dammfläche der Biggetalsperre
		Saathoff, F., Bassen, R., Kohlhase, S. Anwendungsorientierte Untersuchungen an Deponie-Dichtungssystemen
		Heerten, G. Ein geschlossener Ansatz zur Dimensionierung von Geotextilien für Ufersicherungen
		Täubert, U. Das Speicherbecken Geeste - Zwei Millionen Quadratmeter Filtervlies und Asphaltbeton-Dichtung
		Abromeit, H.-U. Maschineller Unterwassereinbau von geotextilen Filtern
		Knipschild, F.-W. Deponie-Abdichtungen mit Kunststoffdichtungsbahnen - Stand der Technik und Entwicklungen
61	1985	**Scheffer, H.-J.** Wellenunruhe in Häfen und Schiffsbewegungen -, ein Beitrag für eine integrierte Hafenplanung
		Dursthoff, W., Mazurkiewicz, B. Problems Related to Subsea Pipeline-Seabed Interaction
		Daemrich, K.-F., Kahle, W., Partenscky, H.-W. Schutzwirkung von Unterwasserwellenbrechern unter dem Einfluß unregelmäßiger Seegangswellen
		Xi, Y. Pile Berthing Structures in Harbour Engineering
60	1985	**Moutzouris, C.I.** Coastal Processes Along the Eroding Western Coast of the Island of Sylt, F.R. Germany
		Dieckmann, R. Geomorphologie, Stabilitäts- und Langzeitverhalten von Watteinzugsgebieten der Deutschen Bucht
		Schwarze, H. Untersuchung von Baumaßnahmen im Tidegebiet
59	1984	**Grett, H.-D.** Das Reibungsverhalten von Geotextilien in bindigem und nichtbindigem Boden
		Wilde, P., Kozakiewicz, A. Application of Kalman Filter to Analysis of Vibrations of Structures Due to Waves
		Burkhardt, O. Bericht über die Arbeiten des Franzius-Instituts in den Jahren 1982 bis 1984
		Partenscky, H.-W. Schleusen und Hebewerke, Überblick und Ausblick
		Passlack, G. Verbau von Hochwasserabflußquerschnitten an der Ems und an der Leine
		Kohlhase, S., Scheffer, H.-J. Modelluntersuchungen für Seehäfen
		Grett, H.-D. Geotextilien im Wasserbau und Eisenbahnbau
		Dieckmann, R. Flächenhafter Küstenschutz
		Nasner, H. Wellenerzeugter Sedimenttransport

Continued on next page

Continued from previous page

Issue	Year	Author and Title
		Partenscky, H.-W. Bemessung von Wellenschutz-Bauwerken
		Dursthoff, W. Seegangskräfte auf horizontale Kreiszylinder
58	1984	**Kao, C.-C.** Seegangsbelastung auf kreisförmige Rohre in Sohlnähe
		Tang, F. A Comparison of the Wave Statistics Between the Eastern Part of Taiwan Strait and the North Sea
		Siefert, W. Energiebetrachtungen zum Tideablauf in Flüssen mit einigen Anwendungsbeispielen
		Horn, P. Stoßschutzanlagen an Schleusen und Hebewerken
57	1983	**Kohlhase, S.** Ozeanographisch-seebauliche Grundlagen der Hafenplanung
		Grabe, W. Kunststoffdichtungsbahnen im Wasserbau
		Kahle, W. Untersuchung des Energiebedarfs beim hydraulischen Feststofftransport von Sanden und Kiesen durch horizontale Rohrleitungen unterschiedlicher äquivalenter Wandrauhigkeit
		Grabe, W. Studentische Exkursion im Sommer 1983 zu Wasserbauwerken im westdeutschen Raum und in den Niederlanden
56	1983	**Eggert, W.-D.** Diffraktion und Wellentransmission an Tauchwänden endlicher Länge. Ein Beitrag zur Bestimmung der Wellendämpfung teildurchlässiger Wellenbrecher
		Partenscky, H.-W. Die Forschungsaktivitäten des Franzius-Instituts in den Jahren 1980 und 1981
		Daemrich, K.-F. Zur Auswertung von Seegangsmessungen am Beispiel von Messungen vor Westerland/Sylt
		Grabe, W. Untersuchungen im Franzius-Institut über die Eigenschaften von Geotextilien
		Passlack, G. Regulierungs- und Ausbaumaßnahmen an Flußläufen
		Grabe, W. Mechanische und hydraulische Eigenschaften von Geotextilien
55	1982	**Flügge, G.** Transport- und Ausbreitungsmechanismen in Flüssen und Tideästuarien unter besonderer Berücksichtigung der Strömungsturbulenz
		Kahle, W. Hydraulische Einflußgrößen beim Rohrleitungstransport von Sand-Wasser-Gemischen
54	1982	**Burkhardt, O.** Vorträge im Rahmen der Fachveranstaltung 'Häfen - Planung, Bau, Betrieb' im Haus der Technik, Essen
		Göhren, H. Aufgaben des öffentlichen Bauherrn bei der Abwicklung hafenbaulicher Vorhaben
		Kohlhase, S. Ermittlung ozeanographisch-seebaulicher Grundlagen für die Planung von Seehäfen
		Wiedemann, G. Fragen der Nautik und der Verkehrssicherung für Planung und Betrieb von Häfen und ihren Zufahrten
		Horn, A. Bodenmechanische und grundbauliche Einflüsse bei der Planung, Konstruktion und Bauausführung von Kaianlagen
		Heyer, E. Konstruktive Gestaltung von Hafenbauwerken
		Stückrath, T. Über die Probleme des Unternehmers beim Hafenbau
		Morisse, M. Der Einfluß der betrieblichen Erfordernisse auf die Hafengestaltung
		Kroh, W. Die Finanzierung von Hafenbauprojekten durch die Kreditanstalt für Wiederaufbau im Rahmen der finanziellen Zusammenarbeit der Bundesrepublik Deutschland mit Entwicklungsländern
		Hemmer, H.-R. Kosten-Nutzen-Betrachtungen bei Planung und Betrieb von Häfen
		Vetter, A. Die Rolle des Beratenden Ingenieurs bei Planung, Bau und Betrieb von Häfen in Entwicklungsländern

Continued on next page

Continued from previous page

Issue	Year	Author and Title
		Meyer, H. Kreuzungsbauwerke am Mittellandkanal
		Mühring, W. Uferauskleidungen beim Ausbau von künstlichen Wasserstraßen am Beispiel des Mittellandkanals
		Zanke, U. Kolke am Pfeiler in richtungskonstanter Strömung und unter Welleneinfluß
53	1981	**Tautenhain, E.** Der Wellenüberlauf an Seedeichen unter Berücksichtigung des Wellenauflaufs - Ein Beitrag zur Bemessung -
		Keska, J.-K. Förderung von inhomogenen Zwei-Phasen-Gemischen durch Rohrleitungen. Ausgewählte theoretische und praktische Probleme der Meßtechnik, der Mechanik und der Methodik
52	1981	**Heerten, G.** Geotextilien im Wasserbau - Prüfung, Anwendung, Bewährung -
		Kazanskij, I. Über theoretische und praxisbezogene Aspekte des hydraulischen Feststofftransportes
51	1980	**Partenscky, H.-W.** Dank an die Gäste und Überleitung zum Festvortrag
		Zitscher, F.-F. Die Bedeutung unseres Wassers im Universum
		Partenscky, H.-W. Dank an Professor Zitscher und Schlußworte
		Lundgren, H. Die zukünftige Rolle natürlicher Wellen in der Küstentechnik (Future Role of Natural Sea States)
		Monkmeyer, D. Wave-Induces in Coastal Protection Works
		Bijker, W. Modern Trends in Coastal Protection Works
		Wilde, P. Problems of Vibration of a Breakwater Structure Due to Wind Waves
		Vischer, D. Durch Felsstürze in Seen erzeugte Wellen
		Price, A.-W. Coastal Engineering - The Impossible Art
		Nougaro, J. Dammbrüche
		Führböter, A. Strömungsvorgänge in den wandnahen Grenzschichten beim hydraulischen Feststofftransport
		Hager, M. Maßnahmen zur Bekämpfung von Erosionserscheinungen in Flüssen
		Simons, H. Planung und Bau neuer Seehäfen im Ausland
		Boe, C. Wasserbau und Umweltschutz
		Salzmann, H. Die Entwicklung des deutschen Offshore-Bauens
		Dillo, H.-G. Kleinkraftwerke - ein Beitrag zur Energieversorgung in Entwicklungsländern
		Brühl, H. Einige technische Aspekte bei der Planung und beim Bau des Mehrzweck-Terminals Limón/Costa Rica
		Stückrath, T. Bau des Unterwasserrückgabetunnels für das Kernkraftwerk Busher am Persischen Golf
		Passlack, G. Wasserbauliche Forschungsarbeiten im Franzius-Institut für Wasserbau und Küsteningenieurwesen der Universität Hannover in den Jahren 1977 bis 1979
50	1980	**Partenscky, H.-W.** Hochschullehrer der Fachgebiete Allgemeiner Wasserbau, Verkehrswasserbau und Küsteningenieurwesen an der Universität Hannover von 1847 bis 1980
		Partenscky, H.-W. Von der Hannoverschen Versuchsanstalt für Grundbau und Wasserbau der Technischen Hochschule Hannover zum Franzius-Institut für Wasserbau und Küsteningenieurwesen der Universität Hannover (1980)
		Partenscky, H.-W. Zum Geleit: Professor Dr.-Ing. Dr.phys. H.-W. Partenscky Direktor des Franzius-Instituts für Wasserbau und Küsteningenieurwesen

Continued on next page

Continued from previous page

Issue	Year	Author and Title
		Krolewski, H. Grußwort des 1. Vorsitzenden der Gesellschaft der Förderer des Franzius-Instituts e.V.
		Passlack, G. Entwicklung des Lehr- und Forschungsgebietes Verkehrswasserbau an der Universität Hannover
		Partenscky, H.-W. Neue Erkenntnisse über das Stabilitätsverhalten und den Sedimenttransport in Watt-Prielsystemen
		Heerten, G. Das Franzius-Institut als Prüfinstanz für Geotextilien
		Ross, C. Möglichkeiten und Grenzen eines geregelten Sperrwerksbetriebs zur Beeinflussung der Tidedynamik
		Burkhardt, O. Über die Bestückung eines Kais mit Hafenkränen
		Falldorf, W. Anwendung, Einsatz und Aussagefähigkeit von hydraulischen Tidemodellen
		Lindlar, A. Die Entwicklung von Tidesteueranlagen - Prozeßrechnergesteuerte Nachbildung von Naturtiden im Franzius-Institut der Universität Hannover
		Mahnken, B., Müller, H., Visscher, G. Wärmebilanzmessungen in der Unterweser
		Daemrich, K.-F., Kohlhase, S. Seegangsforschungsprogramme im Franzius-Institut innerhalb des Sonderforschungsbereichs 79
		Schwarze, H. Grundlagen für den Betrieb von hydraulisch-thermischen Modellen
		Bode, E., Zanke, U. Neue Erkenntnisse im Sedimenttransport - Ergebnisse aus der Arbeit des Teilprojektes B5 im SFB 79 -
		Kazanskij, I., Mathias, H.-J. Feststofftransport in Rohrleitungen - Gegenüberstellung von Untersuchungen im Modell und in der Natur
		Passlack, G. Auswirkungen wasserbaulicher Maßnahmen an Binnengewässern im Raum Hannover
		Dursthoff, W. Entwicklung von Primärwandlern zur Nutzung der Seegangsenergie
		Barg, G. Salzgehaltsverteilungen in Brackwassergebieten als Grundlage ökologischer Betrachtungen
49	1979	**Barg, G.** Untersuchungen über Salzgehaltsverteilungen in Brackwassergebieten von Tideflüssen am Beispiel der Unterweser
		Kunz, H. Regelungen für die Abgabe radioaktiver Stoffe aus einem Leichtwasser-Kernkraftwerk vom Druckwassertyp in einen Tidefluß
		Kunz, H. Das Automatische Meßsystem für die Beweissicherung WASSER beim Kernkraftwerk Unterweser
		Kunz, H. Wasserrechtliche Regelungen für die Einleitung von Kühlwässern in einen Tidefluß unter besonderer Berücksichtigung des Einsatzes von automatischen Meßsystemen, dargestellt am Beispiel des Kernkraftwerks Unterweser
		Zanke, U. Über die Abhängigkeit der Größe des turbulenten Diffusionsaustausches von suspendierten Sedimenten
		Zanke, U. Über die Anwendbarkeit der klassischen Suspensionsverteilungsgleichung über Transportkörpern
		Zanke, U. Konzentrationsverteilung und Kornzusammensetzung der Suspensionsfracht in offenen Gerinnen
		Wundes, R. Entwicklung eines Hybriden Tidemodells
48	1978	**Zanke, U.** Zusammenhänge zwischen Strömung und SedimenttransportTeil 2: Berechnung des Sedimenttransportes hinter befestigten Sohlenstrecken - Sonderfall zweidimensionaler Kolk -

Continued on next page

Continued from previous page

Issue	Year	Author and Title
		Hinsch, J. Anwendung von Pulswellen beim hydraulischen Feststofftransport
		Elahi, K.-Z. Berechnung von lokalen Gezeitenphänomenen in einem Gebiet mit geringem Beobachtungsmaterial mit Anwendung auf die Sonmiani Bucht (Pakistan)
		Passlack, G. Bauliche Maßnahmen zur Senkung der Hochwasserstände in Hochwasserabflußgebieten von Binnenflüssen
47	1978	**Daemrich, K.-F.** Diffraktion gebeugter Wellen - Ein Beitrag zur Berechnung der Wellenunruhe in Häfen -
		Daemrich, K.-F., Hillebrand, W., Kohlhase, S., Tautenhain, E. Versuchseinrichtung Wellenbecken für dreidimensionale, vergleichende Untersuchungen mit regelmäßigen Wellen und Wellenspektren
		Zitscher, F.-F. Schadensursachen an Küstenschutzanlagen herkömmlicher Art während der Sturmflut vom 3.1.1976 an der schleswig-holsteinischen Westküste
		Daemrich, K.-F., Kohlhase, S. Diffraktion an halbunendlichen Wellenbrechern - Diagramme der Wellenhöhenverteilung hinter totalreflektierenden linienförmigen Bauwerken -
		Zanke, U. Zusammenhänge zwischen Strömung und Sedimenttransport Teil 1: Berechnung des Sedimenttransportes - allgemeiner Fall -
46	1977	**Kunz, H.** Schiffsschwall und Sunk in seitlich einer Wasserstraße angeordneten Becken
		Barg, G., Flügge, G., Visscher, G. Experimentelle Bestimmung des Wärmeaustausches an der Gewässeroberfläche
		Zanke, U. Neuer Ansatz zur Berechnung des Transportbeginns von Sedimenten unter Strömungseinfluß
		Hamel, G. Statistische Analyse von Tidewasserständen am Beispiel des Pegels W.shaven 'Seeschleuse'
		Kunz, H. Die Wirkung von Schiffswellen auf Entwässerungsbauwerke an Tideflüssen
		Zanke, U. Berechnung der Sinkgeschwindigkeiten von Sedimenten
		Partenscky, H.-W. Bericht über die Arbeiten des Franzius-Instituts von 1975 bis 1977
		Partenscky, H.-W. Veröffentlichungen von Mitarbeitern des Franzius-Instituts der Technischen Universität Hannover in den Jahren 1975 bis 1977
		Passlack, G. Schwerpunkte der wasserbaulichen Forschungen im Franzius-Institut für Wasserbau und Küsteningenieurwesen (Zeitraum 1975 bis 1977)
		Göhren, H. Perspektiven der Hamburger Hafenplanung
		Visscher, G. Meßprogramm Unterweser
		Flügge, G. Bestimmung des Wärmeaustausches an Wasseroberflächen
		Heerten, G. Problematik der Kühlwasserversorgung an einer Stauhaltungskette
		Schwarze, H. Modelluntersuchungen für die Kühlwasserversorgung der Kernkraftwerke Iran am Persischen Golf
		Kohlhase, S. Numerisches Modell zur Bestimmung der Wellenunruhe in einem Hafen
		Daemrich, K.-F. Grundsatzuntersuchungen zur Diffraktion an Hafeneinfahrten
		Dursthoff, W. Wellenenergie - nutzbare Energie?
		Partenscky, H.-W. Hydrodynamische Belastung von Pipelines auf der Meeressohle
45	1977	**Grcic, J.** Einfluß der pulsartigen Strömung bei hydraulischem Feststofftransport
		Berger, U., Kurpiers, J. Automatisierung der graphischen on-line-Darstellung von umfangreichen Meßreihen

Continued on next page

Continued from previous page

Issue	Year	Author and Title
		Nasner, H., Partenscky, H.-W. Modellversuche für die Tide-Elbe. Strombaumaßnahmen nach 1962 und ihre Auswirkungen auf die Sturmflutwasserstände
		Nasner, H., Partenscky, H.-W. Sturmfluten in der Elbe und an der deutschen Nordseeküste von 1901 bis zum Januar 1976
		Heerten, G., Partenscky, H.-W. Ein Vergleich der Sturmflut vom 3. Januar 1976 auf der Elbe mit anderen Sturmfluten nach 1962
44	1976	**Zanke, U.** Über den Einfluß von Kornmaterial, Strömungen und Wasserständen auf die Kenngrößen von Transportkörpern in offenen Gerinnen
		Rupert, D. Zur Bemessung und Konstruktion von Fendern und Dalben
		Zanke, U. Über die Naturähnlichkeit von Geschiebeversuchen bei einer Gewässersohle mit Transportkörpern
		Partenscky, H.-W. Bericht über die Arbeiten des Franzius-Instituts von 1973 bis 1975 und zukünftige Planungen
		Passlack, G. Wasserbauliche Untersuchungen im Franzius-Institut in den Jahren 1973 bis 1975
		Barjenbruch, K.-H. Entwicklung und Stand des Küstenschutzes in Niedersachsen
		Ohling, J. Ausbau der niedersächsischen Seehäfen
		Schwarze, H. Untersuchungen des Franzius-Instituts über die Einleitung von aufgewärmtem Kühlwasser in Gewässer
		Grüne, J. Neue Wellenrinne des Franzius-Instituts - Untersuchungen mit Seegang -
		Renger, E. Grundzüge der Analyse und Berechnung von morphologischen Veränderungen in Wattengebieten
		Wundes, R.-D. Hybride Modelle - Koppelung von numerischen und hydraulischen Modellen
43	1976	**Renger, E.** Quantitative Analyse der Morphologie von Watteinzugsgebieten und Tidebecken
		Brühl, H. Einfluß von Feinststoffen in Korngemischen auf den hydraulischen Feststofftransport in Rohrleitungen
		Berger, U. MACH-Reflexion als Diffraktionsproblem
42	1975	**Henze, R.** Beitrag zur Abschätzung der bleibenden Verschiebung kleiner Fundamente auf dicht gelagertem Sandboden
		Hager, M. Untersuchungen über MACH-Reflexion an senkrechter Wand
		Rehling, U. Datenerfassung und -auswertung mit Digitalrechnern bei Wasserstands- und Wellenmessungen
41	1974	**Heerten, G.** Einfluß von Schiffbau und Umschlagstechnik auf die Gestaltung von Seehäfen
		Niemeyer, H.-D. Wellenerzeugte Strömungen und Sedimenttransport
		Ramacher, H. Der Ausbau von Unter- und Außenweser
40	1974	Nasner, H. Über das Verhalten von Transportkörpern im Tidegebiet
		Siefert, W. Erste Erfahrungen mit einem neuen Sturmflut-Vorhersageverfahren
		Partenscky, H.-W. Entwicklung und Arbeitslage des Franzius-Instituts für Wasserbau und Küsteningenieurwesen der Technischen Universität Hannover in den Jahren von 1971 bis 1973
		Nasner, H. Dynamisches Verhalten von Transportkörpern. Vergleiche von Messungen in der Natur und im Modell
		Schüttrumpf, R. Maßgebende hydrologische Größen für die Beurteilung von Einleitungen in Tideästuarien
		Schwarze, H. Untersuchungen für die Übertragbarkeit der Ergebnisse aus hydraulisch-thermischen Modellversuchen

Continued on next page

Continued from previous page

Issue	Year	Author and Title
		Passlack, G. Entwicklung des Sonderforschungsbereiches 79 der Technischen Universität Hannover
		Rehling, U. Meßwerterfassung an hydraulischen Tidemodellen
		Renger, E. Untersuchungen von Watteinzugsgebieten
		Daemrich, K.-F. Untersuchungen in dreidimensionalen Wellenbecken
		Grüne, J. Entwurf eines Großen Wellenkanals
		Brühl, H. Hydrografische Untersuchungen über die Einleitung von Abwässern in das Seegebiet von Busan/Korea
		Dursthoff, W., Kohlhase, S. Hydrografische Messungen im Seegebiet von Sonmiani/Pakistan
		Passlack, G. Mitgliederverzeichnis der Gesellschaft der Förderer des Franzius-Instituts e.V. nach dem Stande vom 1.3.1974
39	1973	**Schüttrumpf, R.** Über die Bestimmung von Bemessungswellen für den Seebau am Beispiel der südlichen Nordsee
		Liang, N.-K. Über den Einfluß des Windfeldes bei der Wellenvorhersage
38	1973	**Ackermann, H.** Kriterien und Ansätze für eine integrierte Hafenentwicklungsplanung unter besonderer Berücksichtigung der Probleme in Entwicklungsländern
		Kohlhase, S. Über den Vordrall an Pumpeneinläufen im Wirbelfeld
37	1972	**Buchholz, W.** Die Entwicklung des Franzius-Instituts von 1949 bis 1971 - Eine Würdigung Professor Hensens -
		Wiedemann, G. Dank und Anerkennung für Herrn Professor Hensen
		Laucht, H. Worte zum Abschied von Professor Dr.-Ing. Dr.-Ing. E.h. W. Hensen
		Peter, H. Worte des Dankes an Herrn Professor Hensen
		Lorenzen, J. Grußworte an Professor Hensen
		Partenscky, H.-W. Entwicklungstendenzen in der Wasserbau-Forschung, Gestern und Heute
		Dillo, H.-G. Planungen, Entwürfe und Bauausführungen im Auslande
		Krolewski, H. Neuere Bauvorhaben im Kraftwerksbau
		Rohde, H. Hydrologische Probleme des Wasserbaus im Küstengebiet
		Kazanskij, I. Wechselwirkung zwischen Makroturbulenz und Feststofftransport in Rohrleitungen
		Kohlhase, S. Elektroanaloge Voruntersuchungen für Kühlwasserkreisläufe
		Schwarze, H. Modelluntersuchungen für die deutschen Tideästuarien
		Passlack, G. Kurzbericht über die Arbeiten des Franzius-Instituts von 1969 bis 1971
36	1971	**Führböter, A.** Über die Bedeutung des Lufteinschlages für die Energieumwandlung in Brandungszonen
		Rohde, H. Eine Studie über die Entwicklung der Elbe als Schiffahrtsstraße
		Spataru, A. Über gleichförmige und ungleichförmige Turbulenz in Freispiegelgerinnen
35	1970	**Passlack, G.** Strömungen im Bodensee
		Führböter, A. Zur Frage der hydraulischen Förderung von Meereserzen
		Rocha Felices, A. Wasserableitung aus Flüssen mit Sedimentbewegung
		Stückrath, T. Über die Durchmischung von Süß- und Salzwasser in den Brackwassergebieten von Tideflüssen

Continued on next page

Continued from previous page

Issue	Year	Author and Title
34	1970	**Rodloff, W.** Über Wattwasserläufe
		Schwarz, J. Treibeisdruck auf Pfähle
		Dursthoff, W. Über den quantitativen Wasseraustausch zwischen Fluß und Hafen
33	1969	**Wagner, H.** Meßprogramm am Gußeisen-Ausbau der U-Bahn-Tunnel in Hamburg
		Ayar, H.-R. On the Hydromechanics of Breakers on Steep Slope
		Schwarze, H. Erweiterung des Anwendungsbereiches der REHBOCKschen Brükkenstaugleichung auf Trapezquerschnitte
		Kontur, G. Die Eisverhältnisse der Donau. Erfahrungen mit Eisbrecher-Schiffen
32	1969	**Wittmer, H.-G.** Modellversuche für die Absperrung der Oste
		Roy, S.-C. Hydraulic Investigations on Behalf of Hooghly Estuary
		Roy, S.-C. Hydraulische Untersuchungen über das Hooghly Ästuar
		Stückrath, T. Die Bewegung von Großriffeln an der Sohle des Rio Paraná
		Henningsen, D., Mäckel, R. Fossile Holzreste und Baumstämme in Flußablagerungen
31	1968	**Salzmann, H.** Hydraulische und bodentechnische Vorgänge beim Grundsaugen
		Lehmann, U. Der Einfluß von Filterkies und Brunnenrohr auf die Bemessung eines vollkommenen Brunnens
		Dillo, H.-G. Aufgaben deutscher Consultingfirmen im Ausland
		Dursthoff, W. Die Entwicklung der Turbulenzforschung im Hinblick auf ihre Bedeutung im Wasserbau
		Kohlhase, S. Analogversuche als Leitmodelle - Elektroanalogversuche und HELE-SHAW-Strömungen -
		Krolewski, H. Wasserbauten der Kraftwirtschaft
		Schwarz, J. Über die physikalischen Vorgänge beim Eisdruck
		Stückrath, T. Die 'Regimetheorie' - Entwicklung und Anwendung -
		Christiansen, H., Schäfer, V. Bericht über die Exkursion des Lehrstuhls für Verkehrswasserbau 1967 nach Ceylon, Indien, Pakistan, Afghanistan und in die Türkei
30	1968	**Siefert, W.** Sturmflutvorhersage für den Tidebereich der Elbe aus dem Verlauf der Windstaukurve in Cuxhaven
		Göhren, H. Triftströmungen im Wattenmeer
		Kontur, S. Kinematische Prüfungen des Kapillaranstiegs unter besonderer Berücksichtigung der charakteristischen Eigenschaften des Grundwasser-Strömungsfeldes
		Burkhardt, O. Naturmessungen des Strömungswiderstandes von Hubinsel-Beinen im Seegang
29	1967	**Führböter, A.** Zur Mechanik der Strömungsriffel. Ein Ansatz zur Berechnung der Höhe der Transportkörper und ihres Einflusses auf den Feststofftransport
		Krolewski, H. Die Verteilung der Fließgeschwindigkeiten in einem Vorfluter
		Burkhardt, O. Über den Wellendruck auf senkrechte Kreiszylinder
		Annen, G. Die Bemühungen um das Abflußgesetz aus der Sicht der Praxis
		Gehrig, W. Über die Frage der naturähnlichen Nachbildung der Feststoffbewegung in Modellen
28	1966	**Führböter, A.** Der Druckschlag durch Brecher auf Deichböschungen
		Hensen, W., Führböter, A. Kunststoff zur Sicherung von Abbruchufern
		Domzig, H. Wasserwirtschaftliche Arbeiten im Vorraum der Landeshauptstadt Hannover
		Roy, N. Hydrodynamic Pressure Oscillation Around a Conduit Gate (Hydrodynamische Druckschwankungen im Bereiche eines Tiefschützes)

Continued on next page

Continued from previous page

Issue	Year	Author and Title
27	1966	**Führböter, A., Passlack, G., Wittmer, H.-G.** Entwicklung des Franzius-Instituts für Grund- und Wasserbau der Technischen Hochschule Hannover
		Wittmer, H.-G. Sedimentologische Probleme des Hafens Quequén, Argentinien
		Sindern, J. Die hydrologischen und morphologischen Aufgaben im Küstenraum, dargestellt an den Aufgaben der Wasser- und Schifahrtsdirektion Kiel
		Dettmers, D. Aus der hydraulischen Feststoffförderung
		Lamprecht, H.-O. Uferschutz mit Betonfertigteilen
		Bischofsberger, W. Wupperdurchstich und Wasserkraftanlage des Klärwerks Wuppertal-Buchenhofen
		Passlack, G. Durchführung von hydrologischen Messungen in der Natur
		Simons, H. Zur Gestaltung abgesenkter Unterwassertunnel
		Krolewski, H. Der Verbau von Abflußquerschnitten. (Eine Betrachtung zur Bemessung von Wehr- und Brückenweiten)
		Gutsche, H.-K. Steuerungsmöglichkeiten bei der Nachbildung wellenerzeugter Sandwanderungsvorgänge in hydraulischen Modellen des See- und Seehafenbaues
		Führböter, A. Elektrische Geber für elektronische Meßgeräte im wasserbaulichen Versuchswesen
		Janssen, W. Einige Untersuchungen für die Energieumwandlung an den Auslässen von Kühl- und Triebwasserleitungen sowie an Hochwasserentlastungsanlagen
		Schwarze, H. Modellversuche zur Ermittlung der Einflüsse von baulichen Maßnahmen im Tidegebiet auf die Tide
		Dursthoff, W. Hydrografische und hydrologische Außenarbeiten des Franzius-Instituts
		Burkhardt, O. Die studentischen Auslandsexkursionen des Lehrstuhls für Grund- und Wasserbau der Technischen Hochschule Hannover von 1952 bis 1965
26	1966	**Laucht, H.** Generalplan für einen Freihafen in Malta
		Aujeszky, L., Kontur, G. Das Problem der künstlichen Niederschlagserzeugung
		Nendza, H. Einflüsse auf die Tragfähigkeit von Zugpfählen mit Fußverbreiterung im Sandboden
		Rudavsky, A.-B. Energievernichter und Energieverzehrungsmethoden unter Überfallwehren
25	1965	**Winter, H.** Beitrag zur Berechnung der Grundwasserentspannung im Tidegebiet
		Brösskamp, H. Naßbaggerei und Bodentechnik. Abhängigkeit der Arbeitsvorgänge im Naßbaggerbereich vom Boden. Vorschläge für ein Versuchsprogramm zur Ermittlung fehlender Bodenprüfverfahren
		Franzius, L. Wirkung und Wirtschaftlichkeit von Rauhdeckwerken im Hinblick auf den Wellenauflauf
24	1964	**Aksoy, S.** Über den Kornwiderstand bei offenen Wasserläufen mit beweglicher Sohle
		Fekete, G. Vergleich verschiedener Binnenwasserstraßen auf Grund der möglichen Tragfähigkeitsausnutzung (TN-Faktor, TK-Faktor)
		Domzig, H. Schildvortriebsverfahren (Beitrag zum Ausbau der Tunnels)
		Führböter, A. Modellversuche für das Sturmflutsperrwerk Billwerder Bucht/Hamburg. Untersuchungen über die hydraulischen Belastungen von Toren verschiedener Art
		Wagner, H. Der moderne Tunnelbau im Schildvortrieb. Bericht über die wissenschaftliche Bearbeitung der Untergrundbahnbauten unter der Innenstadt von Hamburg
23	1963	**Löwenberg, H.** Einbau, Verdichtung und Verdichtungsprüfung von Sand beim Spülverfahren im Straßenbau

Continued on next page

Continued from previous page

Issue	Year	Author and Title
		Dettmers, D. Folgerungen aus den Versuchen über die Förderung von Sand-Wasser-Gemischen in Rohrleitungen
		Rogge, T. Über den Bau von Fähranlagen für den rollenden Verkehr
		Laucht, H. Von den Eigenschaften des Eises
22	1963	**Engel, H.** Über die Landgewinnung im Wattengebiet
		Kontur, G. Über die Lagerung hydraulisch geförderter Kohlenstaub-Asche von Kraftwerken
		Ströhmer, P. Die Abflußkennwerte für die Unterweser und ihre Veränderungen seit 1890. (Ein Beitrag zur Frage der Tidewellenberechnungen.)
		Aksoy, S. Modellversuche für das Einlaufbauwerk im St.P.s-River/Liberia
		Hensen, W., Burkhardt, O. Modellversuche für die Aller zwischen Ahlden und Westen
21	1962	**Hensen, W.** Modellversuche für den Vorhafen der Nordschleuse in Bremerhaven
		Hensen, W., Dursthoff, W. Modellversuche für die Ausbildung von Saugkrümmern des Kraftwerkes Westfalen der Vereinigten Elektrizitätswerke Westfalen A.G. in Dortmund
		Hensen, W., Führböter, A. Modellversuche über den Wellenauflauf an den Elbdeichen bei Finkenwerder
20	1961	**Hensen, W., Passlack, G.** Modellversuche für das Emder Fahrwasser
		Gutsche, H.-K. Über den Einfluß von Strandbuhnen auf die Sandwanderung an Flachküsten
19	1961	**Freiherr Schenk zu Schweinsberg, W.-R.** Beitrag zur Beschreibung des Baugrundverhaltens beim Druckluftvortrieb
		Weissenbach, A. Der Erdwiderstand vor schmalen Druckflächen
18	1960	**Rose, D.** Über die quantitative Ermittlung der Gezeiten und Gezeitenströme in Flachwassergebieten mit dem Differenzenverfahren
		Hensen, W., Schiemenz, F. Eine Fischtreppe in Stromlinienformen. Versuche mit lebenden Fischen und Modellversuche
		Hensen, W. Das Aufnahmevermögen von Sanden für Mineralölprodukte
		Hensen, W. Untersuchung der LÜDERSschen Sandfalle
		Hensen, W., Wittmer, H.-G. Modellversuche für die Abdämmung der Wellier Weserschleife (Staustufe Landesbergen)
		Hensen, W. Ein einfaches Tide-Steuergerät
		Hensen, W. Über Rauhigkeit und Ungleichförmigkeit
17	1960	**Dahme, H.** Die Sicherung der Nachtschiffahrt auf Binnenschiffahrtsstraßen
		Dillo, H.-G. Sandwanderung in Tideflüssen
		Führböter, A. Einige elektrische Meßverfahren im wasserbaulichen Versuchswesen
		David, K. Die Tragfähigkeit von Rammpfählen im Sandboden. Ein Beitrag zur Ermittlung der Pfahllasten nach erdstatischen Methoden
		Hensen, W. Auswirkung langperiodischer Wellen in Häfen
16	1959	**Passlack, G.** Über die Berechnung unvollkommener Überfälle bei Sohlenstufen
		Davoudzadeh, E. Beitrag zur Filterausbildung bei der Entwässerung von Feinböden
		Schnoor, E. Leitfaden für das Kubizierungsverfahren
		Krolewski, H. Über das Verhalten von Mineralöl im Boden
		Stehr, E. Berechnungsgrundlagen für Preßluft-Ölsperren
15	1959	**Hensen, W.** Modellversuche für die Unterweser und ihre Nebenflüsse

Continued on next page

Continued from previous page

Issue	Year	Author and Title
		Hensen, W. Modellversuche für die Unterweser und ihre Nebenflüsse
14	1958	**Brandenburg, C.** Über die Verdichtungsprüfung von Schüttungen aus gleichförmigen Sanden
		Blinde, A. Stufenweiser Ausbau von Klärteichdämmen unter Nutzung des Klärgutes
		Klein, H.-A. Ermittlung des Durchflusses aus Strömungsmessungen im Tidegebiet
		Magens, C. Seegang und Brandung als Grundlage für Planung und Entwurf im Seebau und Küstenschutz
13	1958	**Wittmer, H.-G.** Tideänderungen durch Einbauten in Tideflüssen
		Führböter, A. Modellversuche für Talsperren-Tiefschütze
		Krabbe, W. Über die Schrumpfung bindiger Böden
12	1957	**Zitscher, F.-F.** Möglichkeiten und Grenzen in der konstruktiven Anwendung von Asphaltbauweisen bei Küstenschutzwerken
11	1957	**Simons, H.** Über die Gestaltung von Schiffshebewerken
		Wagner, H. Die Luft-Durchlässigkeit wasserhaltiger Böden - Ein Beitrag zum Unterwassertunnelbau im Druckluftverfahren -
		Griesseier, H., Vollbrecht, K. Zur Problematik der modellmäßigen Darstellung litoraler Prozesse
		Dettmers, D. Ablagerungen in Druckrohrleitungen bei hydraulischer Förderung im Naßbaggerbetrieb
		Friedrich, W., Horst, H. FISCHERs Verfahren zur Aufschlüsselung des regionalen Wasserhaushaltes im Lichte neueren Wissens. Ein Beitrag zur Klärung des Wasserhaushaltsproblems
		Natermann, E. Abschließende Stellungnahme des Verfassers
10	1957	**Powell, W.** Gebrauch und Mißbrauch von wasserbaulichen Modellen
		Möller-Hartmann, W. Abfluß in offenen Dreiecksgerinnen
		Hensen, W. Modellversuche über den Strandabbruch an den Enden von befestigten Küstenstrecken - Lee-Erosion -
		Menze, G. Über die Tragfähigkeit von Rammpfählen unter Berücksichtigung des Kräfteverlaufes beim Rammen
		Hensen, W. Erprobungen von pneumatischen Wellenbrechern im Modell und in der Natur
9	1956	**Laucht, H.** Zustand und Entwicklungsmöglichkeiten des Hamburger Stromspaltungsgebietes der Elbe
		Natermann, E. FISCHERs Verfahren zur Aufschlüsselung des regionalen Wasserhaushaltes im Lichte neueren Wissens
		Simons, H. Bodenmechanische Untersuchungen an den Emsdeichen zwischen Papenburg und Leer
		Hensen, W. Zweite Zusammenstellung der wasserbaulichen Modellversuche, die in der Hannoverschen Versuchsanstalt für Grundbau und Wasserbau, Franzius-Institut der Technischen Hochschule Hannover, durchgeführt worden sind
		Hensen, W. Mitgliederverzeichnis der Gesellschaft der Förderer des Franzius-Instituts e.V. nach dem Stande vom 1.11.1956
		Schiemann, E. Bericht über die Auslands-Exkursion des Lehrstuhls für Grundbau und Wasserbau der Technischen Hochschule Hannover im Sommer 1956
8	1955	**Domzig, H.** Wellendruck und druckerzeugender Seegang
		Lamprecht, H.-O. Brandung und Uferveränderungen an der Westküste von Sylt
		Walther, H.-D. Modellversuche für die neue Westmole Helgoland

Continued on next page

Continued from previous page

Issue	Year	Author and Title
7	1955	**Vogl, K.-J.** Gründungen in schrumpf- und schwellfähigen Böden
		Giese, H. Über den räumlichen Erdwiderstand
		Jagau, H. Beitrag zur erdstatischen Berechnung des Fußwiderstandes von Pfählen
		Hensen, W. Modellversuche zur Bestimmung des Einflusses der Form eines Seedeiches auf die Höhe des Wellenauflaufes
		Hensen, W. Modellversuche mit pneumatischen Wellenbrechern
6	1954	**Hensen, W.** Modellversuche für die untere Ems (Text)
		Hensen, W. Modellversuche für die untere Ems (Abbildungen)
		Hensen, W. Sondermodellversuche für die untere Ems
5	1954	**Müller, F.-E.** Stahlrammpfähle Für Dalbenbau. Ergebnisse Von Großversuchen Im Nord-Ostsee-Kanal Bei Flemhude 1951
		Wiegmann, D. Der Erddruck Auf Verankerte Stahlspundwände, Ermittelt Auf Grund Von Verformungsmessungen Am Bauwerk
		Menze, G. Probebelastungen An Fertigbetonpfählen Und Stahlpfählen
		Hensen, W. Modellversuche Über Den Wellenauflauf An Seedeichen Im Wattengebiet
4	1953	**Jarlan, G.** Der Hafen von Le Havre
		Jarlan, G. Die Ausbildung des Ingenieurs in Frankreich
		Dettmers, D. Beitrag zur Frage der Belüftung von Tiefschützen
		Helm, K., Möckel, W., Wöltinger, O. Über die gegenseitige Beeinflussung von Schiffen und Kanälen
		Hensen, W. Modellversuche für den Amerika-Hafen in Cuxhaven
3	1953	**Iribarren, R.** Beim Brechen von Wellen unvermutet auftretende heftige Drücke
		Boos, W. Die Messung kleiner Strömungsgeschwindigkeiten im wasserbaulichen Versuchswesen
		Hensen, W. Das Eindringen von Salzwasser in die Gezeitenflüsse und ihre Nebenflüsse, in Seekanäle und in Häfen
		Steinfeld, K. Über den räumlichen Erdwiderstand
		Petermann, H. Die innere Verformung als Festigkeitsmerkmal von Sand
		Hensen, W. Mitgliederverzeichnis der Gesellschaft der Förderer des Franzius-Instituts e.V. nach dem Stande vom 1.1.1953
2	1952	**Seifert, R.** Maßstäbe der Modellähnlichkeit grundrißgetreuer Gerinne bei Tiefenverzerrung und Gefällverstärkung
		Hensen, W. Untersuchungen der Standfestigkeit von Rohrfestpunkten
		Schiemenz, F. Versuche mit Glasaalen. Beitrag zur Frage des Hineinleitens wandernder Fische in die untere Mündung einer Fischtreppe
		Hansen, W. Beobachtungen des Windstaus und Triftstroms im Modellkanal
		Natermann, E. Die Entschleierung der Grundwasserganglinie
		Schulz, H. Probleme der gewässerkundlichen Meßtechnik
		Helm, K., Moeckel, W. Einfluß des Wasserquerschnittes von Kanalprofilen auf Absenkung, Vertrimmung und Steuereigenschaften eines großen Tankschiffes
		Hensen, W. Kleine Studien aus dem Tidegebiet Nr. 1: Über die Fortschrittsgeschwindigkeit der Tidewelle in einem Flusse

Continued on next page

Continued from previous page

Issue	Year	Author and Title
1	1952	**Hensen, W.** Zusammenstellung der wasserbaulichen Modellversuche, die in der Hannoverschen Versuchsanstalt für Grundbau und Wasserbau, Franzius-Institut der Technischen Hochschule Hannover, seit dem 1. April 1948 durchgeführt worden sind
		Simons, K. Bericht über die Auslands-Exkursion des Lehrstuhls für Grundbau und Wasserbau an der Technischen Hochschule Hannover im Frühjahr 1952
		Hensen, W. Gedanken und Anregungen zu studentischen Exkursionen
		Streck, A. Die Bewertung des Bodens als Baugrund und Baustoff
		Graupner, A. Die Baugrundkarte von Hildesheim als Beispiel einer Baugrundkartierung
		Steinfeld, K. Über Theorie und Praxis elektroosmotischer Bodenentwässerung
		Schmidbauer, J. Die Fließsand- und Schwimmsanderscheinung
		Paproth, E. Neuere Druckluftgründungen
		Streck, A. Die erdstatische Berechnung der Tragfähigkeit von Pfählen
		Förster, K. Bodenmechanische Erfahrungen bei den Kriegsschäden im Hamburger Hafen
		Petermann, H. Auszug aus dem Vortrag 'Baugrundfragen des Straßenbaues'
		Sichardt, W. Überblick über die Wasserhaltungsverfahren (Anwendungsmöglichkeiten und -grenzen, Fortschritte, Aussichten)
		Schmidbauer, J. Bemessung von Straßen- und Flugplatzdecken
		Streck, A. Aktuelle Fragen des Deichbaues im Bergbaugebiet
		Tübbesing, K. Über die hydrologische Baugrundkarte von Hannover

ISSN 0340-0077

Herausgeber
Leibniz Universität Hannover
Franzius-Institut für Wasserbau und Küsteningenieurwesen
Nienburger Str. 4, 30167 Hannover
Prof. Dr.-Ing. habil. T. Schlurmann

www.fi.uni-hannover.de